Bidimensional study of the ionisation mechanisms of the diffuse gas in galaxies of the local universe with MUSE

by
Raúl González Díaz

A dissertation submitted in partial fulfilment of
the requirements for the degree of

DOCTOR IN ASTROPHYSICS

at

Instituto Nacional de Astrofísica, Óptica y Electrónica
July 2024
Tonantzintla, Puebla, México

Advisored by:

Dr. Fernando Fabián Rosales Ortega, INAOE
Dr. Lluís Galbany González, Institute of Space Sciences

under international supervision with

UAB
Universitat Autònoma
de Barcelona

ICE INSTITUT DE
CIÈNCIES
DE L'ESPAI

CSIC
CONSEJO SUPERIOR DE INVESTIGACIONES CIENTÍFICAS

IEEC

Agradecimientos

Primeramente agradezco a CONAHCyT por la beca de doctorado, y a INAOE y la UAB por permitirme realizarlo en cotutela internacional. En particular, quiero agradecer a los investigadores de la coordinación de astrofísica por haberme apoyado y ayudado cuando lo he necesitado. Quiero dar las gracias especialmente a mis asesores, Fabián y Lluís, por todas las innumerables enseñanzas que tan incansablemente me han proporcionado, y por animarme siempre a formarme como científico de la mejor manera; con rigor, buenas prácticas, compañerismo y pasión.

Agradezco a todos mis compañeros, a Bety, Luisa, Edgar, Ara, Arvi, Emmaly, y un largo etc., por soportar a semejante esperpento que les ha llegado de sorpresa. Gracias también a los miembros de la escuela de esgrima histórica de Puebla, *ARCANT*. Llevaré siempre conmigo nuestro lema, ¡DESTREZA Y HONOR! Gracias a todas las personas que he conocido durante mis viajes, en México, Italia, Uruguay... por hacerme ver que aunque estés lejos de casa, tu casa puede estar en cualquier parte.

Y en casa... gracias a Mamá y a Papá, Mariana y Félix, por confiar en mí más de lo que probablementre llegue yo a confiar en mí mismo en mi vida. A mis hermanas, Lina y Horten, por tratarme siempre con un cariño que no sé si merezco, a mi tia y a mí abuela, Cándida y Hortensia, por preocuparse tanto por mí. A ésta última no sólo le doy solo las gracias, le doy una disculpa. A todos mis amigos de mi pueblo, a Balta, José Alberto, Zepe, Antonia, Javi... perdón por desaparecer siempre, y gracias por recibirme siempre como si nunca me hubiera ido. A mis Scronchos les agradezco finalmente haberme ayudado durante tanto tiempo a mejorar tanto como persona. Siempre os lo he dicho y nunca me cansaré de hacerlo, me habéis ayudado más de lo que pensáis. Cada uno de vosotros representáis una de mis virtudes. He aprendido mucho de vosotros. Gracias de corazón.

No ha sido fácil en ningún aspecto, y no sé verbalizar todo lo que he aprendido y sentido estos últimos años. Pero siempre supe que toda aventura es divertida, por dura que sea, y se puede narrar en una *Laugh Tale*. Por eso finalizo dándole las gracias y dedicándole este escrito a mi mayor enemigo, y mi mayor aliado. A mí mismo.

Las palabras más importantes que puede pronunciar alguien son: «Lo haré mejor.» No son las palabras más importantes que pueda pronunciar cualquier persona. Yo soy cualquier persona, y son esas las que necesitaba decir. Un viaje incluirá dolor y fracaso. No son solo los pasos adelante los que debemos aceptar, sino también los traspiés. Las dificultades. El conocimiento de que fracasaremos. Pero si nos detenemos, si aceptamos la persona que somos al caer, el viaje concluye. Ese fracaso pasa a ser nuestro destino. Amar el viaje implica no aceptar ese final. He descubierto, por medio de dolorosas experiencias, que el paso más importante que puede dar alguien es siempre el siguiente. Sin duda, habrá quien se sienta amenazado por esta narración. Quizá unos pocos se sientan liberados. La mayoría, simplemente, sentirá que no debería existir. Debo escribirla de todos modos.

Porque este viaje lo comencé solo y lo terminé solo. Pero no lo caminé solo.

Viaje antes que destino.

Resumen

En este trabajo, presentamos el proyecto Bidimensional Exploration of the warm-Temperature Ionised gaS (BETIS), enfocado en el estudio del gas ionizado difuso (DIG) en galaxias espirales cercanas utilizando el espectrógrafo de campo integral MUSE. El objetivo principal es comprender los diversos mecanismos de ionización que dan lugar al DIG. Esto implica un análisis espacialmente resuelto de especies de alta y baja ionización en espectros ópticos. Hemos introducido un nuevo método para definir espectroscópicamente el DIG, adaptable a diferentes resoluciones de galaxias. Inicialmente, hemos utilizado una técnica de binning adaptativo basada en la relación señal-a-ruido (S/N) de la línea [S II] para mejorar la S/N de otras líneas. Posteriormente creamos una máscara para eliminar regiones H II brillantes y débiles. También hemos evaluado la idoneidad de usar el ancho equivalente de Hα (EW$_{H\alpha}$) para definir el DIG y su régimen de ionización. Hemos encontrado que para EW$_{H\alpha}$< 3Å, esperado de estrellas evolucionadas de baja masa y alta temperatura (HOLMES), el valor depende de la técnica de síntesis de poblaciones utilizada. El análisis de la muestra revela una fracción de DIG consistente del 40%-70% en todas las galaxias. Las tendencias de los cocientes [N II] /Hα , [S II] /Hα , [O I] /Hα y [O III] /Hβ indican una correlación entre la ionización en el DIG y las regiones H II , vinculada al brillo superficial de Hα ($\Sigma_{H\alpha}$). Los diagramas de diagnóstico muestran que el DIG generalmente cae dentro de los cocientes de línea correspondientes a la fotoionización debida a la formación estelar (FE), con un desplazamiento que sugiere ionización debido a choques rápidos. Sin embargo, el análisis individual de las galaxias indica que dicho desplazamiento es atribuido a galaxias Seyfert en la muestra. Esto sugiere que las galaxias con núcleo activo deben ser analizadas por separado, ya que su emisión es indistinguible del DIG de alta excitación.

En un segundo estudio dentro del proyecto BETIS, el enfoque está en el gas ionizado difuso extraplanar (eDIG), un componente clave para entender los procesos de retroalimentación entre los discos y halos galácticos. Hemos aplicado la metodología de binning del primer estudio de BETIS a una muestra de ocho galaxias observadas con MUSE. Los cocientes [N II] /Hα , [S II] /Hα , [O I] /Hα y [O III] /Hβ muestran una estructura de ionización compleja en los halos galácticos, influenciada por la distribución espacial de las regiones H II . Hemos identificado al escape de fotones del continuo de Lyman de las asociaciones OB como la principal fuente de ionización, con la temperatura electrónica y el cociente de ionización S+/S dependiendo de la distribución de las regiones H II dentro de los discos galácticos. El análisis excluye a los HOLMES como fuentes significativas de ionización para explicar los inusuales cocientes de línea a mayores distancias del plano medio galáctico. En cambio, hemos identificado los choques de los mecanismos de retroalimentación relacionados con la FE como fuentes de ionización secundarios prometedores para el eDIG. Los modelos que incorporan ionización por choques rápidos y fotoionización por FE sugieren que la contribución de choques rápidos a la ionización del eDIG varía del 20% al 50% en la muestra, con variaciones locales de hasta el 20% dentro de los halos individuales de las galaxias. Esto se correlaciona con la presencia de filamentos y componentes estructurales en los halos galácticos. Las altas densidades y los altos cocientes de [O I] /Hα , características del gas ionizado comprimido por choques, respaldan la presencia de choques, probablemente provenientes de la retroalimentación en regiones de intensa FE dentro del disco galáctico.

Abstract

In this work, we present the Bidimensional Exploration of the warm-Temperature Ionised gaS (BETIS) project, focused on studying the diffuse ionised gas (DIG) in nearby spiral galaxies using the MUSE integral field spectrograph (IFS). The main goal is to understand the various ionisation mechanisms of the DIG. This involves a spatially resolved analysis of high- and low-ionisation species in optical spectra. We introduce a new method for spectroscopically defining the DIG, adaptable for different galaxy resolutions. Initially, we use an adaptive binning technique based on the signal-to-noise ratio (S/N) of the [S II] line to enhance the S/N of other lines. Then, we create a DIG mask by removing emissions from bright and faint H II regions. The suitability of using Hα equivalent width (EW$_{H\alpha}$) to define the DIG and its ionisation regime was also assessed. We find that for EW$_{H\alpha}$< 3Å, expected from hot low-mass evolved stars (HOLMES), the value depends on the population synthesis technique used. Analysis of the sample reveals a consistent DIG fraction of 40%-70% across all galaxies. The average radial distribution of the [N II] /Hα , [S II] /Hα , [O I] /Hα , and [O III] /Hβ ratios is enhanced in the DIG regimes by up to 0.2 dex. These trends indicate a correlation between ionisation in the DIG and H II regions, linked to the Hα surface brightness ($\Sigma_{H\alpha}$). Diagnostic diagrams show that the DIG generally falls within line ratios corresponding to photoionisation from star formation, with an offset suggesting ionisation due to fast shocks. However, individual galaxy analysis indicates that DIG ionisation is primarily from star formation, with the offset attributed to Seyfert galaxies in the sample. This suggests that galaxies with active galactic nucleus activity should be separately analysed, as their emission is indistinguishable from high-excitation DIG.

In a second study within the BETIS project, the focus is on extraplanar diffuse ionised gas (eDIG), a key component for understanding feedback processes between galactic discs and halos. We apply the binning methodology from the first BETIS study to a eight edge-on galaxies observed with MUSE. The [N II] /Hα , [S II] /Hα , [O I] /Hα , and [O III] /Hβ ratios show a complex ionisation structure in galactic halos, influenced by the spatial distribution of H II regions. We identify the Lyman continuum photon leakage from OB associations as the main ionisation source, with electron temperature and S+/S ionisation ratio depending on H II region distribution within galactic discs. The analysis excludes HOLMES as significant ionisation sources for explaining unusual line ratios at greater distances from the galactic midplane. Instead, we identify shocks from star formation-related feedback mechanisms as promising secondary ionisation sources for the eDIG. Models incorporating ionisation from fast shocks and star formation photoionisation suggest that the ionisation due to fast shocks in the eDIG ranges from 20% to 50% across the sample, with local variations up to 20% within individual galaxy halos. This correlates with the presence of filaments and structural components in galaxy halos. High-density, high [O I] /Hα ratios, characteristic of shock-compressed ionised gas, support the presence of shocks, likely from feedback in regions of intense star formation within the galactic disk.

Contents

Glossaries

List of Figures

List of Tables

List of acronyms

AGB	Asymptotic Giant Branch
AGN	Active Galactic Nuclei
AIS-GALEX	All-Sky Survey of the Galaxy Evolution Explorer
AMUSING	All-weather MUse Supernova Integral-field of Nearby Galaxies
BC03	Bruzual-Charlot 2003
BETIS	Bidimensional Exploration of the warm-Temperature Ionised gaS
BPT	Baldwin-Phillips-Terlevich
CALIFA	Calar Alto Legacy Integral Field spectroscopy Area survey
CARS	Close AGN Reference Survey
CB07	Charlot-Bruzual 2007

CCD	Charge-Coupled Device
CDM	Cold Dark Matter
CGM	Circumgalactic Medium
CNM	Cold Neutral Medium
DIG	Diffuse Ionised Gas
DM	Dispersion Measure
eDIG	extraplanar Diffuse Ionised Gas
EM	Emission Measure
EUV	Extreme Ultraviolet
ESO	European Southern Observatory
EW	Equivalent width
FIR	Far Infrared
FITS	Flexible Image Transport System
FoV	Field of View
FUV	Far Ultraviolet
FWHM	Full Width at Half Maximum
GALEX	GALaxy Evolution Explorer
GASP	GAs Stripping Phenomena
GTM	Great Millimeter Telescope
HIM	Hot Ionised Medium
HOLMES	Hot Low-Mass Evolved Stars
IFS	Integral Field Spectroscopy
IFU	Integral Field Unit
IGM	Intergalactic Medium
IMF	Initial Mass Function
IR	Infrared
ISM	Interstellar Medium
LIER	Low-Ionisation Emission-line Region
LINER	Low-Ionisation Nuclear Emission-line Region
LLAGN	Low-Luminosity Active Galactic Nuclei
LTE	Long Term Evolution
Lyc	Lyman continuum

MAD	Major Axis Distance
MaNGA	Mapping Nearby Galaxies at APO
MAST	Mikulski Archive for Space Telescopes
MUSE	Multi Unit Spectroscopic Explorer
MW	Milky Way
NUV	Near Ultraviolet
PHANGS	Physics at High Angular resolution in Nearby GalaxieS
PrISM	Progressive Integral Step Method
PSF	Point Spread Function
SAMI	Sydney-AAO Multi-object Integral Field Spectrograph
SDSS	Sloan Digital Sky Survey
SED	Spectral Energy Distribution
SF	Star Formation
SFR	Star Formation Rate
sSFR	specific Star Formation Rate
S/N	Signal-to-Noise
SN	Supernova
SNR	Supernova Remnant
SSP	Simple Stellar Population
TIMER	Time Inference with MUSE in Extragalactic Rings
TML	Turbulent Mixing Layer
TP-AGB	Thermally Pulsing Asymptotic Giant Branch
UV	Ultraviolet
UVES	Ultraviolet Visual Echelle Spectrograph
VLT	Very Large Telescope
WCS	World Coordinates System
WFM	Wide Field Mode
WHAM	Wisconsin H-Alpha Mapper
WIM	Warm Ionised Medium
WNM	Warm Neutral Medium

Chapter 1

Introduction

Understanding the relationship between stellar formation processes and the interstellar medium (ISM) is a key step in discerning the complexity in the evolutionary history of galaxies. One problem in this regard has been understanding the nature and importance of feedback processes in which massive stars deposit energy into the interstellar medium through photoionisation, stellar winds, and supernovae. This feedback mechanism affects the physical and dynamic state of the ISM and, therefore, it has an influence on the rate and distribution of stellar formation in galaxies (Ceverino & Klypin 2008, 2009; Hopkins et al. 2014; Klessen & Glover 2016; Gatto et al. 2017; Grisdale 2017). In this context, the existence of a warm and ionised component of the ISM that is ubiquitously distributed in our Galaxy and extragalactic sources has been known for decades. This component is known as the diffuse ionised gas (DIG; Hoyle & Ellis 1963; Hewish et al. 1968; Reynolds 1971; Reynolds et al. 1973; Guélin 1974; Reynolds 1985, 1989; Kennicutt et al. 1989; Rand et al. 1990; Dettmar 1990).

The main objective of this thesis is to shed light on the nature and characteristics of the DIG, particularly the possible ionisation mechanisms responsible for this diffuse component of the ISM. To achieve this, we present an innovative methodology for characterising and analysing the DIG by utilising the simultaneous spectral and spatial information provided by integral field spectroscopy.

In this first chapter, we contextualise the DIG as a component of the ISM and review the current state of research in this field.

1.1 The phases of the interstellar medium

Galaxies are mostly empty, with the stars typically separated by distances ranging from 2 to 3 parsecs (pc). If we take the Milky Way and the Solar System as example, the stars only fill ~3×10^{-10} of the volume available in the Galaxy (Tielens 2005). The rest of the volume is predominantly occupied by the ISM, which is faint and composed mainly of hydrogen (H), helium (He), and traces of metals (Z). The evolution of stars is closely linked to the ISM, as stars are formed from the gas and dust that constitute the ISM. Throughout their lifetimes, many stars return part of their material to the ISM through various processes, such as stellar winds or supernova explosions (Weaver et al. 1977; Gray et al. 2019; Sarkar et al. 2022). This recycled material is enriched with new elements created during nucleosynthesis in the interiors of stars, contributing to the formation of new stars. Therefore, studying the ISM is crucial for understanding both stellar and galactic evolution, given the complex dynamics, structures, and physical processes that occur within it.

Besides the dust (small solid particles), which constitutes only 1% of the ISM by mass, the gaseous component of the ISM can be found in different states of matter and temperatures, each manifesting its properties differently in observations (Lequeux 2005). The ISM phases are presented as follows.

1.1.1 The cold neutral medium

The cold neutral medium (CNM) corresponds to the cold ($T < 10^2$ K) atomic (H I) and molecular (H_2) hydrogen gas. The H I contains most of the mass of the ISM, its density is relatively high (~20 cm^{-3}) and its distribution is extremely inhomogeneous, shaping filaments, sheets and shell along the galactic plane (Draine 2011). These characteristics allow the neutral atomic hydrogen to transition between two hyperfine sublevels, when the spins of the proton and electron transition from being parallel to being antiparallel, emitting spontaneously a photon of energy 5.87 μeV, or $\lambda = 21.1$ cm. Consequently, observing the 21-cm line enables the measurement of the mass, distribution, and kinematics of atomic gas in galaxies (Kulkarni & Heiles 1987; Heiles & Troland 2003).

The CNM also presents different species (e.g., C, N, O) whose fundamental energy levels are split in fine-structure levels due to interactions between the orbital angular momentum L of the electrons and their spin S. The coupling between L and S allows forbidden transitions between different total angular momentum ($J = L + S$). The de-excitation of the upper levels in small atoms of the CNM usually occurs via collisions, resulting in the emission of a far-infrared (FIR) photon (see figure 1.1).

That collisional de-excitation occur with a probability that depends linearly with the electron density (n_e), and also depends on the electron temperature ($\propto T_e^{-1/2}$). When the n_e is much higher than the critical density—i.e., the density threshold where collisions dominate the de-excitation of the upper levels—the levels are in thermal equilibrium. In this state, the intensity of the FIR lines depends only on the density of the respective ion. Therefore,

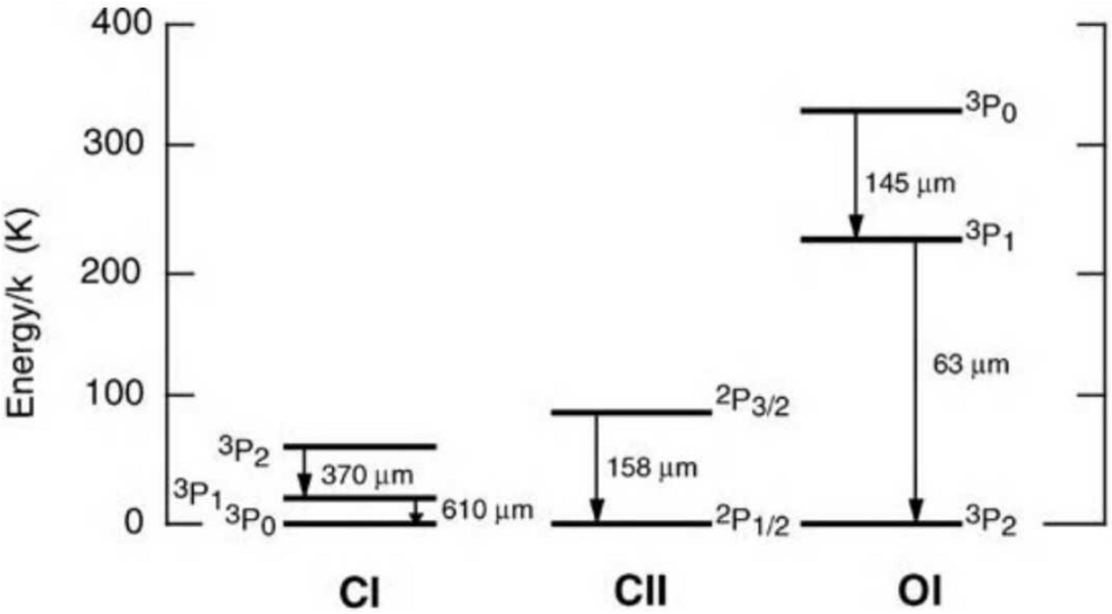

Figure 1.1: Example of the energy levels of the C, C^+ and O species and its FIR transitions. Figure adapted from Lequeux (2005).

studying these fine-structure lines is of major importance in the physics of the ISM, as they are the main coolant of the CNM when temperatures are below 100 K (Lequeux 2005). In addition, not only the emission lines associated to the CNM are relevant in the study of the ISM, the absorption features of neutral elements such as the neutral sodium doublet at 5889 and 5895 Å or the of neutral calcium at 4226 Å, providing relevant information on the chemical composition and physical conditions in the ISM.

On the other hand, the H_2 can be usually found as high density gravitationally bounded clouds (10^3-10^4 cm^{-3}), mixed with other molecules (e.g., CO, H_2O or H_2CO; Turner 1994; Taylor et al. 1998). These clouds usually emits termically (and by electronic transitions) in milimetric-submilimetric wavelengths, as seen in figure 1.2.

In contrast with neutral atoms, molecules can present different types of transitions.

- Electronic transitions: These transitions are the analogous to the atomic transitions. Usually found in the far-UV, their energy is in the order of the eV. For instance, all electronic transitions of the H_2 molecule are at $\lambda < 115$ nm. The CO and OH molecules electronic transitions can also be found in the far-UV, while other molecules, such as CN or C_2 present transitions in the near-UV and near-IR respectively.
- Vibrational transitions: The energy levels resulting from these transitions are due to the quantisation of the different vibrational modes of the molecule. With energies $\sim 10^{-1}$ eV, these transitions can be generally found in the near-IR. In areas where ionisation is primarily influenced by shocks or photodissociation, the excited vibrational levels can be populated through collisions or by radiative cascades from electronic levels (fluorescence).

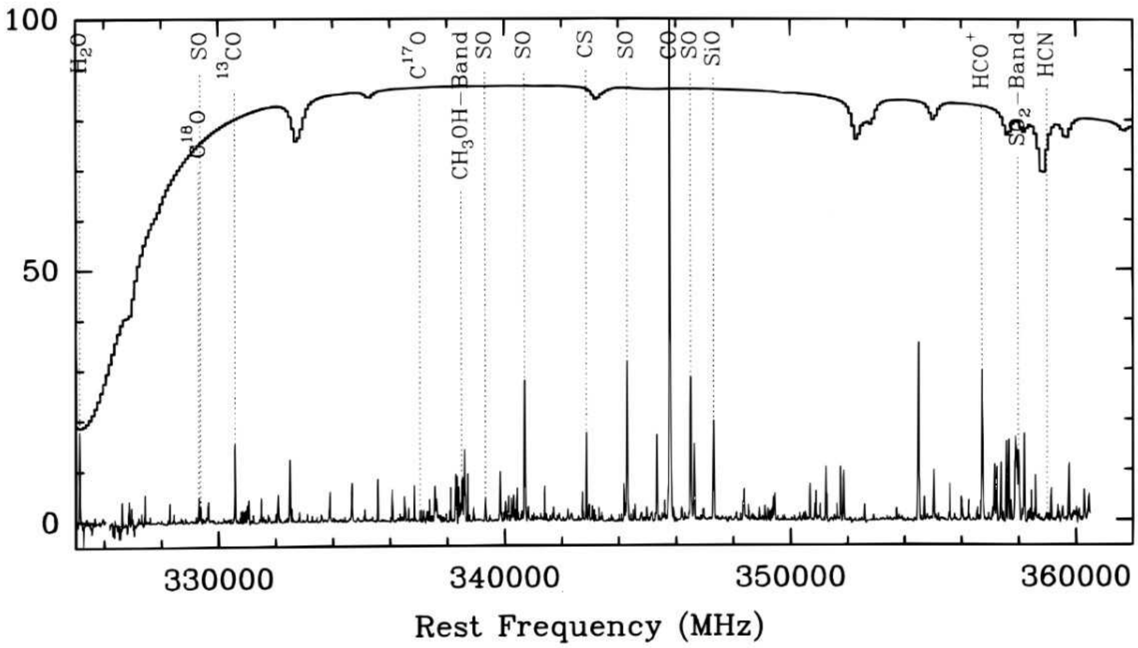

Figure 1.2: Example of a submilimetric spectrum, depicting the different molecular transitions found in the Orion molecular cloud, at T = 60 K. The atmospheric transmission is overplotted above the spectrum. Figure courtesy of Schilke et al. (2001).

- Rotational transitions: Similarly to vibrational transitions, rotational transitions result from the quantisation of the different rotational modes of the molecule. With energies of the order of meV, the transitions can be found between the submilimetric and centimetric range, except for the H_2 molecule, whose rotational transitions are in the IR range.

Each electronic transition can be decomposed into vibrational transitions, and each vibrational transition into rotational transitions (ro-vibrational bands), with the rotational transitions being the least energetic. Additionally, in molecules such as OH and CH, the interaction between the orbital angular momentum of the electron and the rotational modes of the molecule splits the rotational energy levels, producing what are known as Λ-doubling levels (Lequeux 2005).

The complexity of molecular transitions, especially in polyatomic molecules, is reflected in the emission spectra of molecular clouds. These spectra display a wide range of transitions from different molecules with various electronic, vibrational, and rotational states, as shown in Figure 1.2. These complex molecular clouds are the scenarios where the star formation takes place, due to their gravitational collapse, for instance, the Cat's Paw nebula (see figure 1.3[1]).

---

[1] ©ALMA (ESO/NAOJ/NRAO), T. Hunter; C. Brogan, B. Saxton (NRAO/AUI/NSF); GLIMPSE, NASA/JPL-Caltech

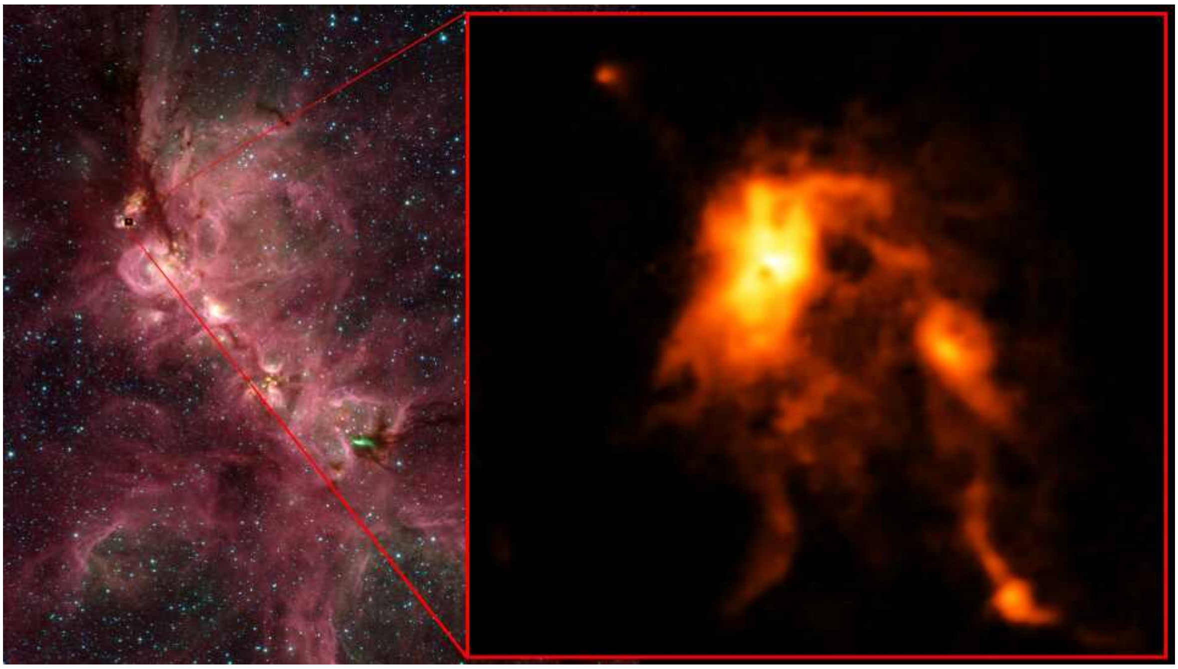

Figure 1.3: The Cat's paw nebula. Left is the infrared image of the star-formation complex from NASA's Spitzer Space Telescope. Right the image of a portion of the nebula from the Submillimeter Array (SMA) in Hawaii, depicting a protocluster; the dense cloud of gas and dust harbouring new-born stars.

1.1.2 The hot ionised medium

The hot ionised medium (HIM) is characterised by a hot (T $\sim 10^5$-10^6 K) and low density ($\sim 10^{-3}$ cm^{-3}) ionised gas.

At these temperatures, gas can be spontaneously ionised via atom-atom collisions. The liberated electrons quickly reach thermal equilibrium and are largely responsible for further ionisation, resulting in the formation of multiple-charged ions (Boehringer & Fabian 1989). Ions such O^{5+} or O^{6+} can be found at temperatures of 3×10^5 - 10^6 K, whose emission lines can be observed in X-ray band (McCray & Snow 1979; Tielens 2005; Draine 2011). When atoms collide with a free electron or absorbs a photon with sufficient energy, a electron can be ejected from its innermost layer (the K-layer). The free space when the electron in the K-layer is liberated is then occupied with an electron of outer layers (L- or M-layer). This transition results in the emission of an X-ray photon ($K\alpha$, $K\beta$, and so on, as depicted in figure 1.4).

Multi-charged ions can also emit optical forbidden lines, firstly identified in the solar corona. For this reason, this hot gas is also known as "coronal gas". The coronal gas can be heated and ionised through shocks driven by stellar winds from OB associations and by supernova explosions, which is usually drawn off the halo in the form of galactic fountains (Shapiro & Field 1976; McCray & Snow 1979; Heiles 1990). This gas thermalises very rapidly in the halo

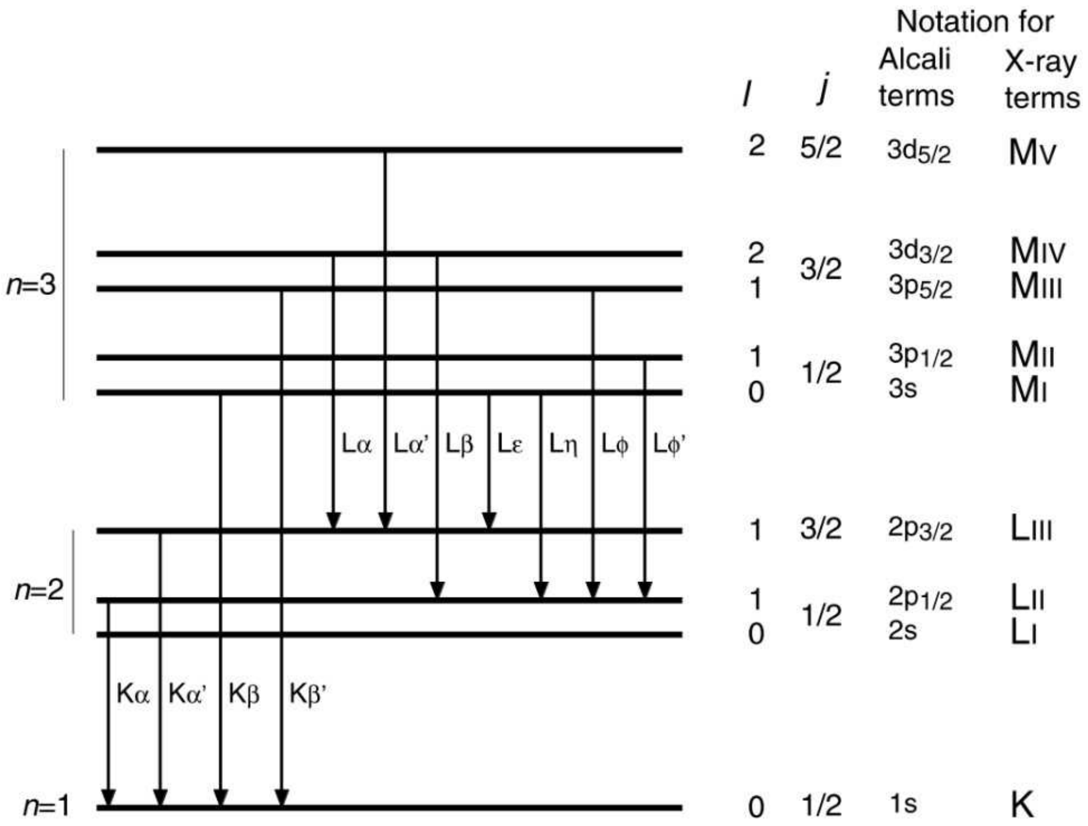

Figure 1.4: Energy diagram of the X-ray transitions. Adapted from Born (1969) and Lequeux (2005).

(~Myr), "condensing" into clouds that eventually rain down onto the disk (Bregman 1980; Mac Low et al. 1989).

In addition to the line emission, the thermal X-ray continuum consists of free-free emission and free-bound emission. As the optical depth is generally small in the ISM, the emissivity is proportional to $T^{1/2}exp(-h\nu/kT)$, so the temperature can be measured.

Figure 1.5 shows the Chandra x-rays image of the Crab Nebula and a composite x-rays, optical and infrared image[2]. The contribution of the coronal gas in this supernova remnant is clear when comparing with the rest of the emission.

1.1.3 The warm neutral and ionised medium

The warm neutral medium (WNM) is mainly atomic gas at $T \approx 10^4$K and density ~ 0.6 cm^{-3}, that fills over 40% of the ISM in volume (Mebold & Hills 1975). The WNM is usually ionised by ultraviolet (UV) radiation of hot stars or other physical mechanisms such as fast shocks, x-ray ionisation or high-energy particles. In particular, when a star is recently formed in a molecular H_2 cloud, the UV radiation from the new-born star dissociates the H_2 into

---

[2] ©NASA/CXC/SAO, NASA/STScI, NASA-JPL-Caltech.

Figure 1.5: Left: Chandra x-ray image of the Crab Nebula image. Right: Composite x-rays, optical and infrared image with Chandra (blue and white), Hubble (purple), and Spitzer (pink) respectively.

H I (Black & Dalgarno 1976; Abgrall et al. 1992), and then photoionises the H I into H^+, resulting in a H II region (e.g., M78, see figure 1.8[3]). These regions are then the best tracers of recent star formation.

The simplest H II region consists of an ionised hydrogen sphere with a hot OB star at its centre, where the number of recombinations equals the number of ionisations, resulting in an ionisation equilibrium. The radius where the ionisation equilibrium is reached delimits a region known as *Strömgren sphere.*

The Lyman continuum (Lyc) radiation from the young OB stars keeps ionising the interior of the H II region, as photons of energy > 13.6 eV are primarily absorbed by the hydrogen. If the photons energy is higher than 24.6 eV, an inner region of ionised He I is produced. Thus, one of the most relevant emission features of these regions are the recombination of the H and He (see figure 1.6).

A most realistic approach of an H II region is of an heterogeneous region with several new born ionising stars in its interior, with a more complex ionisation structure and an irregular density distribution. In this more realistic scenario, not all Lyc photons are absorbed within the cloud; some can escape into the surrounding, lower-density medium. In this case, the cloud is considered *density-bounded.*

The spectrum of an H II region (see figure 1.7 a example) is dominated by hydrogen recombination (permitted) lines, but recombination lines of other elements such as He, C, and O are also present, though with lower intensity. The intensity of these lines depends on the temperature and density of the gas. This is particularly interesting for the Balmer recombination lines, as the ratios between the intensities at different energy levels (e.g., $H\alpha / H\beta$) can be used to estimate the reddening and extinction in the direction of the H II region by comparing the theoretical and observed ratios.

---

[3] ©ESA/Euclid/Euclid Consortium/NASA, image processing by J.-C. Cuillandre (CEA Paris-Saclay), G. Anselmi

The majority of the strongest lines emitted by an H II region are forbidden transition of ions such as O^+, O^{2+}, N^+ or S^+, being [S II] $\lambda\lambda 6717, 31$, [N II] $\lambda 6584$, or [O III] $\lambda 5007$ various of the most common transitions in the optical range (Strömgren 1939; Morgan et al. 1952; de Vaucouleurs et al. 1991; Osterbrock & Ferland 2006; Draine 2011).

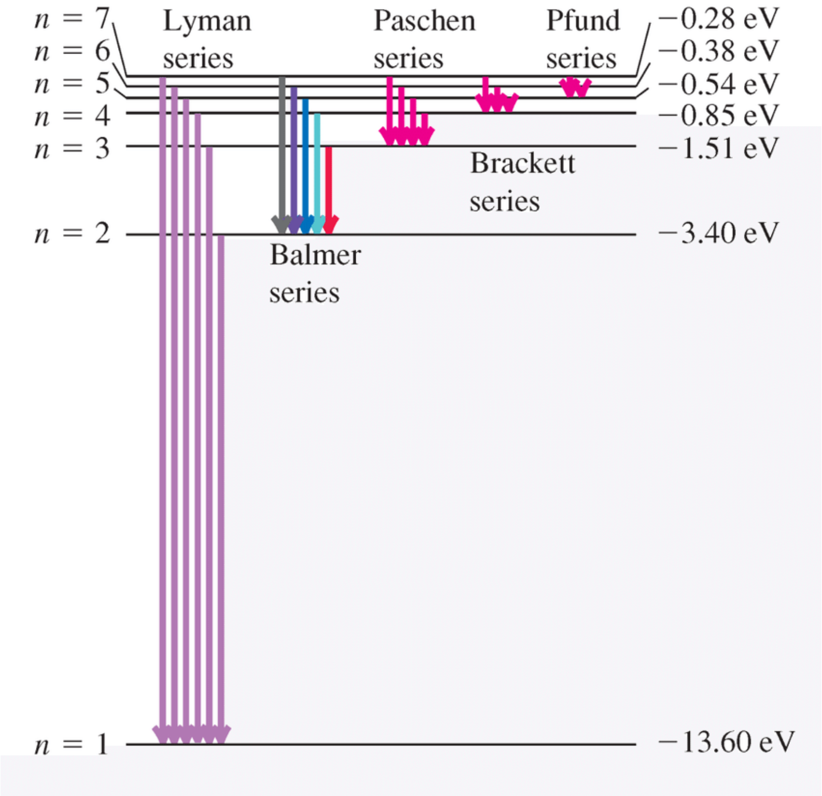

Figure 1.6: Hydrogen recombination energy levels. The Lyman series, those recombinations to the fundamental level, emit UV photons. Successively, Balmer series at n = 2 correspond to optical lines, and Paschen, Brackett and Pfund series at n = 3, 4 and 5 correspond to near-, mid-, and far-IR respectively. Figure adapted from Young et al. (2020).

In addition, other physical processes can produce ionised nebulae in the WNM. For instance, the ejection of the external layers of a red-giant star during the asymptotic giant branch (AGB) phase can result in a planetary nebulae (e.g., The Ring Nebula, see figure 1.8[4]), whose structure and properties can be studied similarly to H II regions, but exhibit strong emission of collisionally excited lines, such as [O III] and [N II] (Kwok 2000; 200 2001). Similarly, supernova remnants (SNRs; e.g., Cassiopea-A, see figure 1.8[5]), which are nebulae resulting from the explosions of stars with $M > 8M_\odot$ at the end of their lives and the thermonuclear explosions of white drafts, are ionised and heated by shock waves, also producing collisionally excited line emission in the optical range (Weiler & Sramek 1988; Fesen & Hurford

---

[4] ©ESA/Webb, NASA, CSA, M. Barlow (UCL), N. Cox (ACRI-ST), R. Wesson (Cardiff University)

[5] ©X-ray: NASA/CXC/SAO; Optical: NASA/ESA/STScI; IR: NASA/ESA/CSA/STScI/Milisavljevic et al., NASA/JPL/CalTech; Image Processing: NASA/CXC/SAO/J. Schmidt and K. Arcand

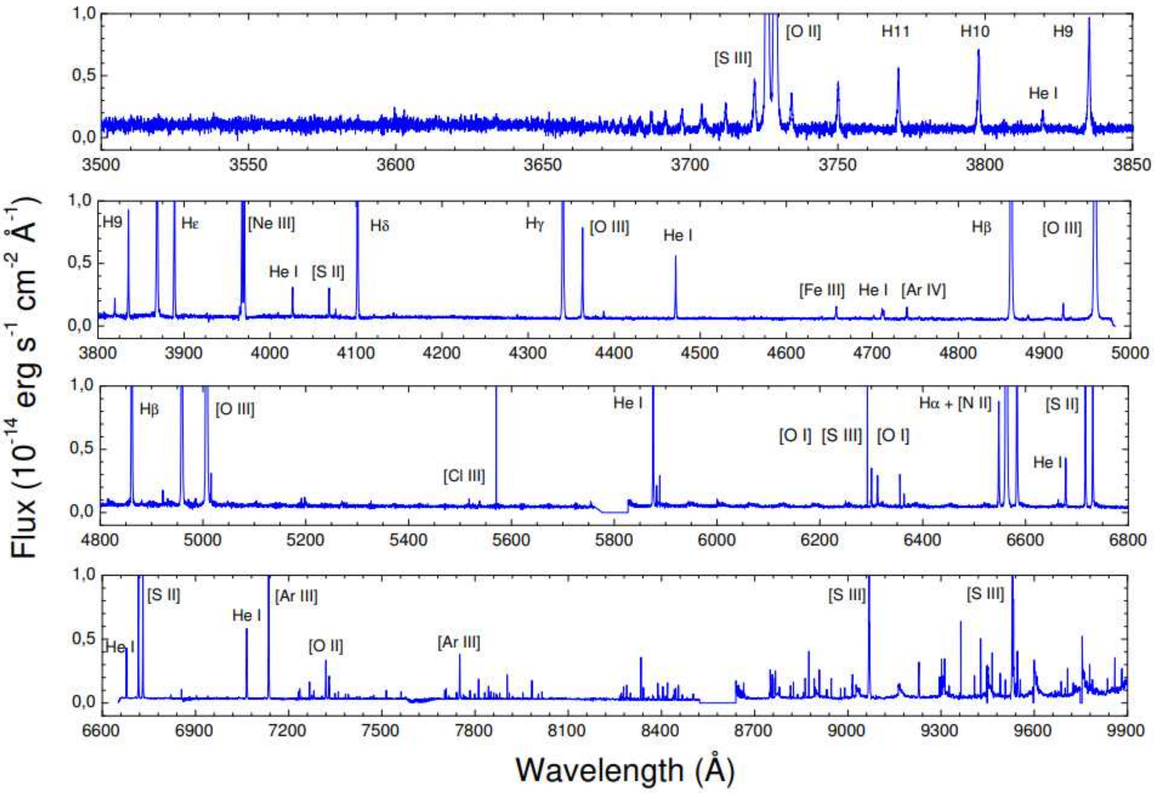

Figure 1.7: UV-Optical spectra of an H II region of the galaxy NGC 5253 obtained from the Ultraviolet Visual Echelle Spectrograph (UVES) at the Very Large Telescope (VLT). Image from of López-Sánchez et al. (2007).

1995).

The existence of the ISM in so many different phases reveals the enormous and complex nature of this environment, as seen in figure 1.9. It serves as a laboratory for understanding physical processes and dynamics at many levels, including the evolution of stars from their birth to their end, the motions of turbulent gas, or wind-driven shocks (Shapiro & Field 1976; McCray & Snow 1979; Heiles 1990; Lequeux 2005; Tielens 2005; Draine 2011).

1.2 The diffuse ionised gas

Besides the WNM, the existence of a warm and ionised component of the ISM, which is ubiquitously distributed in our Galaxy, has been known for decades, being firstly detected through the dispersion of radio radiation from pulsars (Hoyle & Ellis 1963). This component of the Milky Way has been referred to as the warm ionised medium (WIM) (Hoyle & Ellis 1963; Hewish et al. 1968; Reynolds 1971; Reynolds et al. 1973; Guélin 1974; Reynolds 1985, 1989; Kennicutt et al. 1989; Finkbeiner 2003).

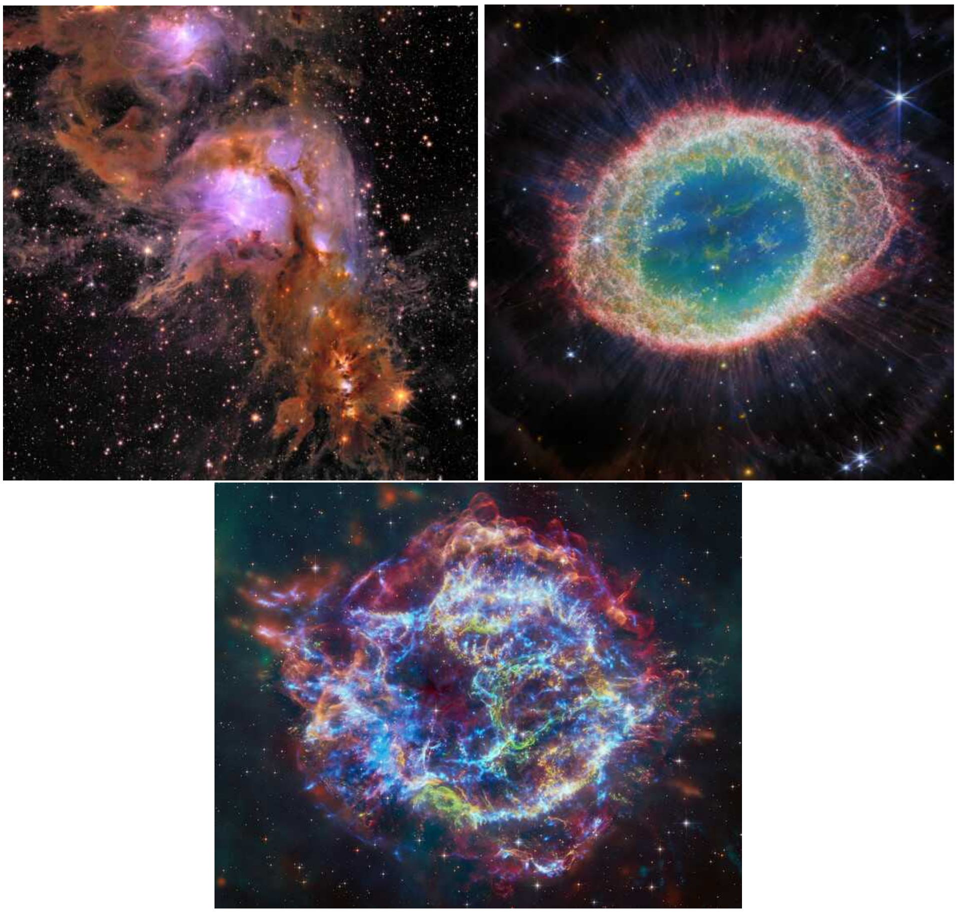

Figure 1.8: Upper left: Euclid image of the H II region M78, composed by three images at 0.7, 1.1, and 1.7 microns (blue, green and red). The excited hydrogen gas is shown in the blue channel. Upper Right: JWST near-infrared image of the ring planetary nebula, depicting the dense globes of H_2 in the outer region, and the hot gas in blue. Down: Composite image of the SNR Cassiopeia-A. X-rays from Chandra (blue), infrared data from JWST (red, green, blue), and optical data from Hubble (red and white)

The measured temperatures ranges between $0.6 - 1 \cdot 10^4$ K, with an average hydrogen ionisation rate of $\sim 4\times10^6 \mathrm{s}^{-1}$ in the solar neighbourhood, which corresponds to 1/8 of the available stellar ionising photons (Reynolds 1985; Madsen et al. 2006).The Hα emission measure (EM$\sim$ 35 cm^{-6} pc) and dispersion measure (DM) derived from pulsar observations allowed the determination of the electron density of the WIM, reaching values as low as 0.03-0.08 cm^{-3}. Moreover, the filling fraction increases as the height with respect to the galactic plane increases, being around 0.1 at the midplane and reaching 0.3-0.4 at 1 kpc from the galactic plane (Kulkarni & Heiles 1987; Reynolds 1991; Berkhuijsen et al. 2006; Gaensler et al. 2008). The WIM represents the 20% of the ISM in volume and the 90% of the ionising hydrogen in mass, being one of the most important components of our Galaxy (Reynolds 1971; Monnet 1971; Reynolds 1991).

Systematic studies of the WIM using Hα CCD imaging have been used to map the distribution

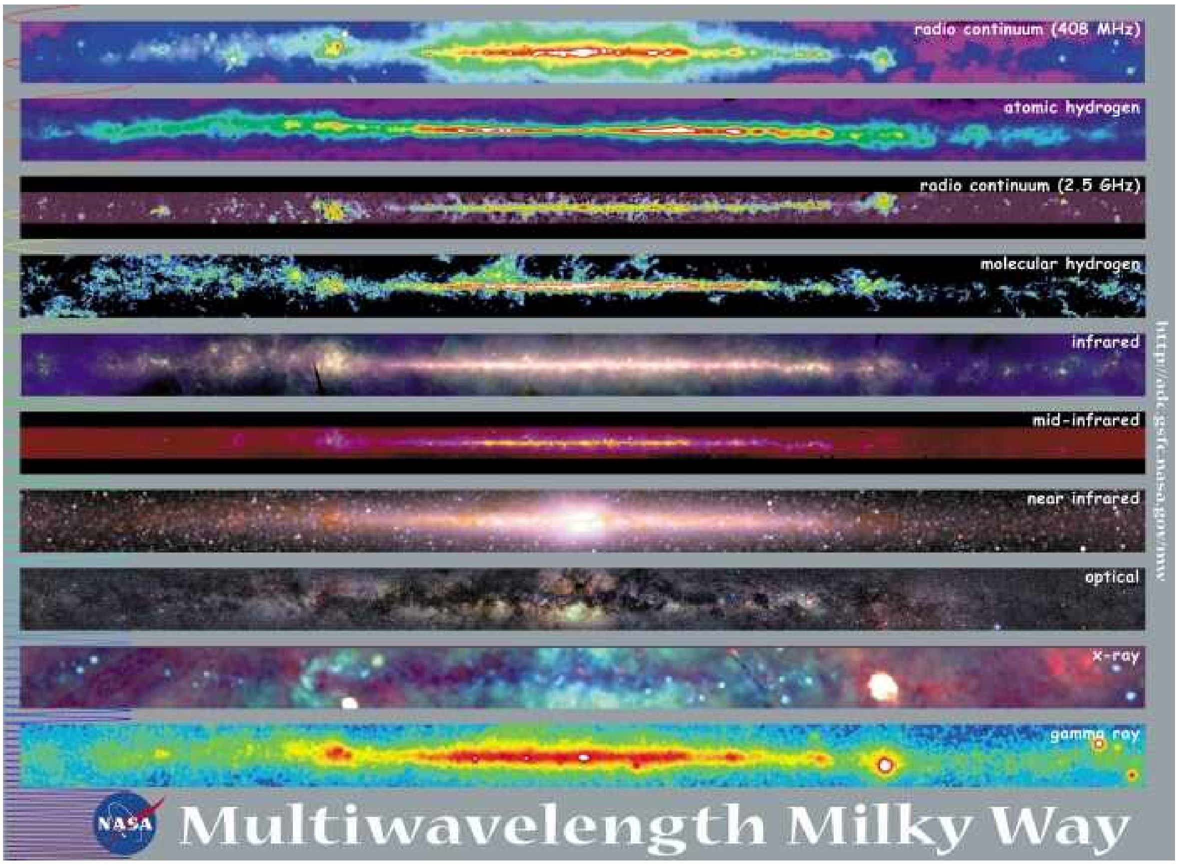

Figure 1.9: Images of the Milky Way in different wavelengths. Credit: NASA Goddard Space Flight Center.

of H^+ throughout the Milky Way, providing a detailed view of the kinematics and distribution of this gas. For instance, the Wisconsin H-Alpha Mapper (WHAM; Tufte et al. 1998), a velocity-resolved survey of the northern sky with a spectral resolution of 12 km/s and a spatial resolution of 1°, characterised the WIM as faint loops, filaments, and blobs of emission superposed on a more diffuse background, as seen in figure 1.10 (Finkbeiner 2003).

In addition, studies of the WIM through Fabry-Perot spectroscopy show that the intensity of the forbidden [S II] λ6716 and [N II] λ6584 lines is found to be higher with respect to the Hα intensity in the WIM in comparison with the typical intensities of the H II regions ($<$ 0.4 and 0.5 respectively); in addition, the measurement of these lines reveals that the ionisation state of the WIM and its temperature vary significantly along the galactic plane, increasing towards the galactic centre (Reynolds 1985; Madsen & Reynolds 2005). Besides, Hα and [O I] λ6300 observations allowed for the measurement of the H^+/H ionisation fraction, since the [O I] /Hα ratio is directly related to the amount of O^0 and H^0 relative to H^+ due to the similar first ionisation potential of O and H. These observations indicate a $H^+/H > 90\%$ within the DIG, and a total interstellar Lyc flux of $2{\times}10^6$ photons$\cdot$cm$^{-2}\cdot$s^{-1}, that implies an ionisation parameter of 10^{-4}-10^{-3}, which is almost two orders of magnitude smaller than

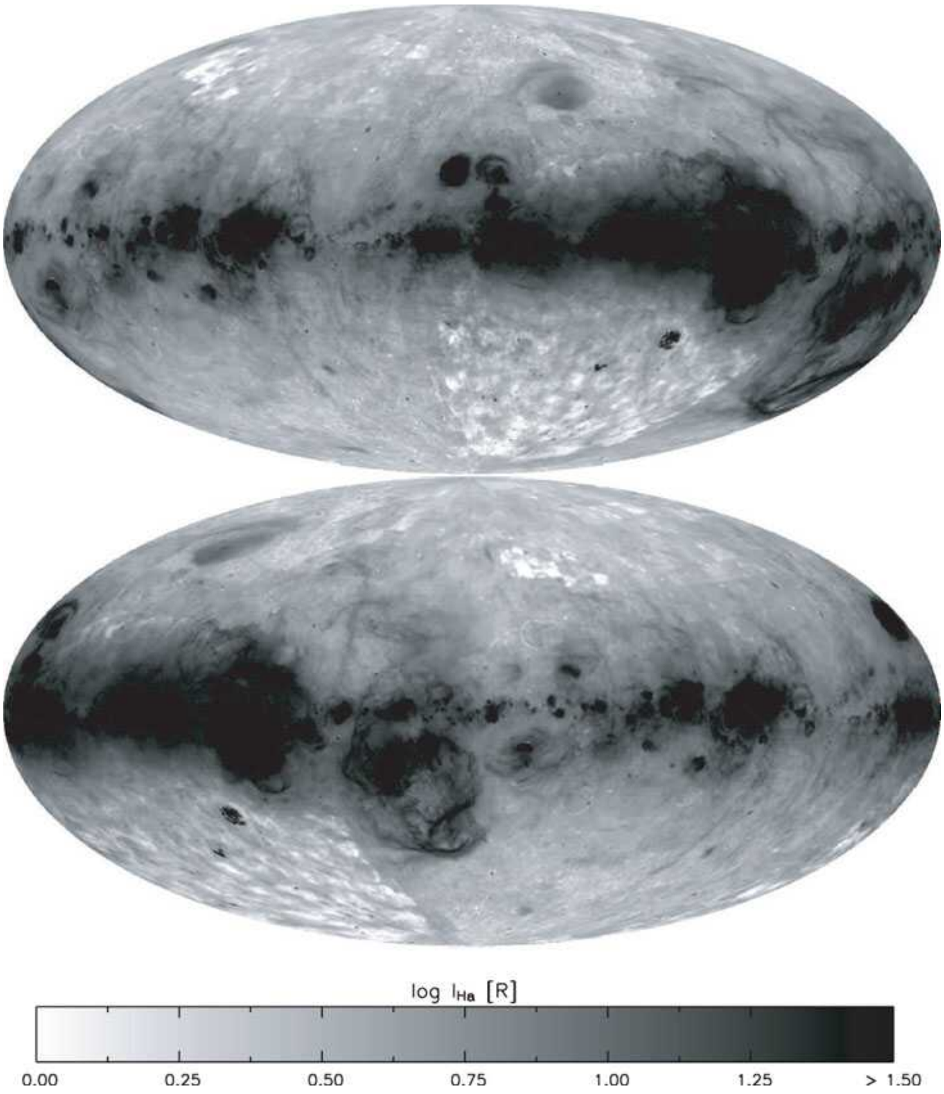

Figure 1.10: Deep Hα Milky Way emission line map (EM$\geq$1 cm^{-6} pc) from WHAM survey. Adapted from Finkbeiner (2003); Haffner et al. (2009b).

the ionisation parameter of the H II regions (Reynolds et al. 1998; Rand 1998; Hausen et al. 2002).

The first detection of this medium in other galaxies, now referred to as diffuse ionised gas (DIG) in the extragalactic context, was carried out through narrowband Hα images of face-on star-forming galaxies (Monnet 1971; Rand et al. 1990; Dettmar 1990). This allow for the identification and classification of extragalactic H II regions and the study the relations of the DIG with galactic properties. In these studies, the H II regions were typically subtracted by defining a limiting value of Hα surface brightness ($\Sigma_{H\alpha}$) or by creating an H II region catalogue. This approach established a lower limit for the DIG, resulting in an Hα image with the H II regions from the catalogue masked out (Zurita et al. 2000). An upper limit can be estimated by the assignation of a local DIG $\Sigma_{H\alpha}$ value to the H II regions, as seen in figure 1.11.

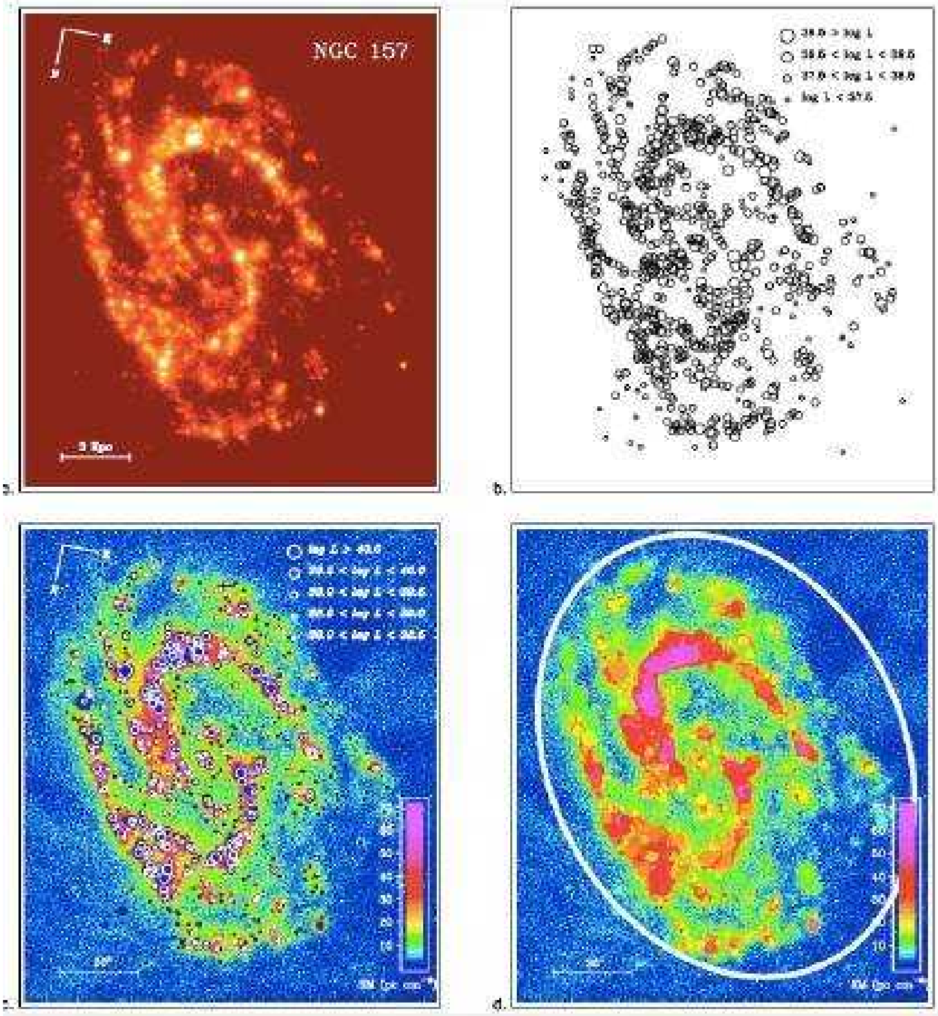

Figure 1.11: Upper and lower DIG estimation for NGC 157. Top-left corresponds to the continuum subtracted Hα image. Top-right depicts the H II regions catalogue. Bottom-left and right are the lower and upper DIG limits respectively. Adapted from Zurita et al. (2000); Haffner et al. (2009b).

It can be seen that the DIG emits almost 30%–50% of the total Hα luminosity of their galaxies correspond, being the 80 ± 10% of the projected area of the disks occupied by DIG (Oey et al. 2007), thereby proving the ubiquitousness and omnipresence of this component in the star-forming galaxies. Besides, some authors detected an anti-correlation between DIG Hα fraction and the star formation rate (SFR) per unit area (Voges & Walterbos 2006).

On the other hand, the spectroscopic studies carried by small samples (< 5) of face-on galaxies with limited spatial coverage (Reynolds 1985; Wang et al. 1997; Otte et al. 2001; Hoopes & Walterbos 2003; Haffner et al. 2009a) shown that the emission of low-ionisation lines, such as [S II] $\lambda\lambda 6717, 31$, [N II] $\lambda 6584$, or [O I] $\lambda 6300$, are enhanced in DIG regimes in comparison with the emission of the H II regions (Wang et al. 1997). Specifically, the ratios of those lines with respect the Hα emission in the DIG are larger than in H II regions (found firstly in edge-on galaxies; Otte et al. 2001). For instance, the [S II] /Hα ratio is found larger than 0.5, and the [N II] /Hα larger than 0.4, being these values larger in DIG regions where the $\Sigma_{H\alpha}$ is lower (see figure 1.12).

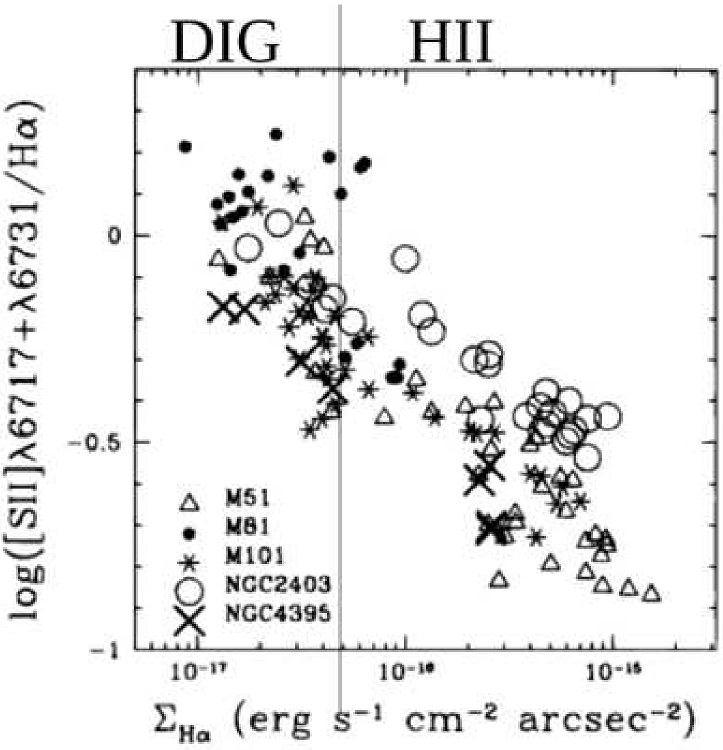

Figure 1.12: [S II] /Hα vs. $\Sigma_{H\alpha}$ for DIG and H II regions of five galaxies, where the DIG was defined by a $\Sigma_{H\alpha}$ cut-off. Adapted from Wang et al. (1997).

1.2.1 The extraplanar diffuse ionised gas

Another perspective of the DIG is provided when study warm diffuse emission in the halo of edge-on galaxies. Firstly detected in NGC 891, the spectroscopic analysis revealed that the behaviour of the main ionisation species reveals that the [N II] /Hα , [S II] /Hα , [O III] /Hβ and [O I] /Hα ratios tends to increase as a function of the distance from the midplane, as seen in figure 1.13 (Rand et al. 1990; Dettmar 1998; Rand 1998, 2000; Collins & Rand 2001).

Moreover, analyses of larger samples of edge-on galaxies (e.g., Rossa & Dettmar 2003a,b; Miller & Veilleux 2003) reveal a connection between the eDIG and the SFR in the disk. These studies generally focused on galaxies with high SFR and starbursts, where a relationship was found between the presence of eDIG and the FIR luminosity, as FIR is an indicator of SFR. When the SFR is low, the presence of halo DIG is indeed observed to diminish, concluding that a minimum of SFR per unit of area is necessary to drive a disk-halo interaction (Lehnert & Heckman 1995; Rossa & Dettmar 2003a; Jo et al. 2018; Lu et al. 2023).

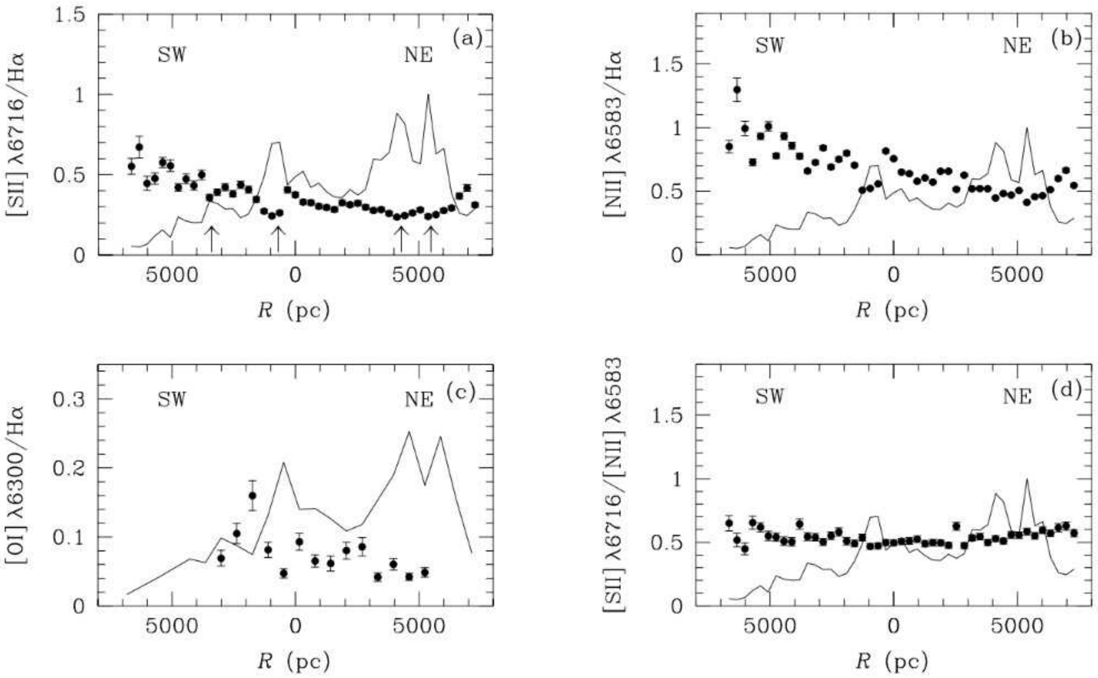

Figure 1.13: Line ratios vs. distance from the midplane. Solid lines are the normalised $\Sigma_{H\alpha}$. Figure from Reynolds et al. (1998).

The scenario of the disk-halo connection predicts outflows of hot gas from the disk into the halo via filaments superbubbles or “chimneys" (also detected in X-rays and radio-emission; Tüllmann et al. 2000, 2006), a phenomenon typically associated with starburst galaxies, presenting eDIG layers that can reach distances from the midplane of 1-2 kpc, of exceptionally 5 kpc (Cecil et al. 2002; Veilleux et al. 2005). Nevertheless, in normal, non-starburst galaxies, there is only circumstantial evidence of the presence of bubbles or chimney structures in their halos, which is often attributed to observational limitations (Norman & Ikeuchi 1989; Howk & Savage 2000; Rossa et al. 2004; Haffner et al. 2009b).

1.2.2 Modern approach to the DIG with IFS

Integral field spectroscopy (IFS) offers simultaneous spatial and spectral information of extended objects. This approach allows for an in-depth characterisation and exploration of the morphology, kinematics, and ionisation of the DIG in nearby galaxies with varying characteristics and inclinations.

Some IFS surveys provides large samples of nearby galaxies at kiloparsec resolution such as the Calar Alto Legacy Integral Field spectroscopy Area survey (CALIFA; Sánchez et al. 2012; Husemann et al. 2013; 391 galaxies at ~0.8 kpc resolution; Lacerda et al. 2018, hereafter Lac18) or the Mapping Nearby Galaxies at APO (MaNGA; Bundy et al. 2015; 356 galaxies at 2 kpc resolution; Zhang et al. 2017, hereafter Z17).

Z17 found an enhancement in the DIG of the ratios [S II] /Hα , [N II] /Hα , [O II] /Hα , and [O I] /Hα , increasing in function of the galactocentric radius, as well as a variable trend of the [O III] /Hβ ratio in comparison with H II regions. Besides, Lac18 defines a criterion of DIG definition in function of the Hα equivalent width (EW$_{H\alpha}$), based on if the region if dominated by photoionisation by HOLMES, corresponding to a EW$_{H\alpha}$< 3Å. This would then be the primary regime in E-S0 galaxies, as the old stellar populations conform to these galaxies.

On the other hand, IFS studies based on the MUSE instrument (Multi Unit Spectroscopic Explorer; Bacon et al. 2010) or wide-field spectroscopic coverage such as TYPHOON (Grasha 2022) offer datasets with a spatial resolution ranging from $\sim$ 50 pc to the resolution of MaNGA-like galaxies, which allows for a spatially resolved study of the DIG and H II regions. Nevertheless, the studies of the DIG using resolutions of $\sim$ 50 pc have predominantly focused on the best galaxies within these surveys in terms of spatial resolution. These studies typically involve individual galaxies, such as M83 (Poetrodjojo et al. 2019; Della Bruna et al. 2022a,b), or the 19 galaxies encompassed by the Physics at High Angular resolution in Nearby GalaxieS project (PHANGS; Emsellem et al. 2022; Belfiore et al. 2022, hereafter Bel22), capable of resolve the ISM structure at $\sim$ 50 pc of resolution and define morphologically individual H II regions and other ionised nebulae (see figure 1.14).

Regarding studies of the eDIG, in order to infer the possible physical processes and the roles played by different morphological structures in the halo leading to the eDIG, the simultaneous spatial and spectral information provided by IFS has resulted in significant progress in this area. One of these studies, carried by the Sydney-AAO Multi-object Integral field spectrograph (SAMI; Croom et al. 2012; Bryant et al. 2015), used a sample of 40 low resolution edge-on galaxies (0.8 kpc - 2.8 kpc) to perform a systematical exploration of the eDIG (Ho et al. 2016) noticing that the disc-halo interaction can influence the eDIG emission through starburst-driven winds. On the other hand, studies with the Mapping Nearby Galaxies at Apache Point (MaNGA; Bundy et al. 2015) IFS using also low resolution large samples found an increment of the [N II] /Hα indicating a temperature gradient in the halo, as well as a flattening in the $\Sigma_{H\alpha}$ comparable with the [O II] emission at higher distances (~6 kpc).

The most recent studies with the Calar Alto Legacy Integral Field Area Survey (CALIFA; Sánchez et al. 2012, 2016) studied the eDIG kinematically using a sample of 25 galaxies with spatial resolution of 0.8 kpc on average (Levy et al. 2019), finding a "lag" in the rotation velocity of the ionised gas, i.e., a decrement of the radial velocity with the increasing of the distance from the midplane (also reported by other authors, e.g., Rand 2000; Miller & Veilleux 2003; Bizyaev et al. 2017). Nevertheless, they did not find correlations between the radial variation of the lag and the origin of the extraplanar gas. In the mentioned studies,

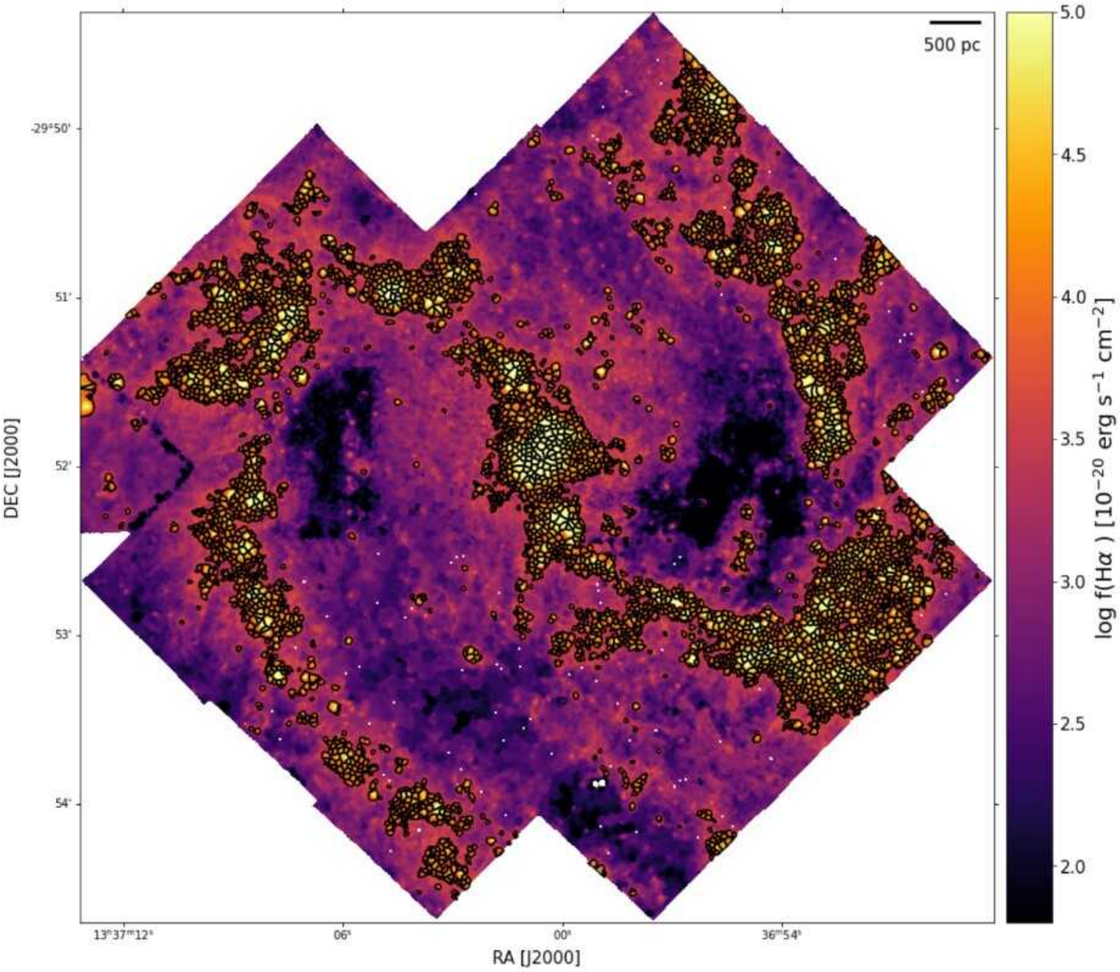

Figure 1.14: M83 Hα image with the boundaries of the detected H II regions based on their Hα emission. Figure adapted from Della Bruna et al. (2022b).

despite the wide variety of large samples used, the spatial resolution of the data is typically insufficient to perform a comprehensive and in-depth bidimensional study of the eDIG. However, the most recent studies with IFS includes datasets of the Multi Unit Spectroscopic Explorer (MUSE, Bacon et al. 2010), whose datasets exhibits spatial resolutions lower than 200 pc, enabling a more complete exploration of the line emission, structure and kinematics of the ionised gas in the halo of edge-on galaxies. For example, Rautio et al. (2022) and Dirks et al. (2023) used a sample of nearby edge-on galaxies from Comerón et al. (2019, Com19 henceforth). The resolution and data quality of this dataset enabled these authors to find that the Hα emission in the halo correlates with the star formation of the galaxy, revealing the possible existence of a feedback mechanism between the plane and the halo that ionised the latter.

1.2.3 The DIG ionisation budget

The observations in edge-on and face-on galaxies show an evident connection between the Hα flux from the DIG comparable to that from the classical H II regions in the Galaxy and in extragalactic sources. Although it is not well understood how Lyc photons can freely travel hundreds of parsecs, the leakage of these photons produced by OB stars within H II regions is commonly regarded as the primary source of ionisation for the WIM in particular, and DIG in general (Haffner et al. 2009b; Seon 2009; Belfiore et al. 2022). Some of the mentioned studies have shown that luminous O-star cluster near the midplane can produce the conditions to ionise the (e)DIG at distances > 1 kpc from the ionising stars (Reynolds et al. 2001; Madsen et al. 2006; Haffner et al. 2009b). However, it has been observed that in some cases, the total energy output of these stars does not appear to provide the necessary power to ionise the DIG uniformly across galactic discs (Ferguson et al. 1996a,b). The substantial power demand, combined with the presence of high-ionisation species like [O III] (enhanced at more than 1 kpc above the galactic plane) and He I (Reynolds et al. 1998; Wood & Mathis 2004; Haffner et al. 2009b) underscores the insufficiency of Lyc photons leaking from H II regions in explaining the existence of the DIG. Additionally, this higher degree of ionisation of the collisional-excited lines such as [N II] and [S II] usually implies higher electron temperatures in the (e)DIG compared to the H II regions (Haffner et al. 1999, 2009b; Boettcher et al. 2019).

The question of the ionisation source for this component continues to be a topic of ongoing debate, with numerous proposals suggesting alternative heating sources for the DIG. Some of these sources include photoelectric heating from interstellar dust particles or large molecules (Reynolds & Cox 1992; Weingartner & Draine 2001), fast shocks provided by Wolf-Rayet stars or supernovae (Reynolds et al. 1998; Collins & Rand 2001; Hidalgo-Gámez 2005), turbulent mixing layers and dissipation of turbulence (Slavin et al. 1993; Minter & Spangler 1997; Reynolds et al. 1998; Binette et al. 2009), cosmic ray heating (Wiener et al. 2013), or microflares and magnetic field reconnections (Raymond 1992; Birk et al. 1998). Another alternative source of ionisation, as proposed by Flores-Fajardo et al. (2011) and Cid Fernandes et al. (2011), is the photoionisation from hot low-mass evolved stars (HOLMES), that could provide an explanation for the high [O III] /Hα ratio observed in the extraplanar DIG (Rand et al. 1990). Initial calculations conducted by Hills (1974) proposed that the ionising radiation emitted by these hot pre-white dwarf stars could have a substantial influence on the interstellar medium, adding harder photons to the ionisation budget of the DIG.

Several studies conducted within CALIFA or PHANGS galaxies (Lac18; Bel22) reveals that photoionisation by HOLMES is more prevalent in central regions where $\mathrm{EW}_{H\alpha}$< 3 Å, besides, the large-scale eDIG emission in edge-on galaxies are also due to HOLMES (Rautio et al. 2022), corresponding to regimes of $\mathrm{EW}_{H\alpha}$< 3 Å, according to these studies (see figure 1.15).

In these regions, approximately 2% of the total Hα emission is powered by HOLMES. The remaining emission arises from photon leakage from H II regions. The mean free path of ionised photons is estimated to be < 1.9 kpc, based on a straightforward thin-slab model for photon propagation through the ISM (Zurita et al. 2002; Seon 2009). This model also predicts an increase in the [O III] /Hβ ratio and the ionisation parameter, which contradicts the decrease in the ratio as $\Sigma_{H\alpha}$ increases. However, the contribution of the spectral hardness of HOLMES to the ionisation budget explains this discrepancy and the trend of increasing [S II] /Hα , [N II] /Hα , and [O I] /Hα line ratios as $\Sigma_{H\alpha}$ decreases.

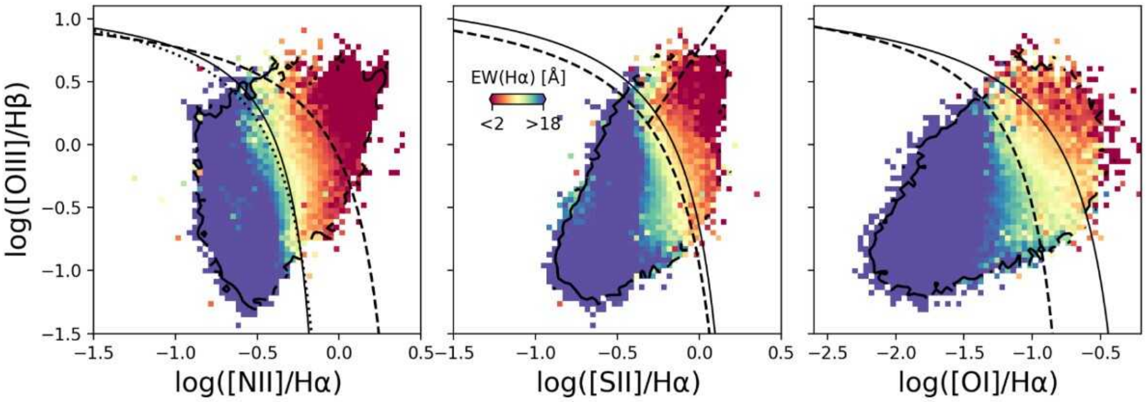

(a) BPT diagram for the PHANGS galaxies. Figure from Bel22.

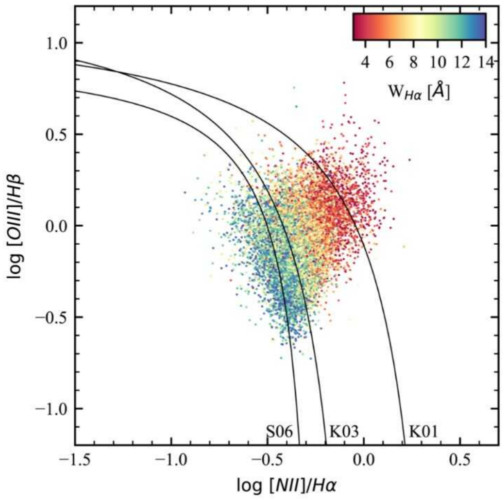

(b) BPT diagram for the CALIFA galaxies. Figure from Lac18.

Figure 1.15: BPT diagnosis diagrams dividing SF-regimes from HOLMES dominated regimes using the EW$_{H\alpha}$(< 3Å) as a proxy.

The extent to which HOLMES contribute to the ionising radiation responsible for the DIG remains uncertain. While they may play a role in ionising specific regions within the sparsely populated interstellar medium, their overall significance is not yet established.

Alternatively, kinematical studies of the DIG with sub-hectoparsec resolution PHANGS galaxies reveal a DIG rich in substructures, whose high ionisation state ([O III] /Hα and [O I] /Hα > 0.5) is indicative of a superposition of non-collisional flows originating from multiple vertical layers of gas or a bar-driven inflow of shocked gas (Della Bruna et al. 2022b), corresponding to $\sim$ 5% of the total ionisation budget of the DIG. The presence of shocks driven by stellar winds, supernova explosions, or galactic and AGN outflows in the ionisation budget of the DIG is becoming more apparent, thanks to the ability to resolve the ISM at sub-hectoparsec resolutions (Congiu et al. 2023). These mechanisms can produce heating rates on the order of 10^{-26} erg$\cdot$s$^{-1}\cdot$cm^{-3}, meeting the power requirement for the additional heat source needed for the DIG. This heating is capable of producing the high excitation lines and the high emission of collisionally excited lines observed in the DIG (Slavin et al. 1993; Rand 1999; Reynolds et al. 1999; Collins & Rand 2001). Moreover, shocks has been also proposed as an additional ionisation source of the eDIG in the galactic halos. Shocks, as well as turbulent mixing layers (TMLs; e.g., Begelman & Fabian 1990; Slavin et al. 1993; Rand 1998; Collins & Rand 2001), have been proposed as possible explanations for the presence of high excitation lines and the increase in electron temperature in the eDIG with the distance from the midplane (Collins & Rand 2001; Otte et al. 2001; Hoopes & Walterbos 2003; Mitronova et al. 2004; Boettcher et al. 2019), since these observed features correspond to interfaces between cold and hot gas, that can generate extreme ultraviolet (EUV) ionising radiation that may constitute a significant source of ionising radiation for distant clouds and regions where Lyc ionising radiation from OB stars in the midplane is either shielded or absent, and can reproduce some of the optical line ratios observed in the eDIG. In addition, the various mechanisms that contribute to the ionisation budget of the eDIG can be closely linked to the different morphological structures found in the halo (Levy et al. 2019). These structures can play a significant role in the feedback mechanisms that can connect the star formation activity of the disk with the ionisation of the halo. Exploring the kinematics of the halo provides valuable insights about these structures. For instance, by studying the radial variation of the "lag" ($\partial lag/\partial r$) in the rotational velocity of the halo (Levy et al. 2019; Dirks et al. 2023). In particular, we are observing a galactic fountain if the sign of $\partial lag/\partial r$ is negative, an inflow if it is positive, or gas accretion if it is equal to zero (Shapiro & Field 1976; Kaufmann et al. 2006; Binney 2005; Combes 2014).

1.2.4 Computational DIG models

Understanding the DIG as a complex 3D medium can help to answer the questions regarding the penetration of Lyc photons over large distances in the ISM.

The first 3D ionisation structure models, employing techniques such as “Strömgren volume” and focusing primarily on Hα emission (Franco et al. 1990; Miller & Cox 1993; Dove et al. 2000), or Monte Carlo simulations (Wood & Loeb 2000; Ciardi et al. 2002), demonstrated that extended DIG layers could be produced by the ionising radiation of O stars in a clumpy medium. These models utilised various approaches to simulate the 3D density structure of the medium, including “standard clouds” (Miller & Cox 1993), superbubbles formed by the action of supernovae and stellar winds (Dove et al. 2000), and two-phase and fractal densities (Wood & Loeb 2000; Ciardi et al. 2002).

This evidences that a 3D density structure is essential for ionising photons to travel large distances from O stars, which are located near the galactic midplane. In a uniform medium with an interstellar density of 1 cm^{-3}, an O star forms a Strömgren sphere with a radius of about 60 pc, and an ionising photon can penetrate only 0.1 pc in the neutral medium. Therefore, 3D structures must create low-density paths, enabling photons to traverse kpc scales and ionise gas far from the O stars and at significant heights above the midplane.

Dove et al. (2000) investigated whether superbubbles formed by supernovae and stellar winds could facilitate the escape of ionising photons through low-density paths. They found that dense shells of drawn material typically trap these photons within the bubbles, preventing them from escaping to the halo unless the bubbles are large enough to reach the halo. However, their models used a smooth, continuous shell structure. The fragmentation of these shells and the formation of holes by supernovae and stellar winds in a clumpy medium might alleviate this trapping effect, allowing more ionising photons to escape. Photoionisation models of bubbles created by stellar winds in a turbulent star-forming cloud also suggest that escape fractions exceeding 20% are possible (Dale et al. 2005). On the other hand, (Miller & Veilleux 2003) modelled the DIG as a two-component vertically stratified density structure of the form: $\mathrm{n(H)} = 0.1e^{-|z|/0.3} + 0.025e^{-|z|/0.9}$. This model represents the concentrated neutral layer and the extended ionised layer, and can reproduce the average observed EM and DM.

These 2D and 3D models tried to explain the structure and formation of the DIG through photoionisation via OB stars. In order to explain the emission line features present in the DIG, several 1D and 2D computational models were proposed (Domgorgen & Mathis 1994; Sembach et al. 2000; Collins & Rand 2001; Hoopes & Walterbos 2003). In particular, plane-parallel slab models (Bland-Hawthorn et al. 1997; Zurita et al. 2002; Seon 2009) demonstrate that the depth dependence of the ionisation and temperature structure can account for the trends observed in most line ratios with increasing distance from the source. However, the increase in the [O III] /Hα ratio with distance from the midplane remains unexplained and is typically attributed to secondary heating sources such as shocks or turbulent mixing layers (see previous subsection).

These slab models present an advantage in modern studies using IFS, as high-resolution datasets enable the identification of individual H II regions. Consequently, the fluxes predicted by these models can be directly compared with observational data. For instance, Bel22, using PHANGS galaxies, applied thin slab models that consider the propagation of ionising Lyc photons leaked from H II regions (see figure 1.16) due to both geometric dilution and absorption by a population of DIG clouds, which is parameterised via an effective absorption coefficient k_0. The model that best fit the data corresponded to a mean free path of the ionising photons of 1.9 kpc. This model also predicts an increase in the ionisation parameter, implying an increase in [O III] /Hβ . However, this is in clear discrepancy with the observation of a flat or decreasing trend with increasing $\Sigma_{H\alpha}$.

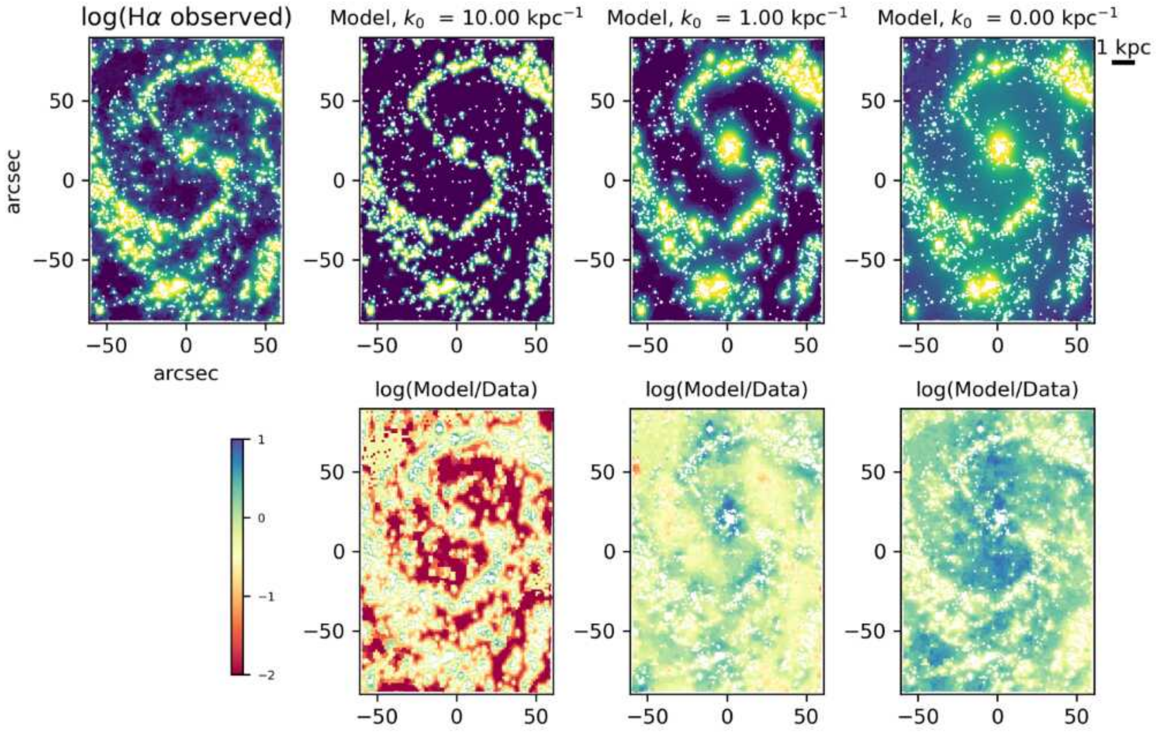

Figure 1.16: Comparison of the observational Hα flux of NGC 4535 with the best fit model of ionising photons propagation. Top row is the observed Hα image among with the models prediction with three different values of k_0. Bottom row is the comparison log(model/data). Figure adapted from Bel22.

Besides 1D models, the development of Monte Carlo photoionisation codes (Och et al. 1998; Ercolano et al. 2003; Wood & Mathis 2004) allows to estimate of the ionisation, temperature structure and emission line strengths for multiple ionising sources within 3D geometries. Their models showed that, due to the hardening of the radiation field in the spectral region between the H I and He I ionisation edges, the temperature increases as we move away from the ionising sources. The models also predict that [N II] /Hα and [S II] /Hα increase with $|z|$, which is supported by observations.

1.3 This work

In order to make progress in quantifying the escape fraction of ionising photons from H II regions, it is imperative to reassess the importance of leaked radiation and HOLMES in contributing to the ionisation of the DIG in star-forming disk galaxies. However, previous studies aimed at this task have relied on large surveys with low spatial resolution or small samples with high spatial resolution. In most cases, these studies have employed methodologies that primarily rely on Hα emissions for the definition and exploration of the DIG. Besides, to advance the characterisation and exploration of the ionisation of extra-planar gas, it is crucial to study the impact of the various structures found in the halos of individual galaxies, such as filaments, plumes or bubbles. Previous studies using IFS have presented large samples of low-resolution galaxies, with the exception of those conducted with the MUSE instrument, but focusing only on one galaxy or without inquiring in the connection between disc and halo that originates these structures and changes the ionisation conditions.

This work introduces the Bidimensional Exploration of the warm-Temperature Ionised gaS (BETIS [6]) project.

In the first part of the BETIS project, we select a sample of several MUSE projects and present the methodology employed, designed to be applicable to galaxies with varying linear resolutions and morphologies, based not only on Hα , but on other emission lines. In addition, we discuss the problematical aspects of performing a general and global study of the ionisation mechanisms of the DIG. We validate this methodology through testing on a representative sample of seven galaxies with diverse characteristics. The goal is to determine the implications of incorporating galaxies exhibiting different physical processes into the same diagnostic of the ionisation mechanisms of the DIG.

In the second part, we focus in the characterisation of the eDIG, examining the processes that link the ionisation of the galactic halo and the disk, as well as exploring the possible ionisation mechanisms for a sample of edge-on galaxies.

This thesis is structured as follows. Chapter 2 shows the characterisation of the BETIS general sample, the representative (showcase) sample to test the methodology, and the sample of edge-on galaxies (eBETIS) for the study of the eDIG. In chapter 3 we describe the methodology employed for characterising and analysing the DIG. Chapters 4 and 5 develop the analysis, findings, and results of the DIG investigation for the showcase sample and the eDIG for the eBETIS sample, respectively. Finally, chapter 6 summaries the main finding and

---

[6] Betis is the ancient roman name of the Guadalquivir river in Andalusia, Spain, and it is still used to name the main mountainous systems of the region. This is why the predominant colour of the figures is the 'green hope' (#00A650), which is the colour of Andalusia's flag.

conclusions of this thesis, as well as the future work that can be further developed based on the presented methodology and sample.

The following notation is used throughout the thesis: [N II] ≡[N II] λ6584; [S II] ≡[S II] λ6717 + [S II] λ6731; [O III] ≡[O III] λ5007; and [O I] ≡[O I] λ6300. We adopt the standard ΛCDM cosmology with $H_0 = 70$ km/s/Mpc, $\Omega_\lambda = 0.7$, $\Omega_M = 0.3$.

Chapter 2

Sample

2.1 Instrumentation choice

The task of characterising and understanding the DIG in nearby star-forming galaxies, both low and high inclination, has initially been approached using narrowband Hα images, complemented by [S II] images. These studies have primarily focused on small samples of fewer than five galaxies, including both edge-on (Dettmar 1990; Rand et al. 1990) and face-on galaxies (Ferguson et al. 1996a; Greenawalt et al. 1997; Zurita et al. 2000). Despite the limited number of galaxies studied, these samples benefit from high spatial resolutions (FWHM $\approx$ 200 pc). This spatially resolved information allows to discern the DIG emission and morphologically define the the H II regions (Zurita et al. 2002). Nevertheless, the lack of spectral information in these studies limits the ability to explore the various physical mechanisms at play in the ionisation of the DIG in the galactic disc and halos.

On the other hand, long-slit spectroscopy studies enable a more in-depth analysis of the ionisation mechanisms of the (e)DIG (Reynolds 1985; Wang et al. 1997; Otte et al. 2001; Hoopes & Walterbos 2003; Haffner et al. 2009a), though they are constrained by limited spatial coverage. Spatial coverage and data sampling are crucial for a proper understanding of the connection between both global and local properties and the (e)DIG in star-forming galaxies. Moreover, this must be accompanied by sufficient spatial resolution to capture the structure of the ISM in the galactic disc and the halos, as well as enough spectral resolution to distinguish the different physical processes within them and how they are interconnected, as well as how this influences the ionisation of the diffuse gas. Simultaneous spatial and spectral information is therefore crucial for conducting an optimal investigation of the (e)DIG in nearby star-forming galaxies.

Integral field spectrographs (IFS) are precisely the instruments capable of obtaining this simultaneous spatial and spectral information. IFS data consist of datacubes, where each pixel of the image is replaced by a full spectrum within the cube, known as a spaxel. The "X" and "Y" axes represent the spatial coordinates, while the third axis, "λ," represents the spectral dimension, as seen in figure 2.1.

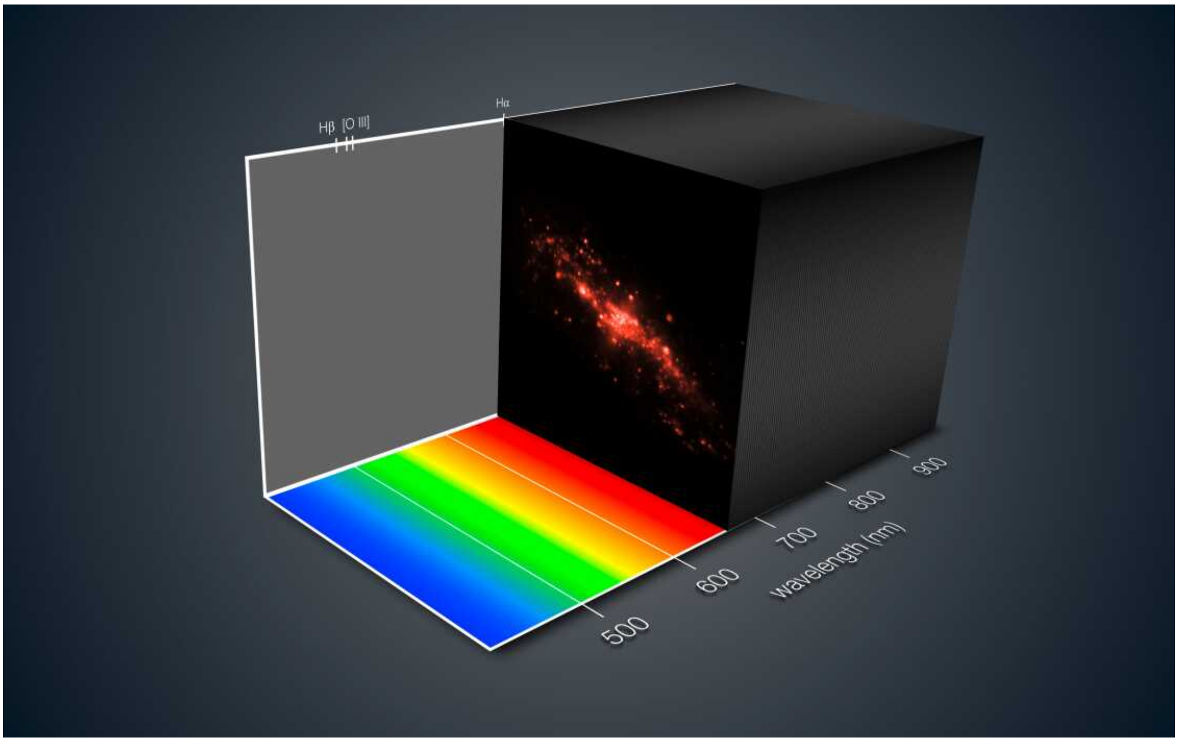

Figure 2.1: Visual representation of an IFS datacube. In particular, the galaxy NGC 4650A obtained with the MUSE IFS, from the ESO public images (R. Bacon/L. Calçada).

Several authors have resumed the task of systematically studying the DIG using IFS data. For example, studies conducted with SAMI (Croom et al. 2012; Bryant et al. 2015) utilised a sample of 40 low-resolution edge-on galaxies (0.8 kpc - 2.8 kpc) to investigate the extraplanar DIG. Other IFS surveys, such as CALIFA and MaNGA, provide large samples of nearby galaxies at kiloparsec resolution, enabling systematic studies of both DIG and eDIG (e.g., Z17, Lac18 or Levy et al. 2019) using samples of ~ 300 galaxies with linear resolutions between 0.8 and 2 kpc. However, the limited spatial resolution has been the primary obstacle in these studies, making it difficult or even impossible to explore in detail the effects of the various physical processes present in the ISM and their contribution to the DIG ionisation budget, especially when the H II regions are unresolved. This is particularly crucial for the eDIG, as the galactic halos may exhibit diverse mechanisms and structures that could contribute to the formation of the ionised extraplanar gas (Levy et al. 2019). These include phenomena such as plumes, fountains, filaments, gas accretion or gas outflows/inflows (Rand 1996; Rossa & Dettmar 2003a,b; Kaufmann et al. 2006; Marinacci et al. 2011; Combes 2014; Levy et al. 2019; Com19).

As a result, the characterisation of the (e)DIG and the exploration of its ionisation mechanisms require not only simultaneous spatial and spectral information but also spatially resolved data. In terms of resolution and spectral coverage, MUSE is one of the best instruments for studying the DIG at an extragalactic level.

2.1.1 MUSE technical overview

MUSE is an optical IFS located at the ESO-VLT 8.1m telescope at Cerro Paranal, Chile. The instrument consists of 24 sub-fields, known as Integral Field Units (IFUs), which are split to be corrected through adaptive optics. These sub-fields combine to form a total field of view (FoV) of 1 arcmin^2 in its Wide Field Mode (WFM), as seen in figure 2.2.

Figure 2.2: Left: A single MUSE pointing of 1 arcmin^2 (white square) over the galaxy NGC 863. Right: Two MUSE pointings of 1 arcmin^2 (white squares) over the galaxy NGC 7514. Both images were downloaded directly from the SDSS DR14.

The WFM brings a sampling of 0.2×0.2 arcsec, limited by seeing with a spatial resolution of 0.4 arcsec. MUSE covers a nominal spectral range of $480 - 930$ nm and an extended spectral range of $465 - 930$, with a resolution of 1750 at 465 nm to 3750 at 930 nm (figure 2.3 left), and a spectral sampling of 12.5 nm. The only notable difference between the nominal and extended modes of the WFM is the suppression of second-order contamination in the red part of the spectrum in the nominal mode. In both modes, the total efficiency reaches a maximum around 700 nm, that drops to zero at 480 nm in the nominal mode and at 465 nm in its extended mode, with an overall efficiency higher than 15% (see figure 2.3 right[1]).

The data observed by the MUSE instrument has already been used to study the DIG (e.g., with PHANGS-MUSE; Bel22; Della Bruna et al. 2022a,b; Congiu et al. 2023) at a spatial resolution of ~ 50 pc, but constrained to only < 20 objects, and also to study the eDIG for edge-on galaxies (e.g., Rautio et al. 2022; Dirks et al. 2023) at a similar resolutions but also limited to one or two galaxies.

---

[1] Both efficiency and resolution curve plots were obtained directly from the ESO archive.

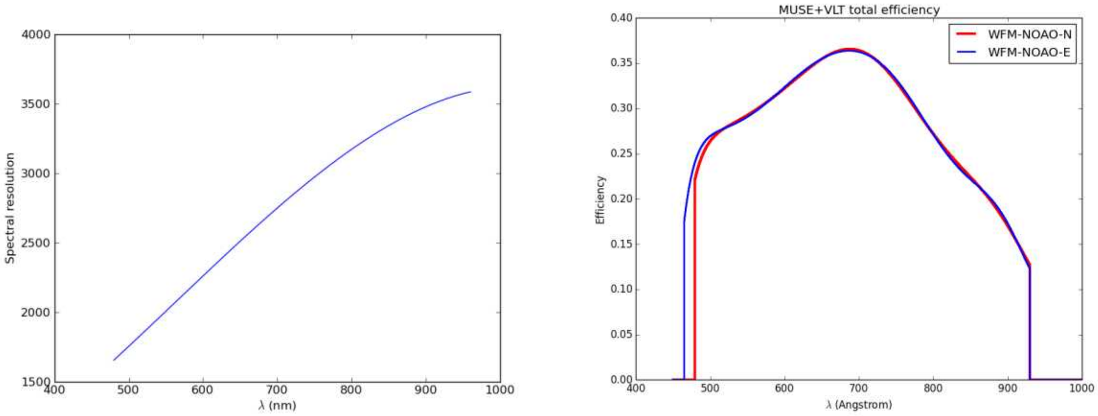

Figure 2.3: Left: MUSE spectral resolution curve. Right: MUSE efficiency curves for the WFM natural seeing (NOAO) extended (E) and nominal (N) modes. Figures obtained from the ESO online portal.

2.2 The BETIS sample

In order to perform an exhaustive, reliable and statistical significant analysis of the DIG, the sample needs to cover a broad range of star-forming galaxies across all morphological types, as well as a suitable spatial resolution to discern the DIG emission from H II regions ($\lesssim 0.5$ kpc). For this reason, the BETIS sample was selected from observational projects of local galaxies that meet the previous conditions.

The first of these projects is AMUSING (The All-weather MUse Supernova Integral-field of Nearby Galaxies; Galbany et al. 2016). This survey is an ongoing project aimed at studying the environments of supernovae by means of the analysis of a large number of nearby supernova host galaxies ($0.005 < z < 0.1$). The AMUSING survey[2] currently comprises 571 supernova hosts observed during the semesters P95-P104 (April 2015-March 2020) and is composed by a wide variety of galaxy types with the common characteristic of having hosted a known supernova.

Alongside the AMUSING survey, several new objects have been observed with MUSE in different programmes; the AMUSING+ sample (Galbany et al. in prep.) aimed to increase the number of supernova hosts, and AMUSING++ (López-Cobá et al. 2020), a compilation of MUSE observations with the goal of investigating the presence of galactic outflows. The AMUSING++ compilation includes galaxies from different MUSE projects:

- CALIFA galaxies observed with MUSE in the ESO archive.
- The GAs Stripping Phenomena in galaxies with MUSE (GASP; Poggianti et al. 2017).
- The MUSE Atlas of Disks (MAD; Erroz-Ferrer et al. 2019).
- The Close AGN Reference Survey (CARS; Husemann et al. 2019).

---

[2] The AMUSING survey characterisation is available online: https://amusing-muse.github.io/sample/

- The Time Inference with MUSE in Extragalactic Rings (TIMER; Gadotti et al. 2019).

AMUSING+ adds 143 objects to the previous AMUSING sample, while AMUSING++ adds up 410 objects, making a total of 1124 objects (AMUSING(+/++) sample henceforth). The datacubes have been reduced using the ESO reduction pipeline[3], more information about the data and data reduction of each project can be found in the corresponding paper. The datacubes are available in the ESO Science Archive Facility.[4]

The main bottleneck for performing a reliable DIG analysis is the spatial resolution. In order to sample the DIG with respect the size, inclination and morphology of star-forming galaxies, and for being able to distinguishing the H II regions emission from DIG emission, the objects need to present enough resolution. For this reason, the sample is selected by performing an exhaustive visual inspection of the 1124 AMUSING(+/++) datacubes using Hα images, obtained summing 10 frames of the datacubes centred in Hα with a 12.5 Å width, excluding galaxies whose resolution or angular size with respect to the FoV is not optimal for the spatially resolved study of the DIG, as it is not possible to resolve star formation complexes in the disk. Additionally, objects whose poor data quality does not allow for the measurement of emission lines other than Hα are also excluded. The reason for performing a visual inspection instead of cut-offs based on redshift or linear resolution is that high resolution (e.g., $\lesssim$ 200 pc) does not always guarantee the resolution of SF regions if the galaxy is at a greater redshift or its physical size is small. Additionally, a low redshift and high linear FWHM cut-off do not guarantee selection for the sample if the observational conditions or the ESO Phase 3 data reduction were not optimal for measuring different line emissions. Two examples of non-considering galaxies are shown in figure 2.4. This criteria leaves us with 265 galaxies optimal for BETIS. The characterisation table of the BETIS sample is available in the GitHub[5]

The BETIS sample is composed by nearby galaxies, between 6.5 and 253.7 Mpc of distance, and redshifts[6] between $0.00 < z < 0.06$, with a mean value of 0.015 and a median of 0.013. The masses spans between $10^8 M_\odot$ and $10^{12} M_\odot$ (López-Cobá et al. 2020), with a mean value of $\sim 10^{11} M_\odot$, and the star formation rate (SFR[7]) between 0.01 and 19.5 $M_\odot$/yr, with a mean value of $1.1 M_\odot$/yr. The sample includes 9 galaxies with low rate of star formation (< 0.1) and one galaxy (UGC1333) considered a starburst galaxy, with a SFR > 10 $M_\odot$/yr (see Fig. 2.6). Thus, most of the sample lies within ranges of typical spiral galaxies SFRs and fits the distribution of masses and SFRs at $z \sim 0$ in the star formation main sequence (SFMS,

---

[3] http://www.eso.org/sci/software/pipelines/.

[4] ESO Science Archive Facility: http://archive.eso.org/cms.html

[5] BETIS GitHub.

[6] All redshift values correspond to the heliocentric redshift, obtained from the NED database: http://ned.ipac.caltech.edu/.

[7] Obtained as SFR = L(Hα)/$7 \cdot 10^{40}$erg/s, using the Hα images previously mentioned.

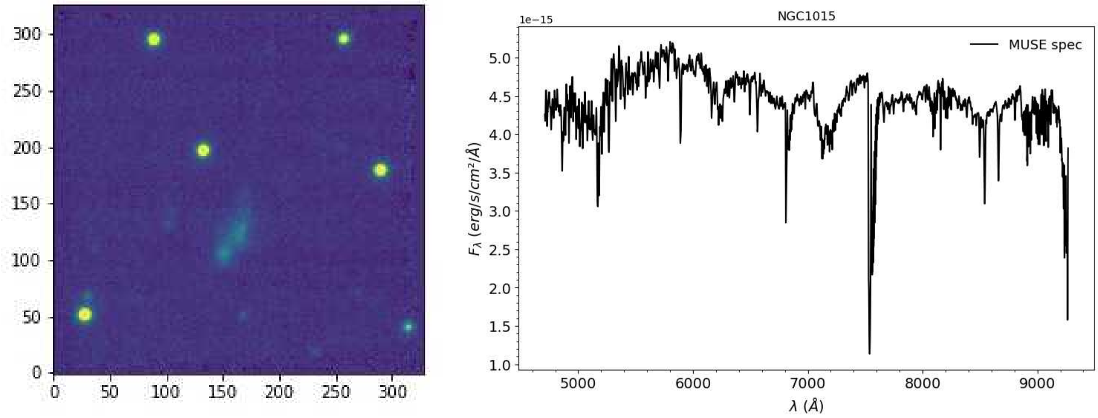

Figure 2.4: Two examples of non-considering galaxies. Left: Hα image of the unclassified host galaxy of the supernova SN2017dgd, not considered for low resolution and angular size. Right: Integrated spectrum of 1 kpc around the centre of the spiral galaxy NGC1015, not considered due to the impossibility of measure emission lines.

Boquien et al. 2014; Sparre et al. 2015).

Fig. 2.5 shows the spatial resolution of the BETIS sample. The resolution is limited by seeing, the physical scale of the galaxies is linked to the PSF FWHM, measured as the seeing. The median seeing is ~ 1.02 arcsec (0.24 standard deviation, Fig. 2.6), this corresponds to mean physical resolution of ~ 275 pc (green line). The 96% of the sample has better resolution than the mean CALIFA FWHM (red line), while the 23% has better resolution than the CALIFA galaxy with the highest resolution (200 pc of FWHM). The BETIS sample includes 10 objects with a spatial resolution comparable with that of the PHANGS sample (blue line, < 50 pc). The combination of spatial resolution and number statistics is a clear advantage of the BETIS data set for the study of the DIG. See Fig. 2.7 for a general overview of the sample resolution.

The BETIS sample has a broad distribution of sizes and inclinations. Around 25% of the galaxies have $r_{25,B} < 42''$, meaning that the entire galaxy fits inside the MUSE FoV, 58 galaxies are mosaics that consist in various pointings of the telescope, and these objects represents the galaxies with the best spatial resolution of the sample. The inclinations span between face-on and edge-on galaxies, being the 37% of the galaxies (99 galaxies) inclined less than 45° with respect the line of sight, and 14% of them (37 galaxies) inclined more than 75°, with an average inclination of 52° for all the sample.

Fig. 2.8 shows the morphological distribution of the 265 galaxies that compose the BETIS sample. The distribution is the following: 17 lenticular (S0) galaxies, 35 Sa, 4 Sab, 62 Sb, 40 Sbc, 72 Sc, 5 Scd, 17 Sd, and 11 irregular galaxies. The sample can be aggregated in 7 main types; S0 (6.5% of the total), Sa/Sab (15%), Sb (23.6%), Sbc (15.2%), Sc (27.3%), Scd/Sd

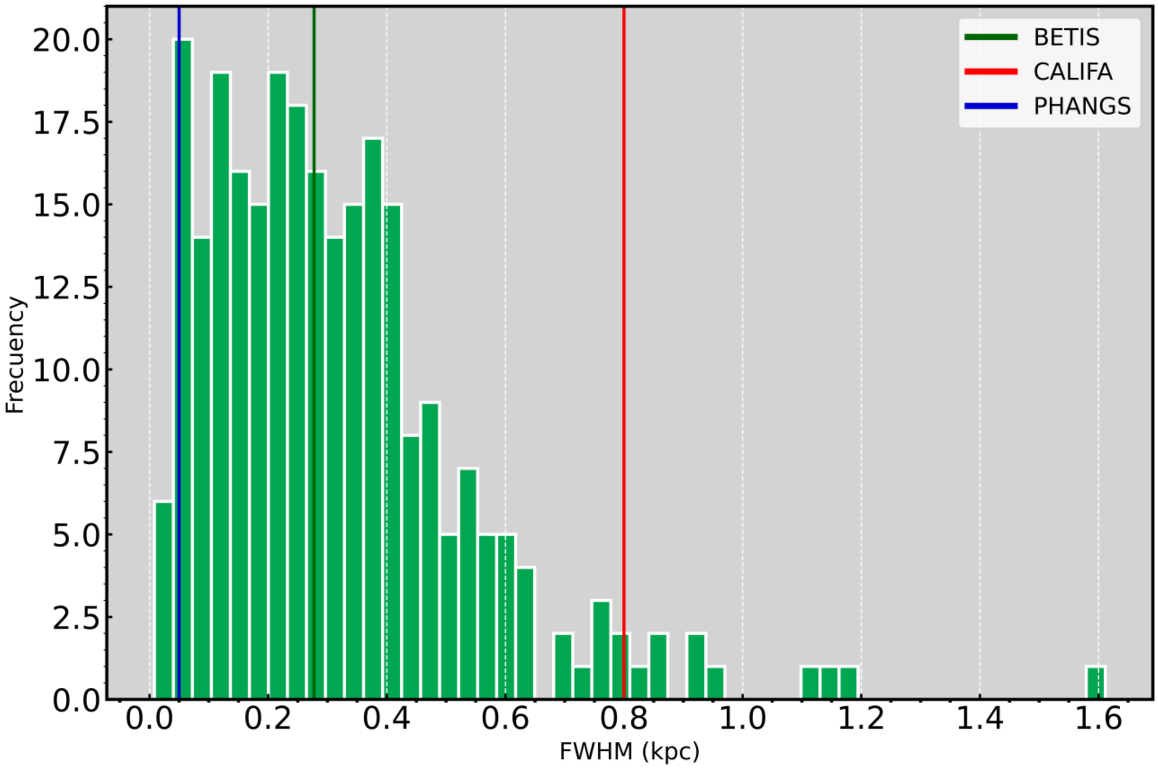

Figure 2.5: PSF spatial resolution (FWHM, in kpc) of the BETIS sample. The three vertical lines represents the mean FWHM of three samples: ∼ 0.8 kpc for Lac18, ∼ 275 pc for BETIS and ∼ 50 pc for Bel22.

(8.4%) and irregulars (4%), so it can inferred general properties of the DIG in function of the morphology. The BETIS sample includes two system of galaxies in interaction; the pair ARP144, and the ring shaped galaxy ESO350-40 (The Cartwheel) in order to study the DIG behaviour in galaxies where matter injections occurs and where the disk of the galaxy is deformed.

Fig. 2.9 shows a BPT diagram (Baldwin et al. 1981) for the nuclear emission of 186 of the galaxies of the samplé, obtained by integrating spectra of a region of 1 kpc region around the center of the galaxies whose nucleus is in the FoV of the observation (for the fluxes measurement see chapter 3). For the remaining galaxies, the entire FoV is integrated. The BETIS sample includes 21 LINER and 35 Seyfert galaxies.

2.2.1 The BETIS showcase sample

In order to develop a methodology to study the DIG at different physical resolutions (from PHANGS-like to CALIFA-like) and present initial findings of this analysis, a representative subset of seven galaxies of different morphologies, characteristics and resolutions has been selected from different MUSE projects (which will be included in the full BETIS sample for the forthcoming papers). This showcase sample has been carefully chosen to provide

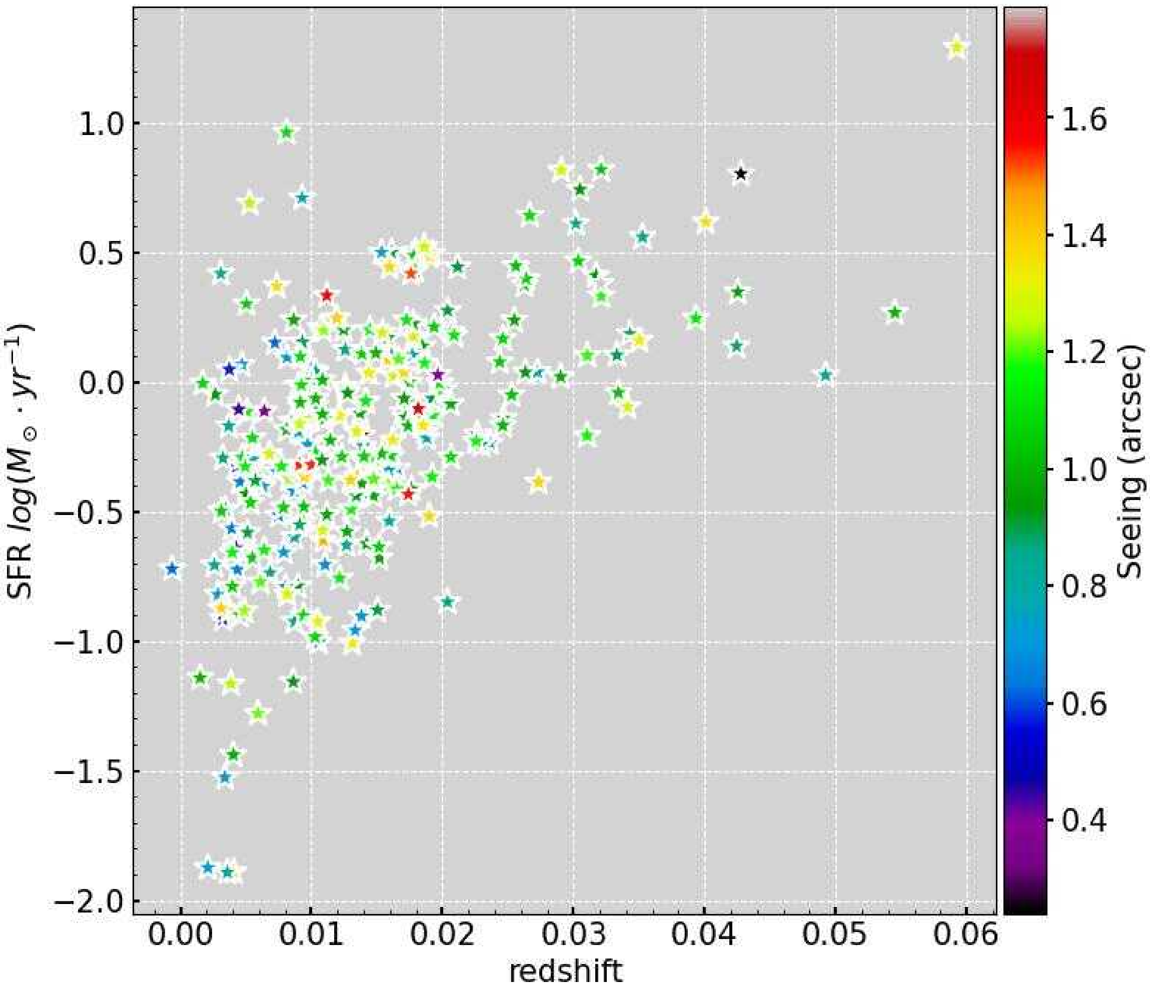

Figure 2.6: SFR distribution versus redshift of the BETIS sample. The colorbar represent the seeing reported in every cube, with a median of ~ 1 arcsec.

insight into the broader study and serves as a demonstration of the methodology employed. In addition, this sample will also serve to prove the impact of using galaxies of different characteristics and physics involved in the same analysis of the DIG.

The showcase sample was selected from the All-weather MUse Supernova Integral-field of Nearby Galaxies (AMUSING; Galbany et al. 2016) and AMUSING+ (Galbany et al. in prep.) project samples. These surveys are ongoing projects aimed at studying the environments of supernovae by means of the analysis of a large number of nearby supernova host galaxies ($0.005 < z < 0.1$). The AMUSING survey[8] currently comprises 571 supernova hosts observed during the semesters P95-P104 (April 2015-March 2020) and is composed by a wide variety of galaxy types with the common characteristic of having hosted a known supernova. The AMUSING+ sample is aimed to increase the number of supernova host, adding 143 objects to the previous AMUSING sample. The criteria followed for selecting the showcase sample

---

[8] The AMUSING survey characterisation is available online: https://amusing-muse.github.io/sample/

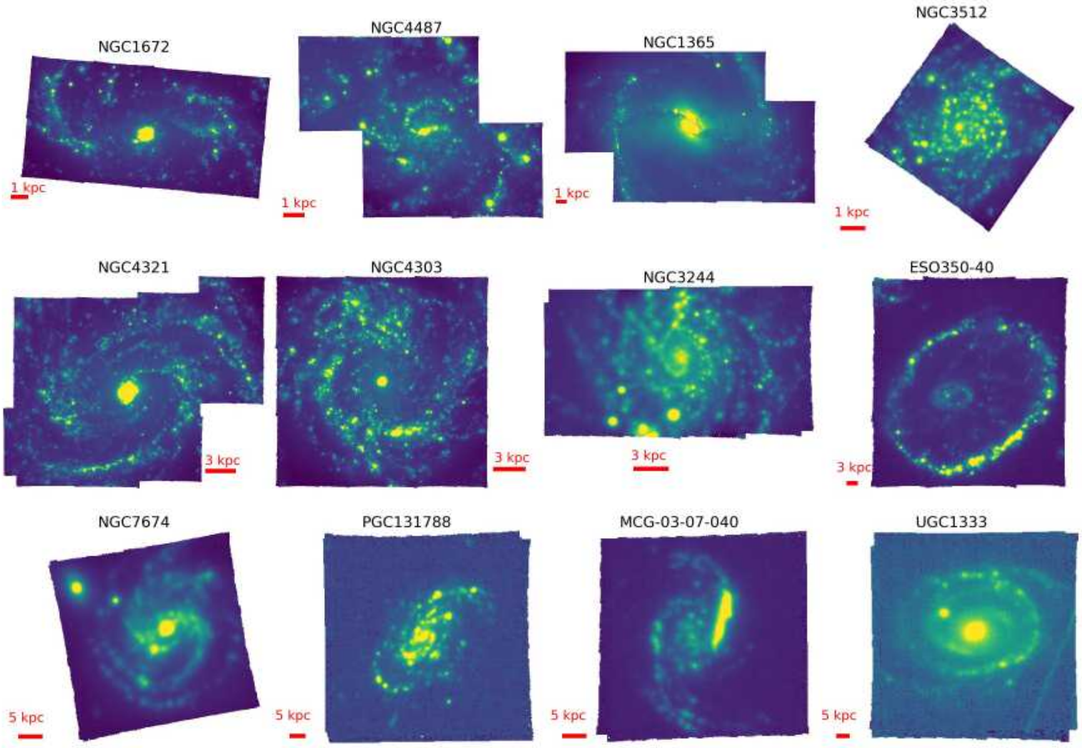

Figure 2.7: Hα images from the BETIS galaxies, constructed integrating the slides of the datacubes centred at λ = 6563 Å with a width of 10 Å. The four on the top are PHANGS-type galaxies, with FWHM = 25, 52, 65 and 86 pc respectively. The four on the middle are BETIS-type, with FWHM = 112, 136, 256 and 528 pc respectively. The four on the bottom are CALIFA-like galaxies, with FWHM = 760, 859, 1191, 1611 pc respectively. The first and the last galaxy of this figure are the best and the worst galaxy of the BETIS sample in terms of spatial resolution.

galaxies from the AMUSING and AMUSING+ samples are as follows.

- First, to test the methodology for different linear resolutions, the galaxies need to present resolutions between the full width at half maximum for PHANGS and CALIFA (41 pc $\lesssim$ FWHM $\lesssim$ 1 kpc).
- Next, since the physical properties of H II regions can vary between the inner and outer parts of the galaxies (Rodríguez-Baras et al. 2019), objects with FoV < 0.5R$_{25}$[9] in the datacube are not included if the resolution is high (FWHM $\lesssim$ 100 pc), in order to avoid limiting this study to the inner regions.
- Then, to test the methodology for different galaxy morphologies, every galaxy must have a different Hubble type, while also exhibiting star-forming regions.

---

[9] R$_{25}$ defined as the isophote at the blue brightness of 25 mag/arcsec^2.

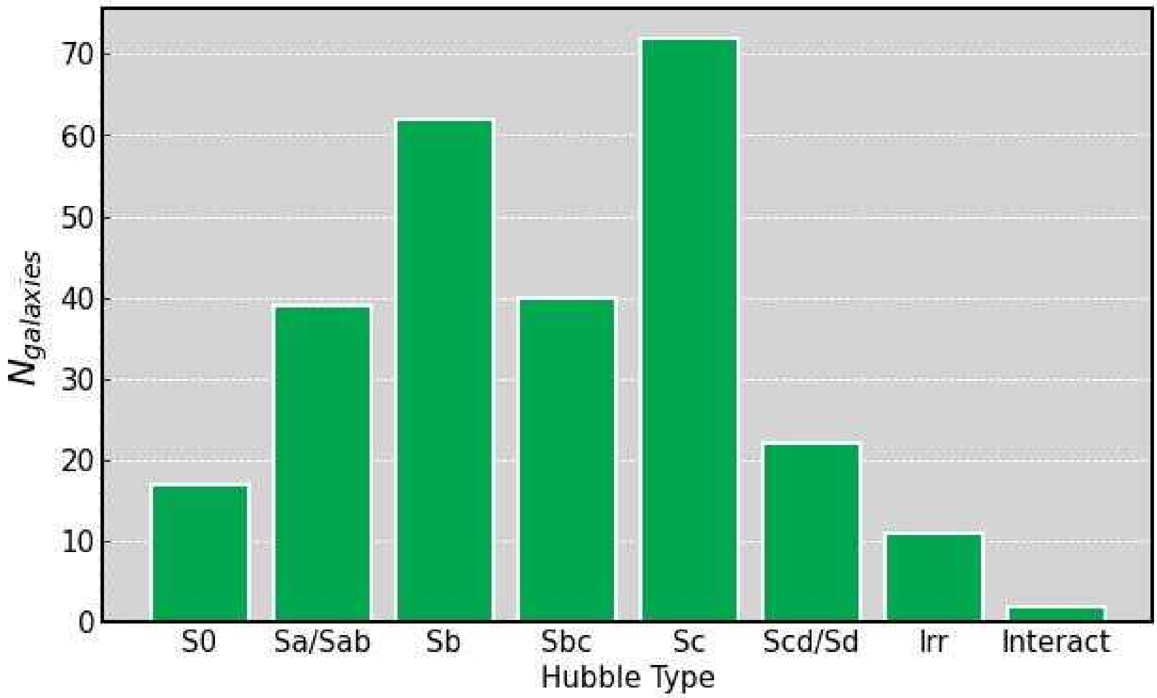

Figure 2.8: Hubble morphological type distribution of the BETIS sample, from the Hyperleda database (Makarov et al. 2014).

- Finally, galaxies with low depth or data-quality are excluded. In particular, if the average spectroscopic S/N of the Hα line in the DIG regions is lower than 3, the galaxy is disregarded.

Seven galaxies were chosen based on the previous criteria, belonging to the ESO periods P95, P98, P99, P101, and P103. The respective datacubes were already reduced by the AMUSING collaboration using the ESO reduction pipeline (Galbany et al. 2016; Weilbacher et al. 2020). Table 2.1 shows the general characteristics of the BETIS showcase sample and Table 2.2 shows the characteristics of the observations. The FWHM measured of the galaxies is derived assuming the seeing reported by the telescope via the `TEL.IA.FWHMOBS` parameter. The integrated stellar mass of the galaxies, obtained from a simple stellar population (SSP) fitting with STARLIGHT (see Ch. 3), spans between $3.31 \cdot 10^{10} M_{\odot} < M_{\star} < 1.04 \cdot 10^{12} M_{\odot}$, while the integrated star formation rate (SFR) spans between $1.31 M_{\odot}/yr$ < SFR < $4.92 M_{\odot}/yr$. The SFR was obtained using the Kennicutt & Evans (2012) relation: log(SFR) = log($L_{H\alpha}$) - log($C_{H\alpha}$), with $L_{H\alpha}$ as the Hα luminosity, corrected for interstellar extinction assuming the Cardelli extinction law, assuming R_V = 3.1 (Cardelli et al. 1989) and a Balmer decrement Hα /Hβ = 2.85. Then, log($C_{H\alpha}$) is the conversion factor between SFR and $L_{H\alpha}$, corresponding to 41.27 (Kennicutt & Evans 2012). Figure 2.10 shows false-colour images of the sample constructed as a composition of the [S II] (green), Hα (red), and [O III] (blue) emission line maps obtained following the methodology described in Sect. 3, but on a spaxel-by-spaxel basis. The native spatial resolutions vary from 49 pc (IC3476, i.e. PHANGS-like) to 960 pc

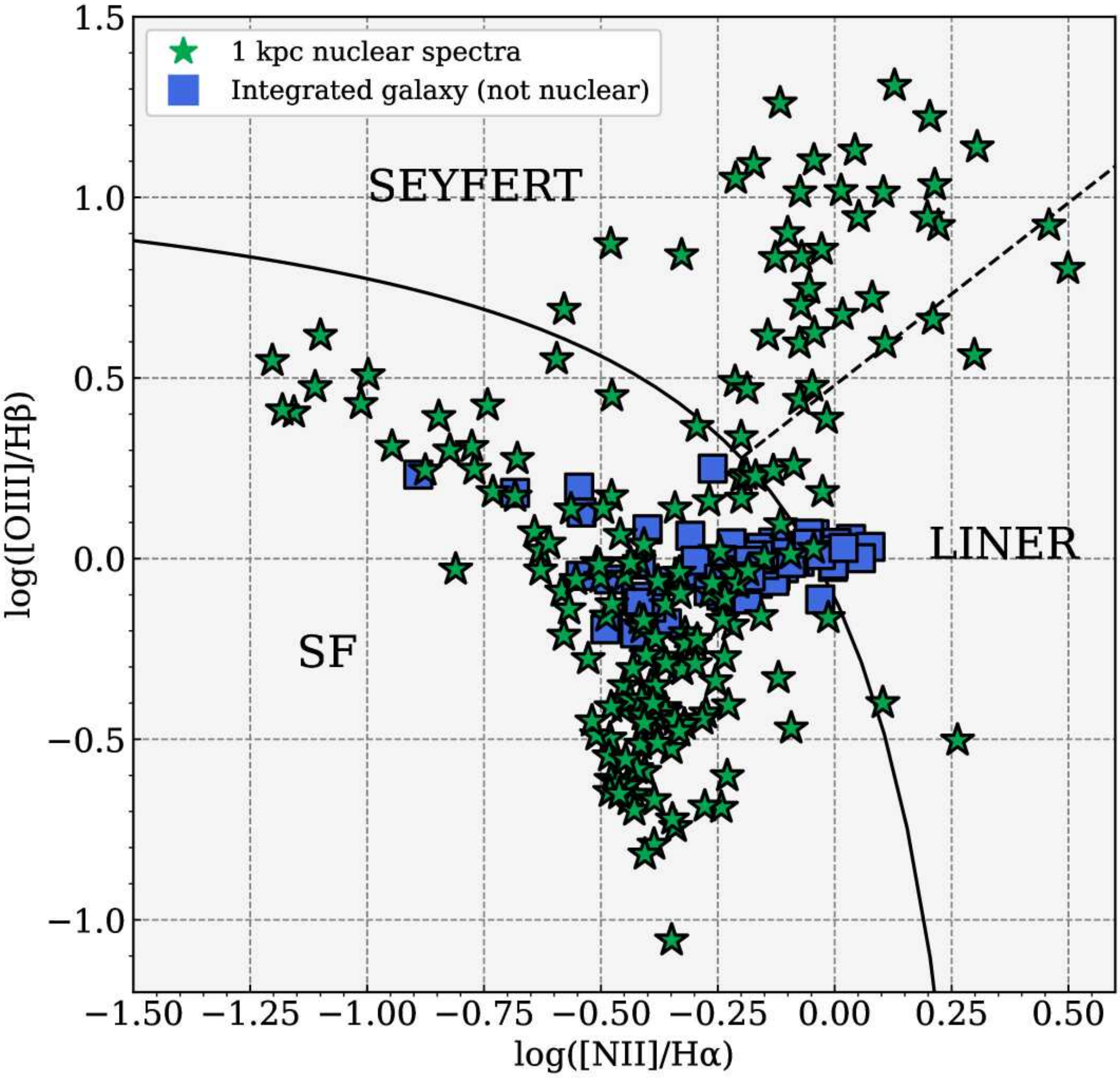

Figure 2.9: BPT diagram for the BETIS sample. The integrated spectra of a 1 kpc aperture centred in the nucleus of 186 galaxies are represented by the green stars. Meanwhile, the blue squares represent the integrated spectra of the galaxies whose nucleus is not included in the datacube. Solid line demarcation between star-forming and AGN regimes is given by Kewley et al. (2001). Dashed line demarcation between Seyfert and LINER regimes is given by Cid Fernandes et al. (2010).

(ESO325-43, CALIFA-like), with a median resolution of 395 pc. The sample includes three known active galactic nuclei (AGNs): NGC863 and NGC3393 are Seyfert 2 (Weedman 1977; Lipovetsky et al. 1988), while NGC692 is a low-luminosity AGN (LLAGN; Zaw et al. 2019). This study deliberately incorporate these galaxies presenting AGN emission. Although the AGN emission of the centre of the galaxy are masked during the methodology and analysis of the results, the aim is to investigate the impact of including galaxies exhibiting different physical processes via a global analysis of the ionisation mechanisms of the DIG in galaxies.

Table 2.1: General characteristics of the BETIS showcase sample, in order of morphological type. The columns represents, from left to right: The designation of the galaxy, the morphological Hubble-De Vaculeurs type, the RA and DEC in the J2000 epoch of the centre of the galaxies, restricted from the Paranal observatory (DEC < 25°), the physical diameter in kpc, the redshift, the PSF FWHM in pc, inclination with respect to the line of sight (in deg), the position angle (in deg) and the physical size of the spaxel, in parsec/spaxel, the log of the integrated stellar mass in solar masses, and the log of the star formation rate in solar masses per year. The RA, DEC, the diameter and the redshift are obtained from NED. The morphological type and position angle, from Hyperleda. $M_\star$ was obtained from López-Cobá et al. (2020), except NGC3393 and NGC6627 that was obtained from SSP fitting. The SFR was obtained as explained in Sect. 2.

Galaxy	**Morphology**	**RA** (J2000)	**DEC** (J2000)	**D** (kpc)	**z**	**FWHM** (pc)	**Incl** (°)	**PA** (°)	**spx size** (pc)	**log $M_\star$** ($M_\odot$)	**log SFR** ($M_\odot$/yr)
NGC863	SA(s)a	02h14m	-00d46m	34	0.02639	591.98	22.40	175.6	109	12.02	0.37
NGC3393	(R')SB(rs)a	10h48m	-25d09m	69	0.01246	253.56	25.74	12.8	51	10.96	0.19
NGC6627	(R')SB(s)b	18h22m	15d41m	28	0.01771	297.82	25.12	70.0	73	10.94	0.12
NGC692	(R')SB(r)bc	01h48m	-48d38m	96	0.02115	395.21	30.30	84.4	87	11.33	0.45
ESO584-7	Sc	16h12m	-21d37m	65	0.03171	618.88	45.12	148.0	131	10.52	0.40
ESO325-43	SAB(s)c pec	13h59m	-37d51m	107	0.03503	960.03	38.37	115.0	145	10.56	0.14
IC3476	IB(s)m	12h32m	14d03m	10	-0.00063	49.60	33.99	30.0	16	11.03	0.69

Table 2.2: Characteristics of the observations. Second column is the project where the galaxy was observed. Last column is the measured seeing in arcesec (as the `TEL.IA.FWHMOBS` parameter in the header of the .fits files from the datacubes). All galaxies were observed following the AMUSING survey strategy: non-optimal weather at Paranal, that is, at any seeing and even a bright moon.

Galaxy	**project**	**PI**	**ESO project ID**	**exp. time (s)**	**seeing (arcsec)**
NGC 0863	The dynamics of the AGN fuelling reservoir in MRK 590	Sandra Raimundo	099.B-0294	8x1100	0.901
NGC 3393	The MUSE atlas of disks (MAD)	C.M. Carollo	098.B-0551	4x900	0.789
NGC 6627	AMUSING survey IX	J. Anderson	103.D-0440	4x601	0.839
NGC 0692	AMUSING survey VII	Hanindyo Kuncarayakti	101.D-0748	4x599	1.403
ESO584-7	AMUSING survey VII	Hanindyo Kuncarayakti	101.D-0748	4x701	0.796
ESO325-43	AMUSING survey V	L. Galbany	099.D-0022	8x701	1.285
IC3476	MUSE study of nearby CC-SNe host environments and parent stellar populations	Hanindyo Kuncarayakti	095.D-0172	4x450	0.742

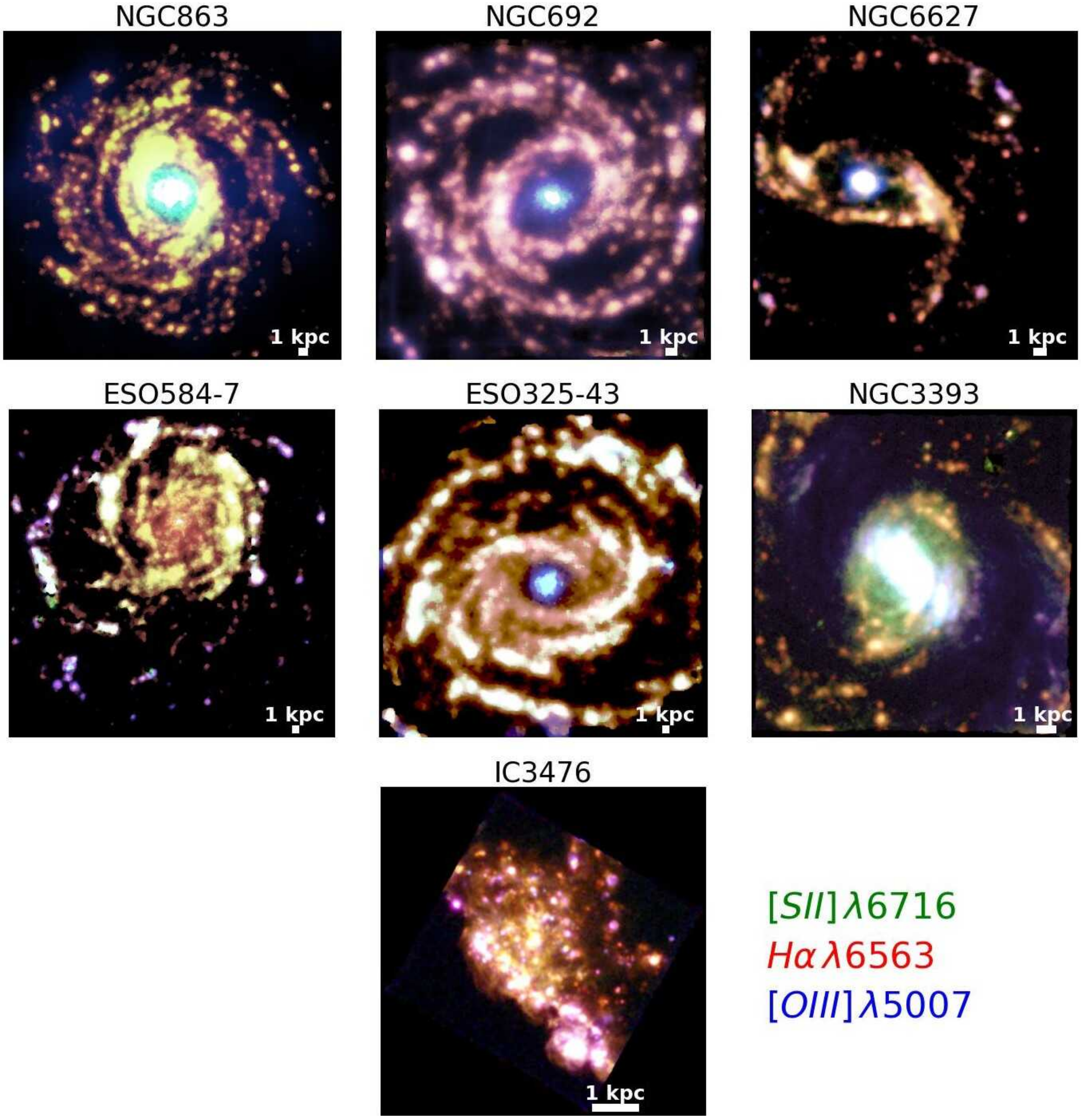

Figure 2.10: RGB synthetic images of the galaxies selected for the sample. The images are constructed as a composition of the [S II] λ6716 (green), Hα (red), and [O III] λ5007 (blue) spaxel-by-spaxel emission maps obtained following the methodology explained in chapter 3.

2.3 The eBETIS sample

For the reasons outlined previously, since galactic halos may exhibit diverse mechanisms and structures that contribute to the formation of ionised extraplanar gas, MUSE IFS data is used to undertake this task, as in the case of the BETIS sample on face-on galaxies. In particular, the sample of Com19 aligns well with the previous criteria. The sample, listed in table 2.3 and shown in figure 2.11, consists on eight edge-on ($i > 75°$) nearby galaxies ($z < 0.00979$, $D < 45.22$ Mpc) with high spatial resolution (FWHM < 200 pc) from the 096.B-0054(A) and 097.B-0041(A) VLT programmes. Table 2.3 shows the integrated star formation rate (SFR) in the disc spans between 0.024 $M_\odot$/yr < SFR < 0.229 $M_\odot$/yr. It was obtained using the Kennicutt & Evans (2012) relation: $\log(\mathrm{SFR}) = \log(L_{H\alpha})$ - 41.27, with $L_{H\alpha}$ as the Hα luminosity, corrected for interstellar extinction assuming the Cardelli extinction law, assuming R_V = 3.1 (Cardelli et al. 1989) and a Balmer decrement Hα /Hβ = 2.87. The galaxies are then normal-disc galaxies with low star formation. This is consistent with the classification of these galaxies in the star formation main sequence, with specific SFR ranging between -10.5 < log(sSFR/yr)< -9.92, corresponding barely to star-forming galaxies (using MUSE data and 3.6 μm stellar masses; Muñoz-Mateos et al. 2015; Zaragoza-Cardiel et al. 2020; Rautio et al. 2022).

This sample, observed with MUSE, is selected since this type of investigation requires more constraints compared to the face-on case, since we are navigating within the galactic halo, where the signal-to-noise ratio of the observed emission line (S/N, Rosales-Ortega et al. 2012;BETIS I) is lower. Consequently, besides high resolution, is required data as deep as possible to observe low surface brightness lines such as [O I] and [O III] , alongside data of sufficient quality to measure the [O I] line without interference from sky lines.

Every datacube consists in four exposures (three for IC217) of 2624 seconds, and at least half of the galaxy is covered by one VLT pointing (from the centre to one of the edges of the galaxy, i.e., $0.5R_{25} < 1$ arcmin). The data was originally reduced using the ESO data-reduction phase 3 using the MUSE pipeline (Weilbacher et al. 2020), and subsequently Com19 performed a sky subtraction using the ZAP software (Soto et al. 2016, see Com19 for more details).

This dataset has previously been used to analyse the eDIG in prior studies. Rautio et al. (2022) employed five of these galaxies, in conjunction with Hα and GALEX-FUV imaging, while Dirks et al. (2023) exclusively utilised IC1553 for a more comprehensive examination of the eDIG ionisation mechanisms within this galaxy. In this work, all eight galaxies from this dataset[10] (eBETIS sample henceforth) are considered to perform an exhaustive

---

[10] We downloaded the reduced datacubes directly from the ESO archive science portal.

spectral and spatial exploration of the eDIG structure and ionisation for every galaxy in particular.

The average sensitivity of the sample is 35.7 log(erg/s/kpc^2), obtained as the 2σ of the distribution of Hα surface brightness ($\Sigma_{H\alpha}$) of the bins of every Hα map. The average physical size of the bins is below 175 pc. Since the average PSF FWHM of the sample is below 200 pc, the binning does not significantly restrict the resolution in the galaxies.

Table 2.3: General characteristics of the eBETIS sample, in order of declination. The columns represents, from left to right: The designation of the galaxy, the RA and DEC in the J2000 epoch, the morphological Hubble type, the redshift, the distance in Mpc, the position angle (in deg), the PSF FWHM in pc, inclination with respect to the line of sight (in deg), the 2σ $\Sigma_{H\alpha}$ limit and the average physical size of the bins in pc. The RA, DEC, the morphological type, the redshift and distances are obtained from NED. The position angles and inclinations are obtained directly from Com19 and Hyperleda. The last columns represent the integrated Hα luminosity within the eDIG and the integrated star formation rate (SFR) of the disc.

Galaxy	**RA (J2000)** (deg)	**DEC (J2000)** (deg)	**Type**	**z**	**D** (Mpc)	**P.A.** (°)	**FWHM** (pc)	**Incl.** (°)	**log SB lim.** (erg/s/kpc^2)	**Bin size** (pc)	**L$_{eDIG}$(Hα)** (erg/s)	**log SFR$_{Disc}$** (M$_\odot$/yr)
IC217	34.0435	-11.9267	Scd	0.00630	24.32	35.7	117.91	82.6	35.6	94.3	39.11	0.063
PGC28308	147.5582	-12.0576	Scd	0.00907	45.22	125.2	153.46	85.5	35.2	175.4	39.12	0.084
PGC30591	156.3603	-15.3492	Sd	0.00676	35.22	169.2	187.83	86.6	36.0	136.6	39.13	0.055
ESO544-27	33.2277	-19.3168	Sb	0.00818	32.81	153.3	159.07	90.0	35.0	127.2	38.92	0.024
IC1553	8.1671	-25.6075	Irr	0.00979	32.25	15.0	171.99	78.6	36.5	125.1	39.80	0.229
ESO443-21	194.9412	-29.6002	Scd	0.00941	40.31	160.8	195.45	79.0	36.6	156.4	39.71	0.184
ESO469-15	347.2317	-30.8579	Sb	0.00545	19.81	149.2	86.44	90.0	35.9	76.9	38.90	0.029
ESO157-49	69.9036	-53.0126	Sc	0.00559	24.82	30.4	96.26	79.3	35.3	96.3	39.46	0.060

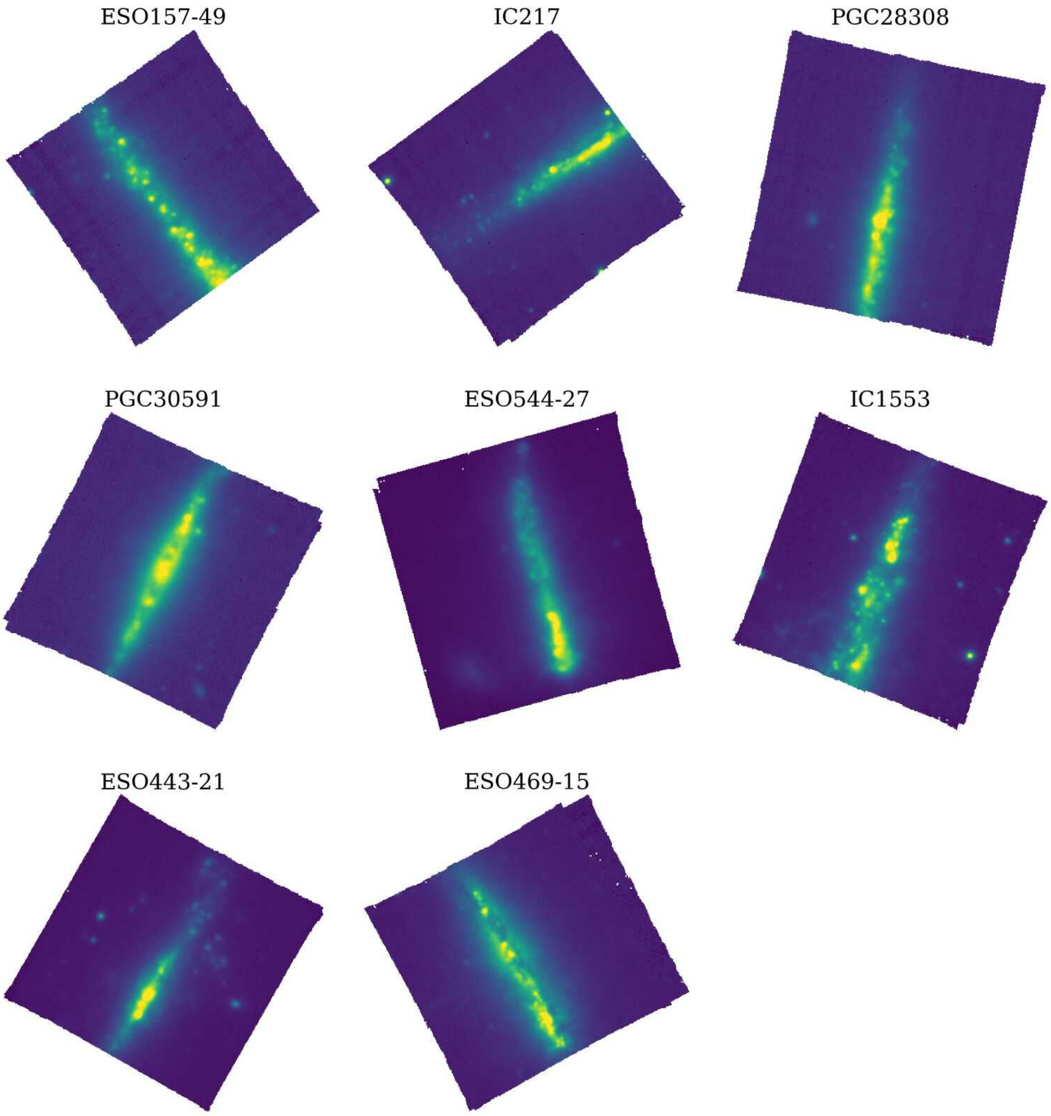

Figure 2.11: Hα images of the eBETIS galaxies. Constructed similarly to figure 2.7.

Chapter 3

Methodology

The study of extragalactic DIG has conventionally relied on analyses of high-resolution narrowband Hα and images of nearby galaxies ($z < 0.01$, Rand et al. 1990; Dettmar 1990; Ferguson et al. 1996a; Zurita et al. 2000) or long-slit spectroscopy with limited spatial coverage (Reynolds 1985; Wang et al. 1997; Otte et al. 2001; Hoopes & Walterbos 2003; Haffner et al. 2009a). In these studies, the methodology for subtracting the DIG from the galaxies and distinguish their emission from the H II regions emission is typically based on using cut-offs in the surface brightness ($\Sigma_{H\alpha}$) of the Hα line. In studies with images at a high resolution, a morphological definition of the H II regions using automatised tools is performed (Walterbos & Braun 1994; Zurita et al. 2000, 2002; Oey et al. 2007). Nevertheless, these studies have been constrained only to less than five face-on and edge-on galaxies in their sample, based only in Hα in those studies with high resolution and with low resolution in those with spectroscopic information. However, the use of the IFS in recent years has allowed for the adoption of methodologies for DIG subtraction and analysis that are based on spatially-resolved spectroscopic information with broad samples, (e.g. MaNGA, CALIFA, or PHANGS).

For example, DIG studies using data from the MaNGA survey (Z17, Jones et al. 2017) made use of 365 nearly face-on star-forming galaxies with 2.5 arcsec PSF FWHM, which is not enough to resolve individual H II regions which typical sizes are ~100 pc. In this particular case, Z17 performed a cut out on $\Sigma_{H\alpha} > 10^{39}$ erg$\cdot$ s$^{-1}\cdot$ kpc^{-2} to select those spaxels dominated by H II regions emission. On the other hand, the studies based on CALIFA data (Lac18), made use of 391 galaxies with a median PSF FWHM of $\sim$ 0.8 kpc and proposed an alternative method to separate the DIG and the H II regions using the Hα equivalent width (EW$_{H\alpha}$), since (according to the authors) this parameter is a more appropriate proxy to distinguish the fundamental differences between the DIG and the star forming regions in comparison with the $\Sigma_{H\alpha}$. In addition, the authors argue that the usage of $\Sigma_{H\alpha}$ could lead to misclassifications of low-surface-brightness H II regions such as DIG.

Other authors have used the criteria to define and classify the DIG regime based on $\mathrm{EW}_{H\alpha}$ continued to be used to define the DIG (Vale Asari et al. 2019; Espinosa-Ponce et al. 2020). However, redefining the DIG a priori as the ionised gas consistent with ionisation from HOLMES could be problematic if the main goal is to discern the different ionisation mechanisms (Bel22). This is a challenging problem, as the standard resolution of CALIFA or MaNGA can not discern individual H II regions in order to characterise the DIG morphologically. In addition, the high spatial resolution of some galaxies observed by IFS (e.g. M83-TYPHOON/PrISM; Poetrodjojo et al. 2019, M83-MUSE; Della Bruna et al. 2022a, PHANGS-MUSE; Bel22, Congiu et al. 2023), enables the use of automated tools in order to detect and remove individual H II regions in IFU datacubes with resolutions of $\sim$ 50 pc, but constrained to a few objects.

This chapter outlines the approach for determining the DIG by utilising the spectroscopic and morphological data generated by the MUSE-IFS, using a broad dataset with high resolution and with spectroscopic information, not only Hα . A summary of the methodology, designed for galaxies of inclinations below 45°, is provided below and it is subsequently explained in further detail in the following sections:

- First, to increase the S/N of the weak, low-surface brightness emission lines involved in the DIG study, a modified version of the adaptive binning technique from Li et al. (2023a) is performed to the S/N map of the [S II] line, obtaining then a segmentation map of the galaxy. The segmentation map is then applied to the datacube, to obtain a binned datacube, in which each bin corresponds to the integrated spectra as the sum of the spaxels contained in the bin.
- Then, a spectral fitting is performed on the binned spectra in order to derive emission line maps of the most important species for the DIG study. The species considered are: the hydrogen Hα and Hβ Balmer recombination lines, the He I λ5876 recombination line, and the collisionally excited forbidden lines: [O III] λ5007, [O I] λ6300, and the doublets [N II] λ6548, 6584 and [S II] λ6717, 6731. The Hα and Hβ equivalent widths (EWs) are also calculated in this step.
- Finally, the DIG is separated from the emission of the H II regions using a combination of an automated tool to detect and subtract the H II regions from the binned Hα maps and a cut-off in the Hα surface brightness ($\Sigma_{H\alpha}$) to subtract bright, irregular H II regions not detected by the automated tools. This results in a mask that corresponds to the lower-limit of the DIG. This mask is applied to all the binned emission line maps, creating a set of the lower-limit DIG emission. The upper-limit DIG emission is derived from the lower-limit binned maps considering a constant DIG emission column above the projected areas of the H II regions. This methodology can be generalised for inclinations above 45° and edge-on galaxies.

3.1 Adaptive binning

Typically, the distinction between SF regions and DIG has been made using Hα , but if the aim is to explore the DIG by using all available spectroscopic information, the key emission lines must be considered, such as [O I] , [N II] , [O III] , and [S II] . For a reliable analysis of the DIG, is crucial to take into account S/N limitations of the data, specially in those lines of lower surface brightness, such as those mentioned above.

The signal of an emission line feature of a spectrum can be defined as the difference between the maximum flux value of an emission line $f(\lambda_{em})$ centred on λ_{em} of width w_{em} (in Å), and the mean of the fluxes in the two adjacent pseudo-continuum bands $f(\lambda_{c1})$ and $f(\lambda_{c1})$ of widths, w_{c1}, w_{c2}, measured on the spectrum of a given spaxel; and the noise corresponds to the mean of the flux within the two adjacent pseudo-continuum bands, $f(\lambda_{c1})$ and $f(\lambda_{c1})$ (Rosales-Ortega et al. 2012). Figure 3.1 shows two spectra illustrating the definition of S/N.

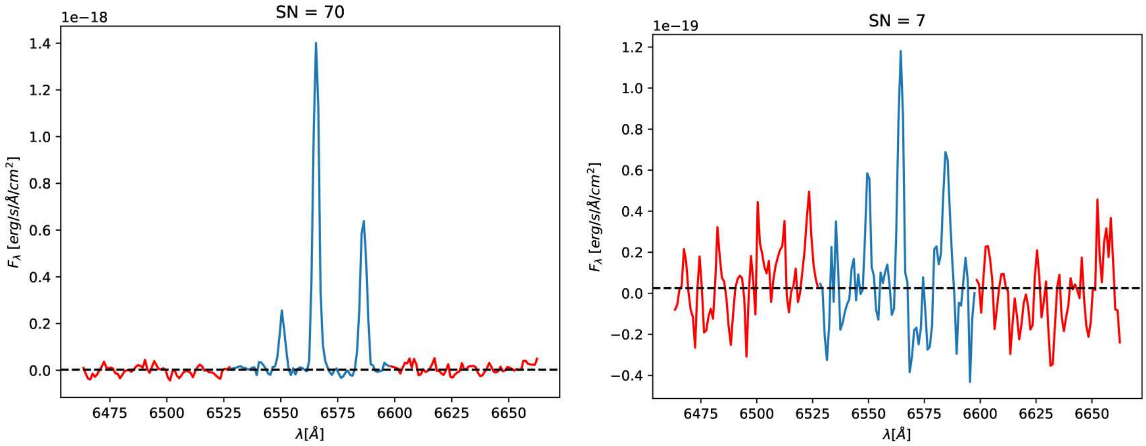

Figure 3.1: Example of two spectra of S/N($H\alpha$) = 70 (left) and S/N($H\beta$) = 7 (right) according to the definition (eq. 3.1). λ_{pc} is coloured in red and the dashed line represents the mean value of λ_{pc}.

For the sake of clarity, in this work, the S/N of an emission line is the ratio of the amplitude of the emission line, defined as the peak of the line minus the mean flux of the pseudo-continuum, over the standard deviation of the adjacent pseudo-continuum on the spectrum:

$$S/N(\lambda_{em}) = \frac{\mu}{\sigma} = \frac{f(\lambda_{em}) - \langle f(\lambda_{c1}), f(\lambda_{c2}) \rangle}{\sqrt{\sigma^2(f(\lambda_{c1}), f(\lambda_{c2}))}}. \tag{3.1}$$

The most commonly employed approach to enhance the S/N ratio of the data is to conduct adaptive binning, where individual pixels are combined into larger entities known as "bins" until the desired target S/N is achieved, However, this comes at the expense of diminished spatial resolution. The Voronoi binning method (Okabe et al. 2000; Cappellari & Copin 2003) generally resolves the issue of retaining the highest spatial resolution of the images while adhering to the minimum S/N limitation. This is achieved by tessellating the image and adjusting the bin size to ensure that every bin attains the desired S/N. However, this technique is particularly well suited for analysing elliptical and featureless galaxies as it relies on the continuum S/N. It may not be as effective for this purpose, as the line maps show irregular structures, such as those depicting nebular gas emission lines. Consequently, an alternative method is required in order to avoid losing the primary morphology of spiral galaxies.

To solve this, we used a modified version of the adaptive binning method, introduced by Li et al. (2023a) in order to enhance the S/N of weak emission lines. The code takes the flux of the line, the noise, and target S/N as its input to create a series of maps that cover the same area as the input data (map_1,...,map_N,...,$\mathrm{map}_{N_{max}}$), as seen in Fig. 3.2. For each map_N the set of N×N pixels are averaged, and, as a consequence, the S/N will be increased. If the S/N of the bin is not the target S/N, the code takes the map_{N+1} value instead. In this new algorithm, the BETIS-binning, the code generates a segmentation map for binning the observed cube and getting a set of binned emission line maps (one per each considered line). The BETIS-binning technique was carried out as follows:

First, we take as input the signal and noise defined in Eq. 3.1 and a target S/N. The code then creates the series of map_N; however, instead of recovering the new averaged flux, we save an index, *k,* in the coordinates [i_0, j_0], [i_0, j_1], [i_1, j_0], [i_1, j_1],...,[i_N, j_N], whose flux can then be averaged. The next subset of coordinates whose flux will be averaged will have an index of k+1. Then, the previous step is repeated for all subsets of coordinates for k = 1,...,N_{bins}. This results in a segmentation map, with the lowest bin indices k corresponding to the higher bins, namely, the 1×1 bins that correspond to the pixels with S/N higher than the S/N target and the lower indices corresponding to the bigger bins, namely, those needing more pixels to reach the target S/N (as seen in Fig. 3.2). Finally, each bin of the segmentation map correspond to the integrated spectra of the observed cube as the sum of the spaxels contained in the bin. This result in a binned observed datacube.

Binning the observed cube offers the advantage of enhancing the S/N of the spectra, rather than merely reducing the relative error associated to the Gaussian fitting of the lines, as is the case with direct binning the emission line maps. Moreover, in order to generate binned EW maps, it is not methodologically correct to bin the EW map obtained through spaxel-by-spaxel fitting. This is because EW is not an additive quantity; it varies when there are changes in the underlying stellar continuum. Hence, it is important to calculate the new EW from the integrated spectra. In order to increase the S/N of all the lines of interest, we need to choose a target feature as a basis to construct the segmentation map for the observed cube, ensuring to recover the maximum spatial information and signal in the DIG regimes. Using S/N([S II]) as the target for adaptive binning is the optimal option since it is a low-ionisation collisional excitation line that remains unaffected by the correction for stellar population after the spectral fitting process.

Considering the most important low-ionisation species that are found to be enhanced in the DIG regimes in SF galaxies, such as [N II] and [S II] (Z17; Lac18), the [S II] line exhibits the lowest S/N (mean of 5, median of 3) among the low-ionisation species. Furthermore, the [O III] line exhibits a mean S/N of 2.5, therefore, if a $\sim 5\sigma$ detection is required, the S/N needs to be increased by a factor of 7 (Bel22). To achieve this, the BETIS-binning method is performed using S/N([S II]) = 10 as the target S/N. Figure 3.5 (right panel) shows the distribution of S/N([S II]) obtained in the integrated spectra, depicting that the average S/N of 10 settled as target is reached.

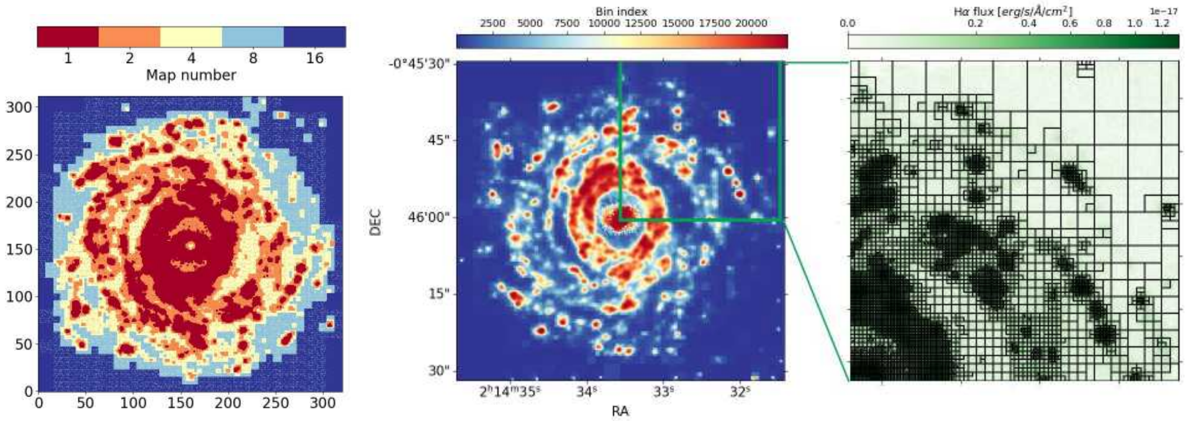

Figure 3.2: Example of an adaptive binning of NGC863 using $S/N([S\,II]) = 10$ as target. The first figure represent the map numbers (map_N) from Li et al. (2023a) algorithm. The second figure is the segmentation map obtained from the BETIS-binning algorithm, where the bin index goes from $k = 1$ to N_{bins}. The third figure is a close-up of the segmentation map plotting the borders of the bins over the Hα map. It is noticeable that the H II regions, whose S/N is higher, are not binned, maintaining the structure pixel by pixel, and the bins are getting bigger as we move out of the H II regions.

3.2 Spectral fitting

Each individual new spectrum, after being brought to the rest-frame, must be corrected for Milky Way extinction. The correction is carried out by multiplying each spectrum by a factor $10^{0.4 \cdot a_\lambda}$, where a_λ is the extinction function of Fitzpatrick (1999), using the Python library *extinction.fitzpatrick99*[1], that reads the $R_V = A_V/E(B-V)$ ratio (fixed at 3.1) and the

---

[1] https://extinction.readthedocs.io/en/latest/index.html

total V-band extinction in magnitudes for each galaxy, obtained from Hyperleda. Values can be found in the table of BETIS characteristics online.

For every new spectrum, the emission line features can be obtained by performing a simple stellar population (SSP) synthesis.

Performing a SSP synthesis (Tinsley 1968) requires an estimation of the type of stellar populations, namely, the masses, ages, and metallicities found in a galaxy, star cluster, or region of a galaxy based upon its spectra. The SSP synthesis is carried by the STARLIGHT software (Cid Fernandes et al. 2005), which fits an observed spectrum, O_λ with a model, M_λ, which adds up N* spectral components from a pre-defined set of base spectra. The synthetic model spectra that the program generates take the form:

$$M_\lambda = M_{\lambda_0}\left(\sum_{j=1}^{N_*} x_j b_{j,\lambda} r_\lambda\right) \otimes G(v_*, \sigma_*), \tag{3.2}$$

where $b_{j,\lambda}$ is the normalised spectrum of the jth SSP; r_λ is the reddening term; M_{λ_0} is the synthetic flux at the normalisation wavelength; $\otimes$ is the convolution operator; $G(v_*, \sigma_*)$ is a Gaussian distribution centred at velocity, v_* and with a dispersion, σ_*; and $\mathbf{x}$ is the population vector. Each component x_j ($j = 1, ..., N_*$) represents the fractional contribution of the SSP with age, t_j, and metallicity, Z_j, to the model flux.

In this work we use CB07 (Bruzual 2007a,b) base spectra for the SSP models. The model spectra have a resolution of $R \sim 2000$ and 1 Å of spectral sampling. The MUSE observed spectra have $1750 < R < 3750$ and 1.25 Å of spectral sampling, so we perform a linear interpolation for every single integrated spectrum to resample it at 1 Å. The integrated observed spectra are then rest-framed, resampled to $\Delta\lambda = 1$ Å and corrected to Milky Way extinction. These spectra are used to perform the SSP fittings.

The CB07 base spectra consists on $N_* = 100$ SSPs that comprises three metallicities: $Z = 0.2Z_\odot, Z_\odot$, and $2.5Z_\odot$, and 15 ages, from $t = 0.001$ to $t = 13$ Gyr. All SSPs are normalised to $1M_\odot$ at $t = 0$. Their spectra were computed with MILES-2007 evolutionary tracks models, and Chabrier (2003) IMF ($0.1M_\odot < M < 100M_\odot$).

The CB07 base comprises SSPs with the same metallicities and age range than the BC03 base (Bruzual & Charlot 2003). The difference between them are the TP-AGB spectra that CB07 adds in the base and the use of MILES-2007 evolutionary tracks models instead of Padova-2004.

STARLIGHT takes the following inputs: the wavelengths (λ), the observed spectrum (O_λ, resampled, rest-framed, and corrected for MW extinction), the errors (e_λ), a base-master file with the SSPs, and a mask file. The mask file specifies the regions of the spectra to be excluded from the modelling process, such as emission lines, artefacts, and outliers in O_λ (see Table 3.1). During the run, STARLIGHT constructs the synthetic spectrum M_λ according to Eq. (3.2) and identifies the best fit to the observed O_λ. The output files include the population mixture of the best fit, with parameters such as x_j, Z_j, t_j, $(L/M)_j$, stellar masses, and the percentage of each component, as well as the synthetic spectrum M_λ.

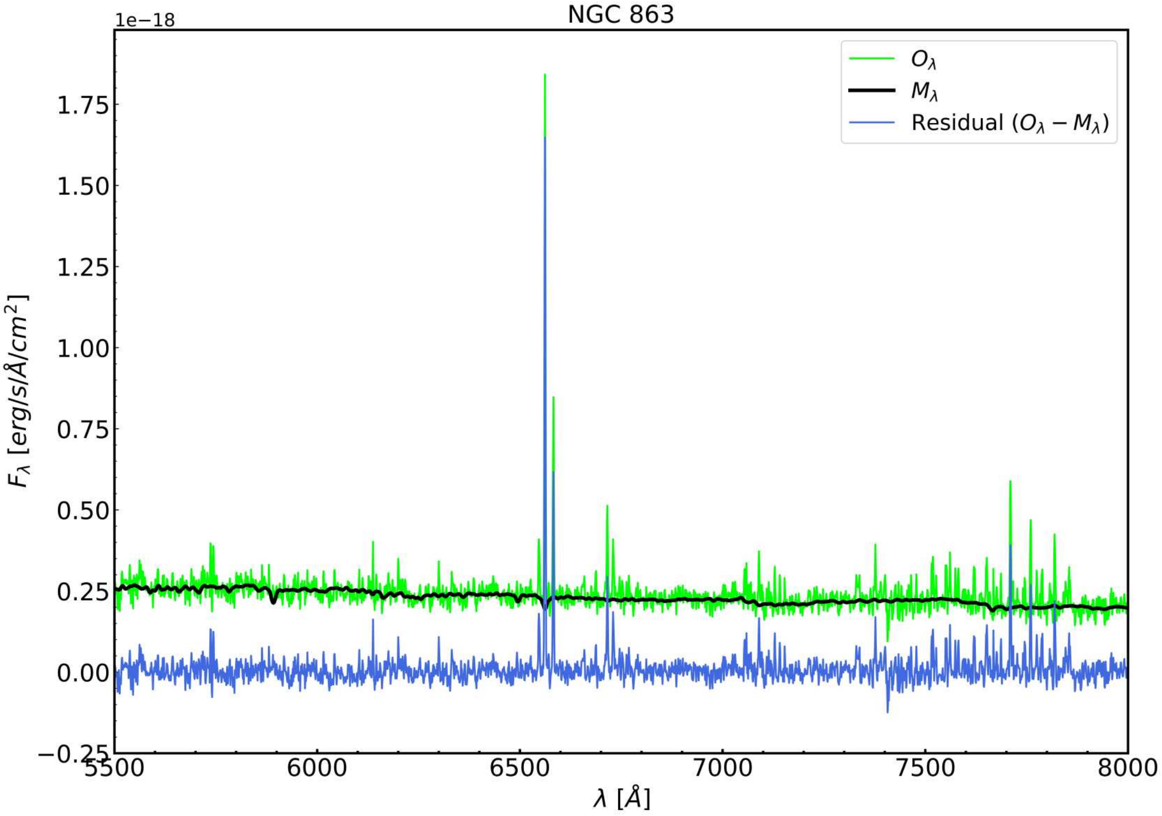

Figure 3.3: Example of a SSP fitting for a simple spaxel of the galaxy NGC 863. The observed, rest-framed and resampled spectrum is coloured in green. The black spectrum is the best fit synthetic spectrum from the STARLIGHT SSP fitting, and the blue spectrum is the nebular emission of the spaxel, obtained from the residue of the fit, subtracting the synthetic spectrum to the observed.

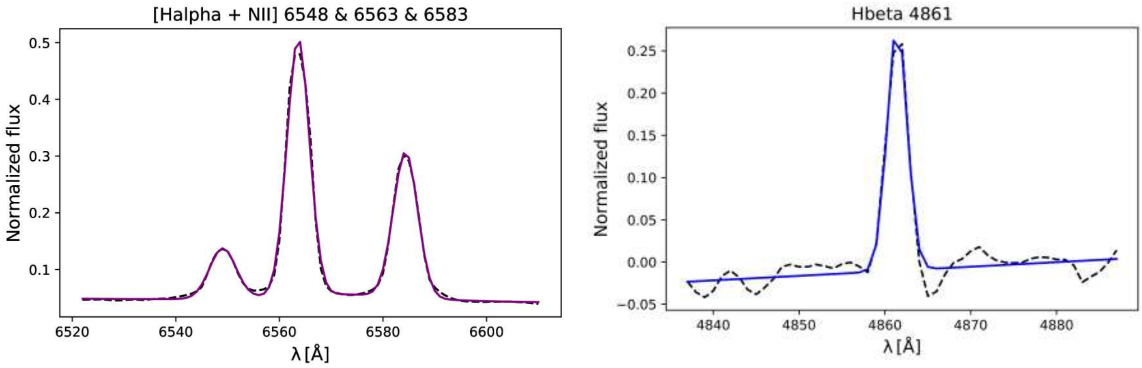

Figure 3.4: Example of the multipeak fitting of Hα and [N II] lines (left). The purple curve is the Gaussian curve fitted. Example for $H\beta$ (right). Blue curve is the Gaussian curve fitted. In both cases, black dashed line is the input spaxel spectrum.

Table 3.1: List of lines masked during the SSP fitting processes. First column represent the wavelength range not considered during the fittings, the second column is the line or source masked, and the third column is the description of the line/source masked.

Wavelength range [Å]	**Line**	**Description**
4550.0 – 4760.0	WR BP	WR blue bump
4848.0 – 4874.0	Hβ	4861 emission line
4940.0 – 5028.0	[O III]	4959 and 5007 emission lines
5190.0 – 5210.0	[NI]	5200 emission line
5740.0 – 5900.0	WR RB, HeI, NaD	WR red bump, 5876 emission line and 5890 ISM absorption (NaD)
6280.0 – 6335.0	[O I] , [SIII]	6300 and 6312 lines
6528.0 – 6608.0	Hα + [N II]	6563, 6548 and 6583 emission lines
6658.0 – 6695.0	He I	6678 emission line
6696.0 – 6752.0	[S II]	6717 and 6731 emission lines
7015.0 – 7080.0	He I	7065 emission line
7118.0 – 7158.0	[ArIII]	7136 emission line
7293.0 – 7353.0	[O II]	7320 and 7330 emission lines
7645.0 – 7720.0	[KI]	7665 and 7699 lines
7735.0 – 7765.0	[ArIII]	7751 emission line
8478.0 – 8682.0	CaII	8498, 8542 and 8662 lines
9000.0 – 9030.0	Pa10	9016 emission line
9043.0 – 9090.0	[SIII]	9069 emission line
5455.0 – 5475.0	SKY_Hg	Mercury sky line
5570.0 – 5585.0	SKY_OI	Oxygen sky line
5685.0 – 5690.0	SKY_Na	Sodium sky line

3.3 Obtaining the data products

A single pointing MUSE datacube typically contains over 90,000 spectra. After applying the adaptive binning method, the number of spectra to be fitted with STARLIGHT is reduced to approximately 15,000 per galaxy. A single SSP fitting takes over 1.5 minutes to complete[2], this means that getting all synthetic continuum spectra from a single binned observed datacube takes over 15.6 days (the binning step only takes ~30 minutes). This issue is

---

[2] Assuming that STARLIGHT is running on a CPU of 64 GB of RAM with a single processor of 3.3 GHz.

mitigated by utilising various high-performance machines, which also enable the execution of codes and programs in parallel. In particular, during the development of this work, we used three superclusters to undertake these tasks: ToLTEC from the Great Millimeter Telescope (GTM) at INAOE, MEXTLI from INAOE and CUETLAXCOAPAN from Laboratorio Nacional de Supercómputo del Sureste de México (LNS). These superclusters, in addition to their superior performance in terms of memory, RAM, and processors, consist of multiple cores that enable the parallel execution of numerous processes simultaneously (240 cores for CUETLAXCOAPAN and 120 for ToLTEC and MEXTLI) distributed through different computing nodes (six for CUETLAXCOAPAN, eight for ToLTEC and one for MEXTLI). The parallel execution of STARLIGHT through the different cores and nodes in one of these computers reduces the execution time from ~16 days for a single cube to less than a hour.

Once all the synthetic continuum spectra for all the integrated spectra of the binned datacube were obtained, we could derive the 'nebular gas' or 'residue' spectra in the form $O_\lambda - M_\lambda$, which contains the nebular emission of the object (see Fig. 3.3).

Finally, with the nebular spectra, we can determine the emission features using the Python module MPFIT[3]. This module allows us to perform Gaussian fitting around all emission lines of interest for all the nebular spectra. By doing so, we can determine the fluxes and construct the binned emission line maps for each of the nine lines mentioned at the beginning of this chapter.

This module performs a multipeak Gaussian fit for each individual line, with $\sigma = FWHM_i/(2\sqrt{2ln2})$, with $FWHM_i$ as the MUSE initial full width at half maximum, corresponding to 3 Å. The module search the peak of the line in a 10 Å (200-300 km/s) range centred in a central wavelength λ_c and performs the Gaussian fit in a range between $0.5\sigma - 2\sigma$. The flux of the kth bin for the λ line is then defined as $F_k(\lambda) = \sqrt{2\pi}(G_{peak} \times G_{width})$, being G_{peak} the peak of the Gaussian fit, and G_{width} its standard deviation (see Fig. 3.4). The error associated to that flux is then: $\delta F_k(\lambda) = \sqrt{2\pi}\sqrt{(\delta G_{peak} \times G_{width})^2 + (G_{peak} \times \delta G_{width})^2}$, with δG_{peak} and δG_{width} being the formal 1-sigma errors of each parameter, computed from the covariance matrix using as the error of the integrated nebular spectra the error of the integrated observed spectra.

Analogously, the Hα and Hβ equivalent widths are also calculated during this step. This is done by using the ratio between the integrated observed spectra and the fitted stellar model, resulting in a normalised stellar absorption spectrum, where the equivalent width is fitted for every bin using MPFIT and following the same steps as for the calculation of the fluxes.

---

[3] https://github.com/segasai/astrolibpy/blob/master/MPFIT/MPFIT.py

Each kth bin will have associated a set of coordinates [i_0, j_0], [i_0, j_1], [i_1, j_0], [i_1, j_1],...,[i_N, j_N]. So, to construct the binned emission line map, each one of the coordinates of the kth bin will have the flux corresponding to $F_k(\lambda)$. All the codes developed are available at the GitHub[4].

Figure 3.5 shows the difference between the [S II] emission line map obtained after performing the SSP fitting on the observed cube spaxel-by-spaxel (left panel) and on the binned cube applying the exposed method (central panel).

3.4 Definition of the (e)DIG

3.4.1 Morphological definition of the DIG in face-on galaxies

The separation between SF regions and the DIG has been always the first topic of discussion when studying and analysing the physics of the DIG. Historically, the most common method has been to separate the DIG from SF regions based on a Hα surface brightness ($\Sigma_{H\alpha}$) cut-off (Zurita et al. 2000; Oey et al. 2007; Z17). However, this method presents the problem of misclassifying low-surface-brightness H II regions as DIG, in addition to the possibility of classifying the emission of two overlapped DIG regions as H II regions (Lac18).

A suitable alternative for this problem is using automatised tools for the detection and subtraction of the H II regions individually. Several tools have been developed for this task, including SExtractor (Bertin & Arnouts 1996), HIIphot (Thilker et al. 2000), HIIexplorer (Sánchez et al. 2012), pyHIIexplorer (Espinosa-Ponce et al. 2020), astrodendro (Della Bruna et al. 2022a), pyHIIextractor (Lugo-Aranda et al. 2022), and CLUMPFIND (Congiu et al. 2023).

The spatial resolution is an important key to detect and define morphologically individual H II regions. For the specific range of resolutions of the BETIS sample, we used pyHIIextractor (Lugo-Aranda et al. 2022) in order to detect H II regions candidates. The code detects the H II regions candidates and assigns them a radius and a centroid, in the image coordinates. It is highly efficient for the detection of circular H II regions, especially those with low $\Sigma_{H\alpha}$, solving the aforementioned problem. Nevertheless, the limiting factor of this algorithms is in the complexity of the regions and in the variety of shapes and sizes of the brighter ones; hence, a circular extraction is not sufficient for those complex regions, since it would not be adapted to their morphology.

In the pursuit of the optimal methodology for segregating DIG emissions from H II regions, we conducted an extensive series of tests employing a variety of galaxies, techniques, and

---

[4] BETIS GitHub.

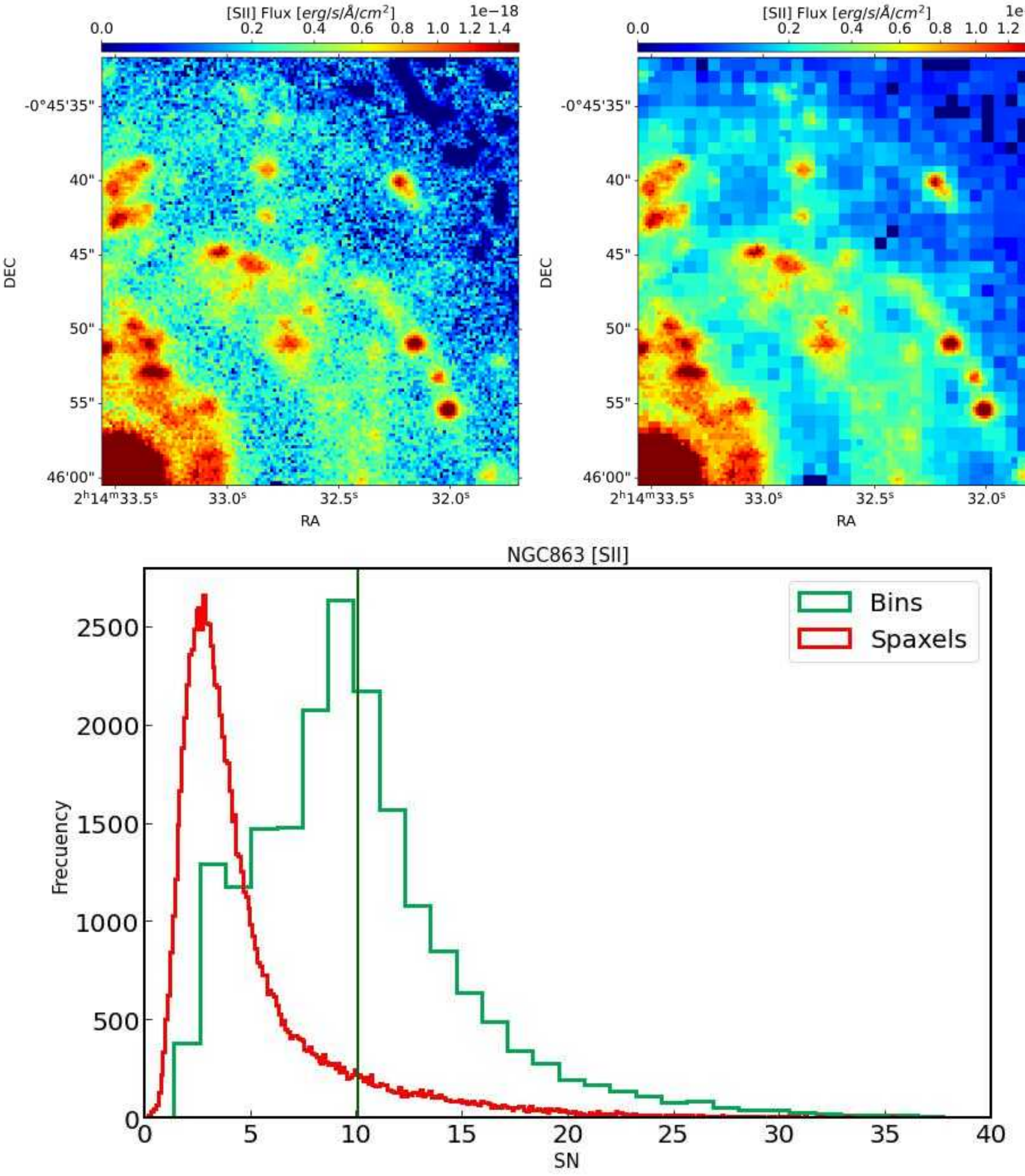

Figure 3.5: NGC863. Left panel: [S II] emission line map obtained following the methodology spaxel-by-spaxel. Central panel: Binned [S II] emission line map, from the binned cube, after performing an adaptive binning with target $S/N([S\,II]) = 10$ to the observed cube, as described. Both panels are close-up of the same region than Fig. 3.2. Right panel: Distributions of S/N of the [S II] line for NGC863, calculated with the equation 3.1. Red distribution corresponds to the $S/N([S\,II])$ measured in the observed cube, namely, the $S/N([S\,II])$ of the spaxels. Green distribution corresponds to the $S/N([S\,II])$ measured in the binned cube, namely, the $S/N([S\,II])$ of the bins. The vertical dark green line marks the mean value of the S/N([[S II]]) of the bins, showing that the adaptive binning technique fulfils the goal of reaching a target $S/N([S\,II]) = 10$, on average.

algorithms, considering the different observing conditions and depth of the BETIS sample. The main findings of this work have led to the conclusion that to establish a reliable morphological definition of the DIG, a combination of two methods is necessary: (i) the detection and masking of bona-fide H II regions exhibiting regular (circular) morphology based on the Hα emission line map; and (ii) the implementation of a cut-off in Hα surface brightness to account for irregular and highly luminous H II regions that may elude automated masking tools.

For the first step, we made use of the code pyHIIextractor for a first detection of the H II regions. The algorithm takes a Hα map and detects the positions and radii of all the candidates H II regions. We used those positions and radii to perform a mask of H II regions, applied to the binned Hα map.

For the second step, we performed a $\Sigma_{H\alpha}$ cut-off to the binned map. This cut-off is defined as three times the standard deviation of the surface brightness distribution of the masked map, as defined in the initial step ($3\sigma_{\Sigma(H\alpha)}$). This cut-off corresponds to three times the average Hα background level of the showcase sample. Performing this cut-off will result in a second DIG mask, that in combination with the first step DIG mask will give us the lower limit of DIG, as seen in Fig. 3.6, since we are assuming that all the emission coming from the H II positions is due to the star formation and the DIG contribution can be neglected.

It is also possible to estimate an upper limit for the DIG, rejecting the previous assumption and considering a constant DIG emission column above the projected areas of the H II regions (Zurita et al. 2000; Congiu et al. 2023). This limit is estimated in two steps. Firstly, for every H II region of centroid ('X','Y') and radius 'R' detected by pyHIIextractor, we define an annulus centred in that detection, with inner radius equal to the radius obtained and outer radius 1.4 times the inner radius. The H II regions are filled with the mean surface brightness measured inside the annulus. After performing this 'filling' with every H II region detection, part of the galaxy is still masked due to the $\Sigma_{H\alpha}$ cut-off. The DIG contribution in these remaining regions is estimated by filling them with the mean value of surface brightness of the border of the region. This result in a upper limit Hα DIG map, as seen in Fig. 3.6. The lower-limit DIG mask is then applied to the rest of the binned emission line and EW maps, which is the basis of this data.

3.4.2 Definition of the galactic plane in edge-on galaxies

For the eBETIS galaxies, the galactic plane is defined as follows. We construct an elliptical mask by conducting a 2D Gaussian fitting to the binned Hα image using the python routine scypy.opt.curve_fit [5], and centring the ellipse in the coordinates of the centre of the galaxy,

---

[5] scypy.opt.curve_fit documentation.

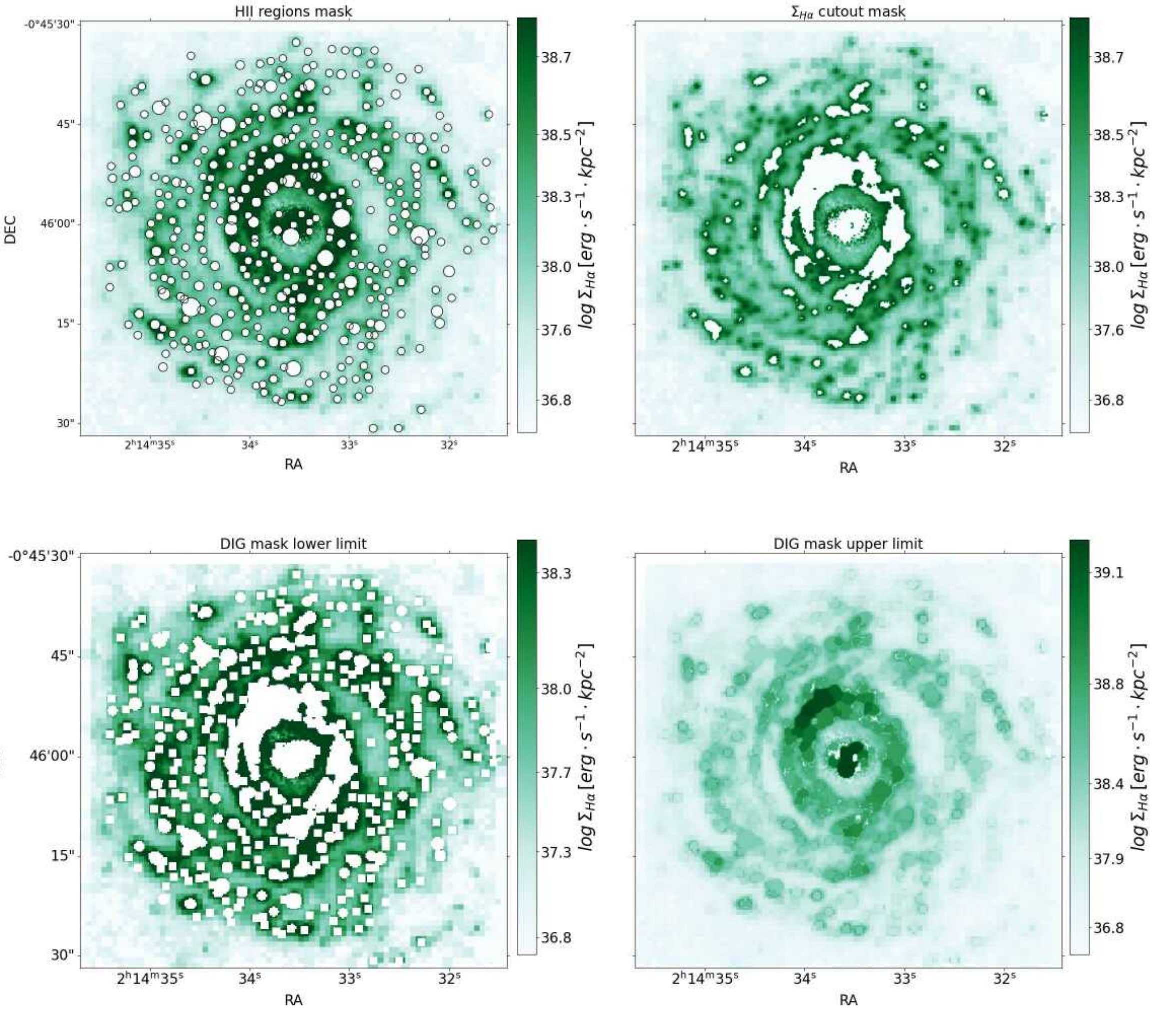

Figure 3.6: Steps to get the lower and upper DIG limit for NGC863 galaxy. The upper-left part corresponds to the DIG mask obtained by masking the H II candidates given by the centroids and radii obtained from pyHIIextractor to the binned Hα map. The upper-right part corresponds to the binned Hα map after applying a $3\sigma_{\Sigma(H\alpha)}$ cut-off. The lower-left part is the mask of the lower limit of the DIG, obtained as the combination of the upper-left and upper-right masks. The lower-right part corresponds to the upper limit, assuming a constant non-zero flux level above the H II regions, interpolating the flux around the these regions.

which also coincides with the centre of the rotation curve of the galaxy. The midplane is then set at z = 0, that corresponds to the centre of the minor axis of the ellipse fitted. The integrated Hα luminosity of the eDIG for all the galaxies is listed in 5.1. It was obtained integrating the Hα flux outside the ellipses previously described, obtaining an average value of $2.5 \cdot 10^{39}$ erg/s, that is consistent with values obtained by previous authors (Rand 2000; Miller & Veilleux 2003; Jo et al. 2018).

Figure 3.7 shows the binned Hα maps of the eBETIS sample. For aesthetic purposes and to highlight the contrast between the galactic plane and the complex structure of the extraplanar gas, the plane of the galaxies are shown in greyscale, and its definition is shown in the following chapters.

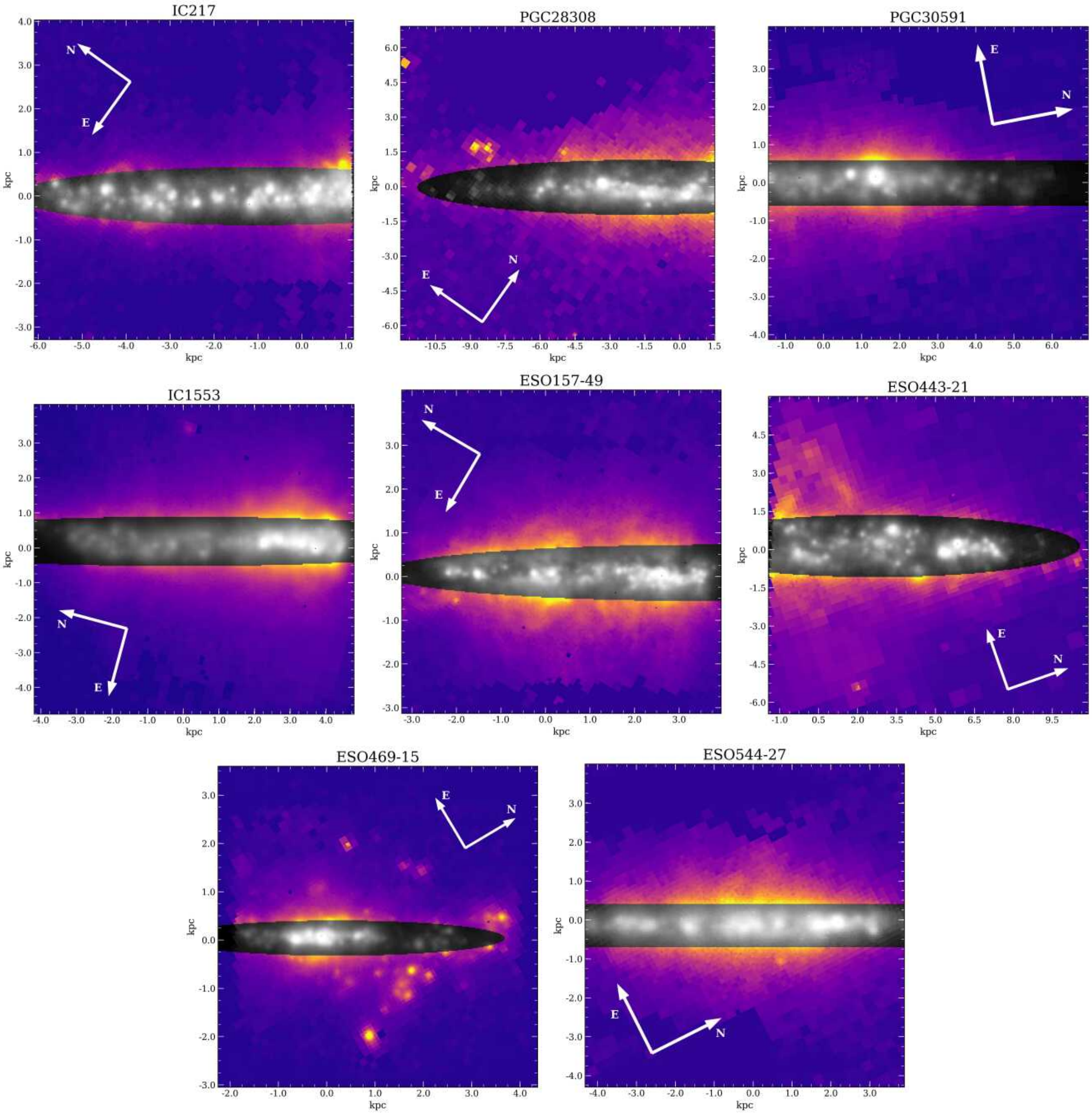
IC217 PGC28308 PGC30591 IC1553 ESO157-49 ESO443-21 ESO469-15 ESO544-27

Figure 3.7: eBETIS sample. The images correspond to the binned Hα emission line maps obtained in Sec. 2.3. Each image is rotated PA-90° with the white arrows indicating the direction of the celestial north and east in the original image. The ellipse fitting of galactic plane (see Sec. 2.3) is coloured in grey scale. The contrast between the galactic plane and the extraplanar gas reveals the complexity of the ionised extraplanar gas, which comprises diffuse gas, filaments, and various structures.

In the data, for the subsequent analyses, we only include bins with S/N of the observed emission line greater than 2 and relative error lower than 40% for all the lines of interest. The resulting binned maps exhibit an average physical bin size (listed in table 2.3) that remains below, or very similar to, the FWHM of the data, determined as the physical size of the seeing reported in the datacube header.

Chapter 4

Analysis and characterisation of the DIG in face-on galaxies

After performing the BETIS-binning methodology outlined in chapter 3, the average bin size of the sample is 627 pc (see Table 4.1 for a overview of the increment of the S/Ns after binning). The average bin size in the sample is larger than the typical bin sizes in studies of narrowband Hα images (e.g. $\sim$ 250 pc, Ferguson et al. 1996a; $\sim$ 35 pc (native), Zurita et al. 2000; $\sim$ 475 pc, Oey et al. 2007). Moreover, the bin dimensions exceed those of the mean Voronoi bins of the PHANGS-MUSE sample ($\sim$ 200 pc; Bel22). Nonetheless, they are smaller than the average PSF FWHM of the CALIFA galaxies ($\sim$ 800 pc; Lac18). The DIG masks obtained after performing the methodology described in chapter 3 and applied for the showcase sample are shown in figure 4.1.

To ensure the robustness of the analysis, we exclusively considered DIG bins with a relative error of 40% or lower and a S/N greater than 3 for all the lines involved in the subsequent analyses of this section. The central part of those exhibiting an AGN is also excluded: NGC863, NGC692 and NGC3393. Those constraints the data to a 80% of the DIG bins.

4.1 The DIG fraction

The visual inspection and variation of the DIG, both within individual galaxies and across them, provide valuable insights into its origins. In the binned Hα maps of the showcase sample galaxies, a diverse range of structures within the ionised gas regions becomes evident. The variations in Hα emissions in different directions yield crucial information about the evenness on the intensity of the DIG distribution and its spatial association with prominent H II regions. Likewise, investigating changes in the diffuse fraction and

Table 4.1: First column is the percentage of spaxels and bins of the sample whose S/N(Hα) is higher than 3. The rest of the columns represent the percentage of the spaxels and bins with the S/N of Hα and where the S/N of the corresponding line higher than 3.

Line	Hα	Hβ	[N II]	[S II]	[O I]	[O III]
% S/N (spax)	65	27	50	41	11	51
% S/N (bin)	96	90	93	91	63	82

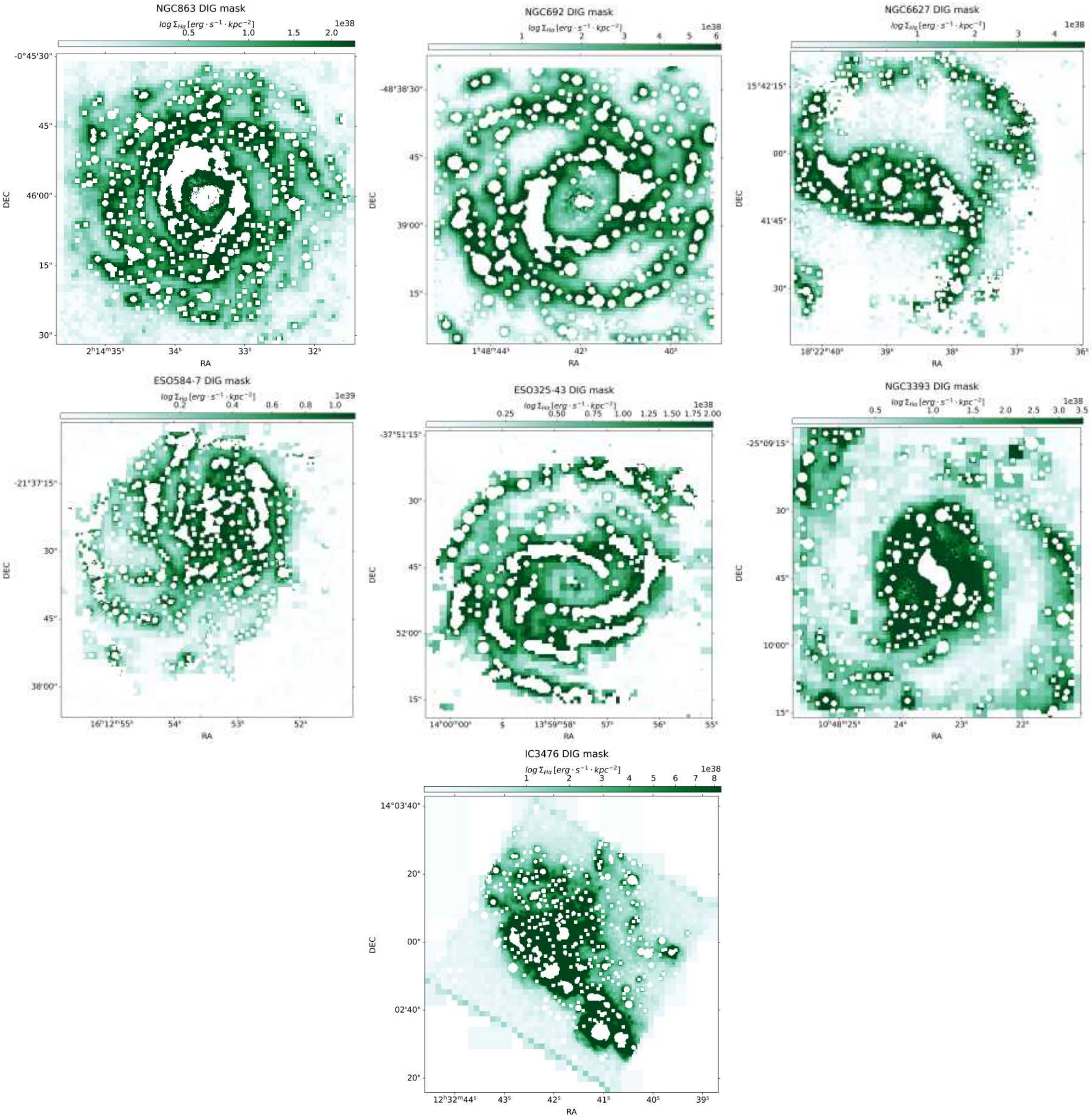

Figure 4.1: Showcase sample binned Hα maps after applying the DIG mask obtained performing the methodology described in chapter 3.

Hα surface distribution within a particular galaxy is of significant interest as it aids in pinpointing the source of the DIG.

Figure 4.2 shows the distribution of the DIG fraction, defined as the ratio of the DIG flux to the total Hα flux, f(Hα)$_{DIG}$/f(Hα)$_{total}$, for each galaxy of the sample, in both the radial and cumulative distributions. The radial distribution is obtained by measuring the DIG fraction from a series of de-projected rings centred at the nucleus of each galaxy with a width of 0.05R$_{25}$, while the cumulative distribution is obtained by performing aperture photometry of the DIG fraction in the same series of de-projected rings that are used for deriving the radial profiles, for both the lower and upper DIG limits. Moreover, using the definition of radial distribution, Fig. 4.3 shows the Hα surface-brightness distributions for the lower DIG limit (green) after applying the mask (defined in Sect. 3.4) for the galaxy with only H II regions (red) and the total galaxy (blue). All the fluxes from this section and hereafter have been corrected for interstellar extinction assuming the Cardelli extinction law, assuming R$_V$ = 3.1 (Cardelli et al. 1989) and a Balmer decrement Hα /Hβ = 2.85.

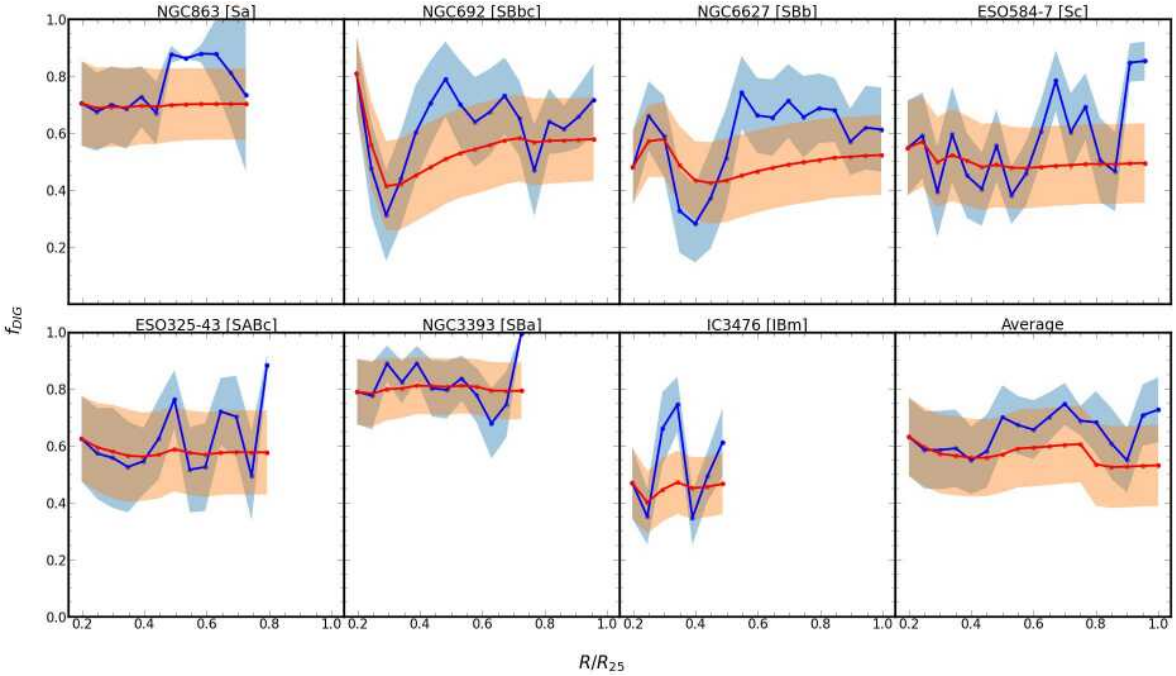

Figure 4.2: Distribution of the DIG fraction (f(Hα)$_{DIG}$/f(Hα)$_{total}$) for each galaxy of the sample. Red area represents the cumulative distribution between the the upper and lower DIG limits, with a step of 0.05R$_{25}$, being the solid red lined the mean value. Blue area is the radial distribution of the DIG obtained integrating the flux between rings of width 0.05R_{25} and with a step of 0.05R$_{25}$, being the solid blue lined the mean value. R$_{25}$ is the isophote at the blue brightness of 25 mag/arcsec^2. This parameter is obtained from Hyperleda database.

Overall, the radial distribution of the DIG fraction tends to increase, while the cumulative distributions remain constant, but it is more affected by the galaxy morphology than the cumulative distribution. The presence of a barred structure in NGC692, NGC6627, and ESO325-43 is evident through a decline in both distributions between 0.2-0.4 R$_{25}$, which decreases up to 20%. This effect is also reflected on the radial distributions of the Hα surface brightness (Fig. 4.3), which show an increment of the $\Sigma_{H\alpha}$ for the H II regions distribution, reaching up to 10^{39} erg· s^{-1}· kpc^{-2} between 0.2-0.4 R_{25} for those galaxies. NGC3393 exhibits the highest DIG fraction for both lower and upper limits (0.69-0.87), presenting a surface brightness that surpasses the H II regions, throughout the entire galaxy, resulting in a maximum difference of around 1 dex. Furthermore, NGC863 also exhibits higher $\Sigma_{H\alpha}$ in the DIG than in the H II regions, notably towards greater galactocentric radii.

The Sc galaxy ESO584-7 and the dwarf IBm galaxy IC3476 present the lower DIG fraction, 0.37-0.66 and 0.4-0.63, respectively. Additionally, they have the highest surface brightness for the H II regions in the sample, being $>10^{39}$ erg· s^{-1}· kpc^{-2} in the inner parts of the galaxy and decreasing to $\sim 5 \cdot 10^{38}$ at $0.5R_{25}$. The average radial distribution of the DIG fraction is not showing any tendency in particular, remaining constant probably due to the mixture of morphologies of the showcase sample. A full analysis considering a general distribution by morphological type will be carried out as part of BETIS in a forthcoming papers.

Table 4.2 summarises the results obtained from the DIG fraction for the showcase sample. The general findings for this showcase sample show that the DIG fraction ranges from 0.4 to 0.7, which coincides with the results of previous research, in terms of both the lower limit (e.g. Ferguson et al. 1996a,b; Zurita et al. 2000; Thilker et al. 2002; Oey et al. 2007; Bel22), and upper limit (e.g. Zurita et al. 2000; Congiu et al. 2023). In addition, the average $\Sigma_{H\alpha}$ cut-out in also consistent with the average upper DIG level of previous studies (Poetrodjojo et al. 2019, Bel22, Congiu et al. 2023). In addition, the tendency of the cumulative distribution is to be constant and indicating approximately a 60% of DIG in these galaxies. The surface brightness of the DIG vary from $\sim 6 \cdot 10^{38}$ in the inner parts of the galaxies and decreasing monotonically to $\sim 5{\cdot}10^{37}$ erg· s^{-1}· kpc^{-2} in the outer regions, with a notably high integrated Hα luminosity between 10^{40} and $5 \cdot 10^{41}$ erg/s. This is consistent with previous studies (e.g. Ferguson et al. 1996a,b; Zurita et al. 2000).

The similarity in the $\Sigma_{H\alpha}$ radial distributions between the H II and DIG regimes and its impact in the DIG fraction supports the correlation between H II regions emission and DIG photoionisation (Ferguson et al. 1996a,b; Zurita et al. 2000). However, performing this exploration individually shows that there are instances where DIG $\Sigma_{H\alpha}$ values exceed those of the H II regions, in particular, in the two Seyfert galaxies, NGC863 and NGC3393. For instance, for NGC863, a total DIG $\Sigma_{H\alpha}$ of $6.6 \cdot 10^{38}$ erg·s^{-1}· kpc^{-2} will require a power per unit area of $1.5{\cdot}10^{-3}$erg·s^{-1}·cm^{-2} to keep the DIG ionised, while the total $\Sigma_{H\alpha}$ of the H II regions of $5.02{\cdot}10^{38}$erg·s^{-1}·kpc^{-2} provides a power of $1.1{\cdot}10^{-3}$erg·s^{-1}·cm^{-2}, which is insufficient to ionise the entire DIG[1].

Hence, it is imperative to contemplate alternative ionisation sources that can provide ad-

---

[1] We are assuming that the average number of photons per recombination is 0.46 for this estimation.

Table 4.2: Total DIG fraction for each galaxy. Here, '$f_{DIG,low}$' and '$f_{DIG,up}$' are the upper and lower limit of the DIG. $3\sigma_{\Sigma(H\alpha)}$ is the $\Sigma_{H\alpha}$ cut-off performed for each galaxy in units of log $erg \cdot s^{-1} \cdot kpc^{-2}$. 'Bin size (pc)' is the average bin size of the galaxy. The last row indicates the average values of the sample.

Galaxy	**Type**	$f_{DIG,low}$	$f_{DIG,up}$	$3\sigma_{\Sigma H\alpha}$	**Bin size (pc)**
NGC863	SA(s)a	0.45	0.75	38.8	743
NGC692	SBbc	0.44	0.73	39.1	578
NGC6627	SBb	0.39	0.67	39.3	490
ESO584-7	Sc	0.37	0.66	39.4	920
ESO325-43	SABc	0.44	0.75	38.5	1129
NGC3393	SBa	0.69	0.87	40.0	427
IC3476	IBm	0.40	0.63	39.8	101
Sample	-	0.40	0.70	39.3	627

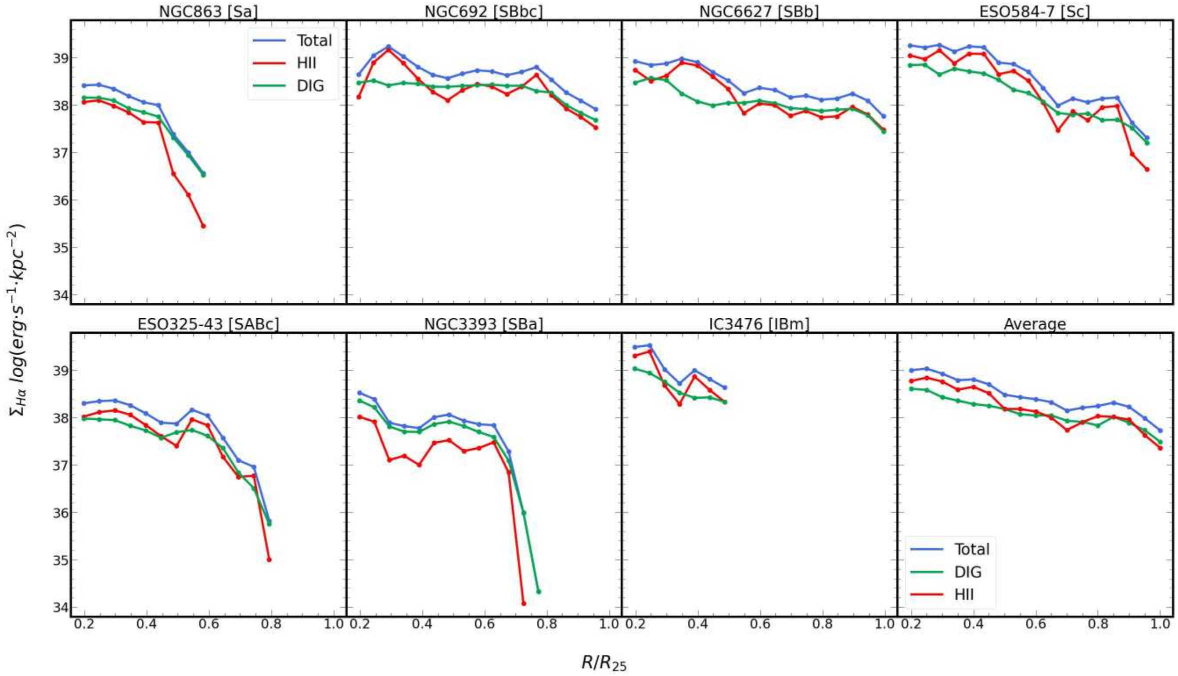

Figure 4.3: Radial distribution of $\Sigma_{H\alpha}$ for each galaxy, obtained by measuring the surface brightness of a series of de-projected annulus centred at the nucleus of each galaxy with a width of $0.05R_{25}$. The distributions are performed for the entire galaxy (blue), the lower DIG limit (green) and HII regions (red). The last panel represent the mean distributions for the sample.

ditional energy supply to the ISM apart from Lyman continuum photons escaping from H II regions to keep the DIG ionised for those particular cases. The incorporation of collisional, low-excitation lines such as [N II] , [S II] , or [O I] , as well as high-excitation lines such as [O III] and He I in the analysis is essential for comprehensively investigating the diverse array of ionisation mechanisms that exist within the ISM.

4.2 BPT diagnosis of the DIG

We can explore the location of the DIG bins in the classical [N II] BPT diagram, as shown in Fig. 4.4. The same figure includes a diagnostic from Kopsacheili et al. (2020) for the separation of shock excited from photoionised regions. The BPT of the global sample shows the DIG falls mostly below the Kewley et al. 2001 demarcation, showing a photoionisation feature due to H II regions, but with high-excitation regions above the demarcation corresponding to AGN-like emission, as noted in previous studies and usually explained as photoionisation due to HOLMES (Lac18; Bel22). However, when performing this diagnosis for individual galaxies, only NGC863 and NGC3393, both Seyfert-2 AGNs, exhibit line ratios characteristic of AGN emission. All the DIG for the rest of the galaxies show photoionisation feature due to H II regions. The central region of NGC863 and NGC3393 is not considered in this analysis, so the AGN outflows could be the source of the gas ionisation with high-excitation lines found in the BPTs. We compare the results with the theoretical models of gas that is highly excited via fast-shocks of Allen et al. (2008), assuming solar metallicity and a pre-shock density of 1 cm^{-3}. The figure shows the predicted line ratios including (red lines) or not (blue lines) a photoionisation by precursor, and given a range of shock velocities (v_s) and magnetic field intensities (B). The line ratios observed in NGC863 are consisted with fast-shock without precursor with v_s between 200 and 500 km/s and B between 0.0001 and 5. In the case of NGC3393, the ratios observed corresponds to fast-shock without a precursor, with v_s between 200 and 1000 km/s and B between 0.0001 and 10 $\mu\mathrm{G}{\cdot}\mathrm{cm}^{3/2}$. Furthermore, the fact that the ionisation bi-cone of NGC3393 and its continuum emission are uncoupled (Maksym et al. 2016), along with the emission line ratios in the BPT diagram indicative of ionisation by fast shocks, suggests that we are tracing gas outflows rather than DIG emission (López-Cobá et al. 2020).

The presence of AGN outflows affects the overall BPT diagnosis, revealing that a section of the DIG is ionised by sources separate from the photon leakage originating from H II regions, but what we are introducing is the ionisation cone of the AGNs, mimicking the DIG emission. Therefore, when conducting a comprehensive diagnostic assessment of the DIG across a global sample, it is crucial to completely exclude galaxies that exhibit AGN emission. This occurs even if the whole DIG is ionised by star-forming regions, as observed in the remaining galaxies in the sample. This effect also explains the high $\Sigma_{H\alpha}$ in the DIG found in the same two galaxies; NGC863 and NGC3393, as the AGN emissions are incorporated in the diagnosis.

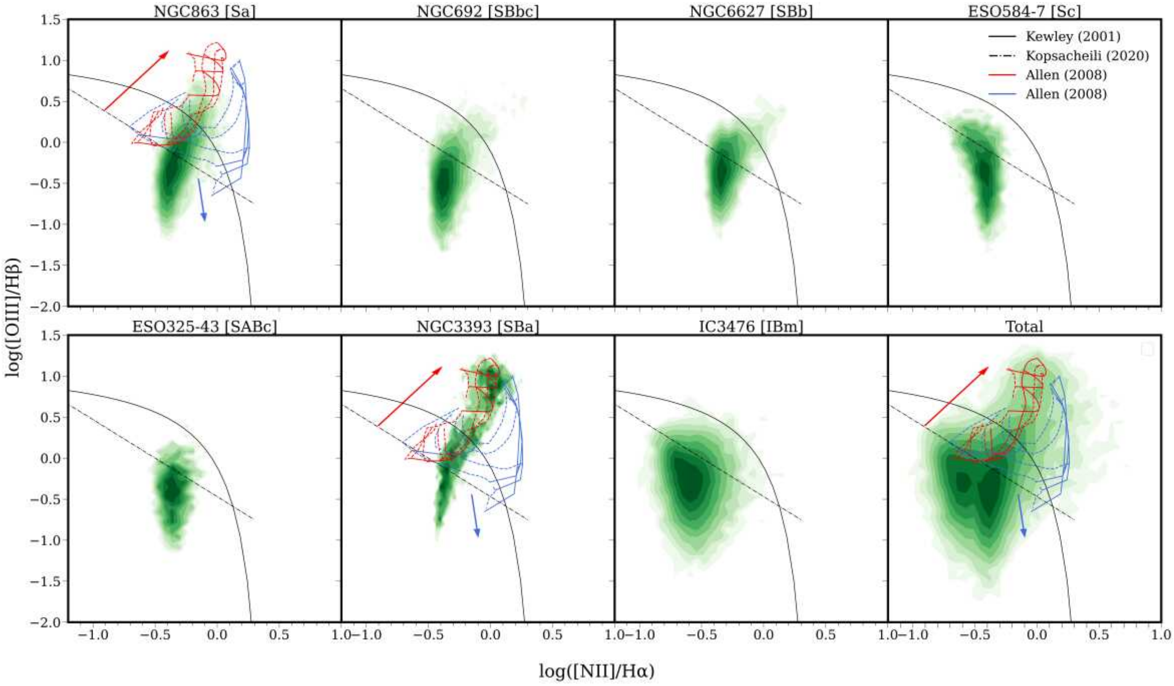

Figure 4.4: BPT Diagnosis of the sample for the DIG bins that verifies that the relative errors of [O III] line bins are below 40% and its S/N above 3. The last panel displays the seven prior panels together. The central parts of NGC863, NGC3393, and NGC692 were excluded in all panels due to their strong AGN emissions. Each contour encloses the 10% of the points, with every point a single bin. Black solid lines are given by Kewley et al. (2001) for the classic H II regions photoionisation and AGN demarcations. The dashed-dot line depicts one of the 2D diagnostics developed by Kopsacheili et al. (2020) for the separation of shock excited (e.g. supernova remnants) from photoionised regions (e.g. H II regions). Coloured lines represent the models of photoionisation by fast shocks from Allen et al. (2008). The blue and red models illustrate photoionisation where only front shocks occur and when pre-ionisation by a precursor is taken into account. The solid model curves plotted represents shocks winds of 200, 400, 500 and 1000 km/s, and dashed model curves represents magnetic field intensities of 0.0001, 1.0, 5.0 and 10 μG·cm$^{3/2}$. Red and blue arrows represent the direction of increasing wind velocity in each model.

4.3 DIG line ratios

Further evidence of the connection between the DIG and H II regions lies in the behaviour of the [S II] /Hα , [N II] /Hα , [O I] /Hα , and [O III] /Hβ ratios. Historically, studying the radial dependence of the DIG has been important, as its trend along different galactocentric distances can constrain its origin (Ferguson et al. 1996a). Furthermore, recent investigations have highlighted the importance of considering possible contamination and/or contribution of the DIG to physical parameters derived from emission lines, such as metallicity and star-formation (Bel22, Lugo-Aranda et al. 2024). Therefore, aperture (or, correspondingly, redshift) biases should be taken into account, for which the study of the DIG in a radial basis is a key element. An observational fact is that the low-ionisation [N II] /Hα and [S II] /Hα line ratios increase with decreasing $\Sigma_{H\alpha}$, the best example being the increase in these line ratios with increasing distance from the mid-plane, both in the Milky Way (Haffner et al. 1999) and other galaxies (Rand 1999; Tüllmann et al. 2000). Although the values for [N II] /Hα and [S II] /Hα could vary considerably in the DIG, they are correlated, often with a nearly constant [S II] /[N II] ratio over large regions (Haffner et al. 2009b).

Figure 4.5, shows the average radial distribution of the [S II] /Hα , [N II] /Hα , [O III] /Hβ , and [O I] /Hα line ratios for the lower DIG limit. The distributions have been generated using the same method as for $\Sigma_{H\alpha}$ (as shown in Fig. 4.3) and f$_{DIG}$ (blue curves of the Fig. 4.2) radial distributions. Each data point is computed as the average value from the seven galaxies in the sample at a specific radius. The distributions are constructed for both the DIG (in green) and the area corresponding to H II regions (red). In all instances, we exclusively consider the bins with a relative error below 40% for each line. In all cases, the DIG line ratios show higher values than the line ratios corresponding to the H II regions.

The [N II] /Hα radial distributions (upper-left panel), for both the DIG and the H II regions, decrease with galactocentric distance. The [N II] /Hα DIG distribution ranges from 0.67 to 0.51, while for the H II regions from 0.44 to 0.37 between 0.2R$_{25}$ and 1R$_{25}$, being the [N II] /Hα line ratio of the DIG 0.15 dex higher in average. The [N II] /Hα line ratio is a well-know metallicity indicator (Storchi-Bergmann et al. 1994; Denicoló et al. 2002; Ho et al. 2015); thus, the decreasing value as a function of radius is primarily reflecting a change in metallicity of the ionised gas, in this case of the metallicity gradient of the spiral galaxies. Nevertheless, given that N^{+}/N and H^{+}/H vary little within the DIG, for a given metallicity, variations in the [N II] /Hα line ratio essentially trace variations in T_e (Haffner et al. 2009b). However, calculating absolute temperatures is uncertain because of the requisite assumptions about the precise ionic fractions and elemental abundances.

Figure 4.5 suggest a flattening in the [N II] /Hα index in both the H II regions and the DIG distributions for $r < 0.6R_{25}$, indicating a potential contribution from the DIG to the observed

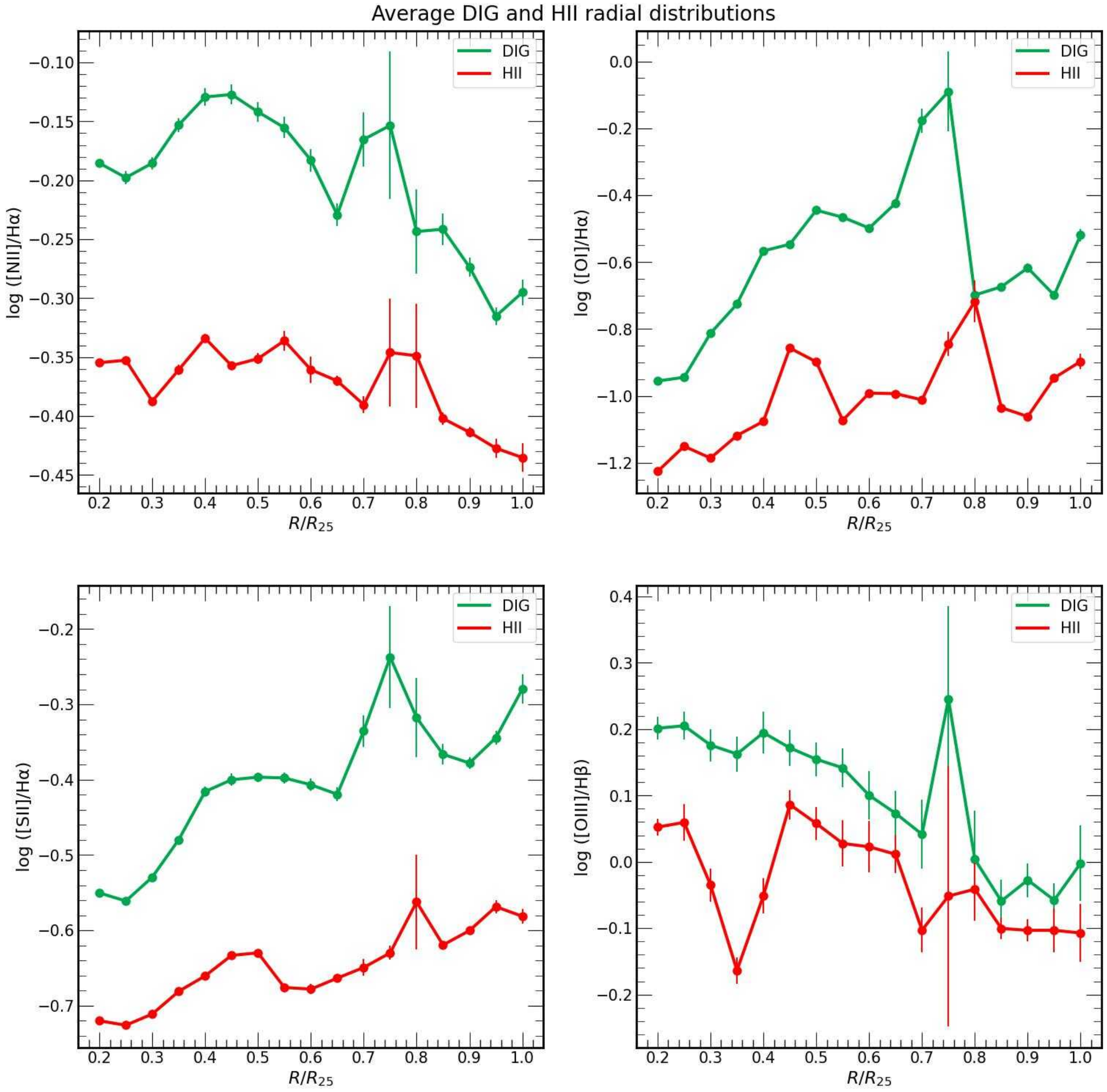

Figure 4.5: Radial distribution of the [S II] /Hα ratio of the DIG bins (green), and H II regions according to the definition (red), obtained as the ratio of the mean values of the respective fluxes within a ring of width $0.05R_{25}$ with a step of $0.05R_{25}$ from $0.2R_{25}$ to R_{25}, only considering those bins whose relative error in [S II] and Hα lines are lower than 40%. To avoid the strong AGN emissions, all the distributions start from $0.2R_{25}$. In general is evident a tendency to increase the ratio as we move to outer regions of the galaxy. Besides, the ratio is in all cases higher in DIG regions, as expected from the literature (Haffner et al. 2009b).

radial metallicity gradients within galactic planes (Z17).

On the other hand, the [S II] /Hα line ratio increases radially in both H II regions and DIG regimes (lower-left panel of Fig. 4.5), with higher values observed in the DIG; from 0.28 to 0.63 for the DIG and from 0.19 to 0.12 for the H II regions between $0.2R_{25}$ and $1R_{25}$, with the [S II] /Hα DIG line ratio higher by 0.15 dex, on average. The shapes of both distributions display comparable patterns, reaching a maximum at $0.75{-}0.8R_{25}$.

The [O I] line is produced by collisions of neutral oxygen with thermal electrons, while its intensity is a measure of the neutral hydrogen content within the DIG. The first ionisation potential of the oxygen is close to that of the hydrogen, and the large H^++O^0 ↔ H^0+O^+ charge-exchange cross-section keeps O^+/O nearly equal to H^+/H. Thus, the [O I] /Hα ratio is related to the amount of H^0 relative to H^+, and it is a sensitive probe of the ionisation state of the emitting gas (Reynolds et al. 1998; Haffner et al. 2009b). The volume photon emissivity e of the O^1D λ6300 transition relative to Hα is related to the hydrogen ionisation ratio $n(H^+)/n(H^0)$, with a linear dependence of the gas-phase abundance of oxygen $n(O)/n(H)$ and a weak dependence that tracks changes in T_e (Haffner et al. 2009b). Observations of [O I] in the Milky Way and objects at $z \sim 0$ are difficult because of the [O I] λ6300 air glow line, which is of order 100 times brighter than the interstellar line. Voges & Walterbos (2006) made the first DIG detection of [O I] λ6300 in any non-edge-on spiral other than the Milky Way near the H II region NGC 604 in M33, with observed [O I] /Hα ratios in the range 0.038 − 0.097. The upper-right panel of Fig. 4.5, shows the azimuthally averaged values of the [O I] /Hα ratio with a significantly steeper slope in the DIG compared to the emission in the H II regions, increasing from 0.12 to 0.79 between 0.25R_{25} to 0.75R_{25} (-0.9 to -0.1 in log), while the H II distribution increases from 0.06 to 0.18 (-1.2 to -0.7 in log), which are higher than the values reported by Voges & Walterbos (2006) for M33, and higher than the values found by Bel22 with an upper limit ∼ 0.3. The high [O I] /Hα line ratio in the DIG found in the BETIS showcase sample is challenging, and will be matter of study in forthcoming studies.

The radial distribution of the [O III] /Hβ line ratio is shown in the lower-right panel of Fig. 4.5. Generally, the variation in this ratio between DIG and H II regions depends on the specific physical characteristics of the ISM (Z17). Normal spiral galaxies show an increasing value of the [O III] /Hβ line ratio with increasing radius, mainly due to secondary dependence on metallicity, with a high dispersion in the central regions (~ 1 dex for $r < 0.4R_{25}$). Previous studies also show a [O III] /Hβ ratio both higher in H II regions (Greenawalt et al. 1997; Galarza et al. 1999) and lower than the DIG regions (Collins & Rand 2001; Otte et al. 2002). In the sample, this ratio remains elevated in DIG regions, but the difference between the DIG and H II distributions is less pronounced compared to the other line ratio distributions. This trend suggests a radial decrease in this ratio; from 1.58 to 1.0 in the DIG (0.2 to 0.0 in log) and from 1.07 to 0.79 in the H II regions (0.05 to -0.1 in log). This results indicate that these line ratios are typically higher in the DIG compared with the H II regions. This trend aligns with what is commonly reported in the existing literature (Haffner et al. 2009b).

The similarity in the trends observed in the radial distribution of $\Sigma_{H\alpha}$ and line ratios between both DIG and H II regions, especially in the case of [N II] /Hα and [S II] /Hα ratios, along with the majority of DIG bins falling within the photoionisation regime on the BPT diagram, suggests that the explanation for DIG behaviour can be attributed to photoionisation processes within the galactic plane, without the need for alternative sources of ionisation.

However, another phenomenon needs to be explained, the low values of EW$_{H\alpha}$ found in the DIG, specially in regions with photoionisation regimes not corresponding to SF regions (Lac18; Bel22).

4.4 EW$_{H\alpha}$ in the DIG

The EW$_{H\alpha}$ has been used by many authors to differentiate between ionisation caused by star formation and AGNs and ionisation caused by a smooth background of hot evolved stars. Cid Fernandes et al. (2011) used SDSS data to demonstrate that the emission-line galaxy population exhibits a bimodal distribution in EW$_{H\alpha}$, and that 3Å serves as an empirical demarcation between these two. Later, Belfiore et al. (2016) using MaNGA data, showed the presence of extended (kpc scale) low-ionisation emission-line regions (LIERs) in both star-forming and quiescent galaxies, associated with low EW$_{H\alpha}$ (< 3Å). In SF galaxies, the LIER emission was associated with diffuse ionised gas, most evident as extraplanar emission in edge-on systems.

Lac18 proposed a separation of DIG ionisation regimes based on the EW$_{H\alpha}$ and applied over all types of galaxies, including elliptical and S0. The regions where EW$_{H\alpha} >$ 14 Å traces SF regime, 3 $<$ EW$_{H\alpha} <$ 14 Å reflects a mixed regime, and regions where EW$_{H\alpha} <$ 3 Å define the component of the DIG where photoionisation is dominated by hot, low-mass, evolved stars (HOLMES; Flores-Fajardo et al. 2011; Cid Fernandes et al. 2011). Those stars were proposed as an additional ionisation source of the DIG, in order to explain the high [O III] /Hβ ratio found in the extraplanar DIG in edge-on galaxies (Reynolds et al. 1998; Rand 1999; Flores-Fajardo et al. 2011).

The significance of employing the EW$_{H\alpha}$to distinguish between various ionisation sources, while considering the contribution of HOLMES to the energy budget, has been a topic of frequent discussion among several authors, even in the context of face-on galaxies (e.g. Cid Fernandes et al. 2011; Lac18; Bel22); however it is not yet clear whether it reveals a true division (if any) between ionisation carried by HOLMES, star formation, or shocks. Moreover, Bel22 also noticed an unclear division for ionisation by HOLMES at EW$_{H\alpha}$= 3 Å and by star formation at EW$_{H\alpha}$= 14 Å suggested by Lac18, since their EW$_{H\alpha}$ for DIG and H II regions tends to overlap in lower EW$_{H\alpha}$ regimes.

4.4.1 The effect of the stellar populations on $EW_{H\alpha}$

The general methodology employed in IFS studies in order to measure both the line intensities and the EW of Balmer recombination lines poses a problem for spectra with low S/N values for the emission lines. This methodology calls for measuring the line intensities and EWs from a nebular spectrum obtained by subtracting a fitted stellar model to the observed spectrum. In the case of the Balmer recombination lines, this procedure typically makes a small correction to the emission line intensity due to the underlying stellar absorption. For $\mathrm{EW}_{H\alpha} > 3$Å, this correction is usually of a few percent. Nevertheless, when the S/N of the Hα line is ~ 1 (Hα emission embedded in the stellar continuum), the resulting Hα emission, and therefore $\mathrm{EW}_{H\alpha}$, would depend on the Balmer stellar absorption feature due to the SSP fitting. In this case, the underlying stellar absorption would not represent just a correction of the emission line, but the resulting flux would be fully originated from the fitted stellar spectrum, generating low $\mathrm{EW}_{H\alpha}$values $\lesssim 3$ Å.

This is shown in Fig. 4.6, where is plot the observed (green), fitted stellar model (black) and nebular (blue) spectra of regions with $\mathrm{EW}_{H\alpha}$ of 0.6, 1, and 3 Å. In the left and central panels, the Hα emission in the observed spectra is totally embedded by the stellar continuum. However, due to the fitted stellar model, the nebular spectra includes a Hα emission line of the same magnitude as the stellar absorption feature of the model, from which an $\mathrm{EW}_{H\alpha}$of 0.6 Å (left) and $\mathrm{EW}_{H\alpha}= 1$ Å (right) are measured. On the other hand, the right panel of Fig. 4.6 shows that for a region with $\mathrm{EW}_{H\alpha}= 3$ Å, the underlying stellar absorption of the model makes just a small correction to the total flux of the emission line.

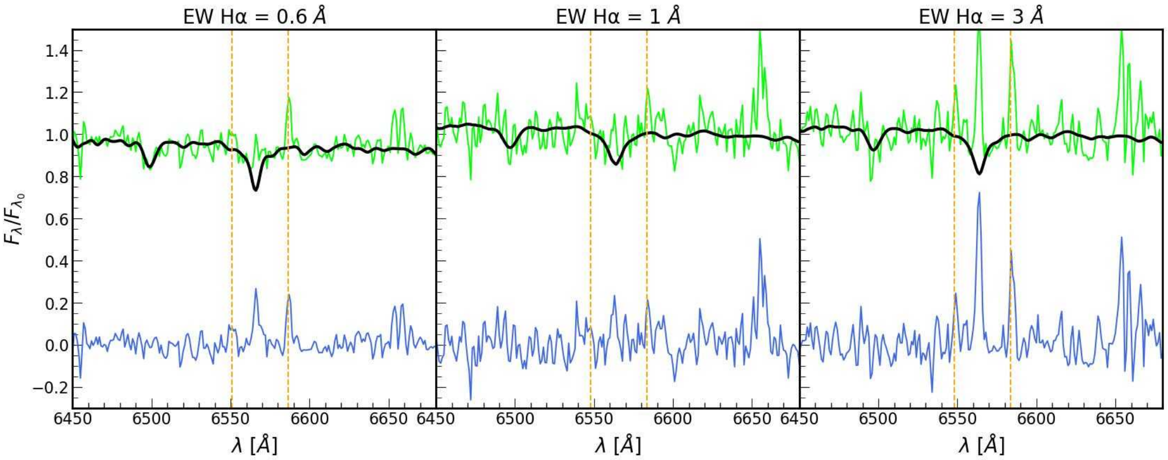

Figure 4.6: Three examples of observed (green), model (black) and nebular (blue) spectra of different $\mathrm{EW}_{H\alpha}$= 0.6, 1 and 3 Å. All observed spectra are integrated spectra from NGC863 bins, the model spectra are obtained from STARLIGHT following the methodology and the nebular spectra are obtained subtracting the model to the observed (see text). Gold lines represent the [N II] doublet.

This sharp differentiation between HOLMES dominated regions, as well as the differentiation between LIERs and passive galaxies (Cid Fernandes et al. 2011; Belfiore et al. 2016) may not be reliable, as it could potentially originate from a methodological artefact. To demonstrate this effect, we compute the EW$_{H\alpha}$for an integrated region of NGC863 with EW$_{H\alpha}$≈ 1Å using 12 different methods. Firstly, selecting both BC03 and CB07 base spectra. For each of these bases, the SSP synthesis is perform by combining the observed spectrum of the region with three different photometric constraints: near-ultraviolet (NUV, λ_{eff} = 2310 Å) and far-ultraviolet (FUV, λ_{eff} = 1528 Å) from All-Sky Survey of the Galaxy Evolution Explorer (AIS-GALEX; Bianchi et al. 2017) and u-SDSS (λ_{eff} = 3543 Å) from Sloan Digital Sky Survey (SDSS) DR16 (Ahumada et al. 2020). This is accomplished using an alternative version of STARLIGHT, PHOTOMETRICSTARLIGHT (López Fernández et al. 2016; Werle et al. 2019), which combines the spectroscopic and photometric data to perform SSP synthesis, utilising photometric points to extrapolate the model spectra to bluer wavelengths.

The main challenge of combining spectral and photometric constraints in an SSP synthesis using PHOTOMETRICSTARLIGHT is the differing spatial scales and resolutions of the MUSE, SDSS, and GALEX data. GALEX images pose the greatest limitation, with $FWHM(FUV) \sim 4.2''$ and $FWHM(NUV) \sim 5.3''$, and a spatial sampling of 1.5”. Degrading the MUSE datacube and the SDSS images is not an option if we aim to calculate the photometric point corresponding to a region of the galaxy smaller than the GALEX pixel scale. This can be addressed by utilising the MONTAGE[2] software, which includes a routine called ’Drizzle’. This Variable-Pixel Linear Reconstruction algorithm (Fruchter & Hook 2002) resamples the GALEX and SDSS images to match the spatial scale of MUSE at 0.2”/px. This process accounts for shift, rotation, and geometric distortion, preserving the photometry and resolution. The images are aligned and cropped using the world coordinates system (WCS) to match the FoV of the MUSE datacubes, which is 1’. This method, which enables simultaneous spectroscopic and photometric analysis using MONTAGE software, is based on the work of (López Fernández et al. 2016), who also combined GALEX and SDSS images with CALIFA datacubes. Once all images are resampled to the same scale, the integrated NUV, FUV, and u-SDSS fluxes can be obtained for the same regions considered in the MUSE datacube.

The GALEX and u-SDSS images were obtained directly from the MAST[3] and SDSS DR16[4] charts. Once the fluxes of the same region in each image are obtained, PHOTOMETRICSTARLIGHT takes these fluxes as new inputs and extrapolates the fitting to ensure the synthetic spectrum passes through the selected photometric points (none, one, or more), as depicted in figure 4.7.

---

[2] http://montage.ipac.caltech.edu/
[3] GALEX finding tool
[4] SDSS finding tool

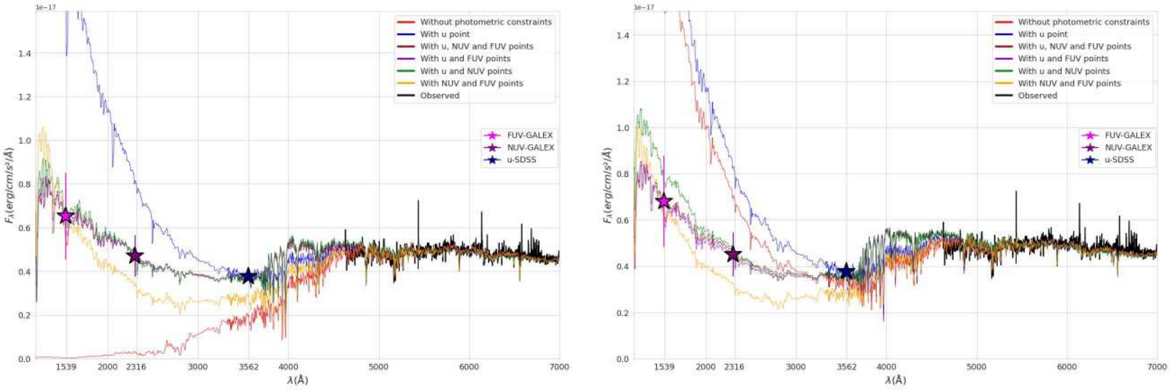

(a) Observed and synthetic spectra obtained using the BC03 base.

(b) Observed and synthetic spectra obtained using the CB07 base.

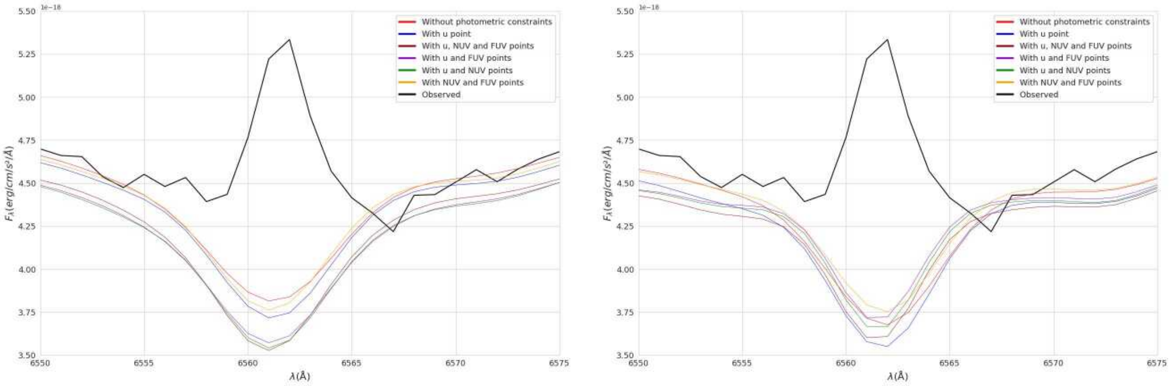

(c) Close-up to the Hα line of the observed and synthetic spectra obtained using the BC03 base.

(d) Close-up to the Hα line of the observed and synthetic spectra obtained using the CB07 base.

Figure 4.7: Synthetic spectra obtained from the SSP synthesis with Photometric-STARLIGHT. The black spectrum is the integrated spectrum obtained from a region of NGC863 of EW$_{H\alpha}\approx$1Å used as the observed spectrum for this test. The magenta, purple and blue stars are the fluxes of the same region for FUV-GALEX, NUV-GALEX and u-SDSS bands used as photometric points for the fitting. Every spectra correspond to the fitting using different photometric constrains.

Figure 4.7 illustrates the variations in the synthetic spectra obtained through six different fitting methods: without photometric constraints, with the addition of the u-SDSS point, with NUV and u-SDSS points, with FUV and u-SDSS points, with FUV and NUV points, and with FUV, NUV, and u-SDSS points. Additionally, the fitting is performed twice using different base spectra: the BC03 base spectra (figure 4.7a) and the CB07 base spectra (figure 4.7b). The differences between all synthetic spectra are evident in the blue and ultraviolet parts of the spectra. However, the crucial differences lie in the recombination lines, such as Hα , as shown in figures 4.7c and 4.7d, since these differences will affect in the calculation of the $EW_{H\alpha}$.

Figure 4.8 shows the different values of EW($H\alpha$) obtained in function of the type of SSP fitting. Considering this effect as a cause of systematic error, the total uncertainly as high as 80% due to the selection of stellar populations considered in the fitting and the type of SSP fitting performed, at low $EW_{H\alpha}$regimes. Consequently, when the S/N of the Hα is ~ 1 and/or when the emission is embedded in the stellar continuum ($EW_{H\alpha} \lesssim 3$ Å), the resulting $EW_{H\alpha}$is dependent on the selection of SSPs and the fitting methodology.

4.4.2 Nonphysical emission in low $EW_{H\alpha}$regimes.

Further evidence that the low $EW_{H\alpha}$regime ($\lesssim 3$ Å) imposes a methodological challenge is manifested when verifying the validity of physical parameters derived from the embedded emission lines, such as the Hα /Hβ Balmer decrement. Figure 4.9 shows the distribution of the Hα /Hβ ratio for different $EW_{H\alpha}$regimes, while for $EW_{H\alpha} > 3$ Å the distributions peaks at the theoretical Hα /Hβ ratio $\gtrsim 2.87$ (Osterbrock & Ferland 2006), for the regions with $EW_{H\alpha} < 3$ Å, the ratio shows non-physical values.

In addition, the values of $EW_{H\alpha} < 14$ Å and < 3 Å are not exclusive to the DIG emission, so the demarcation with H II regions using the $EW_{H\alpha}$is not clear (Bel22). This is also evident in Fig. 4.10, which shows the distribution of $EW_{H\alpha}$for both DIG and H II bins within the sample. The galaxies with lower median $EW_{H\alpha}$in the DIG regions ($\sim$ 9 Å) are NGC863 and NGC3393, both Sa type, followed by NGC692 (Sbc), NGC6627 (Sb) and ESO325-43 (Sc), with $EW_{H\alpha} \sim 18-20$ Å. ESO584-7 (Sc) and IC3476 (Im) have exceptionally high $EW_{H\alpha}$in the DIG regions, with 34 and 36 Å respectively. ESO584-7 is a H II galaxy (Contini et al. 1998), thus, the high luminosity and star formation rate may be the cause of this high median $EW_{H\alpha}$. The case of IC3476 is also special. It is a galaxy suffering the effects of the ram pressure stripping due to the Virgo Cluster intergalactic environment (Boselli et al. 2021). These authors show that the effects of this perturbations reach scales of individual H II regions $r_{eq} \sim 50$ pc. Furthermore, the compression of the gas along its stellar disc may be the cause of the increase of the star formation activity. This increment could explain the

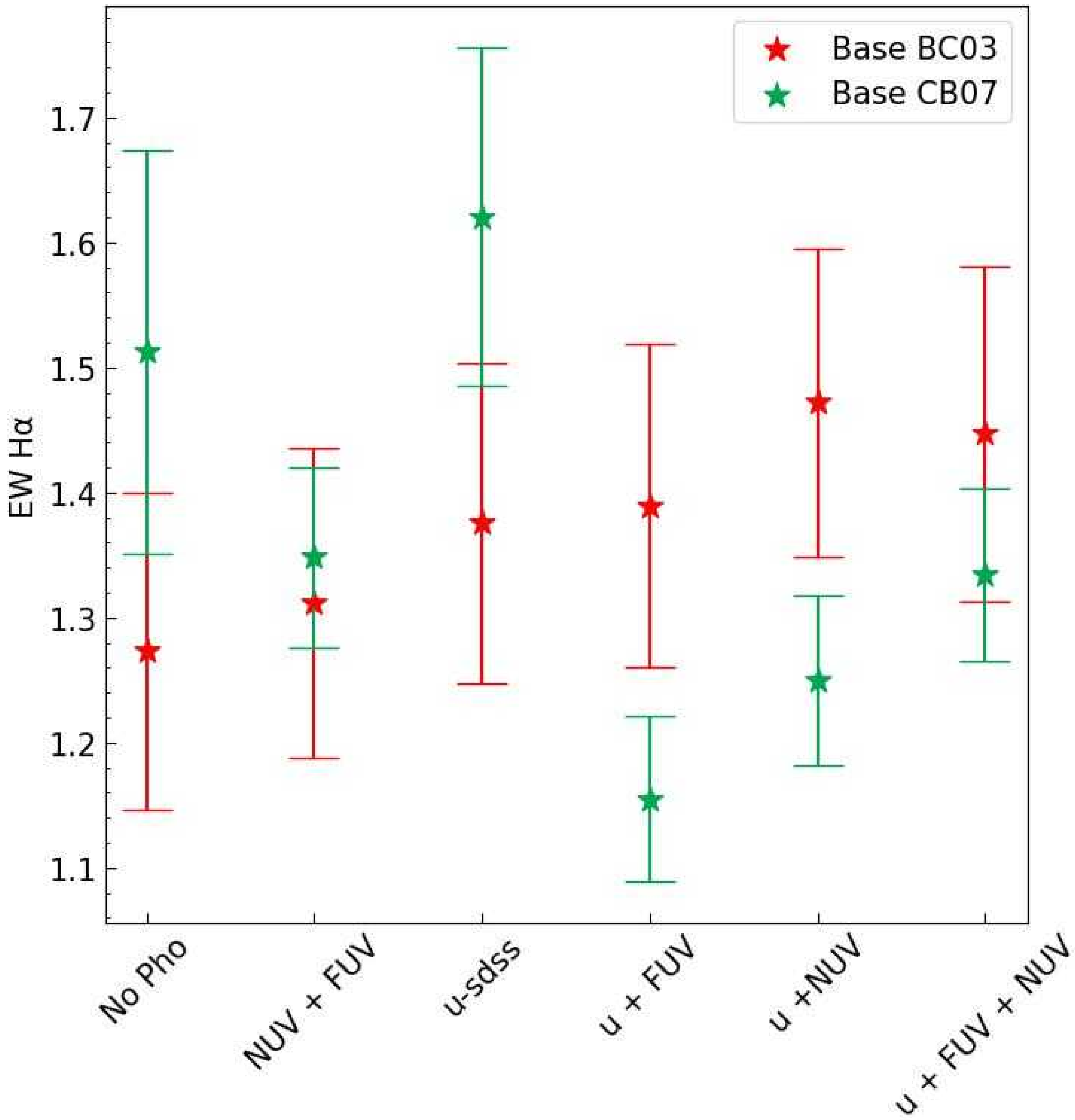

Figure 4.8: EW($H\alpha$) measurement for a NGC863 bin of EW($H\alpha$) $\approx$ 1 Å using 12 different SSP fittings with the *Photometric STARLIGHT* code (Werle et al. 2019). Red values correspond to the those obtained from the synthetic spectrum after setting the BC03 base. Idem for the green, using the CB07 base. The x-axis represent the six different photometric constraints; 1) No photometric constraints; 2) GALEX-NUV and GALEX-FUV photometric points added to the fitting; 3) only u-SDSS point added; 4) u-SDSS and GALEX-FUV points added; 5) u-SDSS and GALEX-NUV points added; 6) u-SDSS, GALEX-FUV, and GALEX-NUV points added to the fitting. It can be seen that the type of fitting affects the EW($H\alpha$) measurement by as much as 80%.

exceptionally high EW$_{H\alpha}$in the DIG regions found in this galaxy, as happened in the case of ESO584-7.

In general, this results are in concordance with previous authors (Lac18; Bel22), being the

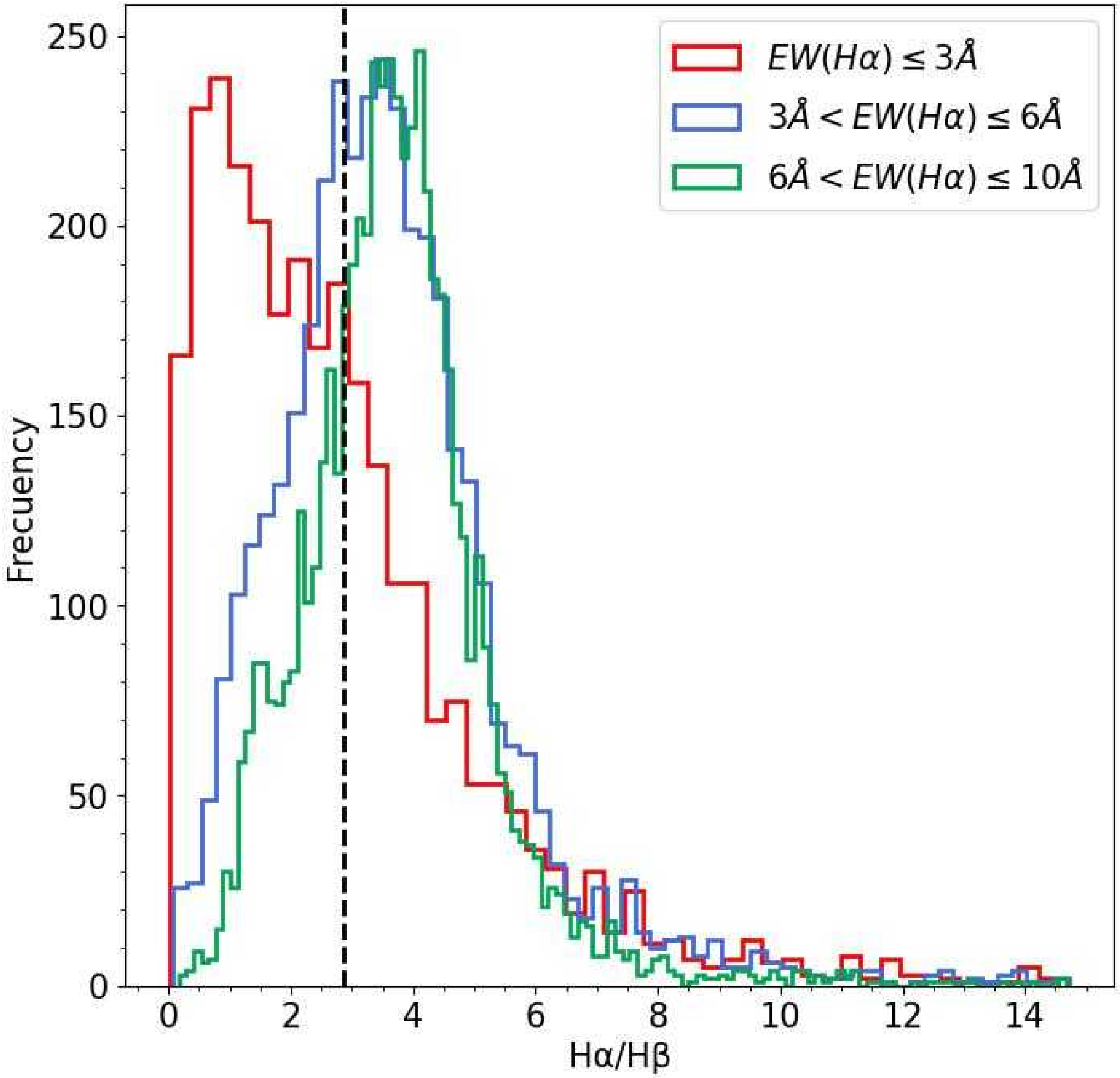

Figure 4.9: Distribution of Hα /Hβ ratio for three different EW$_{H\alpha}$ regimes. Each distribution represent the Hα /Hβ flux ratio for all bins between 6 Å < EW$_{H\alpha} \leq$ 10 Å (green), 3Å<EW$_{H\alpha} \leq$ 6 Å (blue), and EW$_{H\alpha} \leq$ 3 Å (red), for the seven binned galaxies listed in Table 2.1. Black vertical dashed line presents the theoretical ratio of Hα /Hβ = 2.87 (Osterbrock & Ferland 2006). A substantial part of the bins with EW$_{H\alpha} \leq$ 3 Å shows a non-physical ratio (< 2.87).

early type galaxies those with lower EW$_{H\alpha}$, due to the older stellar populations of their bulges, and late-types those with higher EW$_{H\alpha}$. The median EW$_{H\alpha}$of the DIG regions for all sample is ~ 25 Å, substantially higher in comparison with previous studies (~ 5Å) due to the bias given by ESO584-7 and IC3476, and due to the small sample selected.

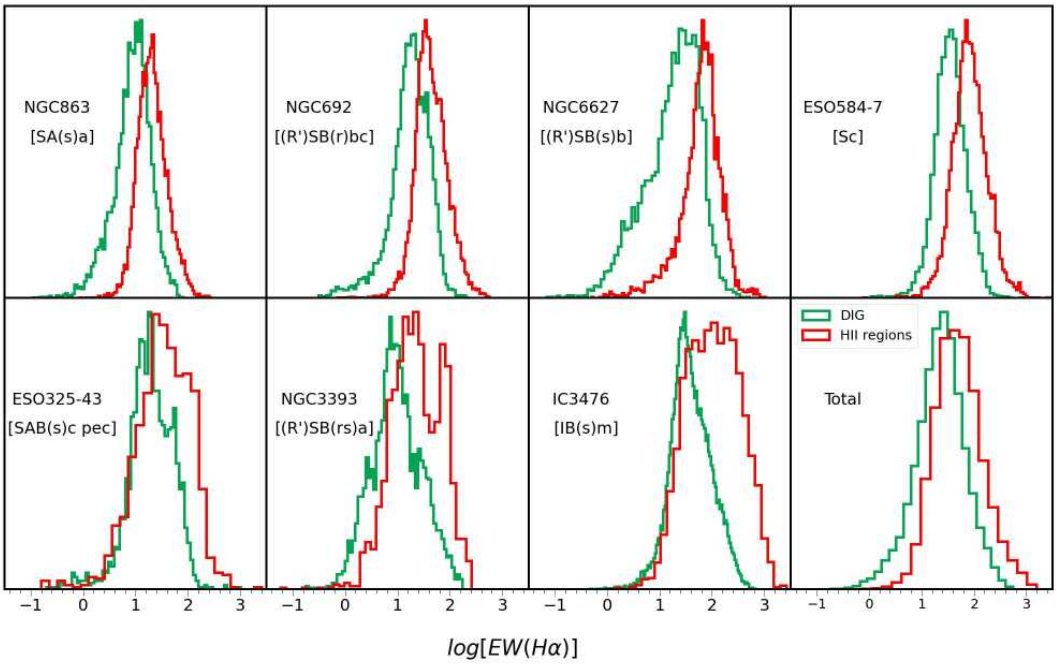

Figure 4.10: $EW_{H\alpha}$distributions for all the bins of the sample. Green histograms represents the distribution for the DIG emission bins, and red for the H II regions emission bins. Last histogram represents the distribution for the seven galaxies.

4.5 Dust reddening in the DIG regime

Fig. 4.11 shows the reddening in the DIG bins, obtained as the radial distribution of the $H\alpha/H\beta$ ratio for the seven galaxies of the sample. This ratio is always lower in the DIG regime (between 3.85 and 2.5), following the same tendency to decrease radially as in the H II regions, with ratio between 4 and 3.25. The decline of the Hα /Hβ ratio in DIG regimes shown are in concordance to the expectations. Since the Hα /Hβ ratio reflects the attenuation of young stars by dust both in H II regions and in the ISM (Chevallard et al. 2013), this ratio is expected to be lower in the DIG, due to the lower optical depth and the increased scatter in the dust attenuation-line luminosity relation (Vale Asari et al. 2020). The fact that the Hα /Hβ ratio is lower in the DIG than in the H II regions suggests that the extinction is consistently lower in the DIG. There could also be an effect of the temperature, as it has been found in the literature that the DIG temperature is $\sim$ 2000 K warmer than in H II regions (Madsen & Reynolds 2005).

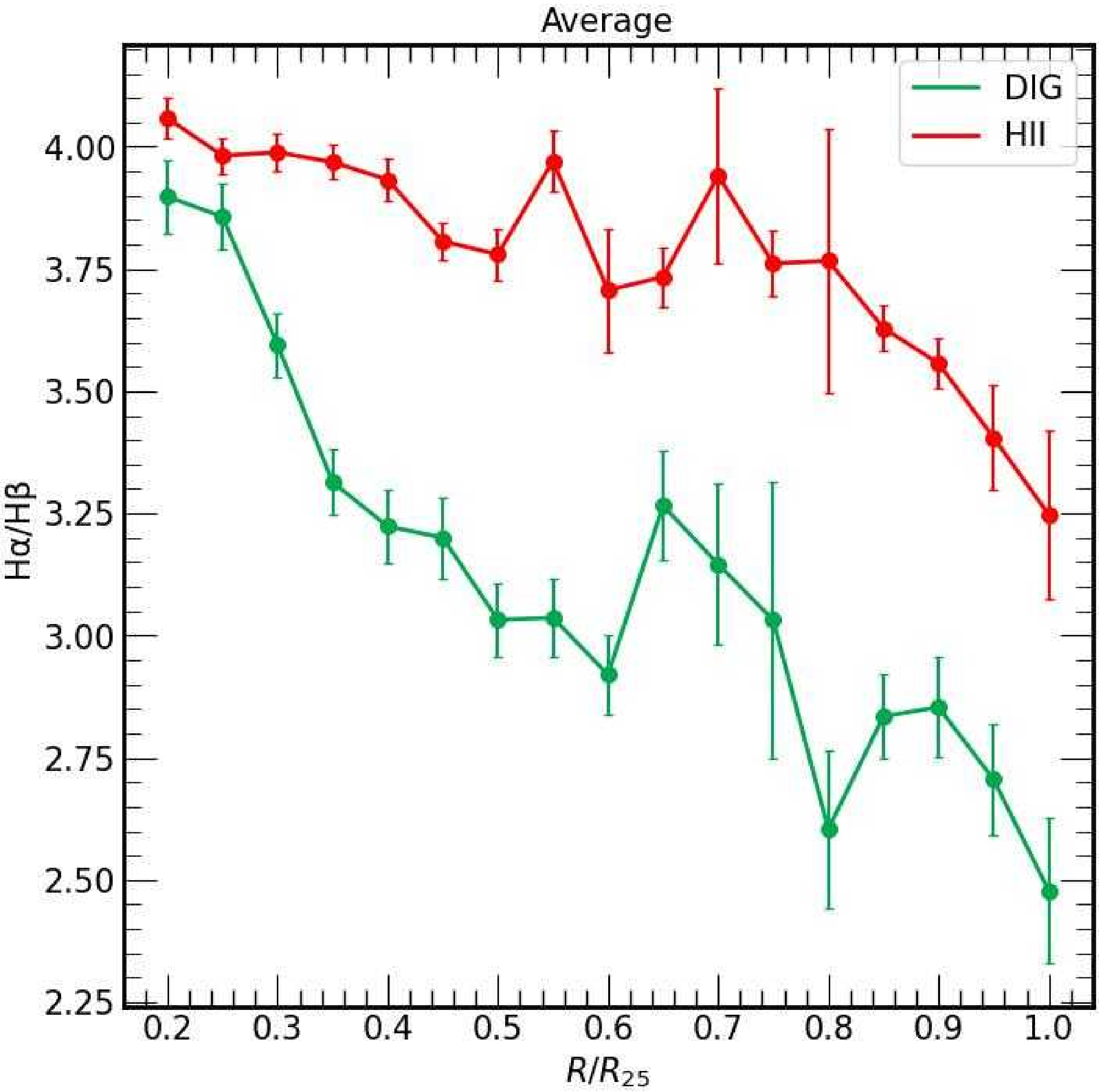

Figure 4.11: Average radial Hα /Hβ ratio distribution of the sample. The distributions are obtained as in Fig. 4.5. Red represent the distribution for the H II regions bins, and green for the DIG bins. Both distributions decrease radially, on average, but the extinction is always lower in the DIG regime.

Chapter 5

Analysis and characterisation of the eDIG in edge-on galaxies

To understand the physical mechanisms involved in feedback processes and the baryon cycle, which are fundamental to galaxy evolution it is essential to study the different gas phases present in the interstellar medium (ISM, Ceverino & Klypin 2008, 2009; Hopkins et al. 2014; Klessen & Glover 2016; Gatto et al. 2017; Grisdale 2017; Barnes et al. 2023). In particular, the DIG component in galactic halos, also known as extraplanar diffuse ionised gas (eDIG), plays a crucial role in the physical processes driving the exchange of gas, metals, and energy between the galactic disk and halo, influencing the evolution of disk galaxies (Tenorio-Tagle & Bodenheimer 1988; Rand et al. 1990; Dettmar 1990; Miller & Veilleux 2003).

5.1 The complex morphology of the eDIG

The Hα maps of Figure 3.7 reveal the complex structure of the extraplanar gas in normal disc galaxies. The most discernible morphological structures observed in the outer regions of the galaxy are the filaments. In galaxies such as ESO157-49 and IC1553, these filaments are especially visible, emerging from the galactic plane and extending more than 2 kpc from the midplane. Other structures can be observed, for instance, in ESO443-21, which features a thick knot-shaped filament around the galactic centre that reaches a distance of ~4.5 kpc from the midplane.

The presence of structures in the halo becomes more evident when examining the maps of the [N II] /Hα , [S II] /Hα , [O I] /Hα , and [O III] /Hβ line ratios. These maps reveal new ionised features that were initially invisible when only examining the H II images. For instance, Figure 5.1 shows the binned maps of the mentioned lines ratios of the IC1553 galaxy.

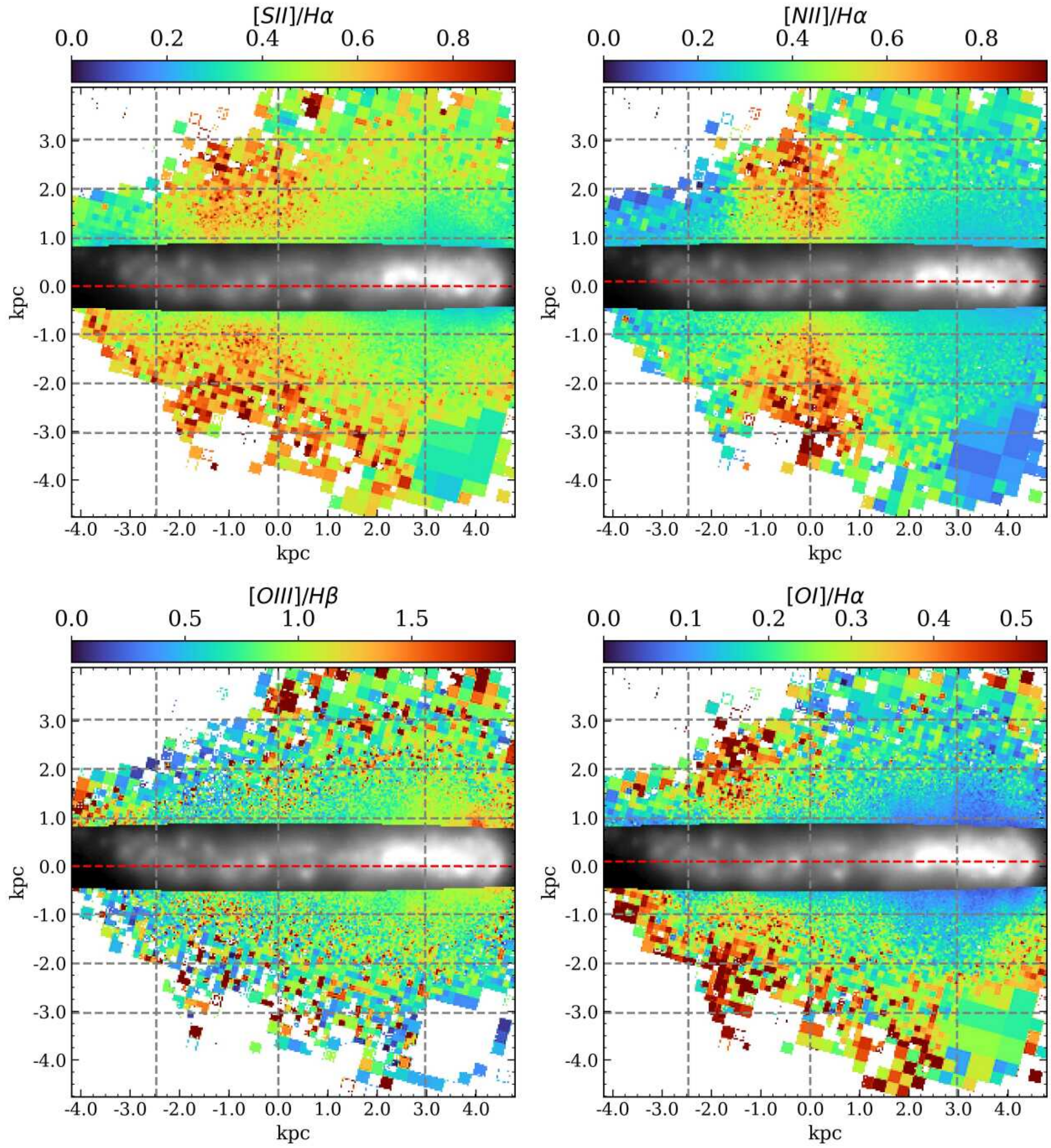

Figure 5.1: IC1553 line ratio maps. Every map is masked, excluding those bins with S/N < 2 or relative error greater than 40% for the respective lines. The same Hα map of the galactic plane masked in Figure 3.7 is overlaid. The dashed red line indicates the midplane, located at z = 0. The y-axis is re-scaled in function of the galaxy inclination.In this case, the galactic plane is defined as a rectangle with the minor side equal to the minor axis of the fitted ellipse and the major side extending the full length of the x-axis. The grey dashed lines indicates the heights with respect the midplane z = ±1, ±2, ±3 kpc and major axis distances MAD = -2.5, 0, 3 kpc.

The images show the intricate and asymmetrical structure of the eDIG. Having differences of 0.4 dex in the [S II] /Hα ratio along the major axis and over 0.8 dex in [N II] /Hα . Additionally, the line ratios increase with respect to the distance from the midplane, a phenomenon that is well-documented in the literature (Rand 1998; Levy et al. 2019). However, the 2D spectroscopic analysis of the eDIG allows to recognise that the variation of the line ratios are dependent not only on height, but along the major axis distance (MAD) of the galaxy.

Between 1.5 kpc $\lesssim$ MAD $\lesssim$ 4.5 kpc, the [N II] /Hα ratio presents significantly lower values than the range between -1 kpc $\lesssim$ MAD $\lesssim$ 1 kpc, showing a a conical-shaped structure that is slightly off-centred with respect to the galaxy. These features are also reported by other authors (Rautio et al. 2022; Dirks et al. 2023). However, with the BETIS adaptive binning method applied (BETIS I), we recover data with S/N > 2 at z > 3, sampling almost the entire MUSE FoV in this galaxy and also in the rest of the galaxies. Besides, this apparent conical structure is shifted at MAD = -0.5 kpc in the [S II] /Hα ratio, and at MAD = -1.5 kpc at [O I] /Hα ratio, being not present in the [O III] /Hβ ratio. This asymmetry in the halo coincides with the asymmetry observed in the galactic plane, where most of the Hα emission from the H II regions is concentrated between 1 kpc $\lesssim$ MAD $\lesssim$ 3.5 kpc. At this radial range, the line ratios found in the eDIG resemble more closely the line ratios of the H II regions rather than the typical DIG line ratios (below 0.3 and 0.4 in the [N II] /Hα and [S II] /Hα , and below 0.1 in [O I] /Hα ; BETIS I).

Subsections from 5.3.2 to 5.3.9 display the line ratio maps for the rest of the sample, where the complex bidimensional structure of the eDIG and its apparent connection between the line-of-sight H II regions of the galactic plane is evident for all galaxies.

5.1.1 Ionisation structure of the eDIG

Figure 5.2 shows the distribution of the eDIG characteristic line ratios with respect the distance from the midplane for IC1553. The stars, triangles, and squares represent the values of the line ratio at that height for MAD equal to -2.5 kpc, 0 kpc, and 3 kpc, respectively. Analogously, this corresponds to the line ratio height distribution in a long-slit located at those MADs and perpendicular to the galactic plane. The solid lines are constructed then integrating the fluxes along the major axis. The dashed lines represent the $\Sigma_{H\alpha}$ distribution, constructed similarly to the solid lines by integrating the Hα flux along the major axis, and the grey background represents the location of the galactic plane. Since the H II regions distribution is not symmetrical with respect z = 0, the minimum of the $\Sigma_{H\alpha}$ and line distributions are shifted with respect z = 0.

The integrated distribution of the [N II] /Hα , [S II] /Hα and [O I] /Hα line ratios tends to increase in height, reaching a minimum inside the galactic plane. The [N II] /Hα and

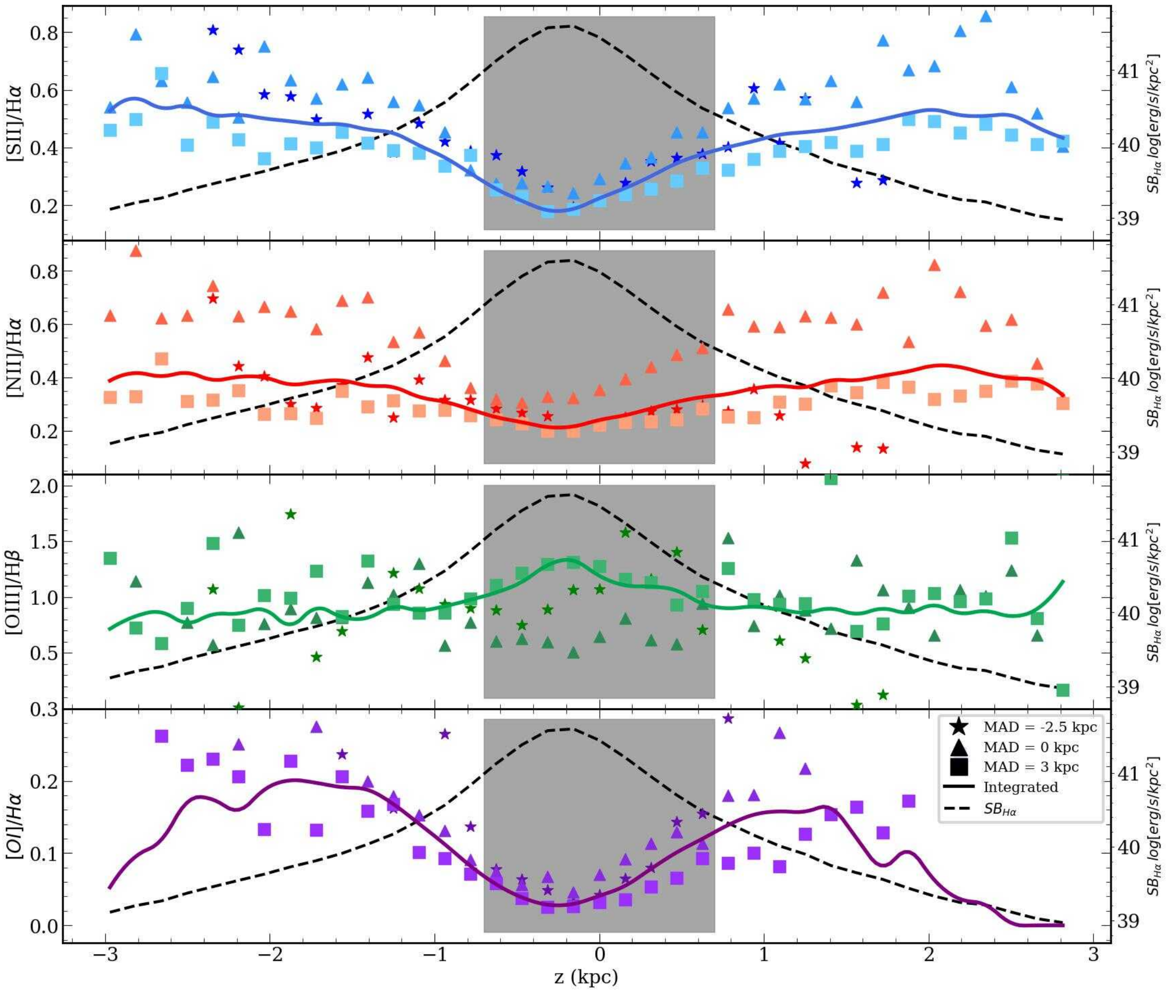

Figure 5.2: Distribution of the line ratios with respect the distance from the midplane for the IC1553 galaxy. The stars, triangular and square markers represent the line ratio at that z for MAD = -2.5, 0 and 3 kpc respectively, analogous to a long-slit perpendicular to the galactic plane at a given MAD. The solid lines represents the integrated values along the major axis distance. The dashed black line represents the $\Sigma_{H\alpha}$ height distribution of the galaxy. The grey background between z = - 0.7 kpc and 0.7 kpc represents the galactic plane.

[S II] /Hα line ratios increase up to 0.4 and 0.6, respectively, from z = 0 to 2 kpc, and then remain constant. [O I] also increases from z = 0 to 2 kpc, reaching up to 0.2, but then decrease dramatically. This line ratios seems anti-correlated with the $\Sigma_{H\alpha}$ vertical distribution. In contrast, for the [O III] /Hβ ratio, at z = 0 it reaches its maximum of 1.3 and then decreases slowly to 0.7.

This trend is consistent with findings from previous studies in other edge-on galaxies (Rand 1998, 2000; Collins & Rand 2001; Haffner et al. 2009b; Ho et al. 2016; Dirks et al. 2023). However, in addition to this, when restricting the height distributions to specific MADs, the overall behaviour of the distributions remains consistent, but the line ratios exhibit notable differences. At MAD = 3 kpc (represented by squares in Figure 5.2, where the most prominent H II regions emission is observed in Figure 5.1), the [N II] /Hα , [S II] /Hα and [O I] /Hα line distributions follow the same trend as their respective integrated distributions, but consistently reach lower values. Similarly, at MAD = 0 (represented by triangles in Figure 5.2, where the H II regions emission observed in Figure 5.1 is lower), the line distributions also follow the same trend, but consistently reach higher values. This behaviour in the line ratio distributions is consistent in all the galaxies, as shown in the subsections from 5.3.2 to 5.3.9.

Figure 5.3 shows the MAD distribution of the [N II] /Hα and [S II] /Hα lines for z = 1 and 1.8 kpc, as well as the normalised $\Sigma_{H\alpha}$ MAD distribution of IC1553. Two effects are noticeable in this figure: Firstly, all the line ratio distributions tend to be lower between 2 kpc and 4.5 kpc, where the $\Sigma_{H\alpha}$ is higher, and increase while the $\Sigma_{H\alpha}$ decreases, particularly for the [N II] /Hα ratio. Secondly, the effect of the increment of the line ratio with height, as seen in Figure 5.2, remains present along the major axis, with the difference being clearer in regions of high $\Sigma_{H\alpha}$, especially for the [S II] /Hα ratio, where there is a constant difference of 0.1 between both distributions. These effects are not exclusive to IC1553, the MAD distributions present the same behaviour for all galaxies in the sample (see section 5.3). These figures evidences the high complexity that the eDIG presents, suggesting that the physical conditions in the eDIG are influenced by the distribution of the H II regions emission along the galactic plane.

5.2 Discussion

5.2.1 The linkage between the galactic plane and the eDIG

The correlation between the morphological distribution of star-forming regions in the disks of edge-on galaxies and the shapes and morphology of the halos presents the strongest evidence supporting the interpretation that energy sources from star formation within the galaxy disks drive the observed disk-halo interactions (Norman & Ikeuchi 1989; Dahlem 1997). Over the past decade, there has been a unanimous consensus in the literature that the primary ionisation mechanism for the WIM (DIG) and the eDIG is attributed to star formation in the discs of late-type galaxies (Ho et al. 2016; Boettcher et al. 2019; Levy et al. 2019; Werle et al. 2019; Belfiore et al. 2022; Della Bruna et al. 2022a,b; Rautio et al. 2022; Tacchella et al. 2022; Dirks et al. 2023; Lu et al. 2023; Sardaneta et al. 2024, etc.). Specifically, Lyc photons leaking from OB associations in the galactic discs escape into the ISM in the halos through transparent pathways, ionising layers of low-density gas that can be traced out to distances of up to 5 kpc or more from the midplane of the disks (Haffner et al. 2009b; Weber et al. 2019a).

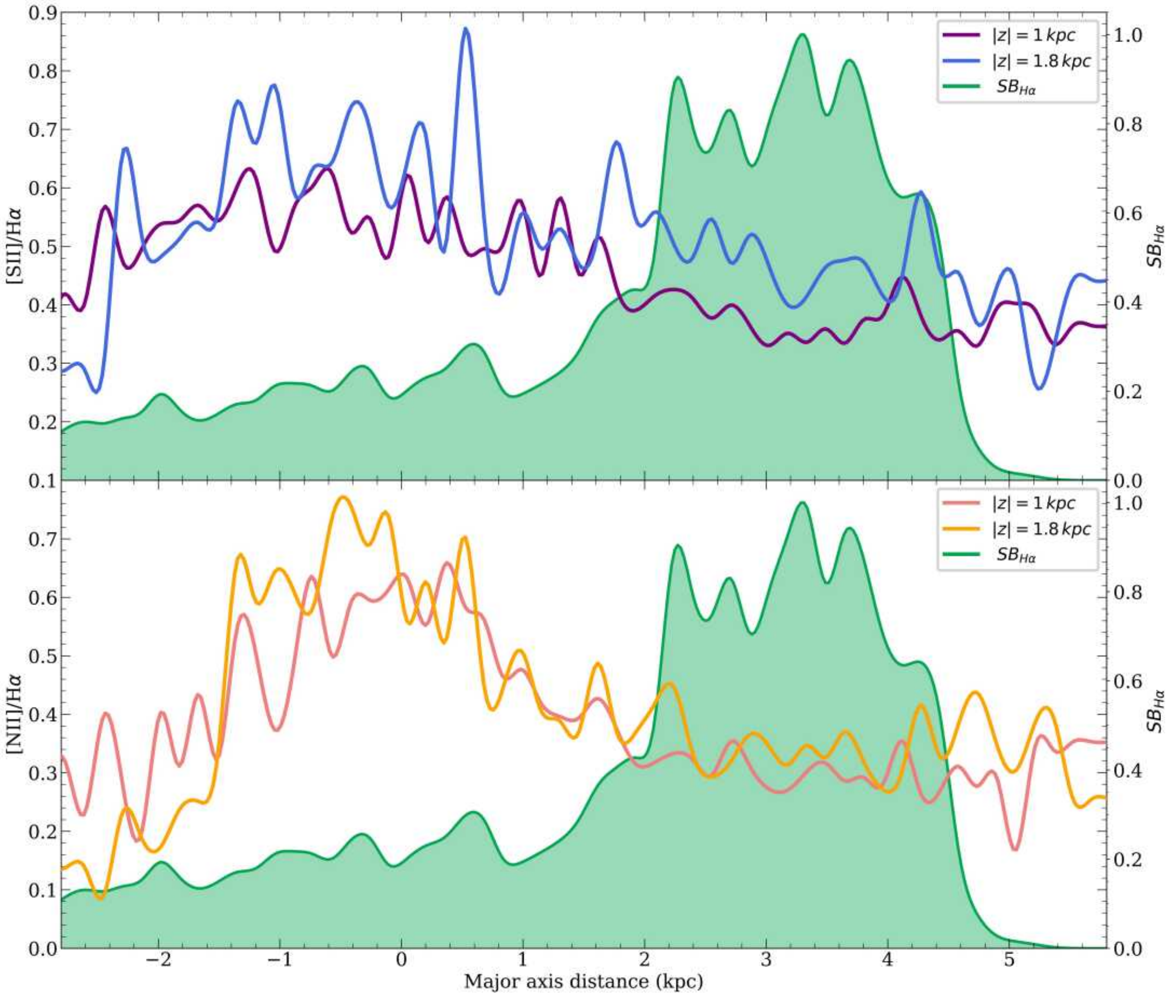

Figure 5.3: Major axis distance (MAD) distribution of the [N II] /Hα and [S II] /Hα lines for IC1553 at z = 1 and 1.8 kpc. In green, the normalised $\Sigma_{H\alpha}$ MAD distribution, constructed integrating the Hα flux within the ellipse fitted in section 2.3 throughout the major axis. Both line distributions show a correspondence with the $\Sigma_{H\alpha}$ distribution, decreasing and showing more difference between both heights as the $\Sigma_{H\alpha}$ increase. This tendency is consistent for all galaxies.

The specifics of the underlying mechanisms governing the disc-halo connection are complex and widely debated. From an energetic perspective, several external sources have been proposed to account for the origin of the eDIG. These include gas accretion from the intergalactic medium (IGM, e.g. Binney 2005; Putman 2017) and the circumgalactic medium (CGM, e.g. Levy et al. 2019; Bizyaev et al. 2022), the latter also being suggested as a probable origin of the UV halo (e.g. Hodges-Kluck et al. 2016; Shinn & Seon 2015) or a hot halo (Marasco et al. 2012; Li et al. 2023b). However, in a recent study, Sardaneta et al. (2024) argue, using a sample of nearby highly inclined ($i \geq 80°$), isolated galaxies, that the eDIG phenomenon is uncorrelated with the galaxy environment. Consequently, the primary energy sources driving the disc-halo interactions should reside within the galaxy discs, as no other pervasive external energy sources are known that could account for the observational data (Dahlem 1997). Therefore, the halo gas expelled or heated by these energy sources must also originate from the discs.

Several heating mechanisms have been proposed to account for the energetics observed in the halos of galaxies: AGNs and high-level star formation, or a combination of both. In the case of AGNs, many spirals exhibit very characteristic outflow cones associated with a nuclear engine, which can be traced using X-rays, radio continuum emission, and optical emission-line maps (e.g. Wilson & Tsvetanov 1994; Colbert et al. 1996; López-Cobá et al. 2019). However, considering that only 10−15% of galaxies in the local universe ($z < 0.1$) exhibit AGN activity, and that disk-halo interactions are observed over extensive regions of the discs, AGNs cannot be the common cause for the observed disk-halo interactions. Indeed, no AGNs are found in the eBETIS sample (Sec. 2.3) or in recent eDIG studies of normal late-type galaxies (Ho et al. 2016; Levy et al. 2019; Lu et al. 2023).

On the other hand, high-level SF can occur in various locations within galaxy discs, either in circumnuclear starbursts or in giant H II regions dispersed across the discs. Several scenarios for the disk-halo interaction due to SF have been proposed: the superbubble breakout model (e.g. Mac Low & McCray 1988), the galactic fountain model (Shapiro & Field 1976), the champagne model (Tenorio-Tagle 1979), the chimney model (Norman & Ikeuchi 1989), and the galactic wind model (Veilleux et al. 2005, and reference therein). For the discussion purpose, we exclude phenomena related to nuclear activity in galaxies or incoming gas from the IGM/CGM, focusing on those models in which ionising radiation originating from SF must not only escape the H II regions but also traverse the dense clouds of neutral hydrogen near the midplane.

In the galactic fountain model, the outflow velocities are expected to be lower than the escape velocity of the gas ($v < v_{esc}$), indicating that all material will ultimately return to the disc, resulting in a dynamic circulation of matter as the primary mechanism of the disc-halo interaction. In the chimneys model, OB associations are born within giant molecular clouds, and the ionising ultraviolet flux and stellar winds from successive generations of OB stars provide significant momentum input, creating free cavities in the surrounding ISM. The sequential explosions of supernovae (SNe) result in the formation of a dense, cool wall of neutral gas and a central flow of hot gas, which constitutes a chimney. The total energy output from stellar winds is comparable to that of SNe, albeit released over a more extended period. For a simple instantaneous starburst model with a canonical IMF and a total mass of 10^6 $M_\odot$, the total energy is approximately 10^{55} ergs (Leitherer et al. 1992). The hot gas ascends to the halo through the chimneys, reaching distances of several kpc. In this model, the chimneys create vertical channels that facilitate the rapid propagation of SN-driven shocks, with gas velocities reaching $v \geq v_{esc}$, thereby enabling the ejection of matter into intergalactic space. The gas rises to $\gtrsim 3$ kpc and returns to the disk after a dynamical time of $\sim 10^7$ years with an infall velocity of $< 10^2$ km s^{-1}, resulting in an ongoing exchange of mass, energy, and momentum. For canonical Galactic parameters, the chimney phase is associated with a mass flow rate of $0.3 - 3$ M$_\odot$ yr^{-1} and a global power input of 10^{40-42} ergs s^{-1} (Norman & Ikeuchi 1989).

This scenario aligns with the observed multiphase nature of the halo ISM (Rossa & Dettmar 2003a;Rich et al. 2010). The chimney model can be described as an intermediate state between a two-phase model (Field 1989)—relevant in galaxies with higher mean ambient density—and a three-phase model (McKee & Ostriker 1977), in which the third hot phase consists of chimneys with a filling factor of about 10% (Norman & Ikeuchi 1989). In both models, disk-halo interactions occur, but in the fountain mode, the energy input over the disk is distributed across extensive areas, whereas in the chimney mode, the energy injection into the ISM is more localised.

Independent of the various outflow scenarios, they provide absorption-free pathways for H-ionising photons into the halo, as well as channels for the vertical transport of hot processed material and cosmic rays into the halo, where a hot gas phase with temperatures of up to $\sim 10^7$ K has been observed. This X-ray emitting plasma offers a further compelling argument favouring SF-related processes as the heating sources of the halo, given that the cooling time for such gas is very short, requiring continuous heating. Indeed, several authors have identified stellar winds and SNe as the principal energy sources driving this process (Weaver et al. 1977; Gray et al. 2019; Sarkar et al. 2022).

However, real galaxies exhibit greater complexity than the models depicted. For instance, the Type II supernova rate and the average gas density at the disc can vary with galactocentric distance, resulting in different processes and phases occurring at various radii within the same galaxy. Additionally, these parameters can fluctuate over time, especially in galaxies experiencing bursts of star formation throughout their lifetimes. The total SFR, the distribution of H II regions, and the local level of star formation in different regions across a galactic disk are not constant over time. Galaxies may undergo cycles of star formation, implying they might temporarily be in states of high, intermediate, or quiescent phases of star formation (Rosa & Richter 1988). The natural extension of the disk ISM into the halo via star-formation-driven outflows also indicates that the halo ISM is dynamic rather than static. The multiphase ISM exists under the influence of both the galaxy's gravitational potential and the energy input from heating sources, leading to interactions between different phases and constituents of the ISM. Consequently, in the presence of ionising UV radiation from hot massive stars, stellar winds, and supernova shock waves, the ISM in galaxy halos is never in local thermodynamic equilibrium.

The morphology and properties of gaseous halos are influenced by the level of SF activity in the underlying disk (Rossa & Dettmar 2003a). Galaxies require a sufficient level of SF to sustain a widespread extraplanar eDIG layer (Dahlem et al. 1995). Here, itt is essential to distinguish between pure starburst galaxies (typically with circumnuclear SF, e.g. M82) and normal galaxies with varying levels of widespread SF in their disks. For the latter, it is known that the most actively star-forming galaxies possess the most prominent halos (Dahlem 1997). In galaxies with intermediate SF levels, such as those in the eBETIS sample, disk-halo interactions occur only in regions with high SFR. Theoretical calculations indicate that only those regions surpassing a threshold of 10^{-2} ergs s^{-1} cm^{-2} are capable of initiating disk-halo interaction (Dahlem et al. 1995).

Indeed, the connection between the $\Sigma_{H\alpha}$ distribution and the ionisation structure of the eDIG in the eBETIS galaxies (see Sec. 5.1.1) demonstrates a clear correlation between the morphology of halo emission and the distribution of SF regions and complexes in the underlying galaxy disks. Furthermore, the detection of extended eDIG in the halos of the eBETIS sample indicates that even low-mass galaxies with modest SFR (Table 5.1) are capable of producing a pervasive layer of extraplanar diffuse ionised emission. This finding contradicts previous assumptions that halos are a rare phenomenon among normal spirals (Hummel et al. 1991), a bias likely caused by the insufficient sensitivity of earlier observations.

In the following, we discuss the observational evidence supporting this scenario as derived from the eBETIS sample.

5.2.2 The ionisation mechanism of the eDIG

In the scenario delineated above, the eDIG emission originates *in situ* within low-density gas environments, induced by ionising photons propagated from the galactic disk via transparent conduits formed by superbubbles or chimneys. However, the precise underlying physics explaining the large distance between the extraplanar gas and ionising stars in the midplane, as well as the fine-tuned details of the ionisation mechanism of the eDIG, remain a topic of ongoing debate.

Long-standing issues regarding the specifics of OB-star-driven ionisation remain prevalent in the literature. A notable characteristic of the DIG that proves difficult to explain through OB star photoionisation is its optical emission-line spectrum. Should the eDIG be ionised by radiation escaping from the midplane H II regions, the spectrum of the ionising radiation would be expected to resemble that of the OB star (or the SED dominated by such stars). Consequently, one would anticipate similar emission-line spectra in the eDIG as in the H II regions. Nonetheless, certain observed optical emission line ratios are not explicable by pure photoionisation from OB stars. The distinctive emission-line ratios observed in the eDIG, namely [N II] $_{\lambda6584}$/Hα , [S II] $_{\lambda6717}$/Hα , [O III] $_{\lambda5007}$/Hβ and [O I] $_{\lambda6300}$/Hα , are elevated compared to those observed in H II regions (Rand 1997, 1998; Collins & Rand 2001; Haffner et al. 2009b; Seon 2009), as illustrated in Fig. 5.2 and elaborated upon in Sec. 5.1.1 for the eBETIS sample, indicating the relative significance of additional heating processes.

Some of the differences between the DIG and H II region emission-line spectra (i.e., enhanced [N II] /Hα and [S II] /Hα) can be explained by differences in temperatures. In a model of photoionised gas, the temperature is determined by the equilibrium between heating and cooling mechanisms. Heating is facilitated through the thermalisation of the excess kinetic energy of electrons during the photoionisation-recombination process, whereas cooling predominantly arises from collisional excitation followed by radiative decay of metastable states of trace ions (Osterbrock & Ferland 2006).

Relative temperatures can be explore by analysing the emission line ratios of the forbidden lines with respect to the H-recombination emission. The line intensities of [N II] and [S II] relative to Hα probe the ionisation fractions (X^+/X) and elemental abundances of ionised the gas, showing a strong dependence on the electron temperature (T$_e$).These parameters relate with the line intensity ratios as follows (Haffner et al. 1999; Osterbrock & Ferland 2006):

$$\frac{I([N\,II]_{\lambda 6583})}{I(H\alpha)} = 1.63 \cdot 10^5 \left(\frac{N^+}{N}\right)\left(\frac{N}{H}\right)\left(\frac{H^+}{H}\right)^{-1} T_4^{0.426} e^{-2.18/T_4}, \tag{5.1}$$

$$\frac{I([S\,II]_{\lambda 6717})}{I(H\alpha)} = 7.64 \cdot 10^5 \left(\frac{S^+}{S}\right)\left(\frac{S}{H}\right)\left(\frac{H^+}{H}\right)^{-1} T_4^{0.307} e^{-2.14/T_4}, \tag{5.2}$$

with T$_4$ being the electron temperature in units of 10^4 K.

We assume that usually the 100% of the hydrogen and the 80% of the nitrogen are ionised in the DIG, varying little within the DIG and basically tracing the T$_e$ (Sembach et al. 2000; Otte et al. 2002; Haffner et al. 2009b). We also assume solar abundances: N/H = $6.8 \cdot 10^{-5}$ and S/H = $1.3 \cdot 10^{-5}$ (Asplund et al. 2021).

Haffner et al. (1999) and Madsen et al. (2006) used these relationships to build diagnostic diagrams to estimate both T$_e$ and S$^+$/S from observations of [N II] /Hα and [S II] /Hα . Given that H and N have similar first ionisation potentials (13.56 eV and 14.5 eV, respectively) and a weak charge-exchange reaction, and assuming that N is not doubly ionised, then N$^+$/N^0 ~ H$^+$/H^0 vary little within the DIG, so that variations in [N II] /Hα essentially traces variations in T$_e$ (Sembach et al. 2000; Otte et al. 2002; Haffner et al. 2009b). Figure 5.4 shows the distribution of [N II] $_{\lambda 6583}$/Hα vs. [S II] $_{\lambda 6717}$/Hα line ratios in function of |z| for IC1553. Circles are the integrated along the major axis for a certain z. Stars, triangles and squares are bins at MAD = -2.5, 0 and 3 kpc respectively. We use the equations 5.1 and 5.2 to show the predicted ratios for a constant T_e (6, 7, 8 and 9 in units of 10^3 K) and S^+/S (0.25, 0.5 and 0.8). Assuming solar abundances: N/H = $6.8 \cdot 10^{-5}$ and S/H = $1.3 \cdot 10^{-5}$ (Asplund et al. 2021).

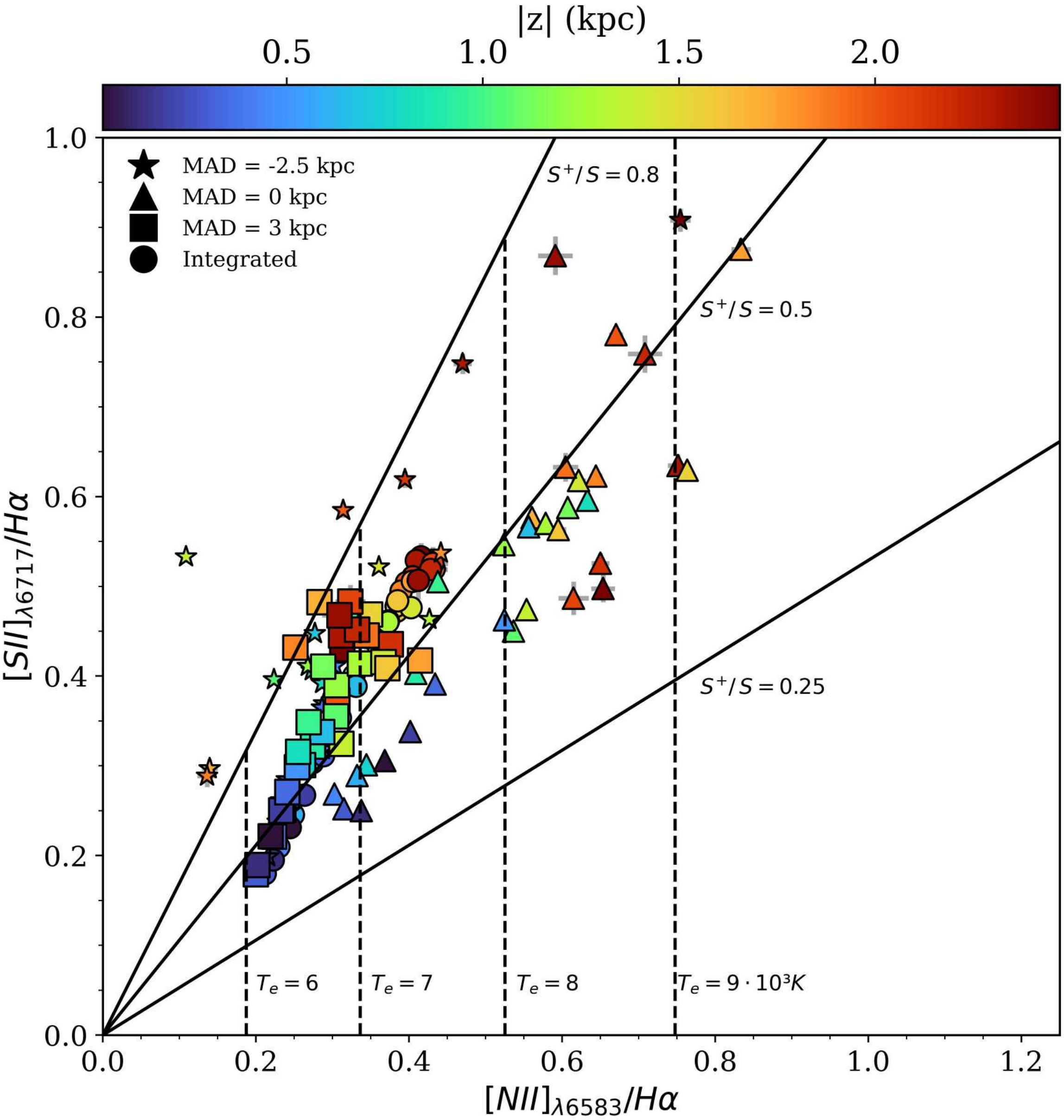

Figure 5.4: [N II] $\lambda 6583$/Hα vs. [S II] $\lambda 6717$/Hα diagnostic diagram for IC1553. Colours represent height with respect the midplane, equally from above or below the plane. Vertical dashed lines are the theoretical ratios obtained from 5.1 at a constant T_e (6, 7, 8 and 9 in units of 10^3 K respectively). Solid lines represent the theoretical ratios from equations 5.1 and 5.2 for at a fixed S^+/S (0.25, 0.5, 0.8 respectively). The circles indicate the line ratios obtained by integrating the fluxes along the major axis at a certain z. Stars, triangles and squares indicate the line ratio at a certain z for MAD = -2.5, 0 and 3 kpc respectively.

The general behaviour indicates a linear, constant increment of T_e with increasing distance from the galactic plane. This trend is consistent with previous studies of the WIM in the Galaxy (Haffner et al. 2009b; Madsen et al. 2006) and with long-slit observations perpendicular to other edge-on galaxies (Collins & Rand 2001; Otte et al. 2001; Hoopes & Walterbos 2003; Boettcher et al. 2019). However, the spatial coverage of the eBETIS galaxies permits the study of the dependence of the eDIG line ratios on temperature at different MADs. Figure 5.4 illustrates significant variations in T_e and S^+/S with respect to the line of sight. For instance, at the galaxy minor-axis (MAD = 0), the temperature increases from 7 to 9 $\times 10^3$ K and the S^+/S ratio rises from 0.3 to 0.5, whereas at MAD = -2.5 kpc, the S^+/S ratio attains high values of approximately 0.8 at all vertical distances. At MAD = 3 kpc, the temperature of the eDIG is confined to a narrow range between $6 - 7.5 \times 10^3$ K, with $S^+/S \approx 0.5 - 0.8$. To comprehend the variations in S^+/S, we could examine the energetics of the eDIG trace ions. The ionisation energies of N and S are 14.5 eV and 10.4 eV, respectively. If N is mostly ionised, then S should also be mostly ionised. However, the energy required to double-ionised S is 23.3 eV ($S^+ \rightarrow S^{++}$), while for N is 29.6 eV ($N^+ \rightarrow N^{++}$). Therefore, S^+/S may vary while N^+/N remains constant if the ionising energy does not reach 29.6 eV. Consequently, we anticipate greater variation in S^+/S under eDIG conditions.

The variations in the temperature and ionisation structure of the eDIG as a function of spatial position within a single galaxy, as illustrated in Fig. 5.4, provide more compelling evidence of the intricate dynamical heating structure of the ISM in the halo of late-type galaxies. A similar trend is observed across the entire eBETIS sample, as depicted in the associated figures in section 5.3, indicating that the eDIG tends towards a lower ionisation state (higher $S^+/S \sim 0.5 - 0.8$) compared to classical H II regions, which would be situated in the lower-left corner of these diagrams (e.g. [N II] /H$\alpha \approx$ 0.25, [S II] /H$\alpha \approx$ 0.1, Madsen et al. 2006). The anomalous [N II] /Hα and [S II] /Hα eDIG line ratios can be attributed to an increase in the T_e temperature in the halo, resulting from photoionisation with a low ionisation parameter Q, i.e., the ratio of ionising photon density to electron density, which measures the diluteness of the radiation field (Domgorgen & Mathis 1994). Nonetheless, while the elevated [N II] /Hα and [S II] /Hα line ratios can be explained by low Q photoionisation, other eDIG line ratios, such as [O III] /Hβ and [O I] /Hα , remain unexplained (Haffner et al. 2009b).

What remains puzzling in this scenario is the increase in T_e with respect to the midplane distance $|z|$, as supplementary heating sources may be necessary to account for this phenomenon. The literature has extensively debated the origin and characteristics of an additional source of ionisation to explain the observational features of the (e)DIG. The observed temperature behaviour of the eDIG, as depicted in Fig. 5.4, could be attributed to the spectrum of the ionising radiation being reprocessed as it traverses the ISM, an effect known as radiation hardening: a preferential absorption of photons near the ionisation thresholds within the sources' environment, resulting in (on average) more energetic photons escaping from the H II regions. This results in higher temperatures in the (e)DIG than in H II regions, which, in turn, leads to stronger emission of collisionally excited optical lines (Hoopes & Walterbos 2003; Wood & Mathis 2004; Wood et al. 2005; Haffner et al. 2009b). This model explains the WIM in our Galaxy but fails to explain an increasing [O III] /Hβ ratio at large distances from the galactic plane (Weber et al. 2019a). Therefore, the rise in the [O III] ratio with H-recombination lines with $|z|$ needs an additional source of heating and/or ionisation.

Several alternative heating mechanisms that may raise the electron temperature of the eDIG have been proposed, including differential absorption and/or scattering of radiation due to dust (Sokolowski 1993; Ferrara et al. 1996), dissipation of turbulence (Minter & Spangler 1997), magnetic reconnection (Reynolds et al. 1999; Hoffmann et al. 2012), photoelectric heating from small grains (Reynolds et al. 2001), cosmic rays heating (Wiener et al. 2013; Boettcher et al. 2019), etc. However, models still struggle to fully reproduce the (e)DIG emission-line spectrum.

A potential heating source that has gained prominence in the literature in recent years is the photoionisation by a hard spectrum produced by the high-temperature end of the white-dwarf distribution and the central stars of planetary nebulae. These low mass, hot, and evolved (post-AGB) stars, known as HOLMES, has been proposed as an ionisation mechanism for the DIG in general (e.g., Sokolowski & Bland-Hawthorn 1991; Lacerda et al. 2018; Belfiore et al. 2022; Lugo-Aranda et al. 2024) and for the eDIG in particular (e.g., Flores-Fajardo et al. 2011; Weber et al. 2019a; Rautio et al. 2022). HOLMES are abundant and smoothly distributed in the thick disc and lower halos of the galaxies, with scale heights greater than those of the OB stars. They are a significant source of ultraviolet emission, capable of reproducing the increment in the line ratios found in the (e)DIG, and specifically for the high ionisation species such as [O III] (Flores-Fajardo et al. 2011). Indeed, Belfiore et al. (2022) and Lugo-Aranda et al. (2024) argue on the existence of two different types of diffuse emission based on the EW$_{H\alpha}$bimodal distributions centered at $\sim$ 1 and $\sim$ 10 Å, which according to the classification by Lacerda et al. (2018), corresponds to the so-called hDIG ionisation (component dominated by HOLMES), and the ionisation of SF complexes (component dominated by unresolved H II region, or photons leaked from them), respectively.

Nevertheless, the behaviour of the line ratios shown in Fig. 5.2 (and related figures in the section 5.3) reveals that the ionisation of the eDIG is highly dependent on the distribution of H II regions in the disc (Sec. 5.1). The [N II] /Hα , [S II] /Hα , and [O III] /Hβ ratios attain their highest values at the greatest distances from the midplane and in regions with lower $\Sigma_{H\alpha}$. This observation is incompatible with a smooth distribution of HOLMES throughout the thick disc and lower halo. Under the HOLMES scenario, higher [O III] /Hβ ratios would be expected in the vicinities of the thick disc, along with a smooth distribution of characteristic high ionisation line ratios within the halos. Furthermore, the few high [O III] /Hβ ratio bins near the galactic planes of the galaxies are clearly associated with SF regions within the discs, as indicated by the emission-line maps of eBETIS (see Fig. 5.1 and related figures in section 5.3).

In addition, as explained in BETIS I, the conventional proxy employed to distinguish between star-forming regions, HOLMES, and mixed regimes—the Hα equivalent width (EW$_{H\alpha}$)—may be unreliable. The EW$_{H\alpha}$ is a parameter that scales with the SFR per unit mass, namely the specific SFR (sSFR), and serves as a proxy for the stellar birthrate parameter b–Scalo, which is the ratio of the present to past-average SFR (Kennicutt et al. 1994; Kennicutt 1998). Observationally, the EW$_{H\alpha}$ is defined as the Hα emission-line luminosity normalised to the adjacent continuum flux, effectively quantifying the SFR per unit luminosity (Kennicutt 1998). Given the relationship between EW$_{H\alpha}$ and surface mass density—a projection of the local mass-metallicity-EW relation ($\mathcal{M}$-Z-EW(Hα)) (Rosales-Ortega et al. 2012)—low EW$_{H\alpha}$ values ~ 1 correspond to very high surface mass densities $\Sigma_{Lum} > 10^3$ M$_\odot$ pc^{-2}, characteristic of early-type galaxies and the bulges of late-type galaxies. This corresponds precisely to the locus of the hDIG distribution at EW$_{H\alpha} \sim 1$Å (see Fig. 2 in Lacerda et al. 2018 and Fig. 9 in Lugo-Aranda et al. 2024).

In the low S/N regimes characteristic of the DIG, the low values of EW$_{H\alpha}$ employed to distinguish HOLMES from other regimes (EW$_{H\alpha}\sim$ 3Å) are highly contingent upon the stellar populations and the techniques utilised for SSP synthesis modelling (BETIS I). Moreover, as noted by (Tacchella et al. 2022), EW$_{H\alpha}$ is an inadequate tracer for discerning whether an Hα photon has originated in dense gas (H II region) or diffuse gas (DIG region). Crucial considerations must be acknowledged, as the EW – a non-additive, ratio quantity – is calculated over binned sections along the line-of-sight of the halos of galaxies, which exhibit significantly different depths and properties.

5.2.3 Hybrid SF and shocks ionisation mechanism of the eDIG

The detection of high ionisation states in the galactic halo of the MW and several other galaxies, either in emission (e.g. O^{5+}; Sembach & Savage 1992; Sembach et al. 2000) or absorption (e.g. O VI, N V, C IV; Jenkins & Meloy 1974; Pettini & West 1982; Hodges-Kluck & Bregman 2014; Hodges-Kluck et al. 2016), implies that interfaces between hot (10^6 K) and cooler ($\leq 10^4$ K) gas are prevalent throughout the ISM at significant z distances from the galaxies' midplanes. The gas at intermediate temperatures of $\sim 10^5$ K at these interfaces generates extreme ultraviolet (EUV) ionising radiation. The radiation of these hot-cool gas interfaces in the halo may constitute a significant source of ionising radiation for distant clouds and regions where Lyc ionising radiation from OB stars in the midplane is either shielded or absent.

Different types of interfaces have been proposed, each exhibiting distinct characteristics contingent on the physical processes and dynamical state of the boundary region between the hot and cooler gas. These include evaporative layers (e.g. Cowie & McKee 1977), cooling-condensation fronts (Shapiro & Benjamin 1991), and turbulent mixing layers (TML, e.g. Begelman & Fabian 1990; Slavin et al. 1993; Rand 1998; Collins & Rand 2001; Binette et al. 2009). Slavin et al. (1993) proposed that self-photoionisation through EUV line emission of collisionally excited gas in mixing layers (with a temperature $\sim 10^{5.0-5.5}$ K) between hot ($\sim 10^6$ K) and cold (~ 100 K) gas can reproduce many optical/UV/EUV emission line ratios as observed in the DIG of several galaxies. However, theoretical models for TML are intricate and may lead to over-ionisation of the hot gas and under-ionisation of the cool gas, contingent on the specific details of the models (Haffner et al. 2009b).

Shocks induced in the ISM by feedback mechanisms, such as supersonic winds originating from high-level SF regions, have been proposed as a significant source of heating for the eDIG[1] (Chevalier & Clegg 1985; Rand 1998; Collins & Rand 2001; Bland-Hawthorn et al. 2007). In this scenario, galactic winds are driven by the stellar winds and subsequent SNe of massive stars. These stellar winds create kpc-sized cavities in the ambient ISM on timescales of several million years (e.g. Mayya et al. 2023). Subsequently, these cavities are overrun by SN remnants (SNRs) from the most massive progenitor stars. Both processes occur at velocities exceeding the local sound speed, v_s, in the ISM, thereby generating strong shocks.

In an analogous way to TML, fast shocks induce comparable ionised conditions, characterised by an ionisation equilibrium between the hot and cold gas phases and slow mixing within the turbulent layer (Slavin et al. 1993; Rossa & Dettmar 2003b; Boettcher et al. 2019; Dirks et al. 2023). Given that shock heating is significant only if the kinetic energy is efficiently thermalised, both photoionisation and shocks can be regarded as "thermal" heating sources of the ISM. Crucially, the observed rising trend in the [O III] /Hβ emission line ratio with height can be expected as a mixing sequence between the predominant shock ionisation in the halo and photoionisation in the disk. Shocks, therefore, emerge as the most promising secondary ionisation mechanism for the eDIG.

In star-forming galaxies, large-scale winds driven by bursts of star formation in the galactic plane create extended wind-driven filaments present in the halo (Sato et al. 2009; Ho et al. 2016). The ionisation of these wind-blown filamentary structures is primarily dominated by

---

[1] Note that tidal interactions and AGN jets can also produce shock ionisation in the halos of galaxies, with similar effects as discussed in the text (e.g., Dopita & Sutherland 1995; Simpson et al. 2007; Rich et al. 2011; Ho et al. 2016; Molina et al. 2018).

fast shocks. This is because the final stages of the wind evolution, driven by star formation, are marked by a flare-up that overshadows the main ionising source, such as the star formation activity of the H II regions observed in the midplane (Sharp & Bland-Hawthorn 2010). For the same reason, the contribution of fast shocks to the ionisation of the eDIG is also expected to be less significant near the galactic plane (Sharp & Bland-Hawthorn 2010; Ho et al. 2016).

The role of fast shocks as a potential alternative ionisation mechanism for the eDIG, as well as the impact of these filaments in the halo, has been studied by several authors (Rand 1998; Collins & Rand 2001; Levy et al. 2019; Dirks et al. 2023). For example, Martin (1997) studied the excitation of the DIG in 14 SF dwarf galaxies, arriving to the conclusion that photoionisation does dominate the excitation of the DIG, and that shocks are only being invoked as a secondary signal in gas with very low surface brightness, require the largest relative contribution from shocks, up to 30-50% of the total emission.

As stated in the previous sections, the eBETIS sample presents diverse ionised structures in the halo, including filaments that extend more than 2 kpc from the midplane. Thus, we explore the combination of photoionisation from H II regions and ionisation due to fast shocks as simultaneous contributors to the ionisation mechanism of the eDIG. This is achieved by constructing a set of hybrid models that incorporate both star formation and fast shock mechanisms.

Firstly, considering the photoionisation models for low-metallicity star-forming galaxies of Levesque et al. (2010). The grids of this models predict the line ratios involved in the typical BPT diagram (Baldwin et al. 1981) for a pure photoionisation regime due to the star formation with ionisation parameters (q) ranging from 10^7 to $2{\cdot}10^8$ cm/s and metallicities (Z) from 0.001 to 0.04. Each model grid is computed for electron densities n_e of 10, 10^2, 10^3 and 10^4 cm^{-3}, assuming either continuous star formation or an instantaneous burst of star formation at 0 Myr.

And, on the other hand, considering the fast shocks models of Allen et al. (2008). This models predict the flux of the ionising radiation produced by a shock. The flux is dependent on the shock velocity ($f \propto v_s^3$). Therefore, if the shock velocity surpasses the velocity of the photoionisation front (in the case of a low ionisation parameter), the ionising photons are absorbed by the surrounding gas, altering its ionisation state. In another scenario, if $v_s \approx 170$ km/s, the ionisation front velocity now exceed the velocity of the shock, pre-ionising the surrounding gas and changing the optical emission lines observed (McKee & Hollenbach 1980). The fast shocks models of Allen et al. (2008) consider this two scenarios, with preshock densities ranging from 0.01 to 1000 cm^{-3}, shock velocities from 100 to 1000 km/s and magnetic field (B/n$^{1/2}$) from 10^{-4} to 100 μG·cm$^{3/2}$.

The hybrid models are constructed as follows: we consider both shock models, with and without assuming pre-ionisation. Then, for each shock model, we assume that the predicted flux corresponding to shock wind velocity of 200, 400, 500 and 1000 km/s and magnetic field of 10^{-4}, 1.0, 5.0 and 10 μG·cm$^{3/2}$ contributes only a fraction $f_{shock} \in [0, 1]$ of the total observed ionising flux. The remaining fraction 1 - f_{shock} corresponds to the flux predicted by a grid model with a certain ionisation parameter and metallicity from Levesque et al. (2010).

Figures 5.5 and 5.6 shows an example of hybrid models for the [N II] /Hα BPT, with Z = Z$_\odot$ and 2Z$_\odot$, q = 10^7, 4·10^7 and 2·10^8 cm/s, and f_{shock} = 0.5 and 0.3. It shows that decreasing f_{shock} shifts the models towards the OB-stars regime, as defined by the Kewley et al. (2001) curve, indicating that photoionisation by star formation becomes more significant in the hybrid models. Additionally, increasing the ionisation parameter in the models tends to flatten them vertically, resulting in higher predicted values for the high excitation [O III] /Hβ ratio. Besides, increasing the metallicity tends to expand the models, predicting a wider range of both [O III] /Hβ and [N II] /Hα ratios.

For instance, Figure 5.7 shows the BPT diagram for all the eDIG bins for IC1553[2]. The models plotted represent the predicted fluxes for a combination of fast shocks with pre-ionisation (black curve lines) and with front shock only (blue curve lines) weighted with f_{shock} = 0.4, plus a photoionisation model correspondent to Z = Z$_\odot$ and q = 10^7 cm/s, for instantaneous burst at 0 Myr and n_e = 100 cm^{-3}. Thus, the fluxes predicted for this particular hybrid models has the form: $F_{hyb} = 0.4F_{shock} + 0.6F_{SF}(n_e, q, Z)$. Solid curves correspond to the shocks winds from 200 to 1000 km/s, and dashed curves represents magnetic field intensities from 0.0001 to 10 μG·cm$^{3/2}$. The parameters were selected to best fit the points in the BPT diagram, particularly the [S II] /Hα and [O I] /Hα diagnostics, as they are more sensitive to changes in ionisation regimes. The points in the [S II] /Hα and [O I] /Hα diagnostics tend to deviate more from photoionisation models than the [N II] /Hα diagnostic if an additional source of ionisation, such as AGN or fast shocks, is present (Dirks et al. 2023).

The presence of shocks in the eDIG is further indicated by the asymmetric increase of [O I] /Hα with respect to height, as illustrated in Fig. 5.2 for IC1553 (and in the corresponding figures in the section 5.3 for the entire eBETIS sample). Given that neutral O and H are

---

[2] Note that these results do not concur with the diagnosis of Rautio et al. (2022) for this galaxy, whose BPT diagrams are predominantly populated within the star formation regime. However, they align more closely with the subsequent study by Dirks et al. (2023). The locus in all three panels of the BPT diagram corresponds with the findings of this latter study, being proximate to the Kewley et al. (2001) line for [S II] /Hα , and achieving values up to 0 (in log scale) for [O I] /Hα . Nevertheless, in comparison to both studies, it can be seen a greater number of data points in the high excitation regimes for [S II] /Hα and [O I] /Hα , corresponding to bins at larger distances. This can be attributed to the enhanced adaptive binning method, which enables sampling data with S/N > 2 at greater distances, and to the exclusion of bins situated within the galactic plane, as discussed in section 5.1.

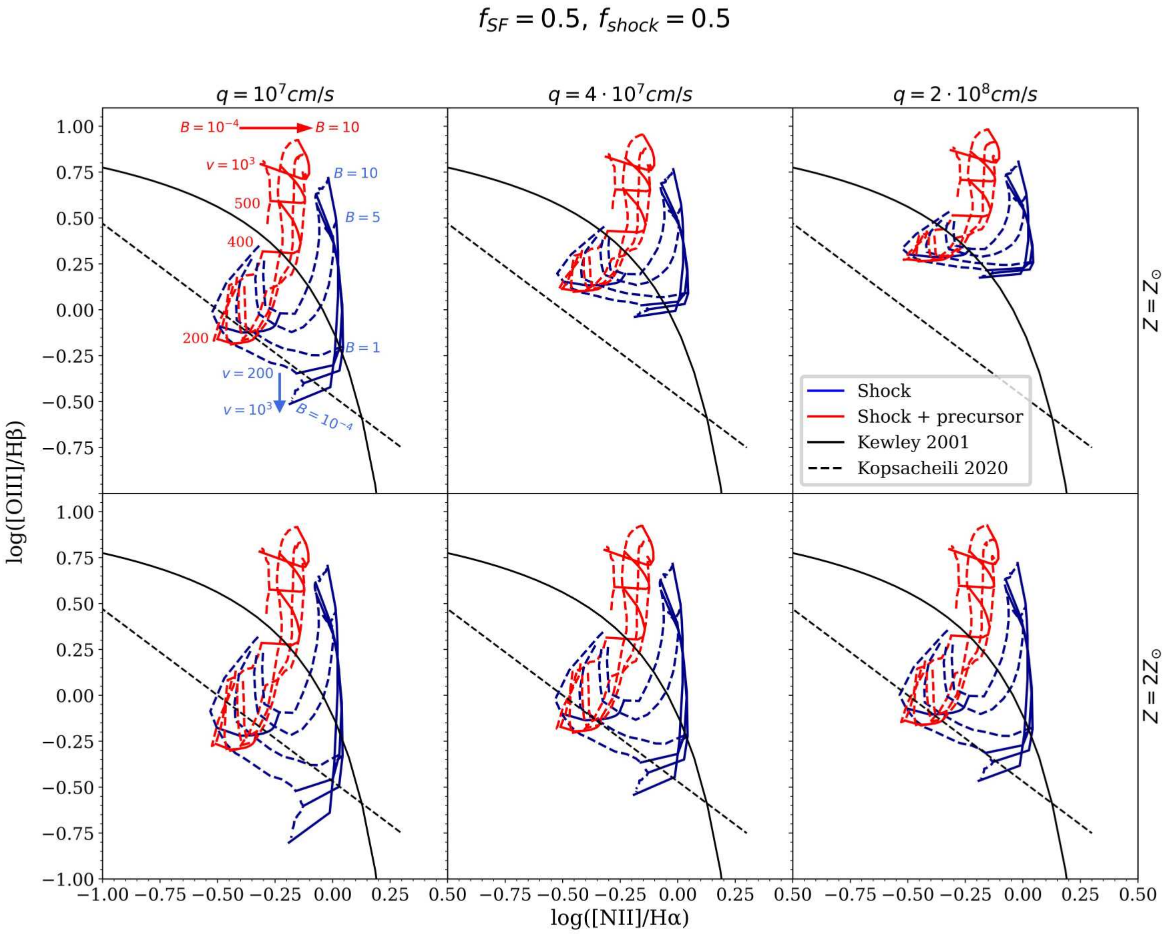

Figure 5.5: Showcase of the star formation + fast shocks hybrid models for the [N II] BPT, corresponding to the hybrid models with a contribution of fast shocks of 50% and 50% star formation. The fast shocks models from Allen et al. (2008) used correspond to shock velocities from 200 to 1000 km/s and magnetic fields from 10^{-4} to 10 in units of μG·cm$^{3/2}$, assuming shocks + a precursor (red curves) and only shocks (blue lines). The red arrow indicates the direction of increasing magnetic field in the shocks + precursor models, and blue arrow indicates the direction of increasing shock velocity in the shock only models. The dashed oblique line in the [N II] /Hα diagnosis represent the separation of shock excited (e.g. supernova remnants) from photoionised regions (e.g. H II regions) from Kopsacheili et al. (2020). The classic demarcation between H II regions photoionisation and AGNs from Kewley et al. (2001) is also plotted in all diagnoses. Every panel represent the hybrid models for a fixed metallicity and ionisation parameter: first and second row correspond to Z = Z$_\odot$ and Z = 2Z$_\odot$, first, second and third column correspond to q = 10^7, 4·10^7 and 2·10^8 cm/s respectively.

coupled via charge-exchange reactions, the observed increase in [O I] /Hα suggests a multiphase medium, characteristic of shock-compressed regions (Collins & Rand 2001; Boettcher et al. 2019).

The top-panel of Figure 5.8 shows the observed [S II] $_{\lambda 6717}$/[S II] $_{\lambda 6731}$ doublet ratio versus the [O I] $_{\lambda 6300}$/Hα line ratio for various binned sections in the halo of IC1553 at different

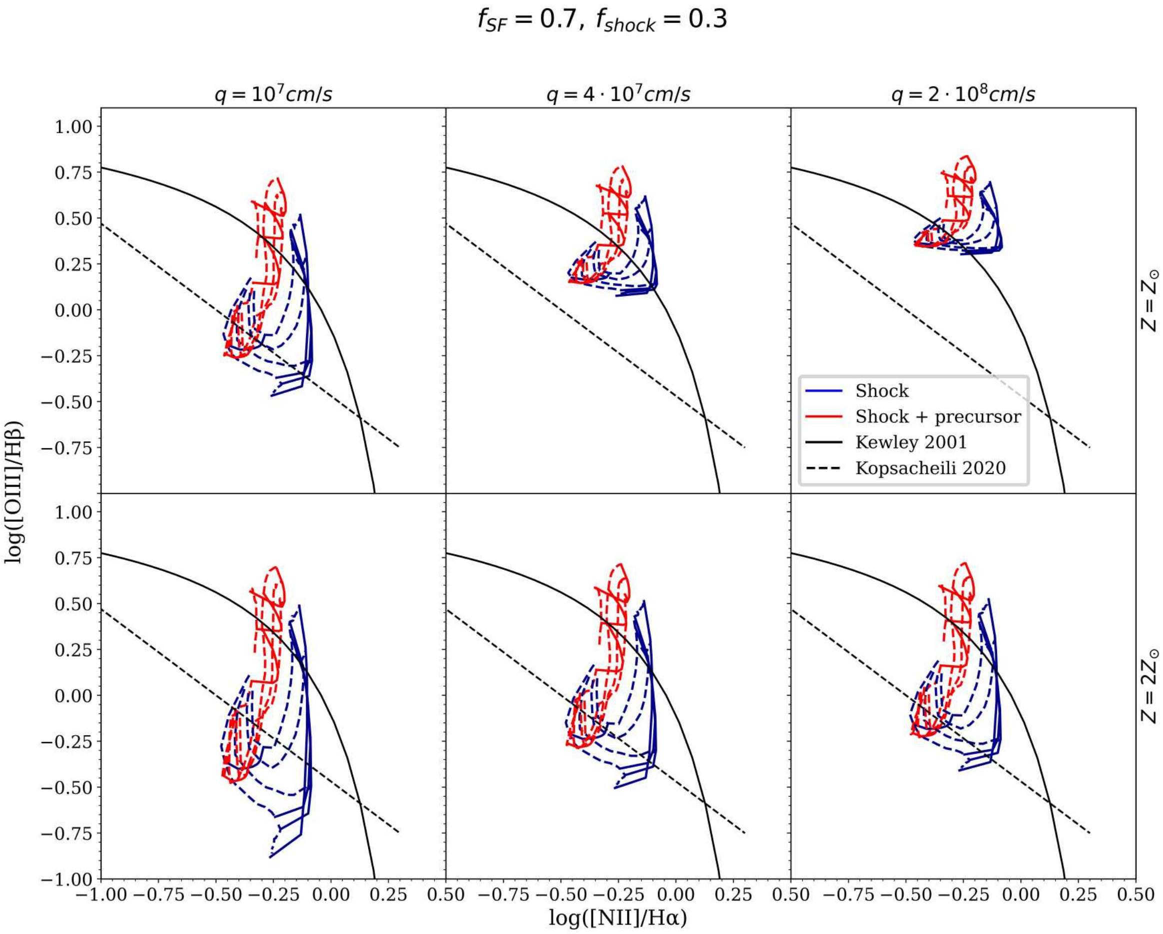

Figure 5.6: Showcase of the star formation + fast shocks hybrid models for the [N II] BPT, similar to 5.5, and corresponding to 30% shocks and 70% star formation.

galactocentric distances. The [S II] doublet is employed to infer the electron gas density; this ratio diminishes as the electron gas density increases, with a low-density limit of approximately 1.5, corresponding to an electron density of $n_e \leq 10$ cm^{-3} (Osterbrock & Ferland 2006). Most of the eDIG regions near the midplane of IC1553 exhibit [S II] line ratios close to this low-density limit, accompanied by low [O I] /Hα values, indicative of H II region emission. However, for bins corresponding to a higher altitude |z| from the midplane, the [S II] $_{\lambda 6717}$/[S II] $_{\lambda 6731}$ ratio decreases to values between 1.0 and 1.3, implying high electron densities in the range of $n_e \sim 200 - 800$ cm^{-3}.

The most striking feature of this figure is that the regions with low [S II] doublet ratios coincide with regions exhibiting high [O I] /Hα values (> 0.25), indicative of shock-compressed ionised gas. Therefore, the low doublet [S II] ratios, their implied high gas density, and the fact that these regions exhibit higher [O I] /Hα values are consistent with a scenario wherein gas emission originates from shocks, likely induced by feedback from high-level SF regions within the galactic disk. In this scenario, fast shocks can account for the increase in the [O I] /Hα ratio with distance from the midplane, with the highest [O I] /Hα ratios

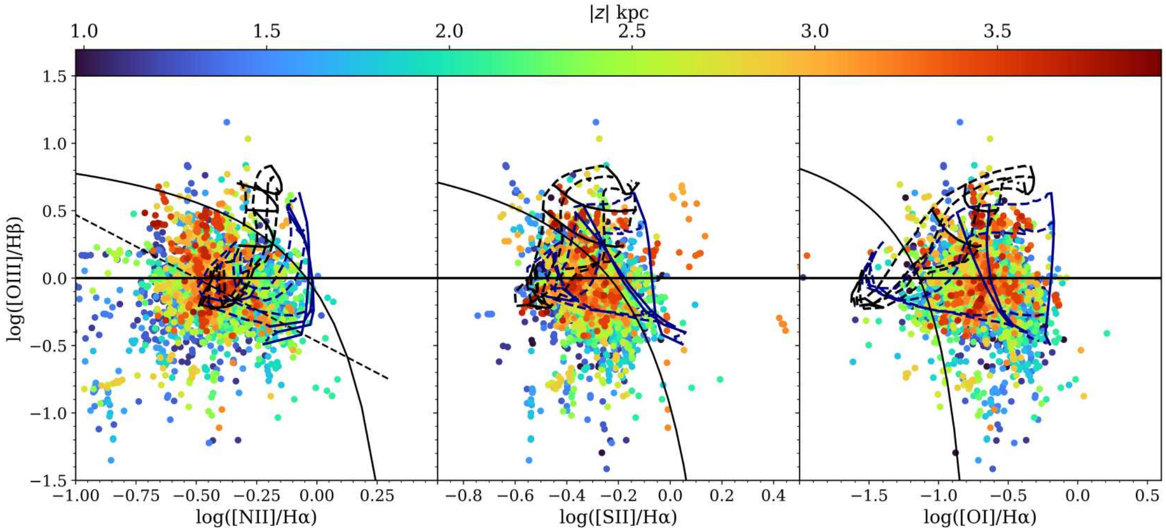

Figure 5.7: BPT for all eDIG bins of IC1553, with the colours coding the vertical distance (both above and below) from the midplane. The plotted hybrid models correspond to a 40% of the flux due to fast shocks with pre-ionisation (curves lines) and with front shock only (blue curves), and with the 60% of the flux due to star formation with Z = $Z_\odot$ and q = 10^7 cm/s. Solid curves correspond to the shocks winds from 200 to 1000 km/s, and dashed curves represents magnetic field intensities from 0.0001 to 10 μG·cm$^{3/2}$. The Kopsacheili et al. (2020) and Kewley et al. (2001) lines are also plotted, as in Figures 5.5 and 5.6.

corresponding to the shocked interface at the greatest distances from the midplane (this is also seen in the equivalent figures for the rest of the galaxies in the section 5.3). This picture can be further validated by comparing the high-density, high [O I] /Hα bins values of IC1553 to the hybrid SF-shocks models in the [O III] /Hβ vs. [O I] /Hα diagnostic diagram shown in the bottom panel of Figure 5.8. The triangles correspond to integrated bins of IC1553 at the minor-axis (MAD = 0 kpc, centred in the biconical structure seen in the [N II] /Hα map) and the squares to bins at 2.5 < MAD < 4.5 kpc, centred at the high-level SF region visible in the disk of the galaxy in Hα . The curves represent a hybrid model with a 60% star-formation and 40% shock contribution (without precursor), with Z = $Z_\odot$ and q = 10^7 cm/s. The parameter space of this specific hybrid model aligns precisely with the locus of the eDIG bins, corresponding to fast shocks between 400 and 600 km s^{-1} and magnetic field values in the range $B = 10^{-4}$– 5, regardless of the MAD distance and the diverse ionisation conditions observed in the halo in those regions.

These results align with recent numerical simulations of the DIG: Weber et al. (2019b) calculated the ionisation structure within the DIG, providing quantitative predictions for diagnostic optical emission lines using advanced 3D non-LTE radiative transfer simulations. These simulations assume ionisation by a matter-bounded stellar population SED, based on a plausible parameter space for the ionising sources (T_{eff}, Z), while considering varying escape fractions f_{esc} and clumpiness of the DIG. The findings support the scenario where

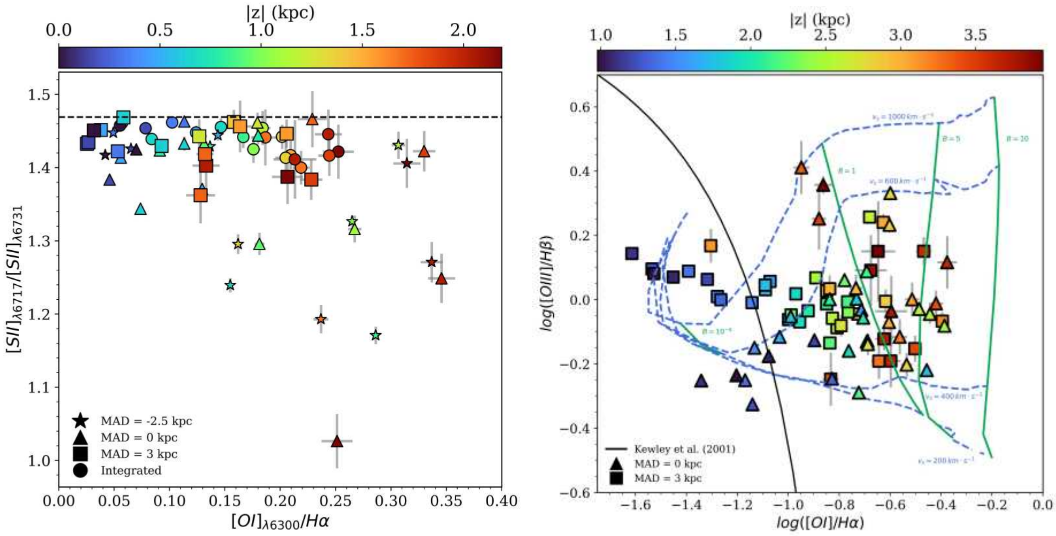

Figure 5.8: Left: Electron density sensitive [S II] $_{\lambda\,6717}$/[S II] $_{\lambda\,6731}$ line ratio vs. shocks-proxy [O I] $_{\lambda\,6300}$/Hα line ratio for IC1553. Dashed horizontal line represents the theoretical low-density limit for the [S II] doublet, corresponding to 1.469 (Osterbrock & Ferland 2006). Right: [O III] /Hβ vs. [O I] /Hα diagnostic diagram for the bins of IC1553 at the minor-axis, centred in the biconical structure seen in the [N II] /Hα map (triangles) and in the region between 2.5 < MAD < 4.5 kpc (squares), coincident with the high-level SF region visible in the disk of the galaxy. Curves represent the hybrid model for 40% shocks (without precursor) and 60% star formation with Z = $Z_{\odot}$ and q = 10^7 cm/s.

the DIG is primarily ionised by (filtered) radiation from hot stars within the galactic plane. Consequently, photoionisation heating results in higher temperatures in the DIG compared to H II regions, leading to stronger emissions of collisionally excited optical lines such as [N II] , [O I] , [O III] , or [S II] . However, these models do not account for the increasing [O III] /Hβ ratio at greater distances from the galactic plane, indicating the need for an additional ionising source. In this proposed SF-shock hybrid model, SF photoionisation is identified as the principal ionisation mechanism for the eDIG, while incorporating shock heating and collisional excitation as supplementary heating processes responsible for the observed increases in the [O III] /Hβ and [O I] /Hα ratios.

In summary, the ionisation of the eDIG is evidently not a phenomenon that can be elucidated by a single mechanism; rather, a multitude of mechanisms is necessary to fully comprehend the nature of the ionisation of extraplanar gas. Additionally, the ionisation mechanisms vary in significance across different galaxies. The prevailing consensus is that photoionisation predominantly governs the excitation of the eDIG, with shocks being considered a secondary source of ionisation. The spatial variation of line ratios, along with their absolute values, suggests the presence of shock excitation. Consequently, a model incorporating star-forming ionisation with shock ionisation as an additional heating source offers the most satisfactory explanation for the relatively high [O I] /Hα and [O III] /Hβ ratios observed in the lowest surface brightness regions as a function of distance from the midplane in edge-on star-forming galaxies.

5.3 Results

5.3.1 The radial variation of shocks contribution and the biconical structure of IC1553

The integration of emission-line ratio maps with hybrid SF+shock models for the eDIG facilitates a comprehensive analysis of the ionisation conditions within targeted regions of specific galaxies. In the case of IC1553, illustrated in the upper-right panel of Figure 5.1, there exists a distinct axisymmetric region with elevated [N II] /Hα ratios between -0.5 kpc < MAD < 0.5 kpc, centred on the galaxy's minor axis (MAD = 0). This enhanced region forms an apparent biconical structure that appears to emanate from the disk, extending to significant heights above and below the midplane $|z| \sim 3.5$ kpc in both the upper and lower halo of IC1553. This phenomenon is also visible in the [S II] /[N II] map, as depicted in Figure 5.9.

This structure was also identified by previous authors (Rautio et al. 2022; Dirks et al. 2023), who suggested that its origin could be attributed to a large off-centred galactic outflow or superbubble. (Rautio et al. 2022) described this feature as a biconical region of OB−shock ionisation caused by significant bidirectional outflows associated with superbubbles that have breached the disk. However, since there are no corresponding Hα emission enhancements in either the disk or the halo at the same spatial position as the biconical structure, they argue that the absence of a visible starburst responsible for the outflow is due to the starburst having quenched 20 Myr ago, or more. Dirks et al. (2023) support the biconical outflow scenario through indirect evidence based on Hα FWHM, which is sensitive to the velocity of gas flows in the presence of shocks. Nevertheless, the enhancement in Hα FWHM identified by Dirks et al. (2023) (see their figure 10) does not morphologically coincide with the [N II] /Hα or [S II] /[N II] structure observed in IC1553.

To elucidate the origin of this structure, we can examine the morphological information provided by the emission-line maps of IC1553, as presented in Figures 3.7 and 5.1. Firstly, as previously discussed, the distribution of H II regions in the galactic plane directly influences the morphology and ionisation conditions of the eDIG. The Hα map of IC1553 shows no evidence of a structure, outflow, or filaments extending from the galactic disk centred on or near the minor axis of the galaxy. Indeed, the strongest emission is observed at the boundaries of the high-level SF regions in the southern part of the galaxy, extending radially within a MAD range of 1.5 to 4.5 kpc, and vertically up to ≥ 3 kpc.

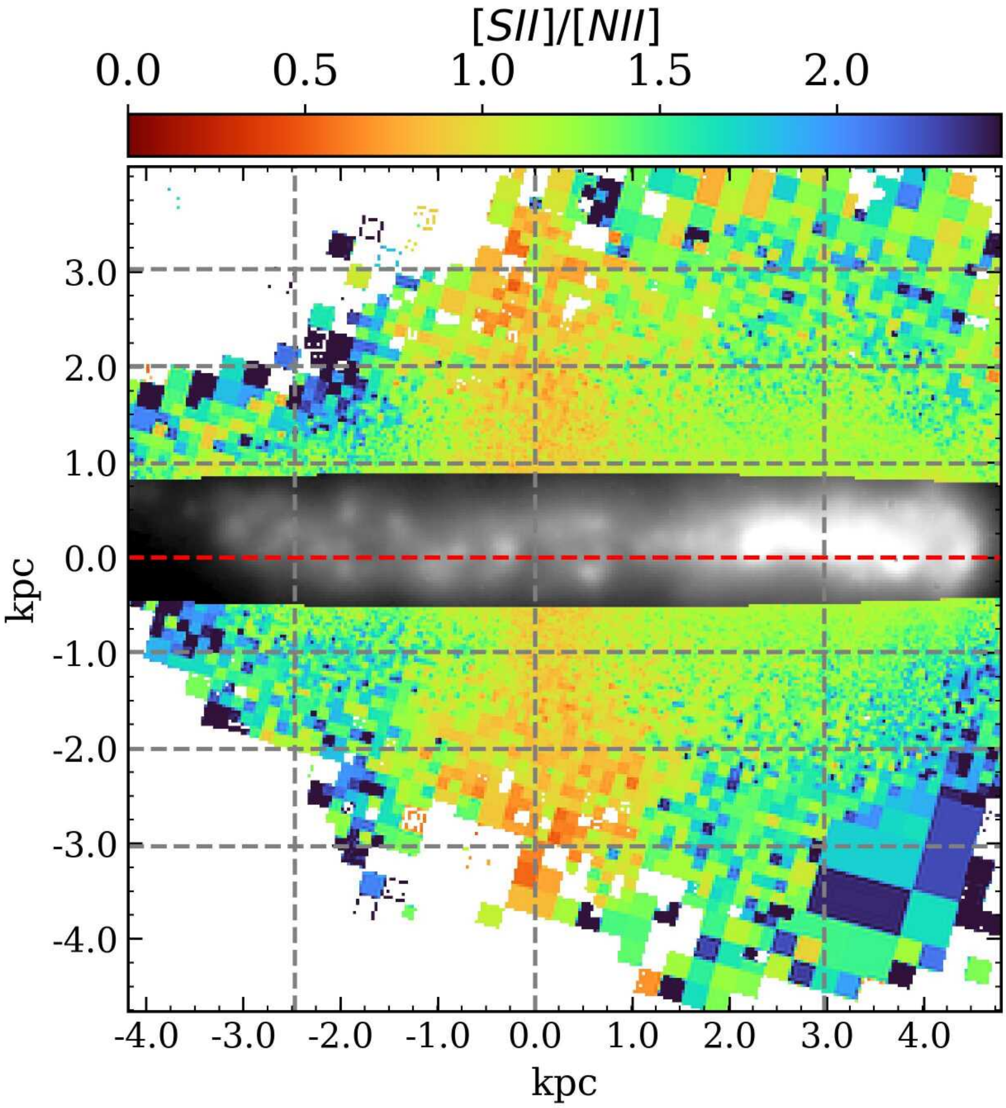

Figure 5.9: [S II] $_{\lambda\,6717}$/[N II] $_{\lambda\,6584}$ emission line map for IC1553. Vertical and horizontal lines represented as in Figure 5.1.

Secondly, while the structure in the [N II] /Hα emission-line map appears to symmetrically originate from the disk at the galaxy's minor axis (MAD ≈ 0 kpc), the [S II] /Hα map reveals a less defined biconical structure with a discernible offset at MAD ~ -1.2 kpc. This same structure is observed in the [S II] /[N II] map, but with an opposite offset at MAD ~ 0.2 kpc. Additionally, the upper part of the [O I] /Hα map hints at this structure, displaying an offset at MAD ~ -1.4 kpc relative to [N II] /Hα . Most strikingly, the [O III] /Hβ line-ratio map reveals no such structure on either side of the midplane. The high [O III] emission relative to H is a key observational feature of galactic outflows, regardless of whether its origin is due to SF (e.g. Tenorio-Tagle & Bodenheimer 1988; Norman & Ikeuchi 1989) or AGNs (e.g. López-Cobá et al. 2020; González-Díaz et al. 2024). The [O III] /Hβ map of IC1553 exhibits the typical increase of the ratio with distance from the midplane in a homogeneous manner, independent of radial distance, but without any characteristic signature of an outflow at MAD $\sim$ 0. Therefore, based on the information provided by the 2D distribution of the eDIG, there is no morphological congruence among the different emission-line maps to definitively confirm the existence of an outflow in IC1553.

The [S II] /[N II] map can also elucidate the origin of this structure. Given the similar ionisation potentials of [S II] and [N II] (10.4 eV and 14.5 eV, respectively), [S II] /[N II] is largely independent of electron temperature. Consequently, variations in [S II] /[N II] imply changes in local ionisation conditions or metallicity (since nitrogen is a secondary nucleosynthetic product while sulphur is a primary product) but primarily reflect variations in S^+/S (Haffner et al. 2009b). In a photoionisation model, [S II] /[N II] is expected to increase with distance from the ionising source, aligning qualitatively with a smooth transition from predominantly doubly ionised to singly ionised states ($S^{++} \rightarrow S^+$), as expected in dilute photoionisation models (e.g. low ionisation parameters, q, Domgorgen & Mathis 1994. The consistency of [S II] /[N II] suggests an additional heating source (Reynolds & Cox 1992; Rand 1998; Reynolds et al. 1999; Collins & Rand 2001), which in the models would be provided by shocks. Indeed, in the Allen et al. (2008) models, shocks naturally produce a lower [N II] flux relative to [S II] compared to photoionisation. In IC1553, we observe a symmetrical increase in the [S II] /[N II] ratio across all galactocentric distances, from values of approximately 1.2 near the galactic disk, up to values ≥ 2, except in the region associated with the biconical structure at a MAD of approximately 0.2 where [S II] /[N II] remains nearly constant at around 0.9 but decreases with height to values around 0.5. An increase in the [S II] /[N II] ratio with height has also been observed at two slit positions perpendicular to the edge-on galaxy NGC 5775 (Boettcher et al. 2019). The overall scenario depicted by the [S II] /[N II] ratio map suggests that sulphur and nitrogen are ionised by a photoionisation field that diminishes with height, yet with localised deficits or enhancements of either [S II] or [N II] , indicating local changes in ionisation conditions within the complex eDIG halo, likely due to shocks.

To further explain the structures observed in IC1553, the hybrid SF-shock models can be applied as previously described. Figure 5.10 depicts the same BPT diagram as in Figure 5.7, but limited to the bins of the biconical structure identified in the [N II] /Hα map. Specifically, it shows bins between -0.5 kpc < MAD < 0.5 kpc (top) and bins between 2.5 kpc < MAD < 3.5 kpc (bottom), corresponding radially to the regions above and below the bright SF regions near the southern edge of the disk. In these latter regions, outside the biconical structure, the hybrid models that best fit the data indicate 80% of the ionisation is due to star formation and 20% to shocks. For regions within the biconical structures, at MAD $\sim$ 0 kpc, the contribution from star formation decreases, with shocks becoming relatively more significant (increasing from 20% to 40%). Hence, while the contribution of shocks within the biconical structure is augmented, the increase is modest; SF remains the predominant source of ionisation, and the emission-line ratios do not exhibit the high [O III] /Hβ values characteristic of a galactic outflow.

The absence of distinct filamentary, outflow-like structures in both the Hα flux and the [O III] /Hβ emission-line ratio maps, the observed offsets, and the conflicting morphology between the [N II] /Hα , [O I] /Hα , and [S II] /[N II] ratios, combined with the lack of direct spatial correlation between the biconical structure and any potential ionisation sources within the disk, and the evidence indicating that the primary ionisation within the structure is attributed to SF photoionisation, suggest an alternative interpretation for the biconical structure observed in the [N II] /Hα ratio map. As discussed throughout this paper, the nature and morphology of the eDIG are directly influenced by the local level of SF within the disk, which drives the feedback mechanisms responsible for ionising the gas in the surrounding vicinity.

From the Hα flux map of IC1553, the high-level star-forming (SF) regions at a MAD between 2 and 4 kpc appear to be very near the edge of the galaxy's disk. Consequently, the halo line-of-sight line ratios in the vicinity of these regions resemble those of H II regions (e.g., [N II] /Hα ≤ 0.4). This effect is more pronounced in the [O III] /Hβ and [O I] /Hα maps, where high [O III] /Hβ values (≥ 1.5) and low [O I] /Hα values (≤ 0.1) are observed immediately above and below the bright H II regions on the plane at 2 < MAD < 4 kpc. A common observational challenge in edge-on galaxies is the invisibility of individual SF regions in the optical spectrum due to the high optical depth for both blue continuum and Hα line emission. This likely occurs at MAD ≥ -2 kpc, where no bright H II regions are visible on the galaxy disk in the Hα flux map. Nevertheless, the [N II] /Hα , [S II] /Hα , [O I] /Hα , and [O III] /Hβ line ratios above and below the galaxy plane in this galactocentric range resemble those near the bright H II regions at MAD > 2 kpc. At the minor axis (MAD = 0 kpc), the galaxy disk is expected to show a lower average star formation rate (SFR) along the line-of-sight due to the presence of the galaxy's bulge, compared to the rest of the galaxy disk. Consequently, the line emission strength near the galaxy's centre would be dominated by the strong emission from the bright visible H II regions to the south of the galaxy (2 < MAD < 4 kpc) and by obscured H II regions on the galaxy disks at projected distances $-1 <$ MAD < -4 kpc.

In this scenario, the biconical structure observed in [N II] /Hα could be an optical artefact, arising from high typical [N II] /Hα eDIG background values (≥ 0.5) due to the overall feedback processes in the galaxy disk (SF+shocks), and low [N II] /Hα values (≤ 0.4) from the bright and obscured H II regions near the minor axis of the galaxy. This results in H II region-like emission in the vicinity of the galactic plane. This scenario is more evident in the [S II] /Hα and [O I] /Hα maps, where the background emission clearly permeates the

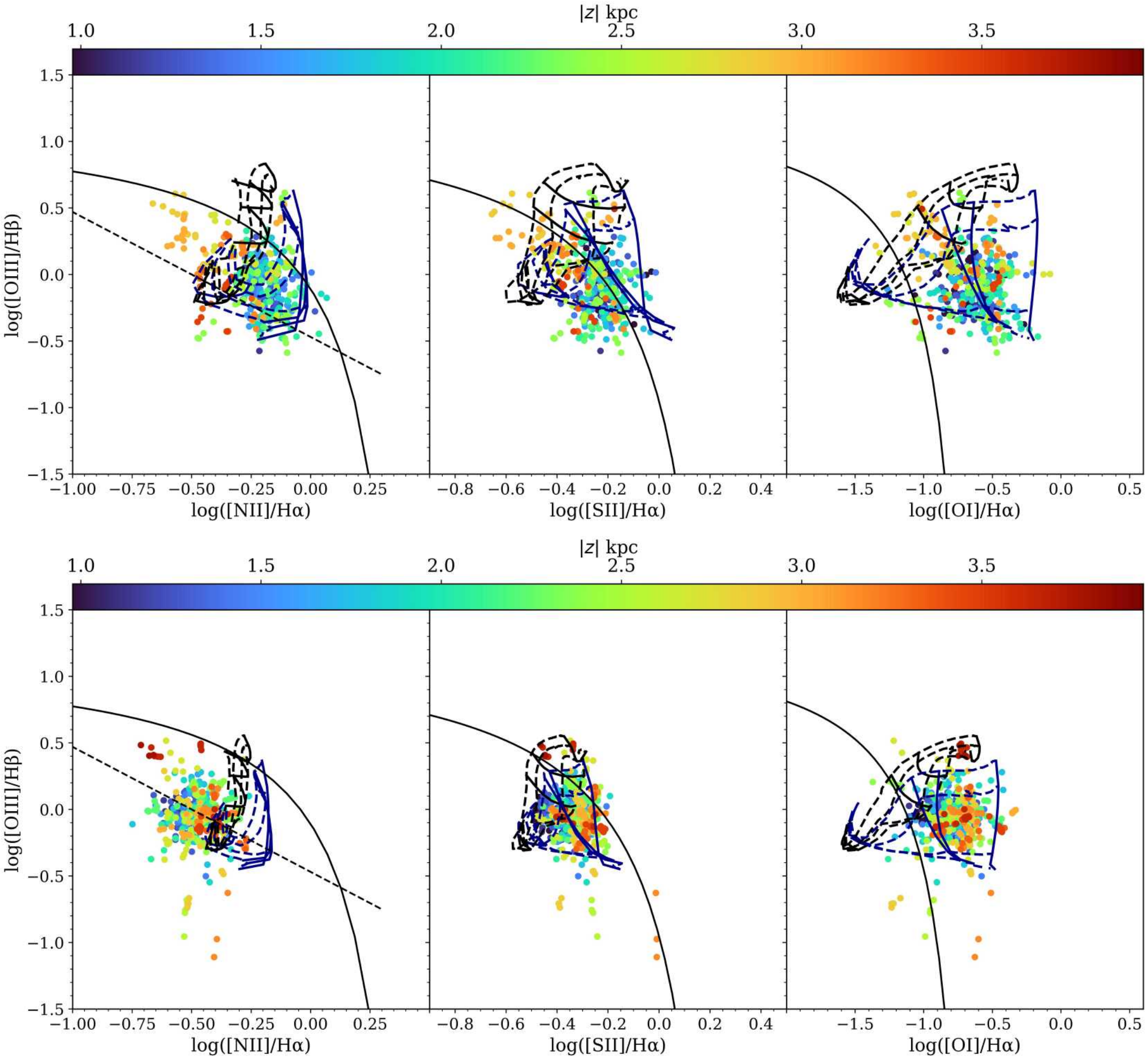

Figure 5.10: IC1553 BPT with hybrid models, similar to Figure 5.7. Top: eDIG bins corresponding to the biconical structure seen in the [N II] /Hα map, between -0.5 kpc < MAD < 0.5 kpc. The hybrid models that best fit the data correspond to 40% shocks and 60% SF with Z = $Z_{\odot}$ and q = 10^7 cm/s. Bottom: eDIG bins corresponding to the high-SF feature on southern edge of the disk, between 2.5 kpc < MAD < 3.5 kpc. The hybrid models that best fit the data correspond to 20% shocks and 80% SF with Z = $Z_{\odot}$ and q = 10^7 cm/s.

halo with typical eDIG values, and the strong emission from the adjacent H II regions is seen in projection, exhibiting typical H II region values. This interpretation accounts for the offset of the biconical structure between the [N II] /Hα and [S II] /Hα maps, as S and N present similar but distinct ionisation potentials, shedding light on the structure of the [S II] /[N II] line-ratio map. It also explains the absence of filaments or outflow features in both the Hα flux and [O III] /Hβ line-ratio maps.

In the case of the biconical structure of IC1553, it becomes evident that results obtained from the global analysis of a galaxy should not be generalised. Limiting the analysis to specific regions reveals that the ionisation mechanisms present in the eDIG can vary. This finding aligns with previous observations in BETIS I: a group of galaxies exhibiting diverse physical processes can lead to misleading conclusions about the ionisation mechanisms of the DIG. Furthermore, even within a single galaxy, when the resolution is sufficiently high, a global (BPT) analysis of the eDIG can still be misleading, as it encompasses regions of the galaxy that display distinct physical processes and ionisation conditions.

In general, the linkage between the star formation activity in the disk and the ionisation of the eDIG is evident in all galaxies. The entire sample shows the same tendencies, with the $\Sigma_{H\alpha}$ distribution in the plane and the line ratios distribution being anti-correlated. Additionally, the increase in T_e with distance from the midplane and the increase in S^+/S at those MADs corresponding to lower $\Sigma_{H\alpha}$ in the midplane are also general behaviours in the sample. However, each galaxy can present differences in the ionisation structure of the eDIG due to the presence of morphological structures in the halo or asymmetries in the disc. This can cause the contribution of fast shocks to the ionisation budget of the eDIG to vary in different zones of the halo.

5.3.2 *PGC28308*

At a distance of 45.22 Mpc, PGC28308 is the most distant galaxy in the sample (Kashibadze 2008). Since all galaxies in the sample have the same total exposure time (except IC217; Com19), this results in lower S/N, a higher average bin size (175.4 pc), and a greater loss of information after performing the S/N and relative error cutout (see section 2.3).

These cutouts left us with data up to $|z| = 2.5$ kpc between -4.5 kpc $\lesssim$ MAD $\lesssim 1.5$ kpc, and $|z| < 1.5$ kpc at MAD < -4.5 kpc for the [S II] /Hα and [N II] /Hα line ratio maps (Figure 5.11).

This data demonstrate that the trend of line ratios is consistent with what is found in the rest of the galaxies, reaching minimum values where the $\Sigma_{H\alpha}$ is maximum, and with the [S II] /Hα and [N II] /Hα ratios increasing in height, reaching values of 0.7 and 1.1 respectively (see Figure 5.12). The [O III] /Hβ ratio remains approximately constant around 1.0 for $|z| >$ 0.7 kpc and, for the [O I] /Hα ratio, the distribution remains flat at 0 for $z < -1$ kpc, probably due to the low S/N of the [O I] line, but reaches values of ~ 0.08 at $z > 0.7$ kpc. In all cases, the squares, triangles, and stars representing the height distributions at MAD = 0, -3, and -9 kpc, respectively, follow a similar trend as the integrated distribution, which is also in line with what is observed in the rest of the galaxies. The radial dependence of the line ratios is not as clear as for the case of IC1553 by only considering Figure 5.12. However, a clearer scenario can be seen in Figure 5.13. Both [S II] /Hα and [N II] /Hα distributions consistently show higher ratios at $z = 2.5$ than at $z = 1.5$. Moreover, the differences between

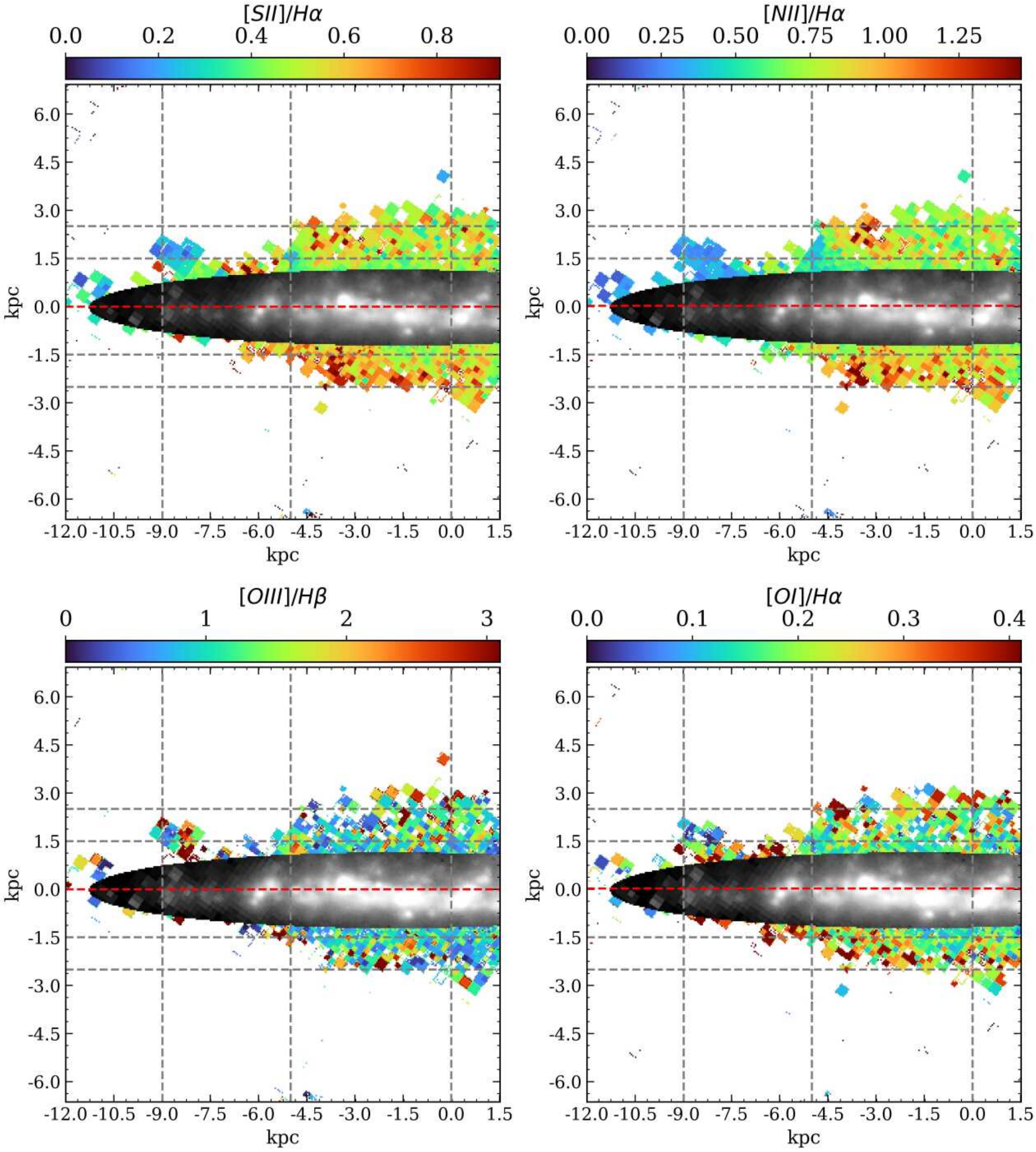

Figure 5.11: PGC28308 line ratio maps, similar to Figure 5.1. The grey dashed lines indicates the heights with respect the midplane z = ±1.5, ±2.5 and major axis distances MAD = -9, -5, 0 kpc.

these distributions becomes more pronounced as the $\Sigma_{H\alpha}$ reaches higher values (at MAD∼-3 kpc and MAD∼0.5 kpc. Examination of the MAD distributions also reveals the bidimensional structure of the eDIG, as the positions of relative maxima shift when the height increases in both [S II] /Hα and [N II] /Hα distributions.

As the sampling of this galaxy is lower due to the resolution and S/N cutouts, Figure 5.15 (left) does not show a dependence of the T_e with |z| as clear as for IC1553. However, it is clear the dependence of the MAD with the ionisation ratio S^+/S. At MAD = 0 kpc (squares)

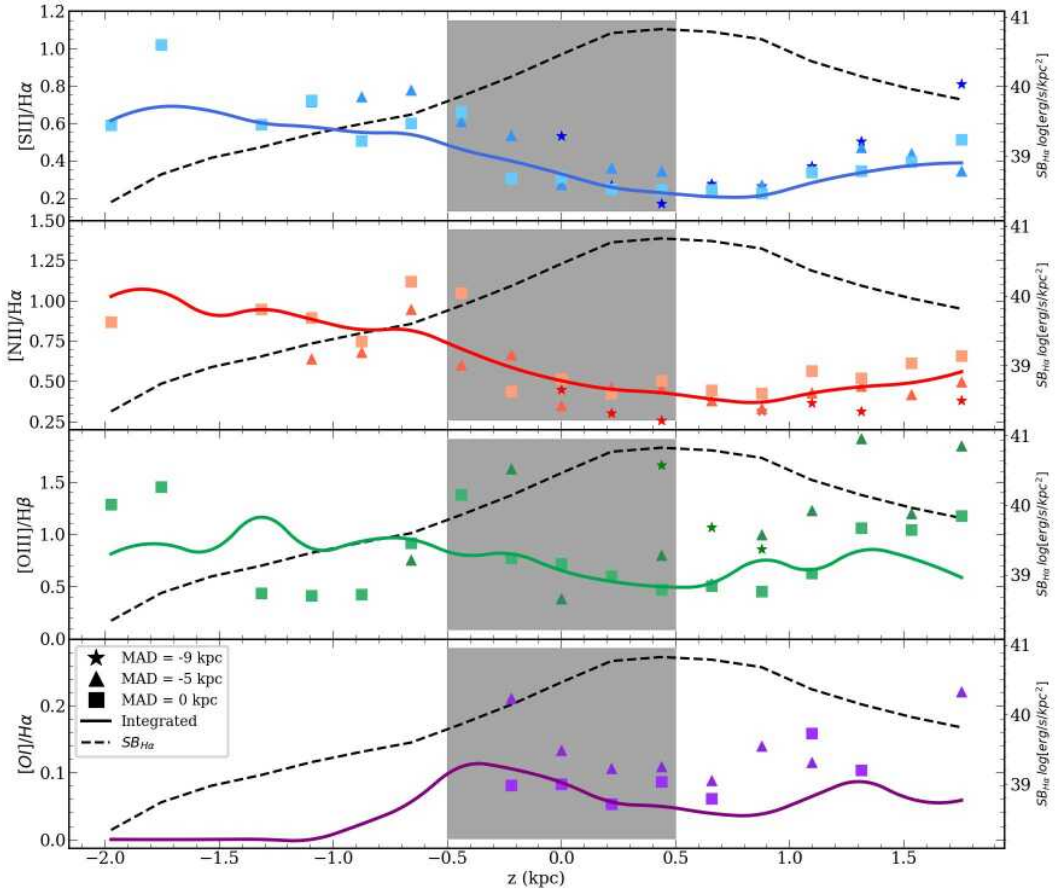

Figure 5.12: PGC28308 line ratio distributions of the with respect the distance from the midplane. Similarly to Figure 5.2, for MAD = -9 (stars), -5 (triangles) and 0 (squares) kpc.

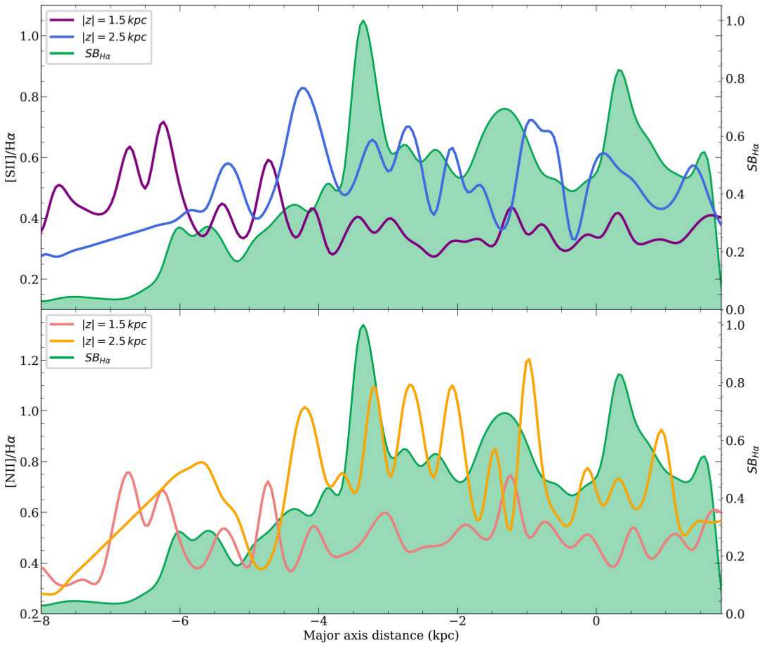

Figure 5.13: PGC28308 MAD distribution for z = 1.5 and 2.5 kpc.

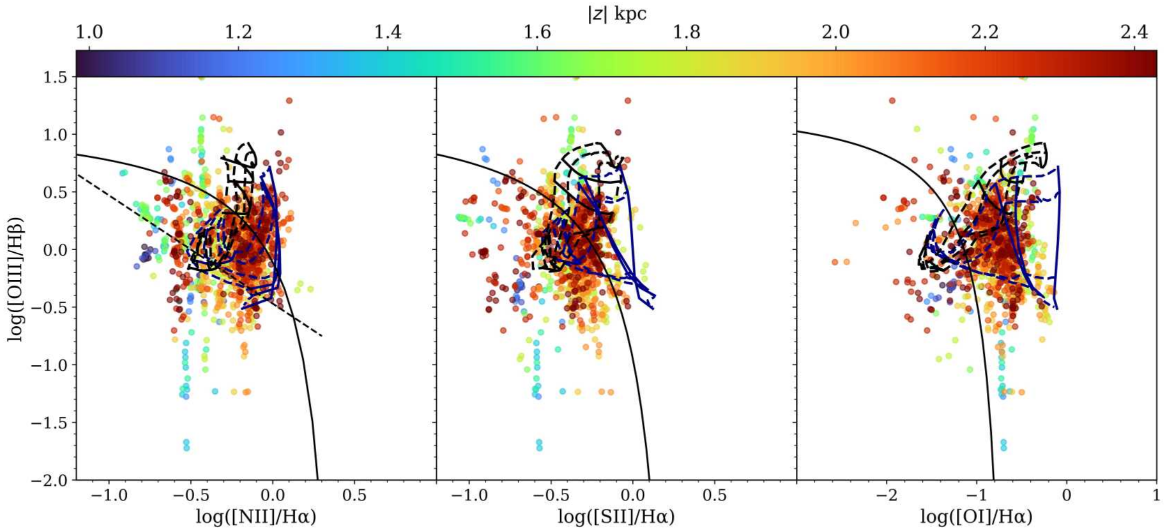

Figure 5.14: PGC28308 BPT with hybrid models, similar to Figure 5.7. 50% fast shocks and 50% star formation with Z = $Z_\odot$ and q = 10^7 cm/s.

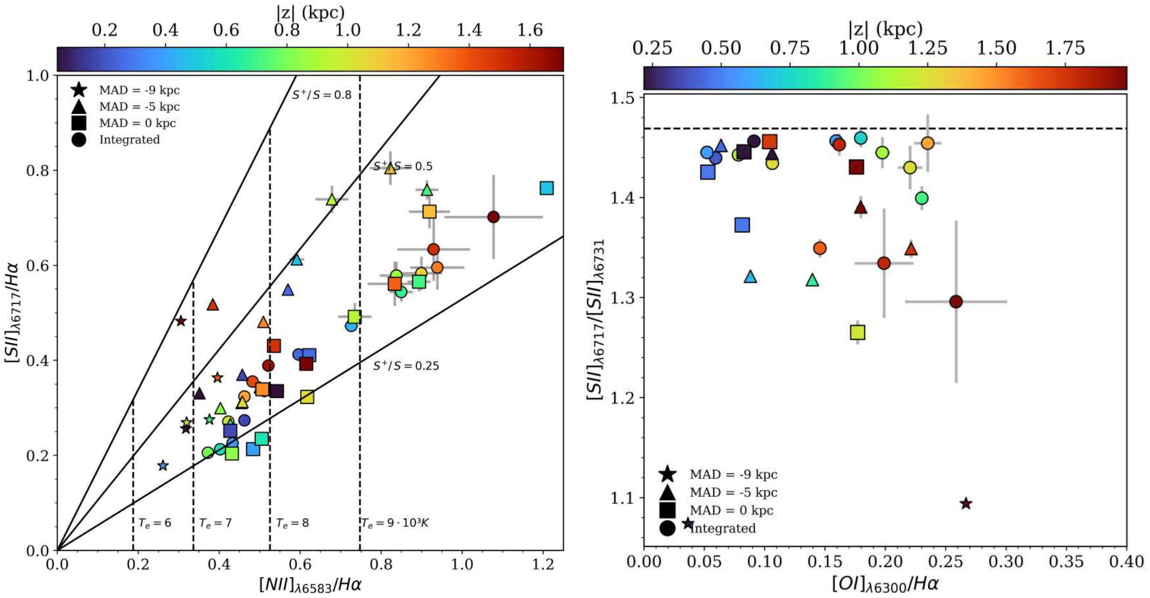

Figure 5.15: Left: PGC28308 [N II] $_{\lambda6583}$/Hα vs.[S II] $_{\lambda6717}$/Hα. Similarly to Figure 5.4, for MAD = -9 (stars), -5 (triangles) and 0 (squares) kpc. Right: PGC28308 [S II] $_{\lambda6717}$/[S II] $_{\lambda6731}$ vs. [O I] /Hα. Similar to Figure 5.8.

$S^+/S \sim 0.3$, in contrast with MAD = -5 kpc (triangles), with $S^+/S \sim 0.5$. Although both MAD are within zones of the galactic plane exhibiting high $\Sigma_{H\alpha}$, Figure 5.11 shows that the emission from H II regions is displaced relative to the line of sight. Specifically, the H II regions nearest to the -1.5 line at MAD = 0 kpc, indicating that the eDIG below the galactic plane at that MAD is highly ionised due to ongoing star formation. This ionisation leads to a reduction in the S^+/S ratio and consequently enhances the S^{++}/S ratio (Baluja et al. 1980; Haffner et al. 1999; Osterbrock & Ferland 2006). In general, the eDIG bins are located in the BPT diagram between both classical regimes of star formation and AGN (see Figure

5.14). The hybrid models that best fit the data correspond to 50% of ionisation due to fast shocks, and 50% star formation with Z = $Z_\odot$ and q = 10^7 cm/s. Similar to IC1553, the presence of fast shocks is further supported by the decrease in the [S II] doublet ratio (indicating an increase in electron density) as the [O I] /Hα ratio increases (figure 5.15 right). This trend is correlated with the distance from the midplane, despite the limited sampling of this galaxy.

5.3.3 PGC30591

As PGC28308, PGC30591 is a late-type spiral galaxy, although it is relatively closer in comparison (de Vaucouleurs et al. 1991). This results in a higher S/N and better data sampling after implementing the cutouts of 2.3, with bins reaching |z| up to 2 kpc between -1.5 kpc < MAD < 3 kpc. From the line of sight, the distribution of H II seems homogeneous along the major axis, but with a brighter region between 1 kpc < MAD < 2 kpc, near to the limit of z = 0.5 kpc (see Figure 5.16). The influence of this region causes a clear decrease in the [N II] /Hα , [S II] /Hα and [O I] /Hα line ratios between z = 0.5 kpc and z = 1.5 kpc in comparison with the rest of the eDIG (see Figure 5.16).

Figure 5.17 shows the same anti-correlation than in the other cases; the line ratios reaching minimum values where the $\Sigma_{H\alpha}$ is maximum, and increasing in height. [N II] /Hα and [S II] /Hα remains approximately flat at z < - 1 kpc, reaching values of 0.3 and 0.6, respectively, but continuing to increase beyond these values at z > 1 kpc. [O I] /Hα also increases up to 0.1 at |z| = 1 kpc and then deceases dramatically. The [O III] /Hβ distribution remains flat around 0.6 for |z| < 1 kpc, and reach ~ 1 at |z| > 1 kpc. The distributions at MAD = 0, 1.25 and 2.5 kpc (stars, triangles and squares respectively) follow the same trend that the integrated distribution, as for the rest of the galaxies.

Additionally, the distribution of triangles, where the most luminous star-forming regions are located in the plane, consistently exhibits lower line ratios compared to the other distributions. This aligns with what has been observed for IC1553 (see section 5.1). This can also be seen in the MAD distribution (Figure 5.18). In addition to the typical increase in the value of the line ratios at higher heights observed in all galaxies of the sample, between 1 kpc < MAD < 2 kpc, where the surface brightness of $\Sigma_{H\alpha}$ reaches its maximum values, both line ratios for both heights decrease.

Furthermore, the difference between the distributions for z = 0.7 kpc and 1.5 kpc becomes maximum for the [S II] /Hα ratio (similarly to IC1553, with up to 0.5 dex). It can also be seen a shift in the relative maxima of the [N II] /Hα MAD distribution (more pronounced than for PGC28308) between 1 kpc < MAD < 2 kpc: where the $\Sigma_{H\alpha}$ distribution reaches its maximum at MAD $\simeq$ 0.4 kpc, the [N II] /Hα distribution at z = 0.7 kpc reaches its relative maximum

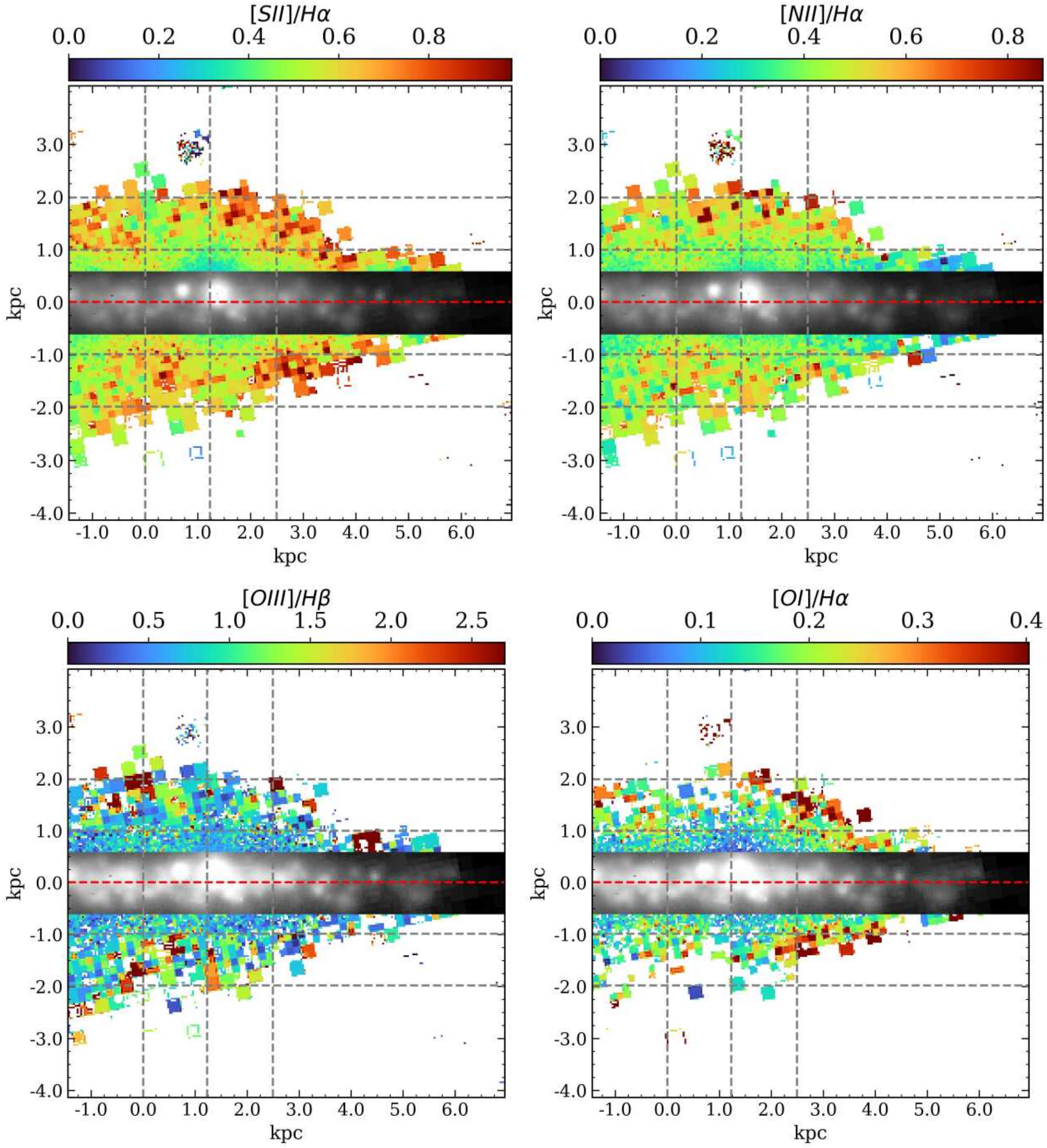

Figure 5.16: PGC30591 line ratio maps, similar to Figure 5.1. The grey dashed lines indicates the heights with respect the midplane z = ±1, ±2 and major axis distances MAD = 0, 1.25, 2.5 kpc.

(0.45) in that interval at MAD ≃ 0.55 kpc, and for z = 1.5 kpc, the relative maximum (0.65) is reached at MAD ≃ 0.7 kpc. This shift of ∼ 0.15 kpc can also be observed in the absolute maximum at MAD ≃ 0.5 kpc. Thus, this shift in the MAD distribution for different heights may be attributed to the spherical structure of ionisation between z = 0.5 kpc and z = 1.5 kpc, situated above the brighter star-forming region between 1 kpc < MAD < 2 kpc (see Figure 5.16).

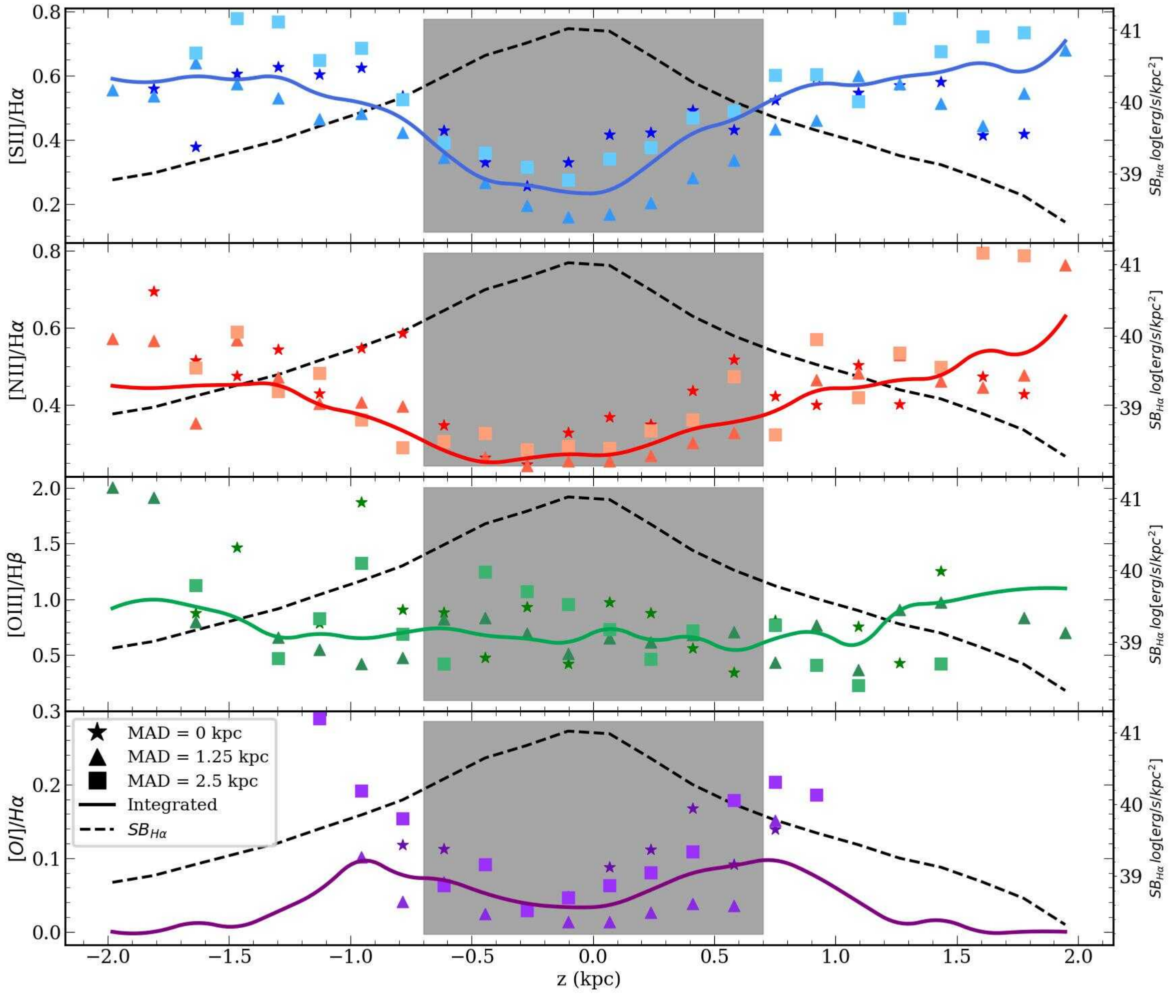

Figure 5.17: PGC30591 line ratio distributions of the with respect the distance from the midplane. Similarly to Figure 5.2, for MAD = 0 (stars), 1.25 (triangles) and 2.5 (squares) kpc.

In Figure 5.20 (left), the T_e follows a dependency on |z|, increasing linearly with respect to the distance from the midplane and reaching values up to $9 \cdot 10^3$ K. This result is also consistent with the findings in IC1553 and other authors (Reynolds 1985; Madsen & Reynolds 2005). However, the ionisation fraction S^+/S does not seem to exhibit strong differences for different MADs, as all the points for S^+/S fall between approximately 0.35 and 0.8. Since the differences in the Hα emission of the galactic plane at differences MADs is not that pronounced (not as IC1553 at least), is expected Figure 5.20 to be more similar to PGC28308 (Figure 5.15 left) than IC1553 (Figure 5.4), and S^+/S to be mixed at different distances from the midplane. Similar results are expected for the BPT diagram (Figure 5.19). The best fit hybrid models correspond to 40% of ionisation due to fast shocks, and 60% star formation with $Z = Z_\odot$ and $q = 10^7$ cm/s. In this case, the dependence on height is more evident, as there is not a strong mixture of different ionisation conditions, and the data sampling due to S/N is better than for PGC28308. The figure illustrates that the points nearest to the galactic plane

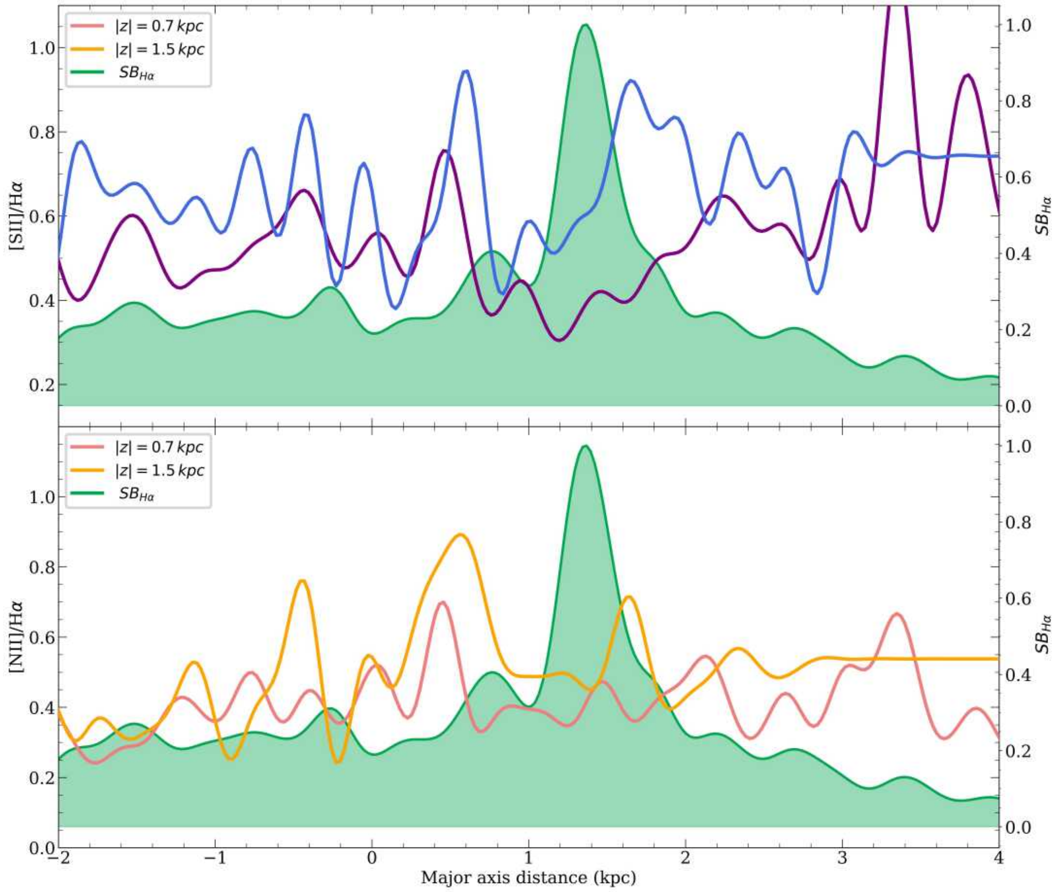

Figure 5.18: PGC30591 MAD distribution for z = 0.7 and 1.5 kpc.

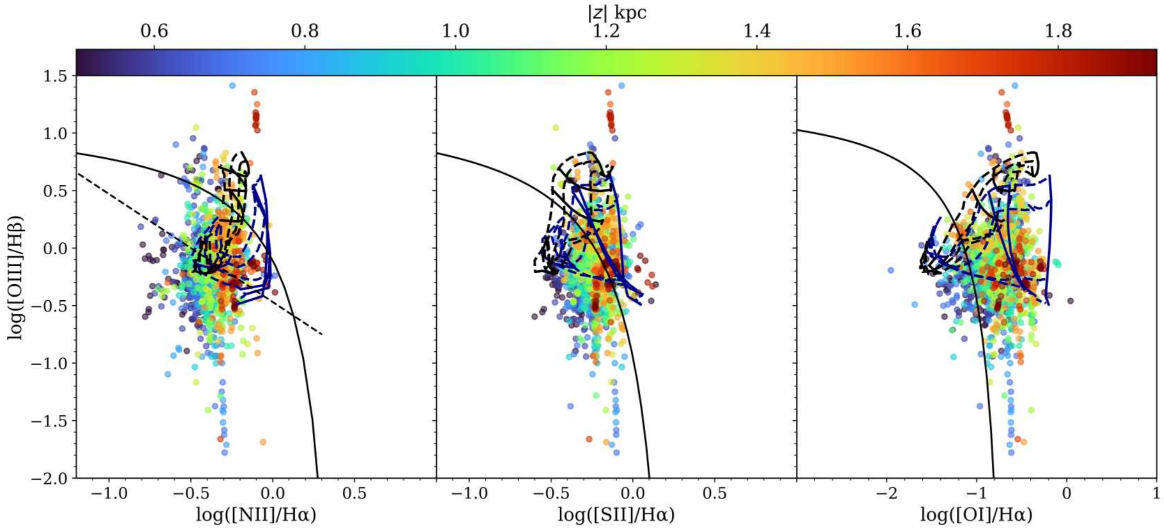

Figure 5.19: PGC30591 BPT with hybrid models, similar to Figure 5.7. 40% fast shocks and 60% star formation with Z = $Z_\odot$ and q = 10^7 cm/s.

tend to align closer to the classical star-forming regime of the BPT diagram, and vice versa. The presence of fast shocks is further supported by the decrease in the [S II] doublet ratio (indicating an increase in electron density) as the [O I] /Hα ratio increases (figure 5.20 right),

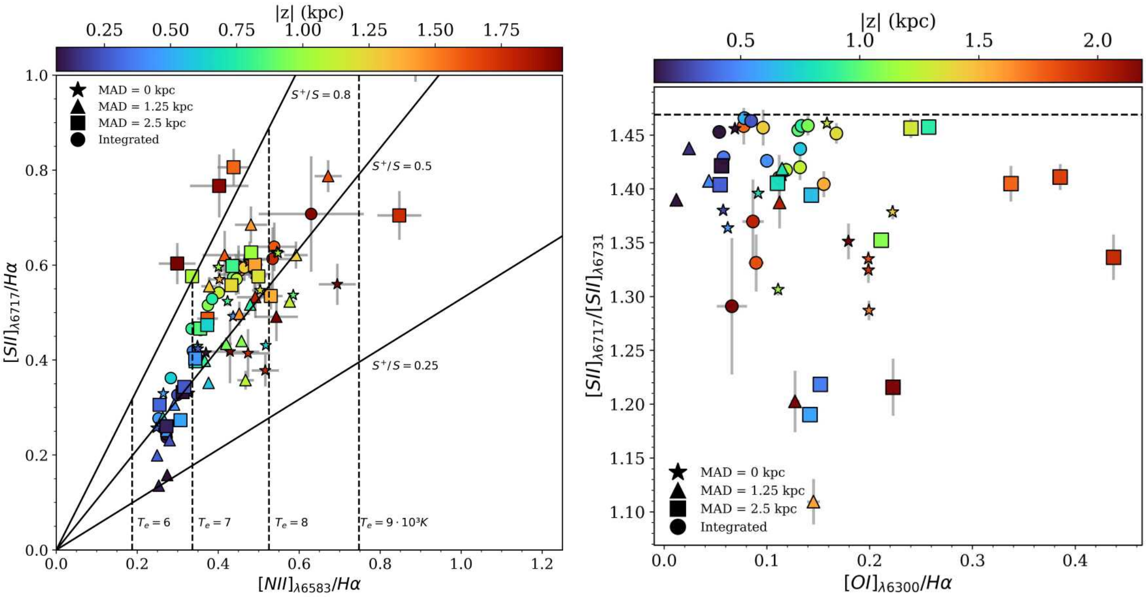

Figure 5.20: Left: [N II] $_{\lambda\,6583}$/Hα vs. [S II] $_{\lambda\,6717}$/Hα for PGC30591. Similarly to Figure 5.4, for MAD = 0 (stars), 1.25 (triangles) and 2.5 (squares) kpc. Right: [S II] $_{\lambda\,6717}$/[S II] $_{\lambda\,6731}$ vs [O I] /Hα for PGC30591. Similar to Figure 5.8.

being this trend clearly correlated with the distance from the midplane.

5.3.4 ESO544-27

ESO544-27, along with ESO469-15, is the most edge-on galaxy in the sample, with $i = 90°$. classified as an Sb galaxy (Mitronova et al. 2004), exhibits a more homogeneous emission from the galactic plane, mildly symmetric with respect to the centre of the galaxy, at MAD = 0 kpc. In consequence, the eDIG line maps exhibits the same symmetry (see Figure 5.21), being evident the increase in the line ratios with respect to the distance from the midplane solely by examining the maps.

The height distributions of the line ratios (Figure 5.22) show the same behaviour than in the rest of the galaxies. The line ratios reach minimum values where the $\Sigma_{H\alpha}$ is maximum, and increase in height, up to 0.8 for [S II] /Hα , 0.9 for [N II] /Hα and 1.5 for [O III] /Hβ . [O I] /Hα reaches ~0.1 at |z| = 1 kpc and then falls dramatically. The stars, triangles and squares distributions were strategically selected to be, respectively, in the middle of two star-forming regions (MAD = -2 kpc), the centre of the galaxy (MAD = 0 kpc) and in the middle of a star forming region (MAD = 2 kpc). All distributions are similar, but the stars at MAD = -2 kpc present lower [N II] /Hα , specially at higher distances from the midplane. In general, all points are mixed between them, showing no clear differences in the height distributions between different MADs. The MAD distribution (Figure 5.23) shows precisely the homogeneity in the eDIG; the [N II] /Hα and [S II] /Hα distributions remains basically flat along the major axis at both heights, being more consistent the difference between the distributions at both heights. This strengthens the evidence regarding the direct effect of the galactic plane on the ionisation structure of the eDIG. Furthermore, within the ranges of -4 kpc < MAD < -2 kpc and 3 kpc < MAD < 4 kpc, where the $\Sigma_{H\alpha}$ is lower, the disparities between the distributions at both heights are maximal for both [N II] /Hα and [S II] /Hα distributions. This consistency aligns with findings in other galaxies of the sample.

The homogeneity in the eDIG for this galaxy is also evident in figures 5.25 (left) and 5.24. The T_e increases lineally with the distance from the midplane, up to $\sim 10^4$ K, and all the points remain close to the diagonal line corresponding to $S^+/S = 0.5$. Also, in the BPT, the hybrid models that best fit the data correspond to 50% of ionisation due to fast shocks, and 50% star formation with $Z = Z_\odot$ and $q = 10^7$ cm/s. As for PGC30591, the dependence on height is more evident, as there is not a strong mixture of different ionisation conditions, with the points nearest to the galactic plane tending to align closer to the classical star-forming regime of the BPT diagram, and vice versa. Similar to the rest of the galaxies, the presence of fast shocks is further supported by the decrease in the [S II] doublet ratio (indicating an increase in electron density) as the [O I] /Hα ratio increases (figure 5.25 right), being this trend is correlated with the distance from the midplane.

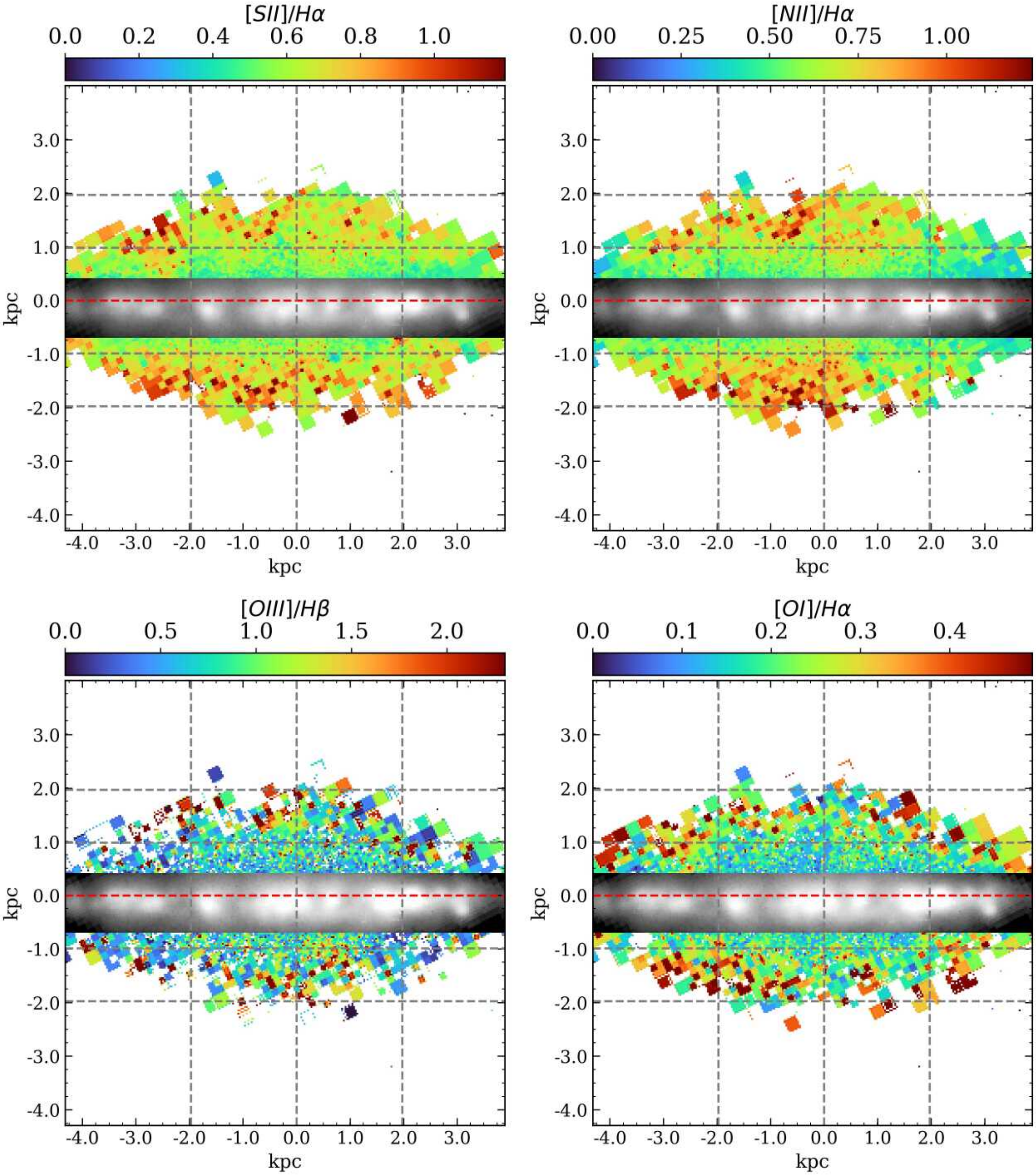

Figure 5.21: ESO544-27 line ratio maps, similar to Figure 5.1. The grey dashed lines indicates the heights with respect the midplane z = ±1, ±2 and major axis distances MAD = -2, 0, 2 kpc.

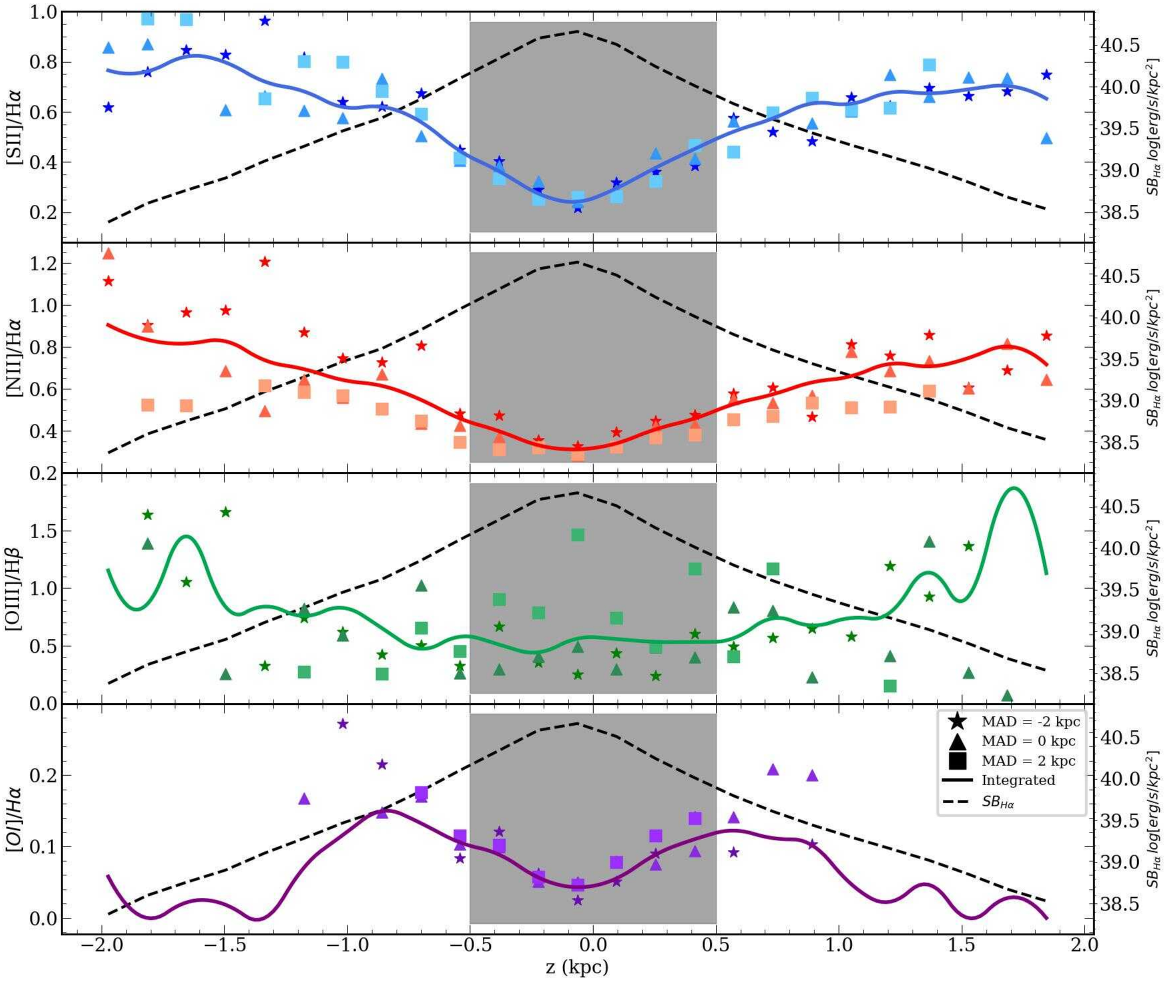

Figure 5.22: ESO544-27 line ratio distributions of the with respect the distance from the midplane. Similarly to Figure 5.2, for MAD = -2 (stars), 0 (triangles) and 2 (squares) kpc.

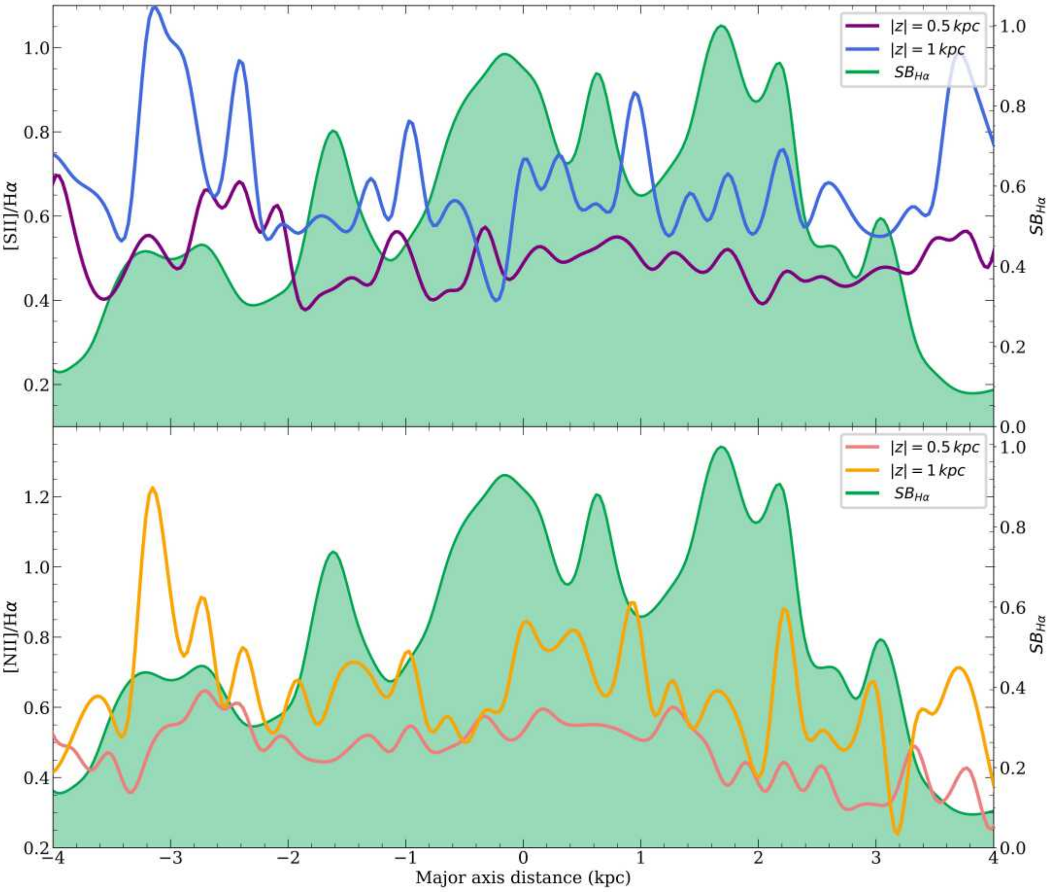

Figure 5.23: ESO544-27 MAD distribution for z = 0.5 and 1 kpc.

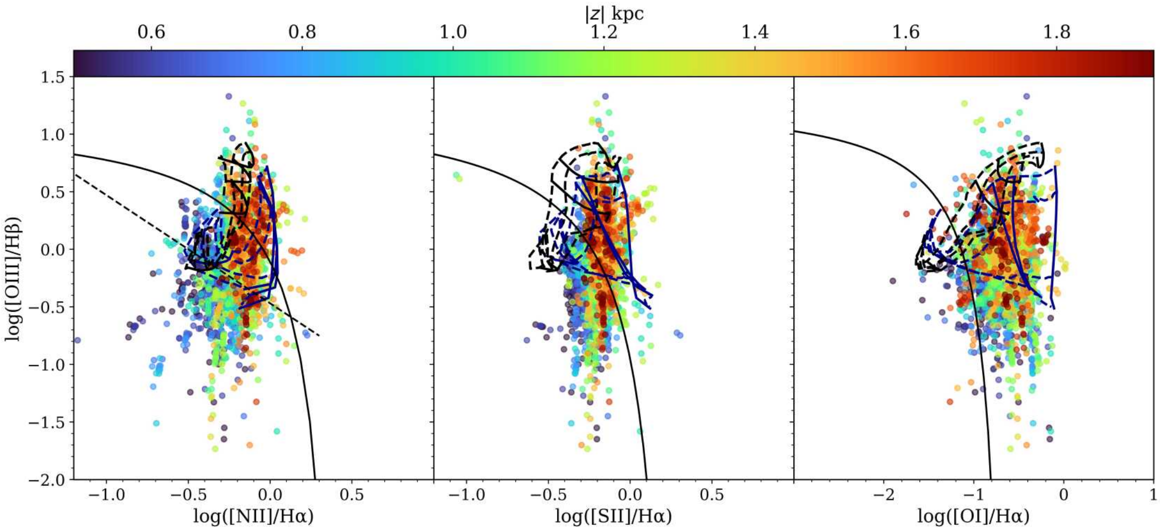

Figure 5.24: ESO544-27 BPT with hybrid models, similar to Figure 5.7. 50% fast shocks and 50% star formation with Z = $Z_\odot$ and q = 10^7 cm/s.

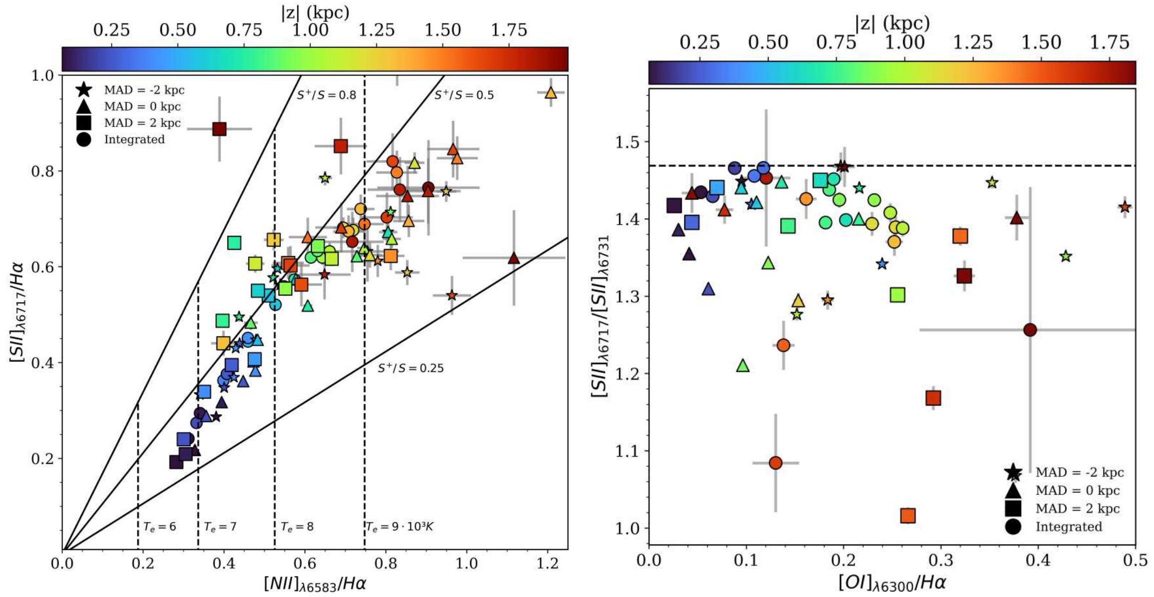

Figure 5.25: Left: [N II] $_{\lambda 6583}$/Hα vs. [S II] $_{\lambda 6717}$/Hα for ESO544-27. Similarly to Figure 5.4, for MAD = -2 (stars), 0 (triangles) and 2 (squares) kpc. Right: [S II] $_{\lambda 6717}$/[S II] $_{\lambda 6731}$ vs [O I] /Hα for ESO544-27. Similar to Figure 5.8.

5.3.5 ESO443-21

The late-type galaxy ESO443-21, along with the irregular galaxy IC1553, stands out as one of the most peculiar galaxies in the eBETIS sample. The excellent S/N of the data for this galaxy enables us to sample the extraplanar gas up to a distance of 4.5 kpc from the midplane. This sampling and high S/N ratio have enabled us to detect a broad knot-shape filamentous structure at a distance of 1.5 kpc, extending up to a height of 4.5 kpc within the range of -1 kpc < MAD < 2.5 kpc. This is evident not only in the Hα map of Figure 3.7, but also when examining the emission line maps in Figure 5.26, where the structure is clearly visible as a filament characterised by low [S II] /Hα and [N II] /Hα ratios.

The presence of this knot significantly influences the overall behaviour of the line ratio distributions and the ionisation structure of the eDIG. Figure 5.27 shows that greater distances from the midplane, the [S II] /Hα and [N II] /Hα ratios deviate from the observed tendency to increase in other galaxies, and instead begin to decrease at $|z| \lesssim 2.5$ kpc. Between 2 kpc < z < 4 kpc, where the filament is located, the decrease is more gradual, with a slight increase in the ratios observed at $z \simeq 3$ kpc. The stars distribution at MAD = 0 kpc consistently falls below the other distributions, particularly between 2 kpc < z < 4 kpc, exhibiting differences of up to 0.6 dex for the [S II] /Hα ratio and 0.4 for the [N II] /Hα ratio. This emphasises the significant impact of the filament on the ratios. In Figure 5.28, the MAD distributions show the impact of the filament as well. The differences in the distributions between z = 1.5 kpc and z = 3 kpc for both line ratios are higher compared to the rest of the galaxies, mainly because of the larger difference in the selected heights. At z = 1.5 kpc, both [S II] /Hα and [N II] /Hα ratios remain relatively flat. However, at z = 3 kpc, the line ratios experience a significant decline at MAD < 2 kpc, reaching levels typical of the eDIG close to H II regions found in other galaxies. This effect is particularly notable for [S II] /Hα , which drops from 0.9 to 0.2, reversing the trend of increasing line ratios with height.

In Figure 5.29 (left), the general trend again indicates an increase in electron temperature with height. However, for the circles representing the integrated fluxes along the major axis, this trend disappears. The S^+/S fraction remains approximately constant at 0.5 but increases in height up to 0.8 for greater distances from the midplane. This finding is consistent with what can be observed in other galaxies: a higher S^+/S ratio when the distance from the H II regions is greater, indicating an ionisation regime favouring collisions. Additionally, for the stars corresponding to MAD = 0 kpc and between 1.5 kpc < z < 3.5 kpc (where the knot is located), the S^+/S ratio drops to ~ 0.3, suggesting a regime more similar to ionisation due to star formation.

This last figure suggests an asymmetry in the ionisation of the eDIG due to the filament, indicating different regimes when considering z < 0 or z > 0. To verify this, the BPT diagrams

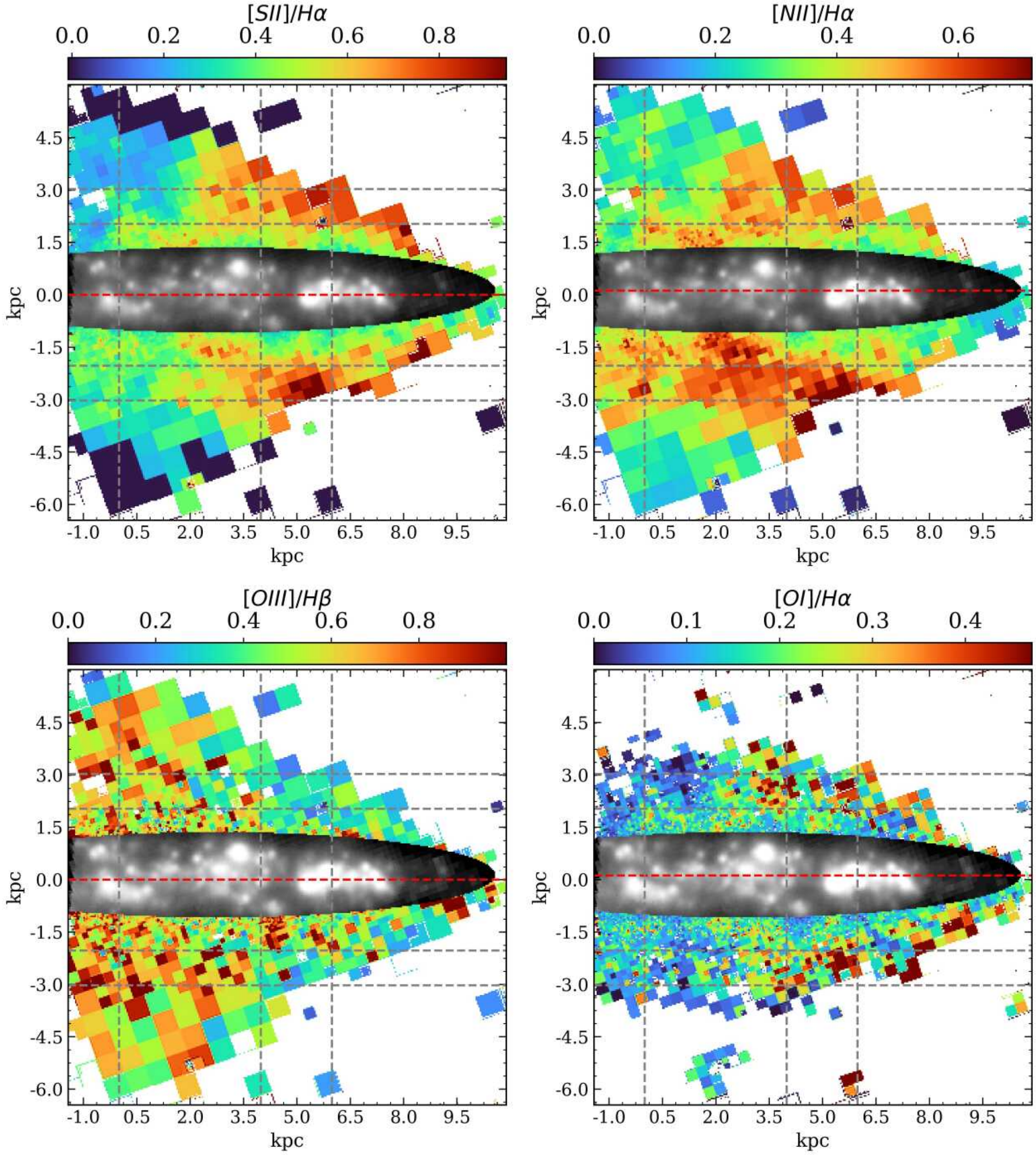

Figure 5.26: ESO443-21 line ratio maps, similar to Figure 5.1. The grey dashed lines indicates the heights with respect the midplane z = ±2, ±3 and major axis distances MAD = 0, 4, 6 kpc.

are presented with the hybrid models separately for z < 0 and for z > 0. The best fit hybrid models for the points at z > 0 correspond to 20% of ionisation due to fast shocks, and 80% star formation with $Z = 2Z_{\odot}$ and $q = 10^7$ cm/s. For z < 0 correspond to 30% of ionisation due to fast shocks, and 70% star formation with the same parameters. The presence of the knot only affects an additional contribution of star formation to the overall ionisation mechanisms by up to 10%. As for the rest of the galaxies, the presence of fast shocks is further supported

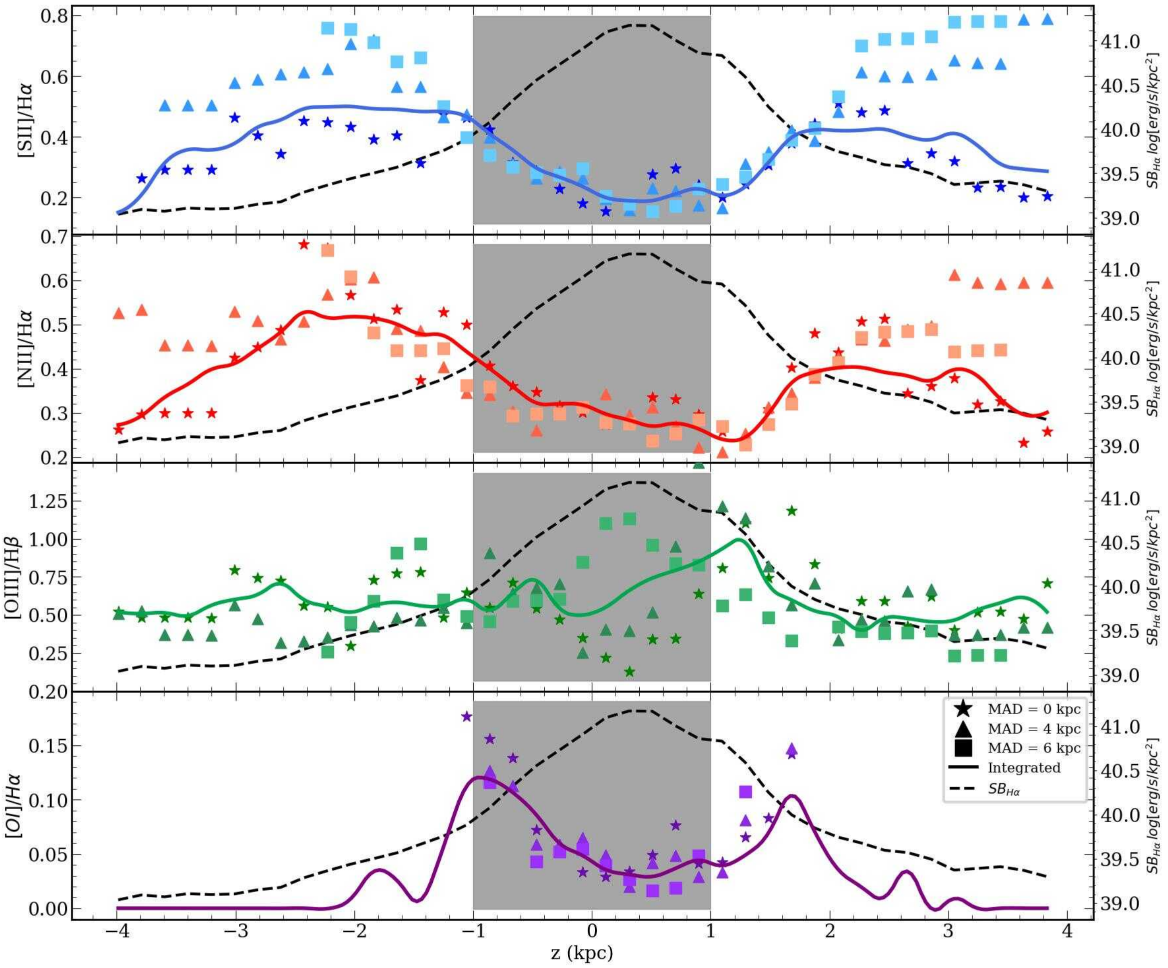

Figure 5.27: ESO443-21 line ratio distributions of the with respect the distance from the midplane. Similarly to Figure 5.2, for MAD = 0 (stars), 4 (triangles) and 6 (squares) kpc.

by the decrease in the [S II] doublet ratio (indicating an increase in electron density) as the [O I] /Hα ratio increases (figure 5.29 right), being this trend is correlated with the distance from the midplane.

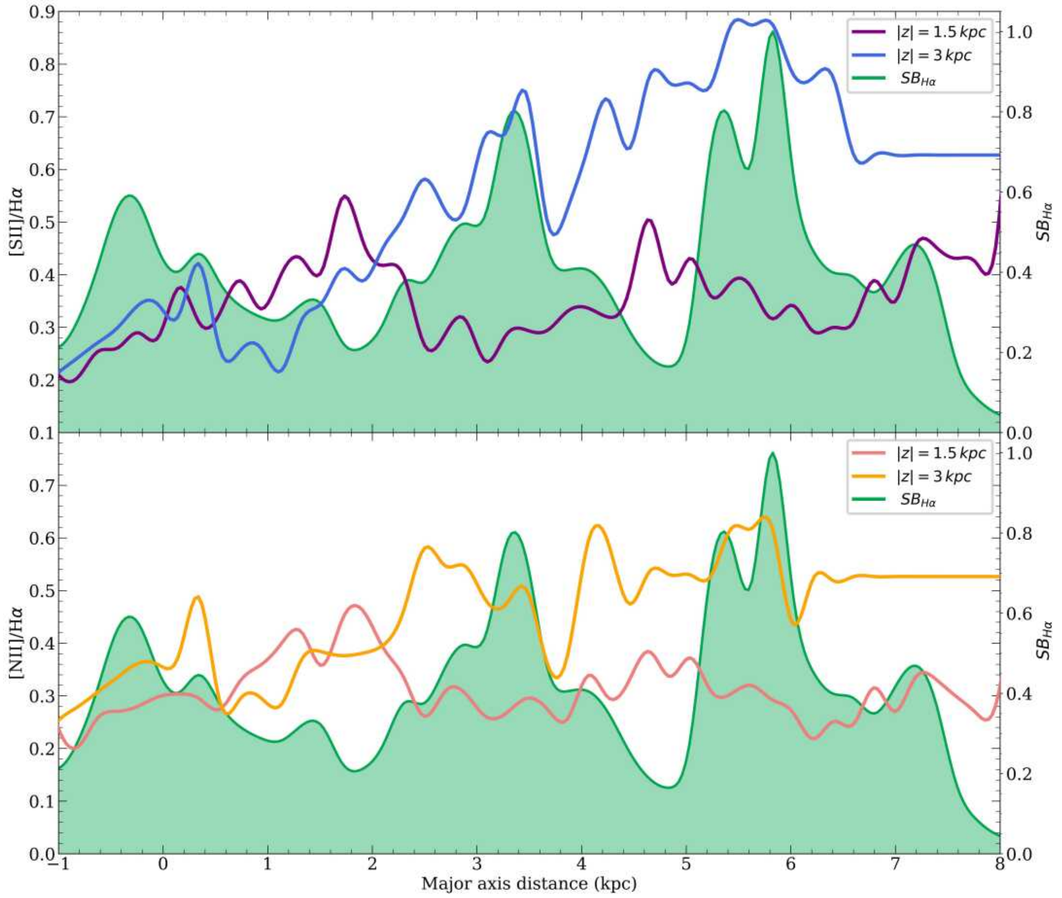

Figure 5.28: ESO443-21 MAD distribution for z = 1.5 and 3 kpc.

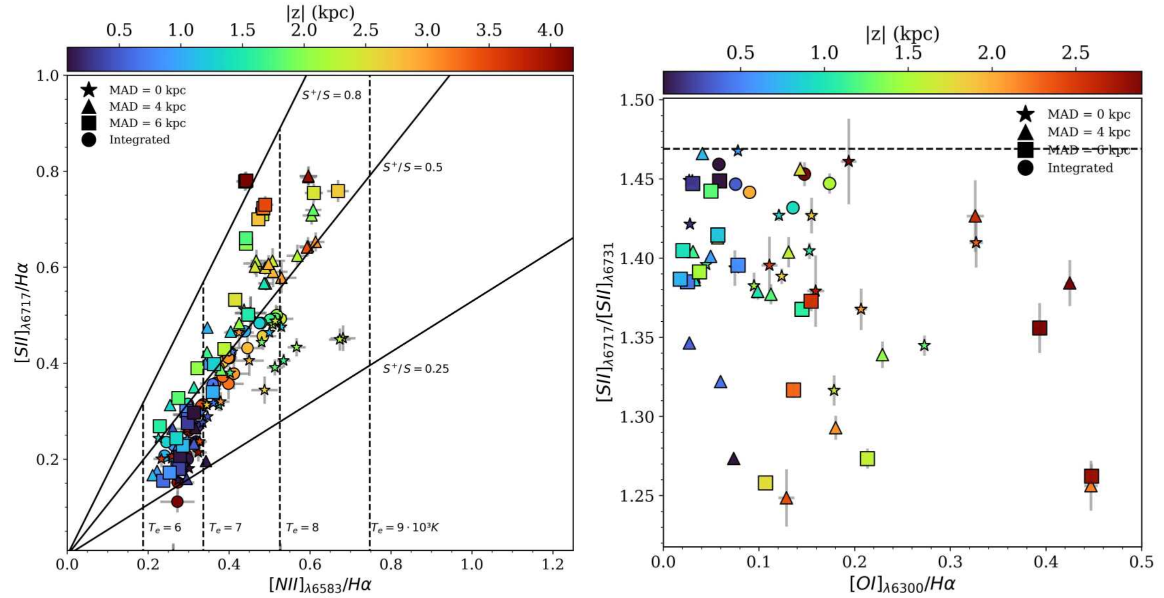

Figure 5.29: Left: [N II] $_{\lambda 6583}$/Hα vs. [S II] $_{\lambda 6717}$/Hα for ESO443-21. Similarly to Figure 5.4, for MAD = 0 (stars), 4 (triangles) and 6 (squares) kpc. Right: [S II] $_{\lambda 6717}$/[S II] $_{\lambda 6731}$ vs [O I] /Hα for ESO443-21. Similar to Figure 5.8.

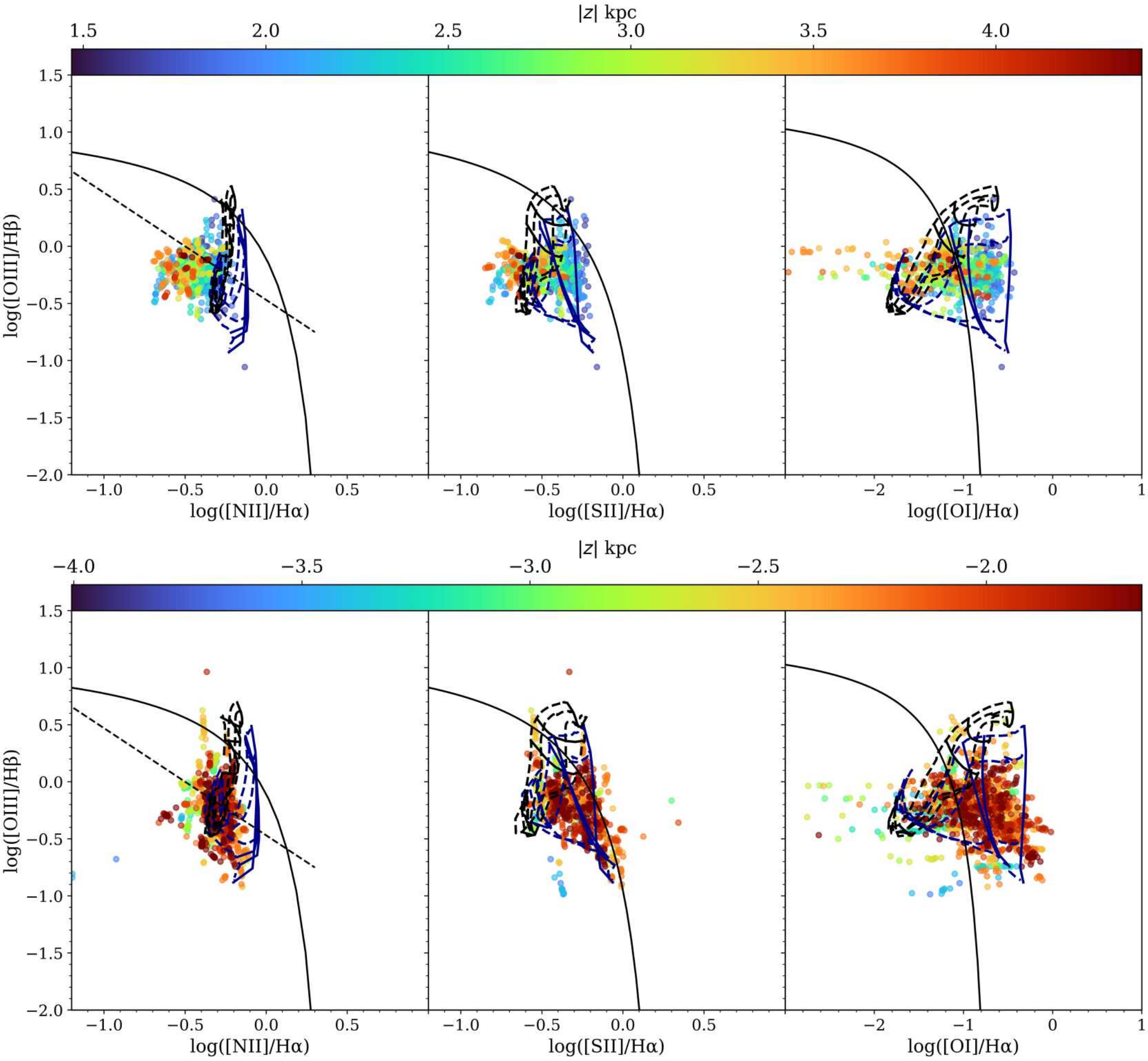

Figure 5.30: ESO443-21 BPT with hybrid models, similar to Figure 5.7. Up: BPT for bins at z > 0. Hybrid models correspond to 20% fast shocks and 80% star formation with $Z = Z_\odot$ and $q = 10^7$ cm/s. Down: BPT for bins at z < 0. Hybrid models correspond to 30% fast shocks and 70% star formation with $Z = 2Z_\odot$ and $q = 10^7$ cm/s.

5.3.6 ESO469-15

The galaxy ESO469-15 exhibits a noticeable presence of discrete extraplanar H II regions (also reported by other authors, e.g. Rautio et al. 2022). Before performing the analysis, all the extraplanar H II regions are masked by using the PYTHON routine DAOSTARFINDER from the PHOTUTILS[3] package. Figure 5.31 shows the line maps after the H II regions removal. The line ratios near to the H II regions are even lower than those close to the bright galactic centre, being considerably low compared to the rest of the eDIG, specially at $z < 0$, where most of the extraplanar H II regions are located. The effect of the extraplanar H II regions is clear in the line distributions (Figure 5.32). The trend of the integrated distribution changes continuously along the distance from the midplane, and squares distributions (at MAD = 1.5, where most of the extraplanar H II regions are located) present considerably lower line ratios in comparison with the rest of the distributions at $z < 0$, up to 0.6 for the [S II] /Hα and [N II] /Hα ratios. [O III] /Hβ ratio shows a mixed tendency for every distribution, as for the rest of the galaxies. Finally, the [O I] /Hα ratio shows lower values at MAD = 0 kpc and $z \simeq 0$ kpc, since for at higher distances the S/N of the [O I] line is not sufficient to sample those regions.

The MAD distributions in Figure 5.33 reinforce what was observed in IC1553, and generally across the entire sample. The $\Sigma_{H\alpha}$ along the major axis of the galaxy is notably more prominent between -1 kpc < MAD < 1 kpc. Subsequently, the [S II] /Hα and [N II] /Hα ratios experience a sudden decrease at these MADs.

The T_e in the eDIG (figure 5.35) is also influenced by the presence of extraplanar H II regions, being notably lower for all the eDIG compared to other galaxies, ranging only between 6 and $8 \cdot 10^3$ K.

In addition to these results, the hybrid models in the BPT diagram for all the eDIG (Figure 5.34) indicate only a 30% contribution of fast shocks in the ionisation mechanisms of the eDIG. This represents the lowest contribution in the sample when the data in the BPT diagram is not restricted by z or MAD.

---

[3] DAOSTARFINDER documentation.

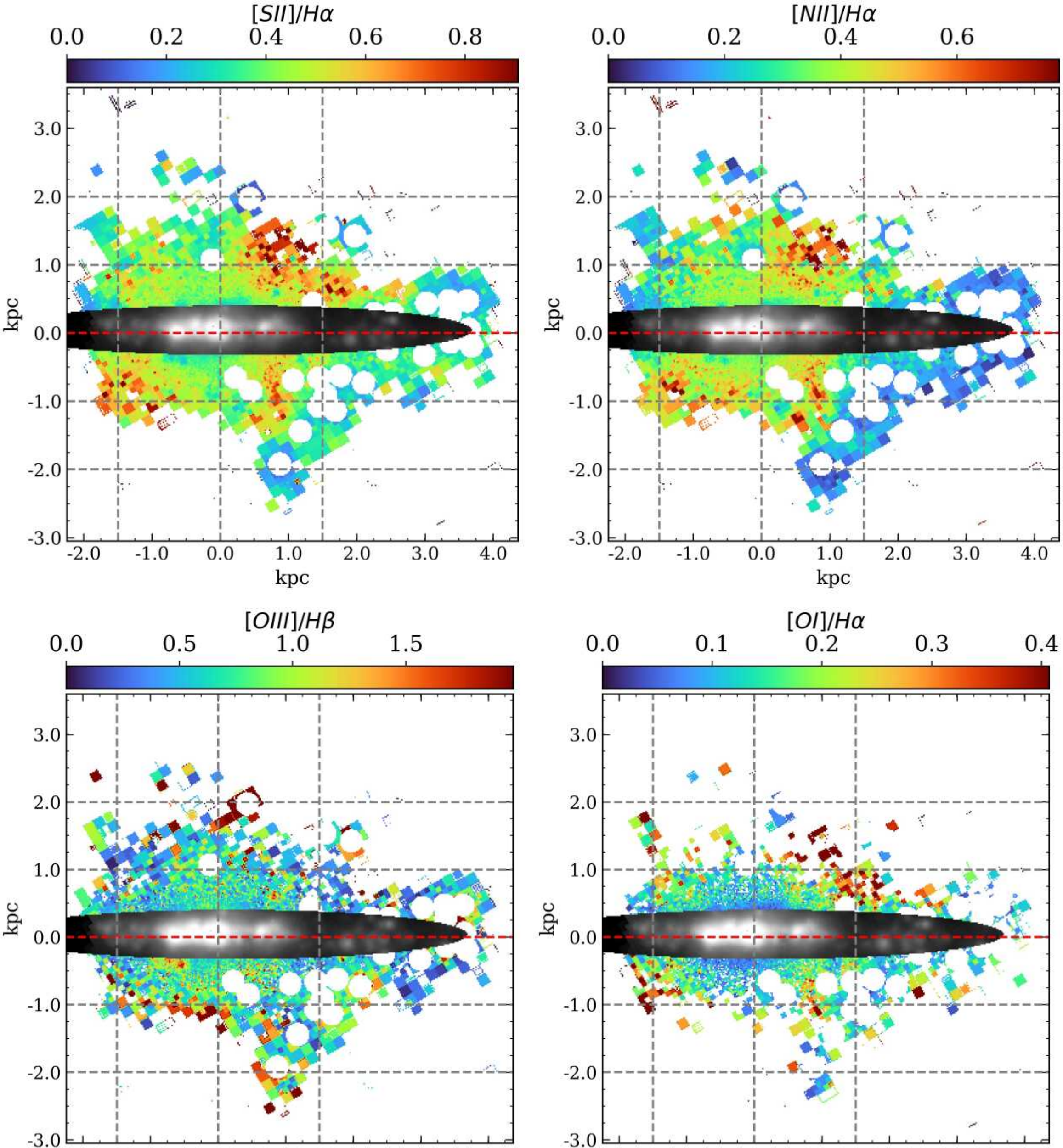

Figure 5.31: ESO469-15 line ratio maps, similar to Figure 5.1. The grey dashed lines indicates the heights with respect the midplane z = ±1, ±2 and major axis distances MAD = -1.5, 0, 1.5 kpc.

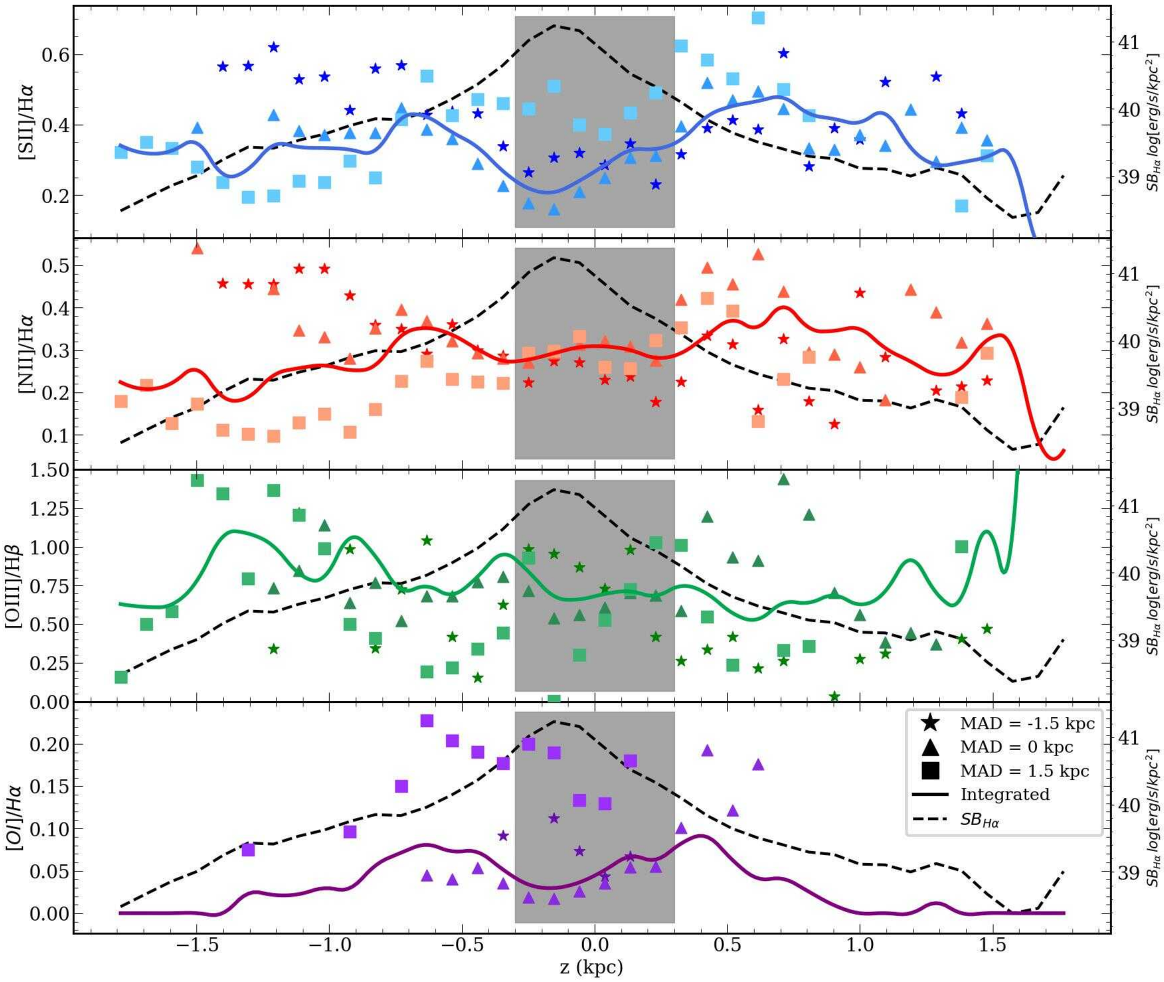

Figure 5.32: ESO469-15 line ratio distributions of the with respect the distance from the midplane. Similarly to Figure 5.2, for MAD = -1.5 (stars), 0 (triangles) and 1.5 (squares) kpc.

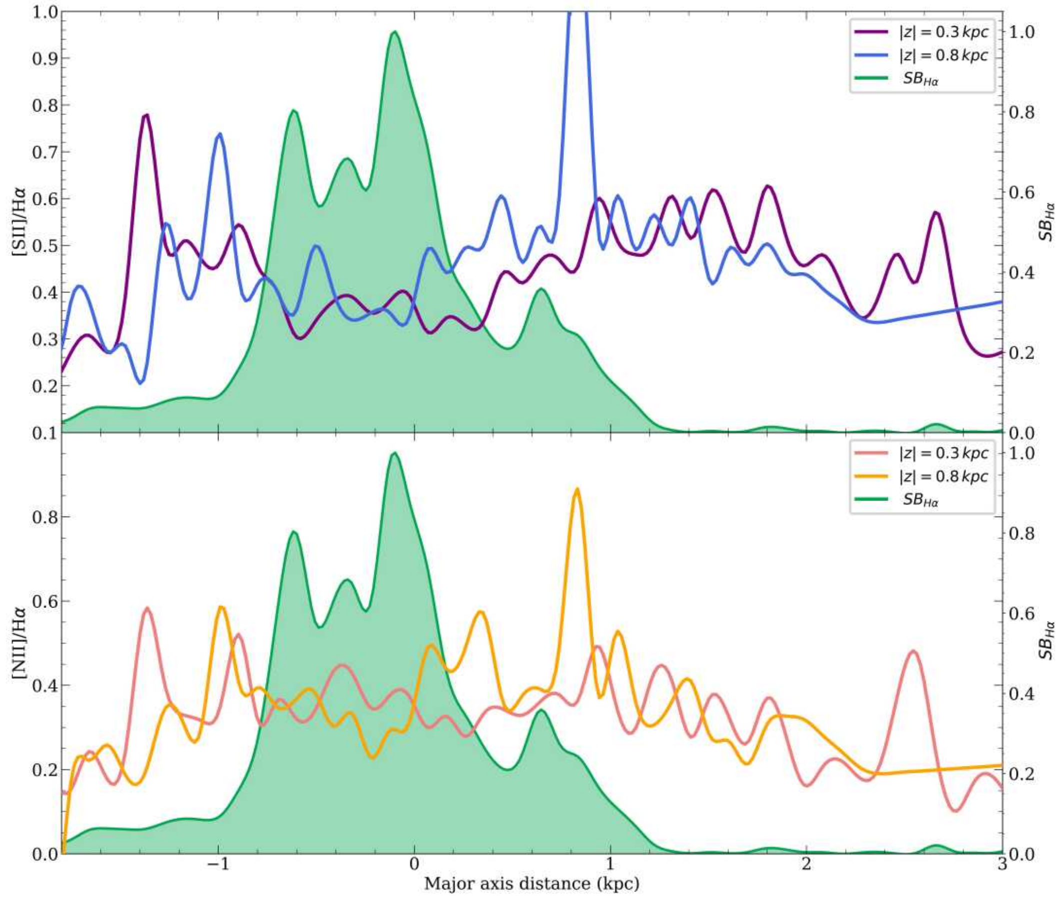

Figure 5.33: ESO469-15 MAD distribution for z = 0.3 and 0.8 kpc.

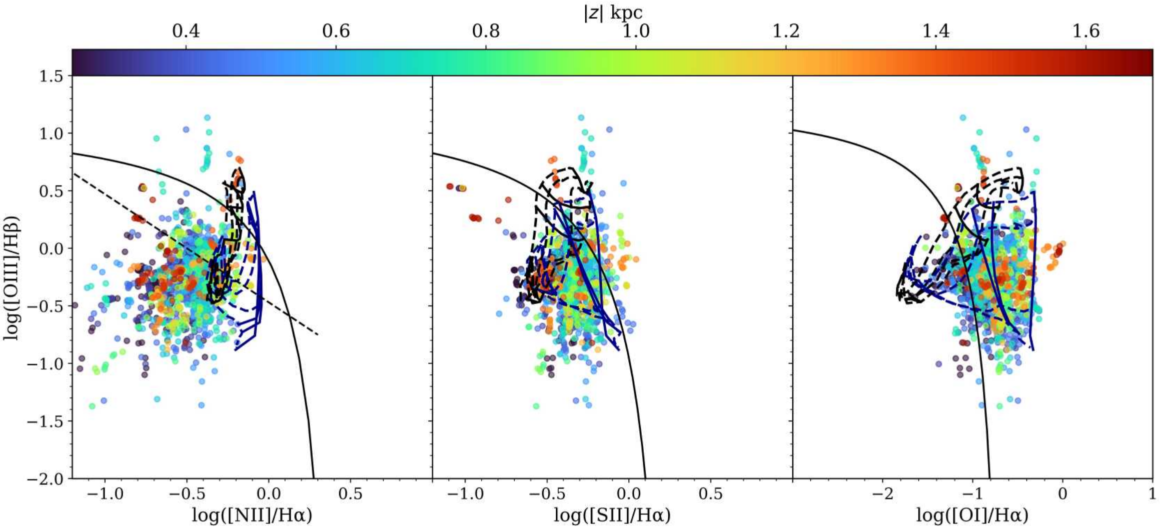

Figure 5.34: ESO469-15 BPT with hybrid models, similar to Figure 5.7. 30% fast shocks and 70% star formation with Z = $2Z_\odot$ and q = 10^7 cm/s.

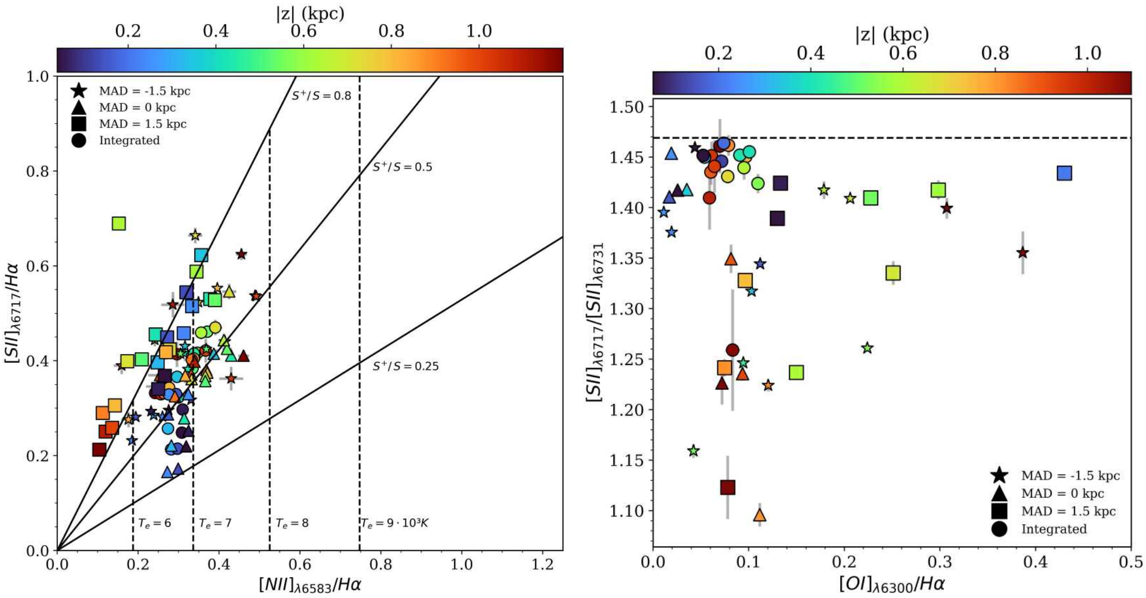

Figure 5.35: Left: [N II] $_{\lambda 6583}$/Hα vs. [S II] $_{\lambda 6717}$/Hα for ESO469-15. Similarly to Figure 5.4, for MAD = -1.5 (stars), 0 (triangles) and 1.5 (squares) kpc. Right: [S II] $_{\lambda 6717}$/[S II] $_{\lambda 6731}$ vs [O I] /Hα for ESO469-15. Similar to Figure 5.8.

5.3.7 ESO157-49

ESO157-49 is the only galaxy in the sample to have nearby neighbours (Kourkchi & Tully 2017). It was observed that its closest neighbour, the dwarf galaxy ESO157-48 located southwest of the galaxy, has influence on its kinematics, that can result in an asymmetry in the properties of the extraplanar ionised gas (Rautio et al. 2022). Figure 5.36 shows precisely this asymmetry. ESO157-49 presents a more uniform emission from the galactic plane, similar to ESO544-27 but with a slightly brighter emission observed between -1.5 kpc $\lesssim$ MAD $\lesssim$ 3 kpc. However, the extraplanar ionised structure at $z > 0$ is clearly different from that at $z < 0$, being the structure of the eDIG at $z < 0$ apparently tilted and shifted compared to the eDIG at $z > 0$. The line ratios height distributions (figure 5.37) show that at $z < 0$ the [N II] /Hα , [S II] /Hα and [O I] /Hα line ratios reach lower maximum values than at $z > 0$ (up to 0.2 on every ratio). Furthermore, at MAD = 2.5 kpc, where the $\Sigma_{H\alpha}$ is higher, the [N II] /Hα and [S II] /Hα line ratios are consistently remain lower, as observed for the rest of the sample (also seen in the MAD distributions; Figure 5.38).

The T_e (see Figure 5.41) increases in height as usual, up to $\sim 9{\cdot}10^3$ K, and the ionisation fraction S^+/S remains approximately constant at ~0.5, dropping to 0.35 at the highest distances from the midplane ($z \simeq 2$ kpc). In addition, at MAD = 2.5 kpc, where the $\Sigma_{H\alpha}$ is higher (corresponding to squares in Figure 5.41 left), the T_e remains below $\sim 8{\cdot}10^3$ K.

Similar to ESO544-27, the significant uniformity in the emission from the galactic plane relative to the line of sight results in hybrid models that best fit the points on the BPT diagram (Figure 5.39) corresponding to 50% ionisation due to fast shocks and 50% due to star formation. However, at 2 kpc < MAD < 3 kpc, where the $\Sigma_{H\alpha}$ is higher, the contribution of fast shocks drops to 30%, and at -0.5 kpc < MAD < 0.5 kpc, the contribution is still 50% (see Figure 5.40). Additionally, in both cases, the dependence of the ionisation regime on height is evident, with bins corresponding to higher z being further from the demarcation of Kewley et al. (2001). As for the rest of the galaxies, the presence of fast shocks is further supported by the decrease in the [S II] doublet ratio (indicating an increase in electron density) as the [O I] /Hα ratio increases (figure 5.41 right), being this trend clearly correlated with the distance from the midplane.

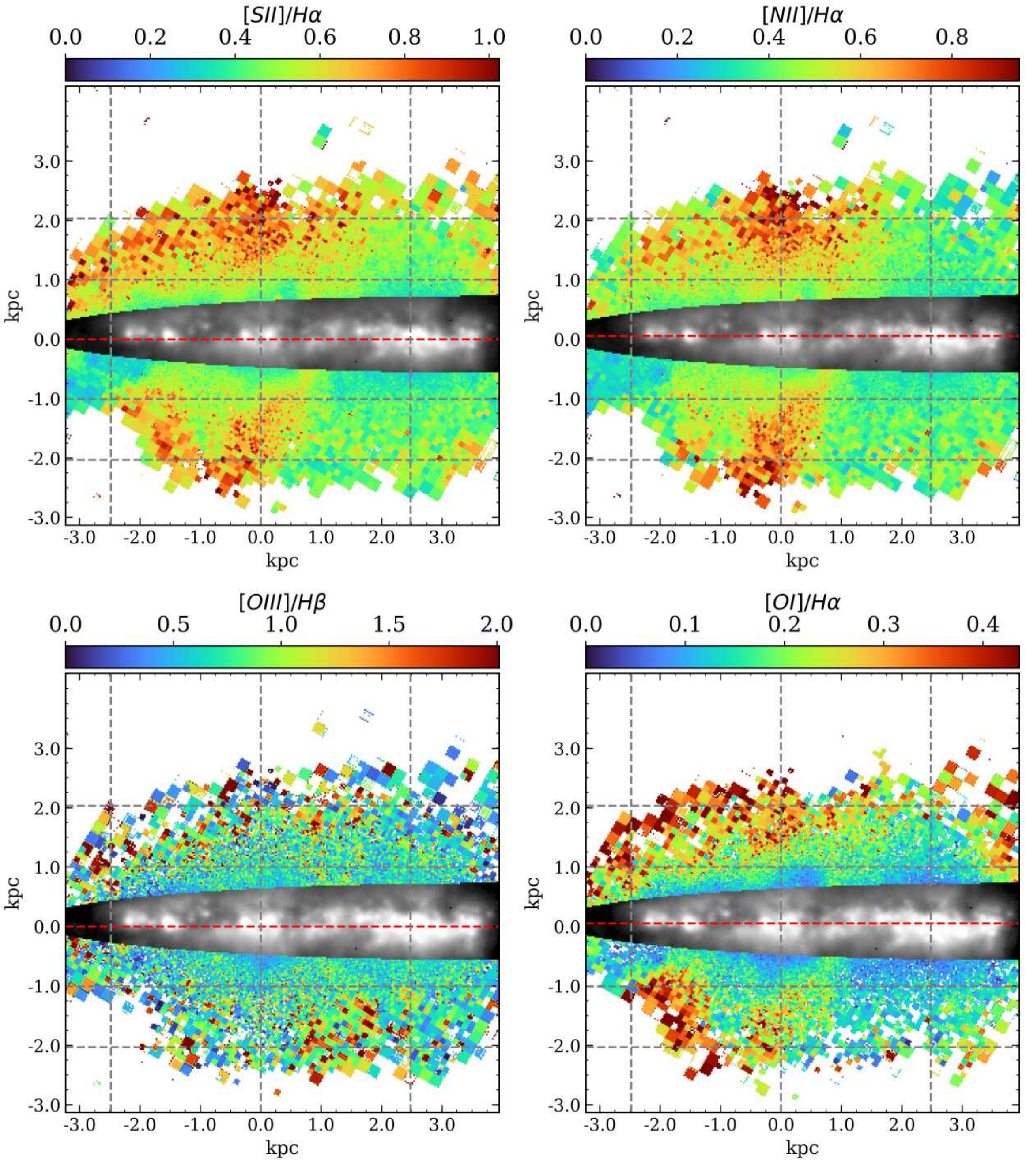

Figure 5.36: ESO157-49 line ratio maps, similar to Figure 5.1. The grey dashed lines indicates the heights with respect the midplane z = ±1, ±2 and major axis distances MAD = -2.5, 0, 2.5 kpc.

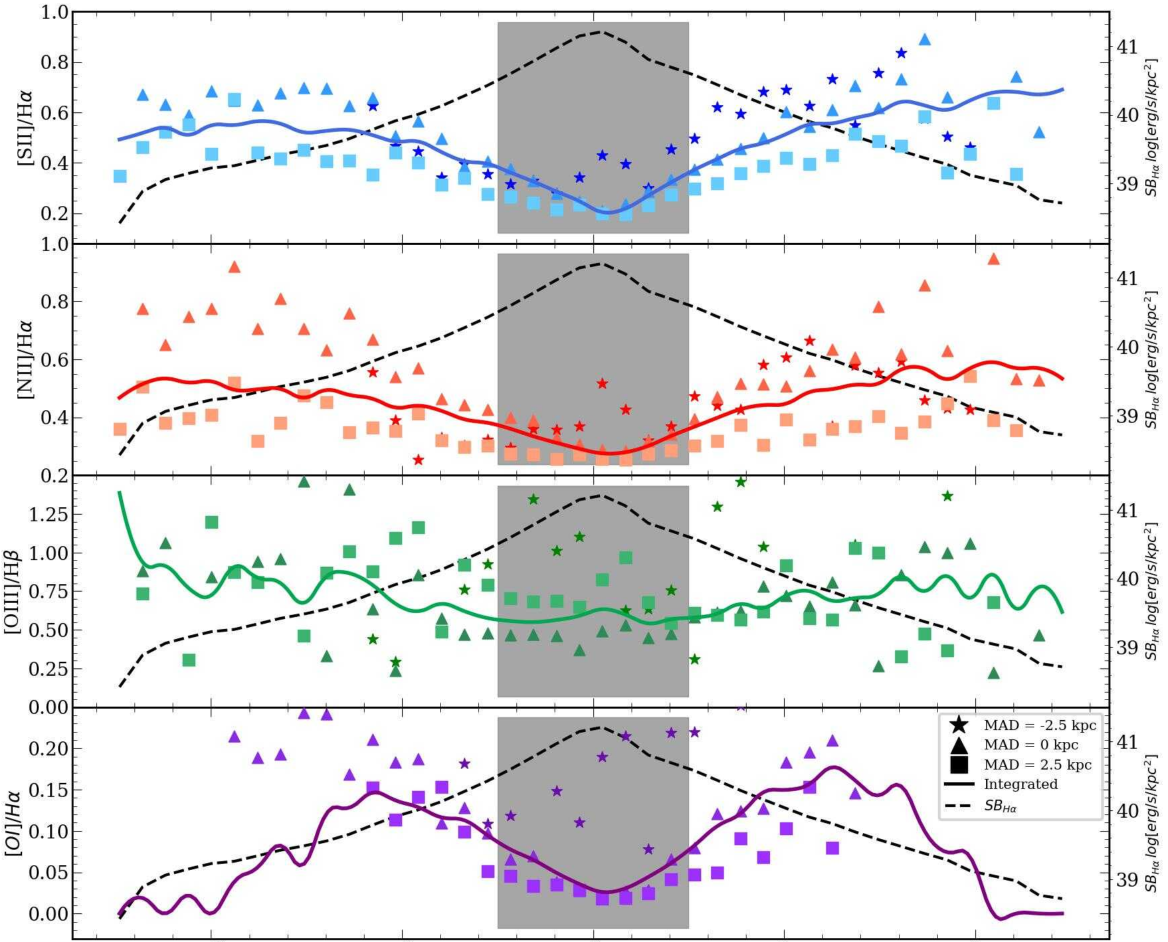

Figure 5.37: ESO157-49 line ratio distributions of the with respect the distance from the midplane. Similarly to Figure 5.2, for MAD = -2.5 (stars), 0 (triangles) and 2.5 (squares) kpc.

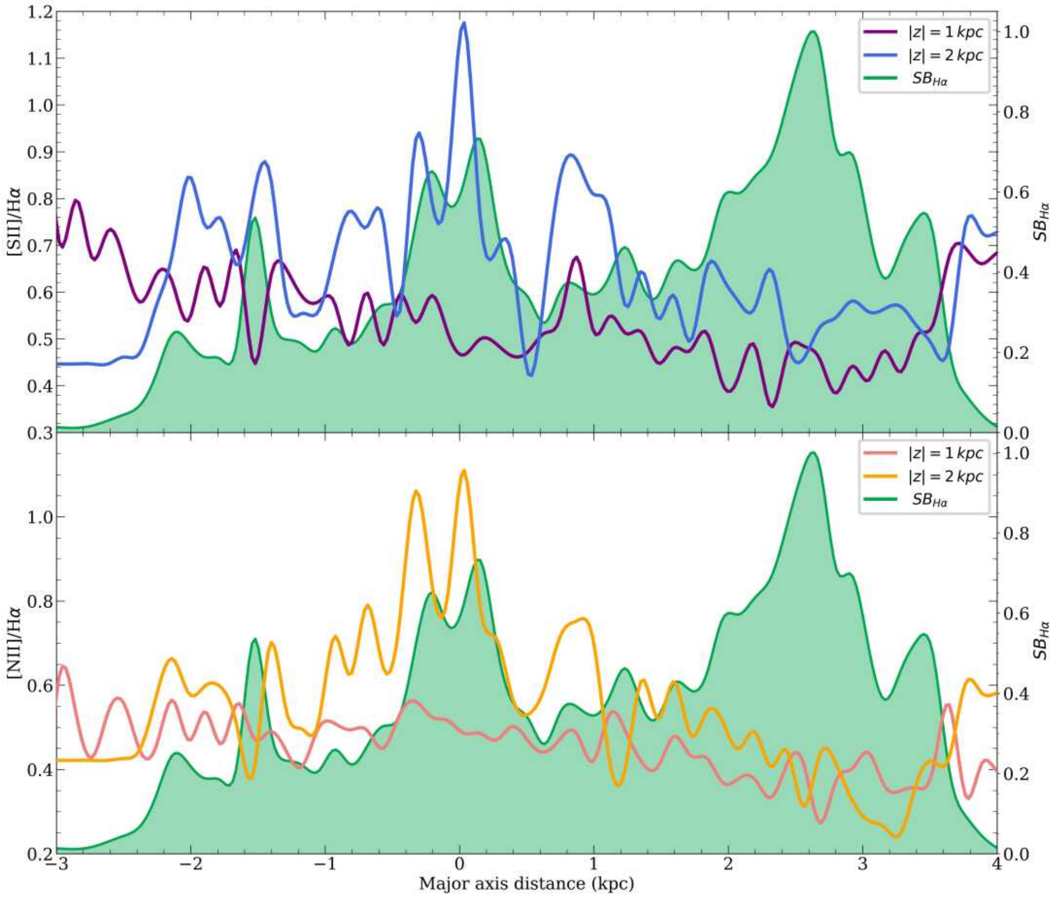

Figure 5.38: ESO157-49 MAD distribution for z = 1 and 2 kpc.

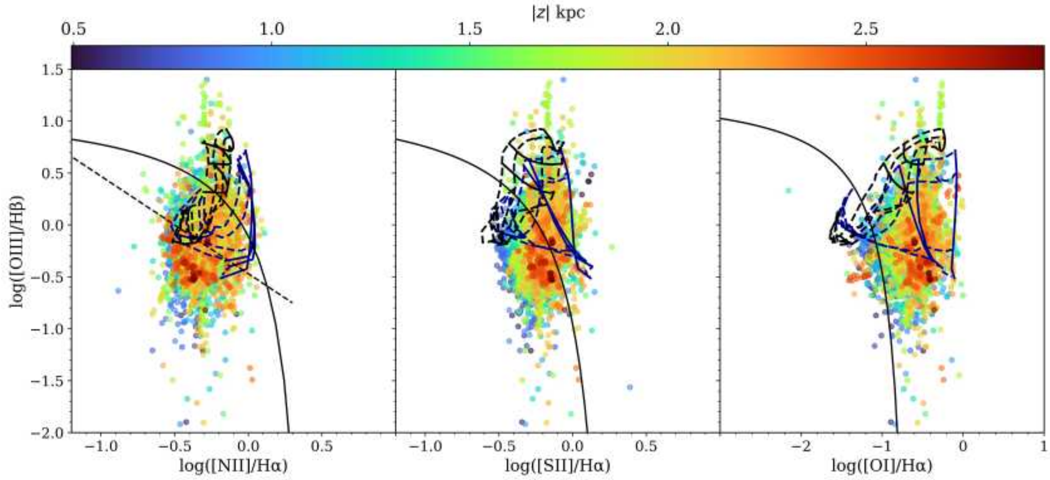

Figure 5.39: ESO157-49 BPT with hybrid models, similar to Figure 5.7. 50% fast shocks and 50% star formation with Z = $2Z_{\odot}$ and q = 10^7 cm/s.

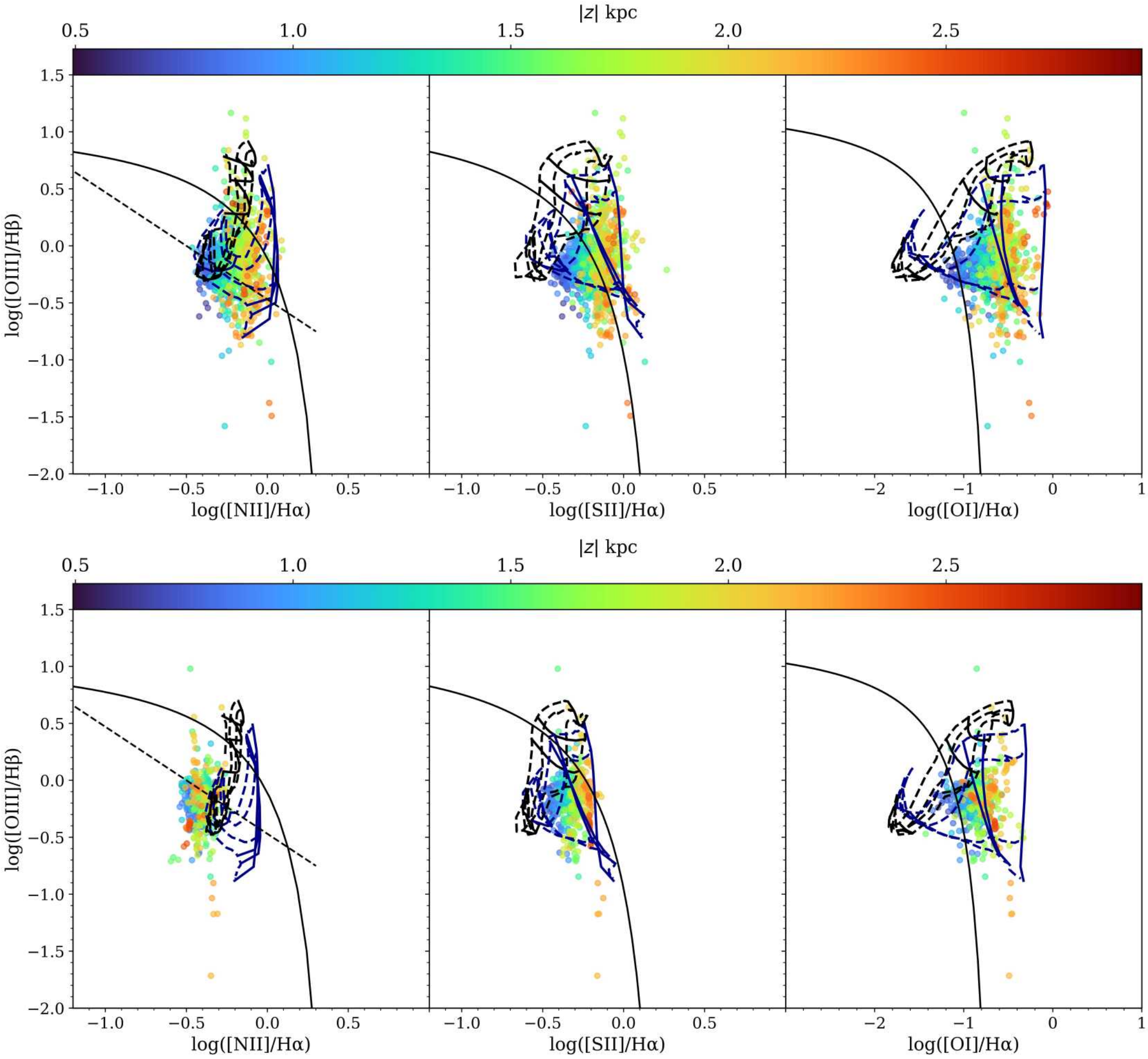

Figure 5.40: ESO157-49 BPT with hybrid models, similar to Figure 5.10. Up: BPT for bins between -0.5 kpc < MAD < 0.5 kpc. Hybrid models correspond to 50% fast shocks and 50% star formation with Z = $2Z_\odot$ and q = 10^7 cm/s. Down: BPT for bins between 2.25 kpc < MAD < 2.75 kpc. Hybrid models correspond to 30% fast shocks and 70% star formation with Z = $2Z_\odot$ and q = 10^7 cm/s.

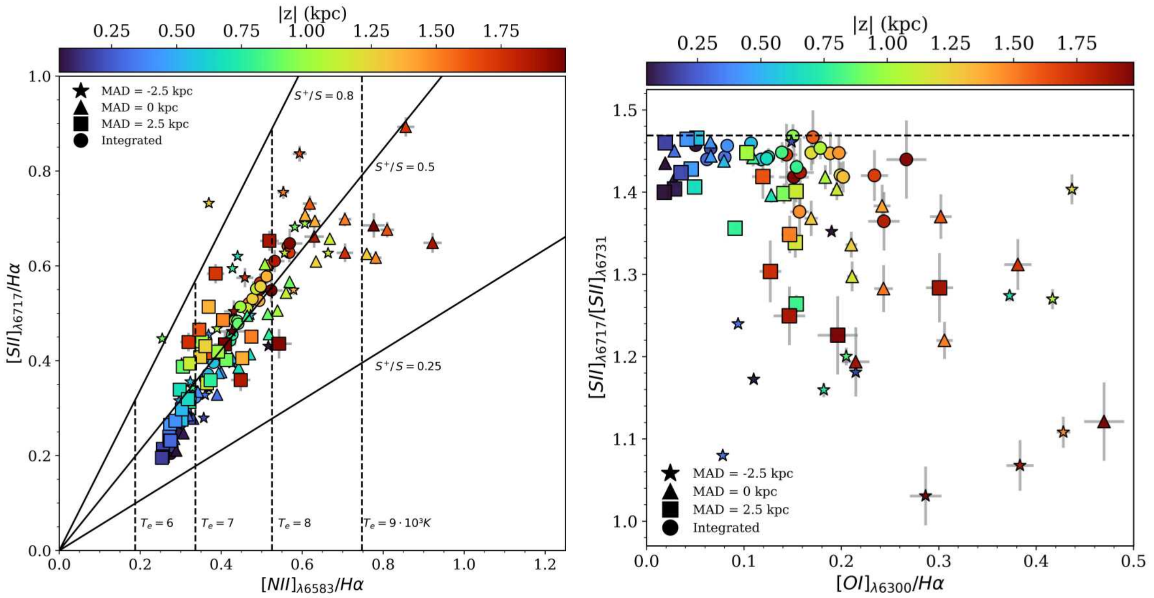

Figure 5.41: Left: [N II]$_{\lambda 6583}$/Hα vs. [S II]$_{\lambda 6717}$/Hα for ESO157-49. Similarly to Figure 5.4, for MAD = -2.5 (stars), 0 (triangles) and 2.5 (squares) kpc. Right: [S II]$_{\lambda 6717}$/[S II]$_{\lambda 6731}$ vs [O I] /Hα for ESO157-49. Similar to Figure 5.8.

5.3.8 IC217

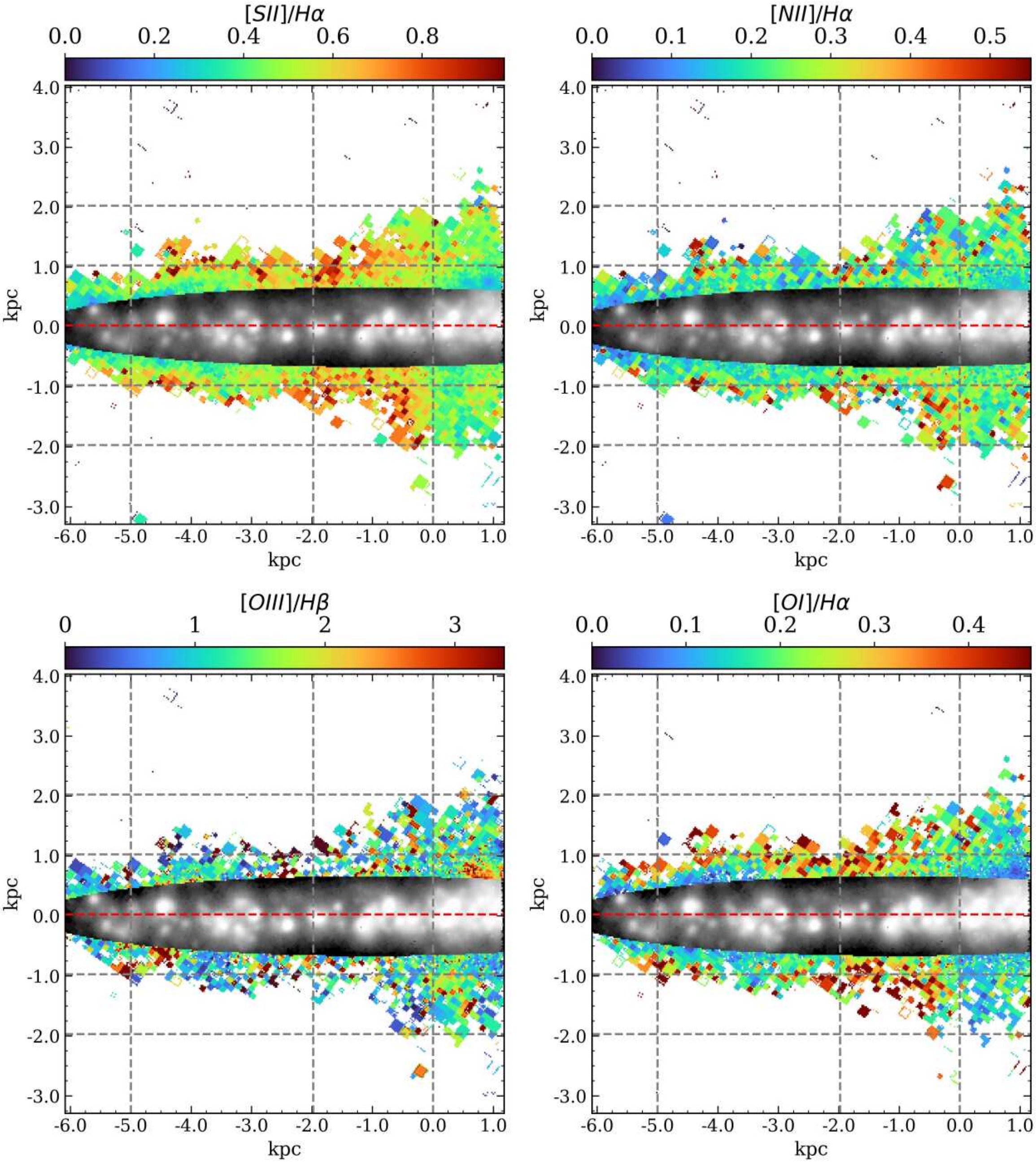

Figure 5.42: IC217 line ratio maps, similar to Figure 5.1. The grey dashed lines indicates the heights with respect the midplane z = ±1, ±2 and major axis distances MAD = -5, -2, 0 kpc.

IC217 has the lowest exposure time among the sample, only three exposures of 2624 seconds in contrast to the four exposures for the other galaxies. After excluding bins with S/N < 2 and relative errors exceeding 40%, this results in the least comprehensive data sampling among the galaxies in the sample. However, Figure 5.42 illustrates the variations in ionisation regimes at different MADs observed in the other galaxies. Between -3 kpc < MAD < -1 kpc, where the concentration of H II regions with respect to the line of sight is lower, the line

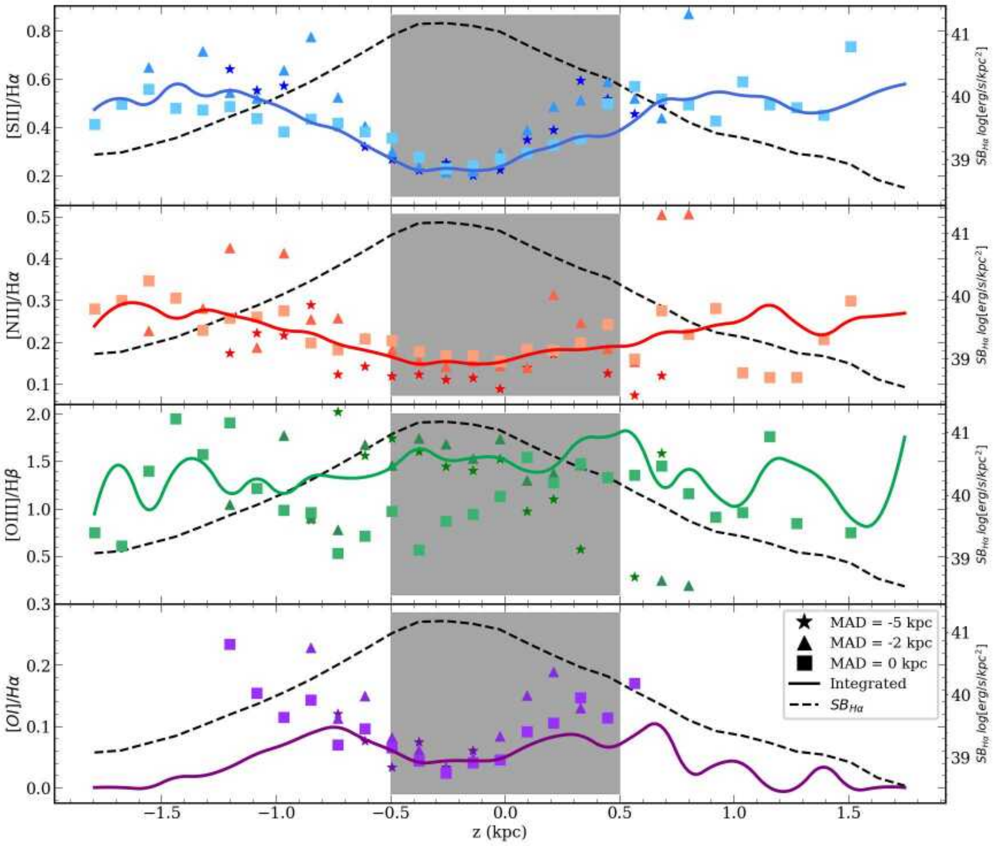

Figure 5.43: IC217 line ratio distributions of the with respect the distance from the midplane. Similarly to Figure 5.2, for MAD = -5 (stars), -2 (triangles) and 0 (squares) kpc.

ratios in the eDIG exhibit higher values compared to the rest of the galaxy. Nevertheless, the level of data sampling is insufficient to conduct a more in-depth analysis of this galaxy. The line ratio distributions (Figure 5.43) and the BPT (Figure 5.44) a mixed regime between different MADs, along with a general eDIG ionisation consisting of a 50% contribution from fast shocks and 50% of star formation.

5.3.9 *IC1553*

IC1553 is classified as an irregular galaxy (Vorontsov-Vel'Yaminov & Arkhipova 1968). Despite its inclination of 78.6°, the irregular morphology of the disk is evident due to the highly asymmetrical distribution of H II regions at 2 kpc $\lesssim$ MAD $\lesssim$ 4 kpc observed with respect the line of sight. For this reason, the differences in the ionisation conditions described in section 5.1 are more evident. The column of eDIG just above the H II regions exhibits a lower degree of ionisation for [N II] and [S II] compared to Hα than in the column of eDIG where the emission from the H II regions is lower. In this latter scenario, the higher electron temperatures favour excitation due to collisions at a low-density regime (Osterbrock & Ferland 2006). This translates to a more collisionally-ionised eDIG compared to the column above the H II regions (with f_{shock} = 0.4 and 0.2 respectively). However, at MAD $\simeq$ 0 kpc, the

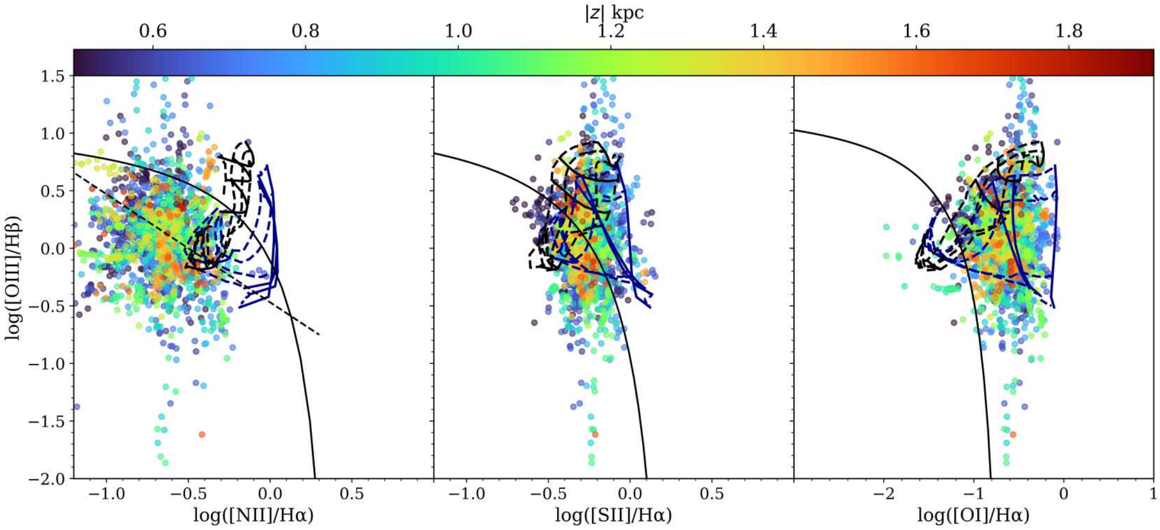

Figure 5.44: IC217 BPT with hybrid models, similar to Figure 5.7. 50% fast shocks and 50% star formation with Z = $Z_\odot$ and q = 10^7 cm/s.

biconical structure observed in Figure 5.1 presents lower ionisation fraction ($S^+/S \simeq 0.35$) than the rest of the eDIG, but with an increasing electron temperature in height, reaching the highest values (~ $9{\cdot}10^3$ K) of all the eDIG. This is consistent with the presence of gas accretion in the galaxy found by Rautio et al. (2022) and Dirks et al. (2023).

The general behaviour of the [O III] /Hβ and [O I] /Hα ratios, as for [N II] /Hα , [S II] /Hα , is to increase with the height, also observed in previous studies (Rand 1998; Haffner et al. 2009b; Ho et al. 2016; Dirks et al. 2023). Nevertheless, in the BPT diagrams, there is no clear correlation between the location of the bins in the diagram and their distance with respect to the midplane. This lack of correlation is due to the two-dimensional dependence between the ionisation conditions and the galactic plane. For the [O I] /Hα ratios, the emission line map is similar to the [N II] /Hα and [S II] /Hα maps. As the [O I] /Hα ratio is related to the amount of H^0 relative to H^+, lower values of this ratio in the DIG will imply a higher degree of ionisation of the neutral hydrogen (Rand 1998; Haffner et al. 2009b; BETIS I). As for the [N II] /Hα and [S II] /Hα ratios, this ratio is also lower in the eDIG between 2 kpc $\lesssim$ MAD $\lesssim$ 4 kpc than between -2 kpc $\lesssim$ MAD $\lesssim$ 2 kpc.

Table 5.1 summaries the general characteristics of the eDIG found in the eBETIS sample.

Table 5.1: Summary of characteristics of the eDIG. The second column represents the DIG morphology observed in the disc and halo from the Hα images. The third column shows the horizontal and vertical distances covered by the eDIG.

galaxy	**DIG morphology**	**MAD, z** (kpc)
IC217	Disc: Homogeneous distribution of bright H II regions Halo: Thin eDIG layer, low S/N	6, 2
PGC28308	Disc: Homogeneous distribution of bright H II regions Halo: Extended and homogeneous eDIG	8, 2
PGC30591	Disc: Few bright H II regions Halo: Inhomogeneous extended eDIG	4, 2
ESO544-27	Disc: Homogeneous distribution of bright H II regions Halo: Homogeneous eDIG and extended filaments	4, 2
IC1553	Disc: Inhomogeneous distribution of H II regions with respect the line of sight, hidden H II regions Halo: Highly asymmetrical eDIG structure with a bicone and extended filaments	4, 3.5
ESO443-21	Disc: Homogeneous distribution of bright H II regions Halo: Extended eDIG with a large filamentary knot	8, 5
ESO469-15	Disc: Bright emission around the centre Halo: Several extraplanar H II regions, mixed eDIG regimes	3, 2
ESO157-49	Disc: Homogeneous distribution of bright H II regions Halo: Tilted and mixed eDIG regimes with extended filaments	4, 2.5

Chapter 6

Conclusions

In this work, we present the Bidimensional Exploration of the warm-Temperature Ionised gaS (BETIS) project, designed for the spatially resolved and spectral study of the diffuse ionised gas (DIG) in a selection of nearby galaxies. In the first part of the project, we present a methodology for characterising and studying, both spatially and spectroscopically, the DIG optimised for galaxies with different linear resolutions and physical characteristics. To validate the new methodology, we selected a showcase sample consisting of seven galaxies with diverse morphological and characteristic traits. This methodology involves the following steps:

- An adaptive binning was performed to the observed datacube in order to increase the S/N of the fainter lines such as [O III] , [O I] , and [S II] . This technique is based on the spectroscopic S/N of the [S II] line, with a target S/N of 10.
- We conducted a SSP synthesis using the STARLIGHT code for each integrated spectrum within the binned datacube. Subsequently, employing a Gaussian fitting to the residuals of each SSP fitting, we derive the binned emission line maps for the nine lines of interest, as well as a binned $EW_{H\alpha}$ map.
- The DIG was separated from the H II regions using a combination of an automated tool to detect and subtract the H II regions from the binned Hα maps, together with a cut-off in Hα surface brightness to subtract bright, irregular H II regions not detected by the automated tools.

The sample exhibits an average DIG faction of 40%-70% in the showcase sample, with NGC3393 the one with the higher DIG fraction (69%-87%), followed by NGC863, ESO325-43, NGC692, NGC6627, ESO584-7, and IC3476. Those with higher DIG fractions are the two Seyferts of the sample: NGC3393 and NGC863. This is further exemplified when analysing the radial distributions of the $\Sigma_{H\alpha}$ in the DIG and H II regions. In these two galaxies, the DIG exhibits higher surface brightness compared to the H II regions, with the disparity between these two regimes reaching up to 1 dex. The overall radial distributions of $\Sigma_{H\alpha}$, as depicted in Fig. 4.3, generally reveal similar trends for both H II regions and DIG, with a radial decrease. However, there is an increase in $\Sigma_{H\alpha}$ within the bars of NGC692 and NGC6627 for the H II regions.

On average, we observe in Fig. 4.5 higher [S II] /Hα , [N II] /Hα , [O III] /Hβ , and [O I] /Hα ratios in the DIG compared to the H II regions. Additionally, the radial trends of the DIG and H II distributions are similar in all cases, indicating a correlation between the ionisation of these species in both the DIG and the H II regions.

Computing the [N II] BPT diagram also highlights a significant distinction between the two Seyfert galaxies and the rest of the sample. It is evident that the DIG is predominantly photoionised by H II regions in all galaxies, except for NGC3393 and NGC863. In these two cases, the ionisation source of the DIG appears to be accounted for by the fast shock models proposed by Allen et al. (2008). Nevertheless, it is worth noting that these two galaxies host prominent AGNs, which can mimic the emission of the DIG when assessing a global BPT for the entire sample. In particular, NGC3393 presents a strong ionisation cone due to galactic outflows.

We also addressed the challenge of employing the EW$_{H\alpha}$ as a proxy for delineating DIG regions and different ionisation regimes. This issue arises because at low EW$_{H\alpha}$, typically used to identify HOLMES or AGNs regimes, the Hα line derived from synthetic spectra after conducting a SSP fitting can be an artefact of the model. This results in an artificial Hα emission line when correcting the observed Hα emission with the stellar model absorption, after subtracting the model from an observed Hα line with a spectroscopic $S/N \sim 1$. Therefore, the low EW$_{H\alpha}$value may be a result of the characteristics of the stellar models, making it dependent on these models – if we do not consider the spectroscopic S/N of the observed Hα .

These results suggest that conducting a global analysis of the DIG using a sample of galaxies with diverse characteristics may lead to misleading conclusions about the ionisation mechanisms. This is because each galaxy can present distinct physical processes, for example large-scale AGNs, which can mimic the emission of high-excitation DIG, making the large-scale AGN emission and and high-excitation DIG indistinguishable in the same diagnosis. For this reason, and due to the lack of reliability of the low EW$_{H\alpha}$ regimes, every galaxy needs to be considered individually when performing a DIG diagnosis.

The distributions of EW$_{H\alpha}$for the DIG regions in the sample exhibit a morphological pattern. Sa-type galaxies, with prominent bulges of older stellar populations, have lower EW$_{H\alpha}$, followed by Sb and Sc galaxies. Notably, ESO584-7 and IC3476 show significantly higher

EWs. ESO584-7 is an H II galaxy, while IC3476 experiences elevated EWs due to ram pressure stripping in the Virgo Cluster's intergalactic environment.

Lastly, we examined the impact of dust reddening in the DIG by assessing the radial distribution of Hα /Hβ ratios within both the DIG and H II regions across the entire sample. These results suggest that extinction is consistently lower in DIG regions.

In the second part of the project we focused on the spatially resolved and spectral study of the extraplanar diffuse ionised gas (eDIG) in a selection of eight edge-on (i > 75°) nearby galaxies. We used the galaxies from the Com19 dataset as the sample and applied the methodology described in BETIS I for adaptively binning the observed datacubes and extracting the binned emission line maps from them.

The Hα emission line maps reveal a complex ionisation structure in the galactic halos composed by diverse structures as filaments or knots that can reach more than 3 kpc from the midplane. The real complexity of the ionisation structure of the eDIG is shown when examining the [N II] /Hα , [S II] /Hα , [O III] /Hβ and [O I] /Hα maps, revealing the presence of new structures as an apparent biconical structure in IC1553 or a broad ionised knot of ESO443-21. The behaviour of these line ratios reveals that the ionisation structure of the eDIG is shown to be influenced by the distribution of H II regions in the galactic plane as seen from the line of sight. In all galaxies, the line ratios increase both vertically and radially, showing an anti-correlation with the $\Sigma_{H\alpha}$ distribution of the galactic disc. These ratios reach higher values at distances further from the H II regions, both in terms of height (z) and major axis distance (MAD).

This correlation between the morphological distribution of star-forming regions in the disks and the morphology of the halos presents the strongest evidence supporting the interpretation that energy sources from star formation within the galaxy disks drive the observed disk-halo interaction, being the Lyc photons leaking from OB associations the main ionisation source of the eDIG.

However, OB-star-driven ionisation can not explain some features found in the eDIG, such as the enhanced [N II] /Hα and [S II] /Hα and the presence of high ionisation species such as [O III] at higher distances from the midplane. From the [N II] /Hα and [S II] /Hα ratios we explored the radial and vertical variations of T_e and S^+/S. The general behaviour indicates a linear, constant increment of T_e with increasing distance from the galactic plane for all the galaxies. Besides, there is significant variations in T_e and S^+/S at different MADs, also linked to the H II regions distribution with respect the line of sight. The variations in temperature and ionisation structure of the eDIG as a function of spatial position within a single galaxy provide compelling evidence of the intricate dynamical heating structure of the ISM in the halo. These variations show that the eDIG tends towards a lower ionisation state (higher

S^+/S) compared to classical H II regions. The anomalous [N II] /Hα and [S II] /Hα line ratios in the eDIG can be attributed to an increase in the T_e temperature in the halo, resulting from photoionisation with a lower ionisation parameter.

To account for the [O III] /Hβ and [O I] /Hα ratios, various ionisation mechanisms have been considered. One such mechanism, recently highlighted in the literature, involves photoionisation by a hard spectrum emanating from the high-temperature end of the white dwarf distribution and the central stars of planetary nebulae; the low-mass, hot, and evolved (post-AGB) stars known as HOLMES. Nevertheless, the correlation between the ionisation structure of the eDIG and the H II regions distribution observed in this study does not support a homogeneous distribution of HOLMES across the thick disc and lower halo. This inconsistency, combined with the unreliability of $EW_{H\alpha}$as a proxy commonly used in the literature to differentiate star-forming regions from HOLMES, effectively negates HOLMES as a plausible ionisation mechanism for the eDIG.

We propose that shocks induced in the ISM by feedback mechanisms serve as a secondary ionisation source for the eDIG. Given that shock heating becomes substantial only when the kinetic energy is efficiently thermalised, both photoionisation and shocks may be regarded as "thermal" heating sources for the ISM. The observed enhancement in the [O III] /Hβ ratio with increasing height can be interpreted as a mixing sequence between the predominant shock ionisation in the halo and the photoionisation in the disk.

To ascertain the impact of shocks on the ionisation budget of the eDIG, we constructed a suite of hybrid models that integrate both star formation and fast shock regimes. We conducted a BPT analysis by computing the hybrid models for each galaxy individually, given that each galaxy may exhibit unique characteristics necessitating a tailored ionisation diagnosis for the eDIG (BETIS I). The results indicate that fast shocks significantly contribute to the ionisation budget of the eDIG, with contributions ranging from 20% to 50% across the sample.

The presence of shocks is further corroborated when examining the density-sensitive [S II] doublet ratio as a function of the [O I] /Hα ratio. For all galaxies, most of the eDIG regions near the midplane exhibit [S II] line ratios close to the low-density limit, accompanied by low [O I] /Hα values, which are indicative of H II region emission. However, regions with low [S II] doublet ratios –typically at high midplane distances– coincide with regions exhibiting high [O I] /Hα values, indicative of shock-compressed ionised gas. Therefore, the low [S II] doublet ratios, along with their implied high gas densities and the fact that these regions exhibit higher [O I] /Hα values, support a scenario in which wherein gas emission originates from shocks, likely induced by feedback from high-level star-forming regions within the galactic disk. These scenarios can occur even in galaxies with a disc exhibiting a sub-MW integrated SFR, such as the eBETIS galaxies. In this context, fast shocks may explain the increase in the [O I] /Hα ratio with distance from the midplane, with the highest [O I] /Hα ratios corresponding to the shocked interface at the greatest distances from the midplane.

The contribution of fast shocks can vary significantly across different regions of the halo, with variations reaching up to 20% within the same galaxy. This variability arises from the distinct properties, physical processes, and structures inherent to each galaxy that affect the ionisation of the extraplanar gas. These structures include filaments, knots, extraplanar H II regions, and nearby neighbouring galaxies. Nonetheless, the distribution of H II regions within the disc consistently exerts a substantial influence on the ionisation of the halo gas.

A prime example of this phenomenon is IC1553. In the [N II] /Hα emission line map, it reveals a biconical central structure within the halo, previously interpreted as indicative of outflows or superbubbles. Nonetheless, at the bicone's location (MAD = 0), the galaxy's disk is expected to exhibit a lower specific star formation rate (sSFR) along the line-of-sight due to the presence of the galaxy's bulge, in contrast to the intense emission from the bright adjacent SF regions at the edge of the disk, as observed in projection, exhibiting typical H II region (low) emission values. This scenario is more pronounced in the [S II] /Hα and [O I] /Hα maps, where the background emission conspicuously permeates the halo with typical extended eDIG values. These observations, coupled with the absence of any structure in Hα , [O III] /Hβ , the consistent [S II] /[N II] ratio, and the lack of spatial correlation with potential ionisation sources within the disk, indicate that this bicone is an optical artefact resulting from the projection effect relative to the line-of-sight of the high-level SF regions in the galaxy's disk, in relation to a pervasive background eDIG emission in the halo.

From this perspective, it can be inferred that the extended eDIG emission comprises multiple overlapping components contingent upon the line of sight: eDIG emanating from low-density gas, typified by elevated [N II] , [S II] line ratios, and gas ionised through star formation (SF) activity proximate to the midplane of edge-on galaxies, with typical H II line emission values. The overlaying patterns vary according to the morphology and extent of SF regions within the galactic plane, resulting in a complex morphology of the eDIG concerning line emissions.

6.1 Future work

The methodology and the diverse sample presented, in terms of morphology, properties, and resolution, have significant potential for further detailed investigation of the DIG.

For instance, 6.1 shows the Hα line map of the NGC1365 galaxy, with its respective segmentation map, obtained by applying the methodology described in Chapter 3, plotted in the background. This galaxy, which also belongs to the PHANGS-MUSE survey, exhibits extraordinary spatial resolution (FWHM $\approx$ 65 pc). The figure demonstrates that the methodology can be applied to galaxies with these characteristics, enabling the exploration of the DIG at sub-hectoparsec resolution, where the structure of the ISM can be resolved.

In the future, this methodology can be applied and expanded the analysis to the full BETIS sample selected from the AMUSING, AMUSING+, and AMUSING++ project samples (López-Cobá et al. 2020). We can explore how the results and methodology may vary based on galaxy morphology, resolution and inclination (including galaxies in interaction and mergers), and we will investigate the influence of the (e)DIG on the determination of various parameters, including chemical abundances and star formation rates. In addition, we can asses correlations of the DIG properties with global galactic properties, such as the morphology or the neutral hydrogen abundance. Additionally, we can explore other spectroscopic lines of interest for the DIG study, such the high-excitation He I, aiming to uncover potential secondary ionisation mechanisms of the DIG.

In regard to the eDIG, we can examine the kinematic reflection of the eDIG connection with the galactic plane. Specifically, we will analyse radial variations in rotational velocity gradients, referred to as "lag," which are also observed in galaxies of the eBETIS sample (see figure 6.2). These variations are correlated with the SFR and associated with morphological structures within the halo. Additionally, we will investigate the energy deposition into the ISM through SF-related feedback mechanisms, the primary source of the eDIG ionisation.

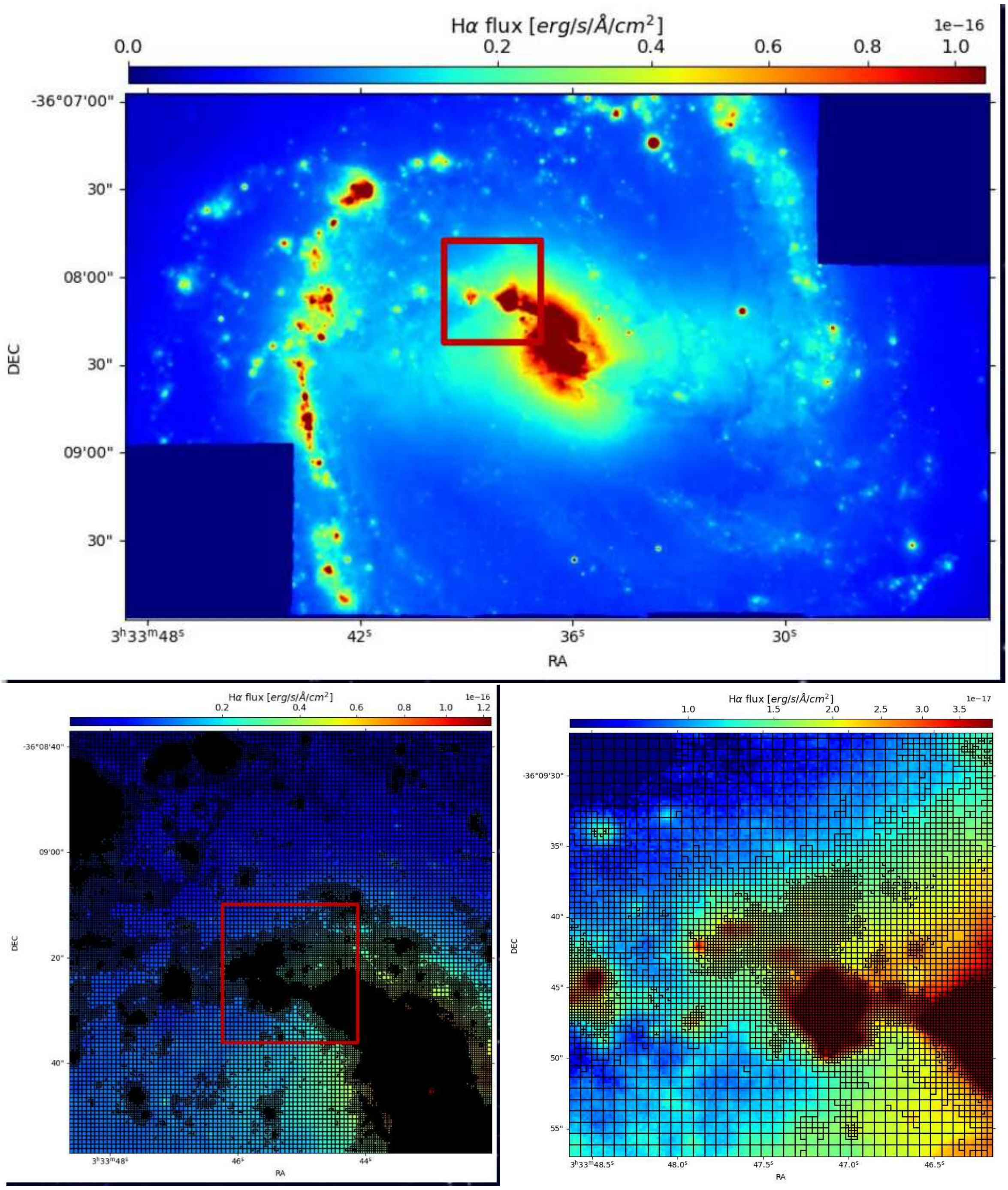

Figure 6.1: NGC1365 Hα line map (top image). Down-left image is the zoom-in of the region squared in the top image, and down-right image is the zoom-in of the region squared in the down left-image, all with their respective segmentation map obtained applying the methodology of Ch. 3.

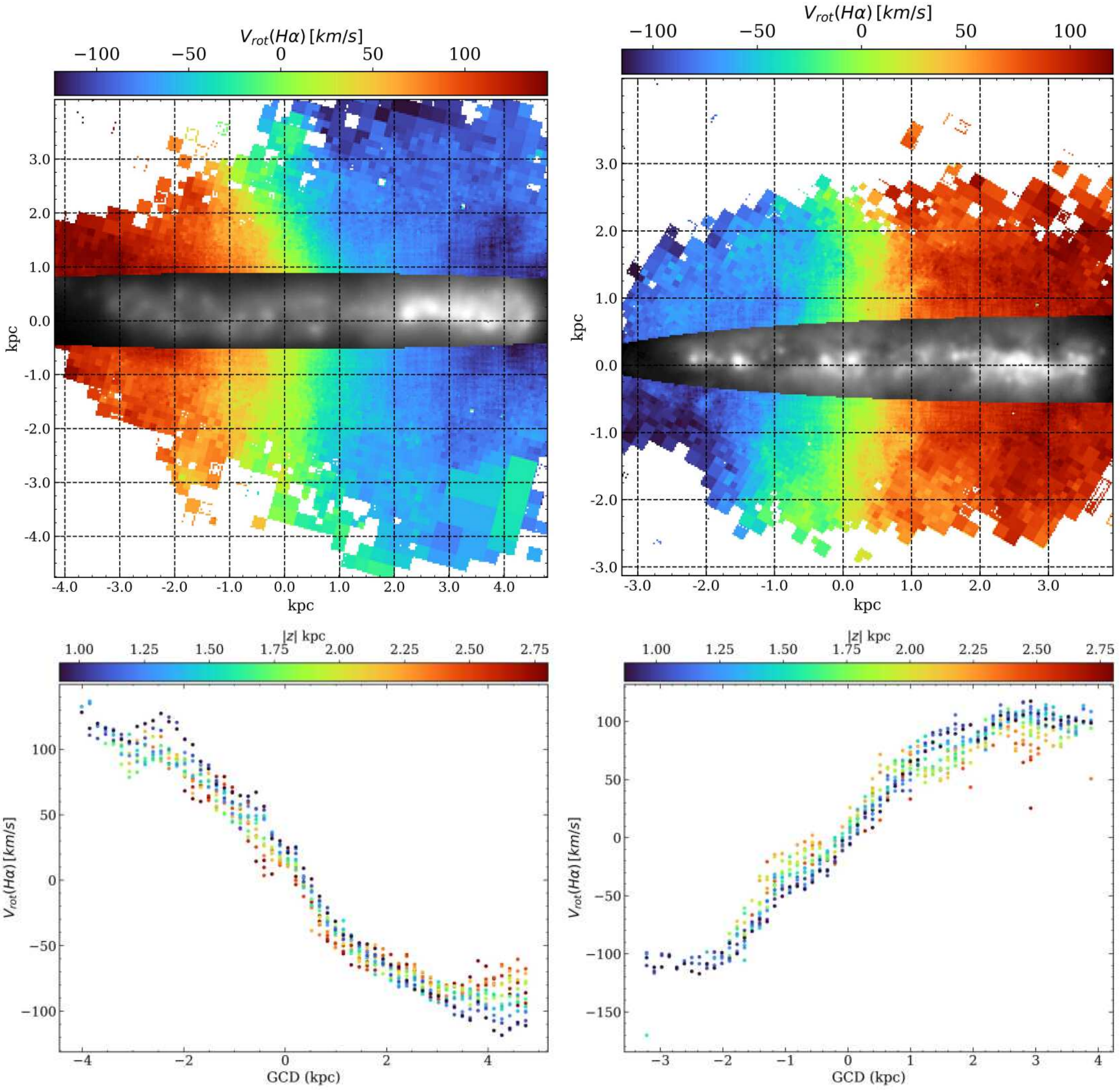

Figure 6.2: IC1553 (left) and ESO157-49 (right) Hα rotation velocity map and curves. The curves show clearly the "lag" in the rotation velocity of the halo. Besides the velocity gradients seems to be correlated with the H II regions distribution.

List of publications

The following papers have been published during the development of the PhD.

As first author

3) Bidimensional Exploration of the warm-Temperature Ionised gaS (BETIS) II. Revisiting the ionisation mechanism of the extraplanar diffuse ionised gas.
R. González-Díaz, F. Fabián Rosales-Ortega, & L. Galbany
A&A Accepted, DOI: https://doi.org/10.48550/arXiv.2406.17123

2) Bidimensional Exploration of the warm-Temperature Ionised gaS (BETIS) I. Sample presentation and first results.
R. González-Díaz, F. Fabián Rosales-Ortega, L. Galbany et al.
A&A 687, A20 (2024), DOI: https://doi.org/10.1051/0004-6361/202348453

1) Supernova environments in J-PLUS: Normalized cumulative rank distributions and stellar population synthesis combining narrow- and broad-band filters.
R. González-Díaz, L. Galbany, Tuomas Kangas, R. García-Benito, J. P. Anderson et al.
A&A 684, A104 (2024), DOI: https://doi.org/10.1051/0004-6361/202349029

As co-author

3) Supernova Remnant properties and Luminosity Functions in NGC 7793 using MUSE IFS.
Kopsacheili, M; Jiménez-Palau, C.; **González-Díaz, R.** et al.
MNRAS 530, 1 (2024), DOI: https://doi.org/10.1093/mnras/stae874

2) A characterization of ASAS-SN core-collapse supernova environments with VLT+MUSE: I. Sample selection, analysis of local environments, and correlations with light curve properties.
Pessi, Thallis ; Prieto, Jose L. ; Anderson, Joseph P. ; Galbany, Lluís ; Lyman, Joseph D. ; Kochanek, Christopher ; Dong, Subo ; Forster, Francisco ; **González Díaz, R.** et al.
A&A 677, A28 (2023), DOI: https://doi.org/10.1051/0004-6361/202346512

1) Transitional events in the spectrophotometric regime between stripped envelope and superluminous supernovae.
Prentice, S. J., Inserra, C., Schulze, S. Nicholl, M. Mazzali, P. A. Vergani, S. D. Galbany, L. Anderson, J. P. Ashall, C. Chen, T. W. Deckers, M. Delgado Mancheño, M. **González Díaz, R.** et al.
MNRAS 508, 3 (2021), DOI: https://doi.org/10.1093/mnras/stab2864

Bibliography

2001, Post-AGB Objects as a Phase of Stellar Evolution Astrophysics and Space Science Library Vol. 265, doi:10.1007/978-94-015-9688-6.

Abgrall H., Le Bourlot J., Pineau Des Forets G., Roueff E., Flower D. R., Heck L., 1992, , 253, 525

Ahumada R., et al., 2020, , 249, 3

Allen M. G., Groves B. A., Dopita M. A., Sutherland R. S., Kewley L. J., 2008, , 178, 20

Asplund M., Amarsi A. M., Grevesse N., 2021, , 653, A141

Bacon R., et al., 2010, in McLean I. S., Ramsay S. K., Takami H., eds, Society of Photo-Optical Instrumentation Engineers (SPIE) Conference Series Vol. 7735, Ground-based and Airborne Instrumentation for Astronomy III. p. 773508 (`arXiv:2211.16795`), doi:10.1117/12.856027

Baldwin J. A., Phillips M. M., Terlevich R., 1981, , 93, 5

Baluja K. L., Burke P. G., Kingston A. E., 1980, Journal of Physics B Atomic Molecular Physics, 13, L543

Barnes A. T., et al., 2023, , 944, L22

Begelman M. C., Fabian A. C., 1990, , 244, 26P

Belfiore F., et al., 2016, , 461, 3111

Belfiore F., et al., 2022, , 659, A26

Berkhuijsen E. M., Mitra D., Mueller P., 2006, Astronomische Nachrichten, 327, 82

Bertin E., Arnouts S., 1996, , 117, 393

Bianchi L., Shiao B., Thilker D., 2017, , 230, 24

Binette L., Flores-Fajardo N., Raga A. C., Drissen L., Morisset C., 2009, , 695, 552

Binney J., 2005, in Braun R., ed., Astronomical Society of the Pacific Conference Series Vol. 331, Extra-Planar Gas. p. 131 (`arXiv:astro-ph/0409639`), doi:10.48550/arXiv.astro-ph/0409639

Birk G. T., Lesch H., Neukirch T., 1998, , 296, 165

Bizyaev D., et al., 2017, , 839, 87

Bizyaev D., Chen Y.-M., Shi Y., Roy N., Riffel R., Riffel R. A., Fernández-Trincado J. G., 2022, , 516, 3092

Black J. H., Dalgarno A., 1976, , 203, 132

Bland-Hawthorn J., Freeman K. C., Quinn P. J., 1997, , 490, 143

Bland-Hawthorn J., Sutherland R., Agertz O., Moore B., 2007, , 670, L109

Boehringer H., Fabian A. C., 1989, , 237, 1147

Boettcher E., Gallagher J. S. I., Zweibel E. G., 2019, , 885, 160

Boquien M., Buat V., Perret V., 2014, , 571, A72

Born M., 1969, Modern Physics. Atomic Physics

Boselli A., et al., 2021, , 646, A139

Bregman J. N., 1980, , 236, 577

Bruzual A. G., 2007a, in Vazdekis A., Peletier R., eds, Vol. 241, Stellar Populations as Building Blocks of Galaxies. pp 125–132 (`arXiv:astro-ph/0703052`), doi:10.1017/S1743921307007624

Bruzual G., 2007b, in Vallenari A., Tantalo R., Portinari L., Moretti A., eds, Astronomical Society of the Pacific Conference Series Vol. 374, From Stars to Galaxies: Building the Pieces to Build Up the Universe. p. 303 (`arXiv:astro-ph/0702091`), doi:10.48550/arXiv.astro-ph/0702091

Bruzual G., Charlot S., 2003, , 344, 1000

Bryant J. J., et al., 2015, , 447, 2857

Bundy K., et al., 2015, , 798, 7

Cappellari M., Copin Y., 2003, , 342, 345

Cardelli J. A., Clayton G. C., Mathis J. S., 1989, , 345, 245

Cecil G., Bland-Hawthorn J., Veilleux S., 2002, , 576, 745

Ceverino D., Klypin A., 2008, in Bureau M., Athanassoula E., Barbuy B., eds, Vol. 245, Formation and Evolution of Galaxy Bulges. pp 33–34 (`arXiv:0710.1666`), doi:10.1017/S1743921308017213

Ceverino D., Klypin A., 2009, , 695, 292

Chabrier G., 2003, , 115, 763

Chevalier R. A., Clegg A. W., 1985, , 317, 44

Chevallard J., Charlot S., Wandelt B., Wild V., 2013, , 432, 2061

Ciardi B., Bianchi S., Ferrara A., 2002, , 331, 463

Cid Fernandes R., Mateus A., Sodré L., Stasińska G., Gomes J. M., 2005, , 358, 363

Cid Fernandes R., Stasińska G., Schlickmann M. S., Mateus A., Vale Asari N., Schoenell W., Sodré L., 2010, , 403, 1036

Cid Fernandes R., Stasińska G., Mateus A., Vale Asari N., 2011, , 413, 1687

Colbert E. J. M., Baum S. A., Gallimore J. F., O'Dea C. P., Christensen J. A., 1996, , 467, 551

Collins J. A., Rand R. J., 2001, , 551, 57

Combes F., 2014, in Seigar M. S., Treuthardt P., eds, Astronomical Society of the Pacific Conference Series Vol. 480, Structure and Dynamics of Disk Galaxies. p. 211 (`arXiv:1309.1603`), doi:10.48550/arXiv.1309.1603

Comerón S., Salo H., Knapen J. H., Peletier R. F., 2019, , 623, A89

Congiu E., et al., 2023, , 672, A148

Contini T., Considere S., Davoust E., 1998, , 130, 285

Cowie L. L., McKee C. F., 1977, , 211, 135

Croom S. M., et al., 2012, , 421, 872

Dahlem M., 1997, , 109, 1298

Dahlem M., Lisenfeld U., Golla G., 1995, , 444, 119

Dale J. E., Bonnell I. A., Clarke C. J., Bate M. R., 2005, , 358, 291

Della Bruna L., et al., 2022a, , 660, A77

Della Bruna L., et al., 2022b, , 666, A29

Denicoló G., Terlevich R., Terlevich E., 2002, , 330, 69

Dettmar R. J., 1990, , 232, L15

Dettmar R. J., 1998, in Breitschwerdt D., Freyberg M. J., Truemper J., eds, , Vol. 506, IAU Colloq. 166: The Local Bubble and Beyond. pp 527–538

Dirks L., Dettmar R. J., Bomans D. J., Kamphuis P., Schilling U., 2023, , 678, A84

Domgorgen H., Mathis J. S., 1994, , 428, 647

Dopita M. A., Sutherland R. S., 1995, , 455, 468

Dove J. B., Shull J. M., Ferrara A., 2000, , 531, 846

Draine B. T., 2011, Physics of the Interstellar and Intergalactic Medium

Emsellem E., et al., 2022, , 659, A191

Ercolano B., Barlow M. J., Storey P. J., Liu X. W., 2003, , 340, 1136

Erroz-Ferrer S., et al., 2019, , 484, 5009

Espinosa-Ponce C., Sánchez S. F., Morisset C., Barrera-Ballesteros J. K., Galbany L., García-Benito R., Lacerda E. A. D., Mast D., 2020, , 494, 1622

Ferguson A. M. N., Wyse R. F. G., Gallagher J. S. I., Hunter D. A., 1996a, , 111, 2265

Ferguson A. M. N., Wyse R. F. G., Gallagher J. S., 1996b, , 112, 2567

Ferrara A., Bianchi S., Dettmar R.-J., Giovanardi C., 1996, , 467, L69

Fesen R. A., Hurford A. P., 1995, , 110, 747

Field G. B., 1989, Highlights of Astronomy, 8, 567

Finkbeiner D. P., 2003, , 146, 407

Fitzpatrick E. L., 1999, , 111, 63

Flores-Fajardo N., Morisset C., Stasińska G., Binette L., 2011, , 415, 2182

Franco J., Tenorio-Tagle G., Bodenheimer P., 1990, , 349, 126

Fruchter A. S., Hook R. N., 2002, , 114, 144

Gadotti D. A., et al., 2019, , 482, 506

Gaensler B. M., Madsen G. J., Chatterjee S., Mao S. A., 2008, , 25, 184

Galarza V. C., Walterbos R. A. M., Braun R., 1999, , 118, 2775

Galbany L., et al., 2016, , 455, 4087

Gatto A., et al., 2017, , 466, 1903

González-Díaz R., et al., 2024, , 687, A20

Grasha K., 2022, arXiv e-prints, p. arXiv:2211.06005

Gray W. J., Oey M. S., Silich S., Scannapieco E., 2019, , 887, 161

Greenawalt B., Walterbos R. A. M., Braun R., 1997, , 483, 666

Grisdale K. M., 2017, PhD thesis, University of Surrey, UK

Guélin M., 1974, in Kerr F. J., Simonson S. C., eds, Vol. 60, Galactic Radio Astronomy. p. 51

Haffner L. M., Reynolds R. J., Tufte S. L., 1999, , 523, 223

Haffner L. M., et al., 2009a, Rev. Mod. Phys., 81, 969

Haffner L. M., et al., 2009b, Reviews of Modern Physics, 81, 969

Hausen N. R., Reynolds R. J., Haffner L. M., 2002, , 124, 3336

Heiles C., 1990, , 354, 483

Heiles C., Troland T. H., 2003, , 586, 1067

Hewish A., Bell S. J., Pilkington J. D. H., Scott P. F., Collins R. A., 1968, , 217, 709

Hidalgo-Gámez A. M., 2005, , 442, 443

Hills J. G., 1974, , 190, 109

Ho I. T., Kudritzki R.-P., Kewley L. J., Zahid H. J., Dopita M. A., Bresolin F., Rupke D. S. N., 2015, , 448, 2030

Ho I. T., et al., 2016, , 457, 1257

Hodges-Kluck E., Bregman J. N., 2014, , 789, 131

Hodges-Kluck E., Cafmeyer J., Bregman J. N., 2016, , 833, 58

Hoffmann T. L., Lieb S., Pauldrach A. W. A., Lesch H., Hultzsch P. J. N., Birk G. T., 2012, , 544, A57

Hoopes C. G., Walterbos R. A. M., 2003, , 586, 902

Hopkins P. F., Kereš D., Oñorbe J., Faucher-Giguère C.-A., Quataert E., Murray N., Bullock J. S., 2014, , 445, 581

Howk J. C., Savage B. D., 2000, , 119, 644

Hoyle F., Ellis G. R. A., 1963, Australian Journal of Physics, 16, 1

Hummel E., Beck R., Dahlem M., 1991, , 248, 23

Husemann B., et al., 2013, , 549, A87

Husemann B., et al., 2019, , 627, A53

Jenkins E. B., Meloy D. A., 1974, , 193, L121

Jo Y.-S., Seon K.-i., Shinn J.-H., Yang Y., Lee D., Min K.-W., 2018, , 862, 25

Jones A., et al., 2017, , 599, A141

Kashibadze O. G., 2008, Astrophysics, 51, 336

Kaufmann T., Mayer L., Wadsley J., Stadel J., Moore B., 2006, , 370, 1612

Kennicutt Robert C. J., 1998, , 36, 189

Kennicutt R. C., Evans N. J., 2012, , 50, 531

Kennicutt Robert C. J., Edgar B. K., Hodge P. W., 1989, , 337, 761

Kennicutt Robert C. J., Tamblyn P., Congdon C. E., 1994, , 435, 22

Kewley L. J., Dopita M. A., Sutherland R. S., Heisler C. A., Trevena J., 2001, , 556, 121

Klessen R. S., Glover S. C. O., 2016, in Revaz Y., Jablonka P., Teyssier R., Mayer L., eds, Saas-Fee Advanced Course Vol. 43, Saas-Fee Advanced Course. p. 85 (`arXiv:1412.5182`), doi:10.1007/978-3-662-47890-5_2

Kopsacheili M., Zezas A., Leonidaki I., 2020, , 491, 889

Kourkchi E., Tully R. B., 2017, , 843, 16

Kulkarni S. R., Heiles C., 1987, in Hollenbach D. J., Thronson Harley A. J., eds, Vol. 134, Interstellar Processes. p. 87, doi:10.1007/978-94-009-3861-8_5

Kwok S., 2000, The Origin and Evolution of Planetary Nebulae

Lacerda E. A. D., et al., 2018, , 474, 3727

Lehnert M. D., Heckman T. M., 1995, , 97, 89

Leitherer C., Robert C., Drissen L., 1992, , 401, 596

Lequeux J., 2005, The Interstellar Medium, doi:10.1007/b137959.

Levesque E. M., Kewley L. J., Larson K. L., 2010, , 139, 712

Levy R. C., et al., 2019, , 882, 84

Li Z., et al., 2023a, , 518, 286

Li A., Fraternali F., Marasco A., Trager S. C., Pezzulli G., Mancera Piña P. E., Verheijen M. A. W., 2023b, , 520, 147

Lipovetsky V. A., Neizvestny S. I., Neizvestnaya O. M., 1988, Soobshcheniya Spetsial'noj Astrofizicheskoj Observatorii, 55, 5

López-Cobá C., Sánchez S. F., Bland-Hawthorn J., Moiseev A. V., Cruz-González I., García-Benito R., Barrera-Ballesteros J. K., Galbany L., 2019, , 482, 4032

López-Cobá C., et al., 2020, , 159, 167

López Fernández R., et al., 2016, , 458, 184

López-Sánchez Á. R., Esteban C., García-Rojas J., Peimbert M., Rodríguez M., 2007, , 656, 168

Lu L.-Y., et al., 2023, , 519, 6098

Lugo-Aranda A. Z., Sánchez S. F., Espinosa-Ponce C., López-Cobá C., Galbany L., Barrera-Ballesteros J. K., Sánchez-Menguiano L., Anderson J. P., 2022, RAS Techniques and Instruments, 1, 3

Lugo-Aranda A. Z., Sánchez S. F., Barrera-Ballesteros J. K., López-Cobá C., Espinosa-Ponce C., Galbany L., Anderson J. P., 2024, ,

Mac Low M.-M., McCray R., 1988, , 324, 776

Mac Low M.-M., McCray R., Norman M. L., 1989, , 337, 141

Madsen G. J., Reynolds R. J., 2005, , 630, 925

Madsen G. J., Reynolds R. J., Haffner L. M., 2006, , 652, 401

Makarov D., Prugniel P., Terekhova N., Courtois H., Vauglin I., 2014, , 570, A13

Maksym W. P., Fabbiano G., Elvis M., Karovska M., Paggi A., Raymond J., Wang J., Storchi-Bergmann T., 2016, , 829, 46

Marasco A., Fraternali F., Binney J. J., 2012, , 419, 1107

Marinacci F., Fraternali F., Nipoti C., Binney J., Ciotti L., Londrillo P., 2011, , 415, 1534

Martin C. L., 1997, , 491, 561

Mayya Y. D., et al., 2023, , 521, 5492

McCray R., Snow T. P. J., 1979, , 17, 213

McKee C. F., Hollenbach D. J., 1980, , 18, 219

McKee C. F., Ostriker J. P., 1977, , 218, 148

Mebold U., Hills D. L., 1975, , 42, 187

Miller Walter Warren I., Cox D. P., 1993, , 417, 579

Miller S. T., Veilleux S., 2003, , 148, 383

Minter A. H., Spangler S. R., 1997, , 485, 182

Mitronova S. N., Karachentsev I. D., Karachentseva V. E., Jarrett T. H., Kudrya Y. N., 2004, Bulletin of the Special Astrophysics Observatory, 57, 5

Molina M., Eracleous M., Barth A. J., Maoz D., Runnoe J. C., Ho L. C., Shields J. C., Walsh J. L., 2018, , 864, 90

Monnet G., 1971, , 12, 379

Morgan W. W., Sharpless S., Osterbrock D., 1952, , 57, 3

Muñoz-Mateos J. C., et al., 2015, , 219, 3

Norman C. A., Ikeuchi S., 1989, , 345, 372

Och S. R., Lucy L. B., Rosa M. R., 1998, , 336, 301

Oey M. S., et al., 2007, , 661, 801

Okabe A., Boots B., Sugihara K., Chiu S., 2000, Spatial Tessellations: Concepts and Applications of Voronoi Diagrams. Vol. 43, doi:10.2307/2687299,

Osterbrock D. E., Ferland G. J., 2006, Astrophysics of gaseous nebulae and active galactic nuclei. University Science Books

Otte B., Reynolds R. J., Gallagher J. S. I., Ferguson A. M. N., 2001, , 560, 207

Otte B., Gallagher J. S. I., Reynolds R. J., 2002, , 572, 823

Pettini M., West K. A., 1982, , 260, 561

Poetrodjojo H., D'Agostino J. J., Groves B., Kewley L., Ho I. T., Rich J., Madore B. F., Seibert M., 2019, , 487, 79

Poggianti B. M., et al., 2017, , 844, 48

Putman M. E., 2017, in Fox A., Davé R., eds, Astrophysics and Space Science Library Vol. 430, Gas Accretion onto Galaxies. p. 1 (`arXiv:1612.00461`), doi:10.1007/978-3-319-52512-9_1

Rand R. J., 1996, , 462, 712

Rand R. J., 1997, , 474, 129

Rand R. J., 1998, , 501, 137

Rand R. J., 1999, , 521, 492

Rand R. J., 2000, , 537, L13

Rand R. J., Kulkarni S. R., Hester J. J., 1990, , 352, L1

Rautio R. P. V., Watkins A. E., Comerón S., Salo H., Díaz-García S., Janz J., 2022, , 659, A153

Raymond J. C., 1992, , 384, 502

Reynolds R. J., 1971, PhD thesis, University of Wisconsin, Madison

Reynolds R. J., 1985, , 294, 256

Reynolds R. J., 1989, , 345, 811

Reynolds R. J., 1991, in Bloemen H., ed., Vol. 144, The Interstellar Disk-Halo Connection in Galaxies. p. 67

Reynolds R. J., Cox D. P., 1992, , 400, L33

Reynolds R. J., Roesler F. L., Scherb F., 1973, , 179, 651

Reynolds R. J., Hausen N. R., Tufte S. L., Haffner L. M., 1998, , 494, L99

Reynolds R. J., Haffner L. M., Tufte S. L., 1999, , 525, L21

Reynolds R. J., Sterling N. C., Haffner L. M., 2001, , 558, L101

Rich J. A., Dopita M. A., Kewley L. J., Rupke D. S. N., 2010, , 721, 505

Rich J. A., Kewley L. J., Dopita M. A., 2011, , 734, 87

Rodríguez-Baras M., Díaz A. I., Rosales-Ortega F. F., 2019, , 631, A23

Rosa M., Richter O. G., 1988, , 192, 57

Rosales-Ortega F. F., Arribas S., Colina L., 2012, , 539, A73

Rossa J., Dettmar R. J., 2003a, , 406, 493

Rossa J., Dettmar R. J., 2003b, , 406, 505

Rossa J., Dettmar R.-J., Walterbos R. A. M., Norman C. A., 2004, , 128, 674

Sánchez S. F., et al., 2012, , 538, A8

Sánchez S. F., et al., 2016, , 52, 171

Sardaneta M. M., Amram P., Rampazzo R., Rosado M., Sánchez-Cruces M., Fuentes-Carrera I., Ghosh S., 2024, , 528, 2145

Sarkar K. C., Sternberg A., Gnat O., 2022, , 940, 44

Sato T., Martin C. L., Noeske K. G., Koo D. C., Lotz J. M., 2009, , 696, 214

Schilke P., Benford D. J., Hunter T. R., Lis D. C., Phillips T. G., 2001, , 132, 281

Sembach K. R., Savage B. D., 1992, in American Astronomical Society Meeting Abstracts #180. p. 25.05

Sembach K. R., Howk J. C., Ryans R. S. I., Keenan F. P., 2000, , 528, 310

Seon K.-I., 2009, , 703, 1159

Shapiro P. R., Benjamin R. A., 1991, , 103, 923

Shapiro P. R., Field G. B., 1976, , 205, 762

Sharp R. G., Bland-Hawthorn J., 2010, , 711, 818

Shinn J.-H., Seon K.-I., 2015, , 815, 133

Simpson J. P., Colgan S. W. J., Cotera A. S., Erickson E. F., Hollenbach D. J., Kaufman M. J., Rubin R. H., 2007, , 670, 1115

Slavin J. D., Shull J. M., Begelman M. C., 1993, , 407, 83

Sokolowski J., 1993, in Cassinelli J. P., Churchwell E. B., eds, Astronomical Society of the Pacific Conference Series Vol. 35, Massive Stars: Their Lives in the Interstellar Medium. p. 540

Sokolowski J., Bland-Hawthorn J., 1991, , 103, 911

Soto K. T., Lilly S. J., Bacon R., Richard J., Conseil S., 2016, , 458, 3210

Sparre M., et al., 2015, , 447, 3548

Storchi-Bergmann T., Calzetti D., Kinney A. L., 1994, , 429, 572

Strömgren B., 1939, , 89, 526

Tacchella S., et al., 2022, , 513, 2904

Taylor S. D., Morata O., Williams D. A., 1998, , 336, 309

Tenorio-Tagle G., 1979, , 71, 59

Tenorio-Tagle G., Bodenheimer P., 1988, , 26, 145

Thilker D. A., Braun R., Walterbos R. A. M., 2000, , 120, 3070

Thilker D. A., Walterbos R. A. M., Braun R., Hoopes C. G., 2002, , 124, 3118

Tielens A. G. G. M., 2005, The Physics and Chemistry of the Interstellar Medium

Tinsley B. M., 1968, , 151, 547

Tufte S. L., Reynolds R. J., Haffner L. M., 1998, , 504, 773

Tüllmann R., Dettmar R. J., Soida M., Urbanik M., Rossa J., 2000, , 364, L36

Tüllmann R., Pietsch W., Rossa J., Breitschwerdt D., Dettmar R. J., 2006, , 448, 43

Turner B. E., 1994, , 437, 658

Vale Asari N., Couto G. S., Cid Fernandes R., Stasińska G., de Amorim A. L., Ruschel-Dutra D., Werle A., Florido T. Z., 2019, , 489, 4721

Vale Asari N., et al., 2020, , 498, 4205

Veilleux S., Cecil G., Bland-Hawthorn J., 2005, , 43, 769

Voges E. S., Walterbos R. A. M., 2006, , 644, L29

Vorontsov-Vel'Yaminov B. A., Arkhipova V. P., 1968, Trudy Gosudarstvennogo Astronomicheskogo Instituta, 38, 1

Walterbos R. A. M., Braun R., 1994, , 431, 156

Wang J., Heckman T. M., Lehnert M. D., 1997, , 491, 114

Weaver T. A., Zimmerman G. B., Woosley S. E., 1977, Presupernova evolution of massive stars

Weber J. A., Pauldrach A. W. A., Hoffmann T. L., 2019a, , 622, A115

Weber J. A., Pauldrach A. W. A., Hoffmann T. L., 2019b, , 622, A115

Weedman D. W., 1977, , 15, 69

Weilbacher P. M., et al., 2020, , 641, A28

Weiler K. W., Sramek R. A., 1988, , 26, 295

Weingartner J. C., Draine B. T., 2001, , 134, 263

Werle A., Cid Fernandes R., Vale Asari N., Bruzual G., Charlot S., Gonzalez Delgado R., Herpich F. R., 2019, , 483, 2382

Wiener J., Zweibel E. G., Oh S. P., 2013, , 767, 87

Wilson A. S., Tsvetanov Z. I., 1994, , 107, 1227

Wood K., Loeb A., 2000, , 545, 86

Wood K., Mathis J. S., 2004, , 353, 1126

Wood K., Haffner L. M., Reynolds R. J., Mathis J. S., Madsen G., 2005, , 633, 295

Young H. D., Freedman R. A., Ford L. A., 2020, University physics with modern physics

Zaragoza-Cardiel J., Fritz J., Aretxaga I., Mayya Y. D., Rosa-González D., Beckman J. E., Bruzual G., Charlot S., 2020, , 499, 1172

Zaw I., Chen Y.-P., Farrar G. R., 2019, , 872, 134

Zhang K., et al., 2017, , 466, 3217

Zurita A., Rozas M., Beckman J. E., 2000, , 363, 9

Zurita A., Beckman J. E., Rozas M., Ryder S., 2002, , 386, 801

de Vaucouleurs G., de Vaucouleurs A., Corwin Herold G. J., Buta R. J., Paturel G., Fouque P., 1991, Third Reference Catalogue of Bright Galaxies